

DISS. ETH NO. 22864

**Phase relations, compositions and trace element
partitioning of solid and mobile phases in the hydrous
MORB system at 2-3 GPa**

A thesis submitted to attain the degree of

DOCTOR OF SCIENCES of ETH ZURICH

(Dr. sc. ETH Zurich)

presented by

Stefanie Marianne Luginbühl

Dipl. Geol.
University of Zurich

born on 22.01.1980
citizen of Schlosswil (BE)

accepted on the recommendation of

Prof. Dr. Peter Ulmer
Prof. Dr. Thomas Pettke
Prof. Dr. Max W. Schmidt
Prof. Dr. Roland Stalder

2015

Table of contents

Abstract/Zusammenfassung	7
Chapter 1. Introduction	
1.1. Background	13
1.2. Previous experimental work	17
1.3. Goals of this study	18
1.4. Organization of the thesis	19
Chapter 2. Methodology	
2.1. Experimental approach	21
2.2. Starting materials and oxygen fugacity	22
2.3. Capsule design and diamond traps	25
2.4. Piston cylinder experiments	26
2.5. Analytical methods	29
2.5.1. Diamond-trap experiments and the freezing stage	29
2.5.2. Laser ablation ICP-MS	32
2.5.3. Sample preparation for minerals analysis	34
2.5.4. Electron probe micro-analysis	34
Chapter 3. Zoisite in the subducting oceanic crust: Implications for the release of mobile phases during dehydration of the slab	
Abstract	35
3.1. Introduction	36
3.2. Catching fluids: Experimental and analytical methods	37
3.3. Bulk volatile composition	38
3.4. Zoisite composition	42
3.5. Zoisite/fluid partitioning	44
3.6. Summary and conclusions	46
3.7. Electronic appendix	48
Chapter 4. Composition and trace element partitioning of mobile volatile phases and solid mineral residues during water-saturated dehydration and melting of basalt	
Abstract	53
4.1. Introduction	54
4.2. Experimental methods	55
4.2.1. Synthesis of the starting material	55
4.2.2. Experimental setup	58
4.3. Analytical methods	59
4.3.1. LA-ICP-MS	59
4.3.2. Electron probe micro-analysis	62

4.4. Results	63
4.4.1. Phase relations	63
4.4.2. Nature of the volatile phase	68
4.4.3. Major element composition	69
4.4.3.1. Bulk volatile phase	69
4.4.3.2. Garnet	74
4.4.3.3. Clinopyroxene	75
4.4.3.4. Amphibole	77
4.4.3.5. Ti-phases	78
4.4.3.6. Other minerals	78
4.4.4. Trace element composition and partitioning	83
4.4.4.1. Garnet	83
4.4.4.2. Clinopyroxene	85
4.4.4.3. Ti-phases	86
4.5. Discussion	92
4.5.1. Garnet	92
4.5.2. Clinopyroxene	95
4.5.3. Ti-phases	100
4.5.4. Implications for subduction zone dehydration	102
4.6. Summary and concluding remarks	106

Chapter 5. The influence of phengite in subducted crust: implications for arc magmatism

Abstract	109
5.1. Introduction	110
5.2. Methods	111
5.2.1. Synthesis of the starting material	111
5.2.2. Experimental methods	112
5.2.3. Analytical methods	114
5.2.3.1. Internal standard solution	114
5.2.3.2. LA-ICP-MS	117
5.2.3.3. Electron probe micro-analysis (EPMA)	117
5.3. Results	118
5.3.1. Phase relations	118
5.3.2. Water content of the volatile phase	121
5.3.3. Major element composition	122
5.3.3.1. Bulk volatile phase	122
5.3.3.2. Garnet	125
5.3.3.3. Clinopyroxene	125
5.3.3.4. Phengite	125
5.3.3.5. Minor minerals	126
5.3.4. Trace element partitioning	128
5.3.4.1. Garnet	128
5.3.4.2. Phengite	129

5.3.4.3. Rutile	133
5.3.4.4. Clinopyroxene	135
5.3.4.5. Bulk residues	135
5.4. Discussion	140
5.4.1. Position of the wet solidus	140
5.4.2. Element transport from subducted AOC/sediment compositions	142
5.4.3. Comparison to MORB and the influence of phengite	146
5.5. Summary and concluding remarks	147
Chapter 6. Conclusions and outlook	
6.1. Synthesis	149
6.2. K-free MORB system	149
6.3. Altered MORB/sediment system	151
6.4. Outlook	152
Bibliography	155
Appendix A	167
Appendix B	181
Acknowledgements	187
Curriculum vitae	189

Abstract

Subduction-related arc volcanic and plutonic magmas are generated in the depleted upper mantle, yet the most characteristic geochemical marks in arc rocks compared to MOR basalts are left by fluids and melts originating from the subducted oceanic lithosphere. The latter experiences enrichment of a broad range of trace elements on the way from its origin to subduction and the various lithologies present contribute their specific element signature to the overlying mantle wedge during dehydration and melting of the slab. The release of elements is mainly governed by the prevailing pressure and temperature conditions at depth and consequently by the stable residual mineral assemblage in the subducted slab. However, the nature and composition of the mobile slab components still remain largely unknown. In this study, we have experimentally examined the composition of bulk volatiles (aqueous fluids and hydrous melts) in equilibrium with an eclogitic phase assemblage. Furthermore, we have determined partition coefficients between those mobile phases and the stable minerals with a special focus on minor and accessory minerals. Two chemical systems were investigated, a potassium-free basalt and a strongly altered basalt/sediment system with the attempt to compare their distinct influence on the signature of arc rocks generated by partial melting of the metasomatically modified subarc mantle.

Piston cylinder experiments were conducted at 2 and 3 GPa and 700 to 1200°C using diamond traps to collect the bulk volatiles. The latter were subsequently analyzed by the cryogenic laser ablation-ICP-MS technique which allows for direct and full major and trace element quantification independent from mass balance calculations. We have adapted the technique to systems containing potassium by the use of bromine as new, external standard for LA-ICP-MS analyses. The residual minerals were measured in order to obtain a full set of partition coefficients describing the entire system.

The results from the K-free basalt system demonstrate that the low-temperature, water-rich and peralkaline bulk volatiles (predominantly aqueous fluids) emerging from the slab have a very limited capacity to transport major and trace elements to the mantle with the exception of large ion lithophile elements (LILE). With increasing temperatures, fluids are replaced by predominantly metaluminous hydrous melts with an orders of magnitude larger potential to carry certain trace elements such as light rare earth elements (LREE) and Th. Those elements are almost exclusively controlled by zoisite. Zoisite partition coefficients ($D(\text{zoi}/\text{fluid})$) have been determined independently from mass balance calculations for the first time and reveal similar compatibility for light rare earth elements and Th as literature $D(\text{allanite}/\text{melt})$ values. Additionally, partition coefficients have been determined for garnet, clinopyroxene and rutile. Garnet is the major host for heavy rare earth elements (HREE) while rutile controls the high field strength elements (HFSE),

ABSTRACT

especially Nb and Ta. Clinopyroxene exerts only little control on the trace element signature of the bulk volatiles. A characteristic arc rock signature can only be obtained at suprasolidus conditions and when zoisite is exhausted.

The altered basalt/sediment system mainly differs from the K-free MORB system in the presence of the white mica phengite. Based on the results of this study, the wet pelite solidus is located below 800°C. Determined partition coefficients show that phengite is the exclusive host for the LILE with Ba being the most compatible element. Despite the presence of phengite, the resulting bulk volatile trace element patterns reveal that most of the LILE behave volatile-compatible, i.e., are free to migrate into the mantle wedge. Similar to the K-free system, garnet, zoisite and rutile moderate HREE, LREE and Th as well as HFSE, respectively. Arc-typical LILE enrichment over LREE only occurs when both phengite and zoisite are stable, as soon as zoisite becomes exhausted, the ratio changes in favor of LREE due to the lack of a major host mineral. This puts tight constraints on the element ratios observed in natural rocks. Comparison of the two systems examined in this study shows that the resulting bulk volatile trace element patterns are surprisingly similar.

Overall, this study provides bulk volatile (fluid and melt) compositions that were directly and completely analyzed. Especially fluid-dominated volatiles are highly desirable as pertinent data are virtually absent in the literature up to date. Obtained partition coefficients of the residual phases confirm the strong influence of the slab assemblage on the element signature of arc rocks.

Zusammenfassung

Vulkanische und plutonische Magmen über Subduktionszonen entstehen im abgereicherten oberen Erdmantel. Die typischen geochemischen Merkmale von Inselbogengesteinen, welche sie von Basalten an mittelozeanischen Rücken unterscheiden, stammen jedoch von wässrigen Fluiden und Schmelzen, die von der subduzierten ozeanischen Lithosphäre in den oberen Mantel gelangen. Die Lithosphäre wird auf dem Weg von ihrer Entstehung bis zur Subduktion mit einer Bandbreite an Spurenelementen angereichert. Diese Spurenelemente werden während der Dehydratisierung und dem Aufschmelzen der abtauchenden Platte entsprechend der spezifischen Elementsignaturen der verschiedenen vorhandenen Lithologien an den überliegenden Mantel abgegeben. Welche Elemente freigegeben werden, hängt hauptsächlich von den vorherrschenden Druck- und Temperaturbedingungen in der Tiefe, und somit von den stabilen Restmineralvergesellschaftungen in der abtauchenden Lithosphäre ab. Die Beschaffenheit und Zusammensetzung der flüchtigen Bestandteile, die von der abtauchenden Platte freigegeben werden, sind jedoch grösstenteils immer noch unbekannt.

Für diese Studie haben wir die Zusammensetzung mobiler Phasen (wasserhaltiger Fluide und wasserführenden Schmelzen) im Gleichgewicht mit einem eklogitischen Phasengefüge experimentell untersucht. Des Weiteren haben wir die Element-Verteilungskoeffizienten zwischen diesen mobilen Fluiden und Schmelzen und den stabilen Mineralien, mit Schwerpunkt auf Neben- und Begleitmineralien, ermittelt. Zwei chemisch unterschiedliche Systeme, ein kaliumfreies Basalt- und ein stark alteriertes Basalt/Sediment-System, wurden untersucht mit dem Ziel, deren individuellen Einfluss auf die Chemie der Inselbogengesteine, welche durch partielles Schmelzen des metasomatisch veränderten Mantels gebildet werden, zu vergleichen. Die Stempel-Zylinder-Experimente, welche bei 2 und 3 GPa und 700 bis 1200°C durchgeführt wurden, enthalten Diamantfallen, um darin die Fluide und Schmelzen zu sammeln. Diese wurden anschliessend mit einer Tieftemperatur-Laserablation ICP-MS Technik analysiert, welche eine direkte und komplette Quantifizierung der Haupt- und Spurenelemente, unabhängig von Massenbilanzberechnungen, erlaubt. Wir haben die Technik an Systeme mit Kalium angepasst, wobei Brom als neuer externer Standard für die LA-ICP-MS-Analysen dient. Die stabilen Restmineralien wurden ebenfalls gemessen, um ein komplettes Set von Verteilungskoeffizienten zu erhalten mit dem Ziel, das untersuchte System vollständig zu beschreiben.

Die Resultate des kaliumfreien Systems zeigen, dass die wasserreichen und peralkalinen Gesamtfluide (hauptsächlich wasserreiche Fluide), welche vom Slab bei tiefen

ZUSAMMENFASSUNG

Temperaturen gelöst werden, nur eine begrenzte Kapazität haben, um Haupt- und Spurenelemente von der abtauchenden Platte in den Mantel zu transportieren. Die einzige Ausnahme sind lithophile Elemente mit grossem Ionenradius (auch LIL-Elemente, large ion lithophile elements), die sich bei diesen Bedingungen flüchtig verhalten. Mit steigender Temperatur werden Fluide durch metalumine, wasserhaltige Schmelzen ersetzt, welche ein viel grösseres Potential haben, bestimmte Spurenelemente, wie zum Beispiel leichte Seltenerdmetalle (LREE, light rare earth elements) und Thorium, zu transportieren. Diese Elemente sind fast ausschliesslich vom Mineral Zoisit kontrolliert. Zoisit-Verteilungskoeffiziente ($D_{\text{Zoi/Fluid}}$) im Gleichgewicht mit wasserhaltigen Gesamtfluiden wurden zum ersten Mal unabhängig von Massenbilanzberechnungen bestimmt und zeigen eine ähnliche Kompatibilität der leichten Seltenerdmetalle und Thorium wie Allanit im Gleichgewicht mit Schmelzen gemäss vorherigen Studien. Zusätzlich wurden Verteilungskoeffiziente von Granat, Klinopyroxen und Rutil bestimmt. Granat beherbergt die meisten schweren Seltenerdelemente (HREE, heavy rare earth elements), während Rutil die Elemente mit hohen Ionenvalenzen (HFSE, high field strength elements), namentlich Nb und Ta, kontrolliert. Klinopyroxen hat nur wenig Einfluss auf die Spurenelementsignaturen von Fluiden und Schmelzen. Eine typische Inselbogensignatur kann nur in Druck- und Temperaturbereichen, wo Zoisit nicht mehr stabil ist, reproduziert werden.

Das alterierte Basalt/Sediment-System unterscheidet sich vom kaliumfreien MORB-System vor allem durch die Anwesenheit vom Hellglimmer Phengit. Gemäss der Resultate dieser Studie liegt der wassergesättigte Pelit-Solidus tiefer als 800°C. Die ermittelten Verteilungskoeffiziente zeigen, dass Phengit als einziges Mineral LILE (mit Ba als stärkstem kompatiblen Element) einbindet. Trotz der Anwesenheit von Phengit zeigen die Gesamtfluidgesteinsmuster der Spurenelemente, dass die meisten LIL-Elemente dennoch Fluid-kompatibel sind und deshalb in den überliegenden Mantel migrieren dürften. Ähnlich wie im kaliumfreien System überwachen Granat, Zoisit und Rutil die Verteilung von HREE, LREE und Thorium, sowie HFSE. Die typische Anreicherung von LIL-Elementen in Bezug auf LREE in Inselbogengesteinen tritt nur auf, wenn Phengit und Zoisit gleichzeitig stabil sind. Sobald Zoisit abgebaut wird, ändert sich das Verhältnis zu Gunsten von LREE, da nun das Hauptmineral fehlt, um die LREE einzubauen. Das bringt eine starke Einschränkung für die Elementverhältnisse, welche in natürlichen Gesteinen beobachtet werden. Die Gegenüberstellung der beiden untersuchten Systeme zeigt ausserdem, dass die resultierenden Spurenelementmuster von Fluiden und Schmelzen überraschend ähnlich sind.

Insgesamt liefert diese Studie Fluid- und Schmelzzusammensetzungen, welche direkt und vollständig gemessen wurden. Besonders die Ersteren sind höchst wünschenswert, da geeignete Daten in der Literatur bis heute nahezu fehlen. Die erhaltenen

Verteilungskoeffizienten der Restphasen bestätigen den starken Einfluss der Mineralvergesellschaftungen in der abtauchenden Platte auf die Elementsignatur der Inselbogengesteine.

CHAPTER 1

General Introduction

1.1 Background

Subduction zone settings are arguably Earth's most important element cycling centers. The concept of subduction implies relatively oxidized and volatile-rich oceanic lithosphere being drawn into the more reducing mantle where it undergoes metamorphic and chemical modification as a function of pressure and temperature. Fluids and melts that are liberated from the slab during the course of dehydration and melting play an essential role in promoting arc magmatism which eventually leads to the generation of juvenile continental crust (e.g. Tatsumi and Eggins, 1995; Gaetani and Grove, 1996; Schmidt and Poli, 1998; Johnson and Plank, 1999; Grove et al., 2006).

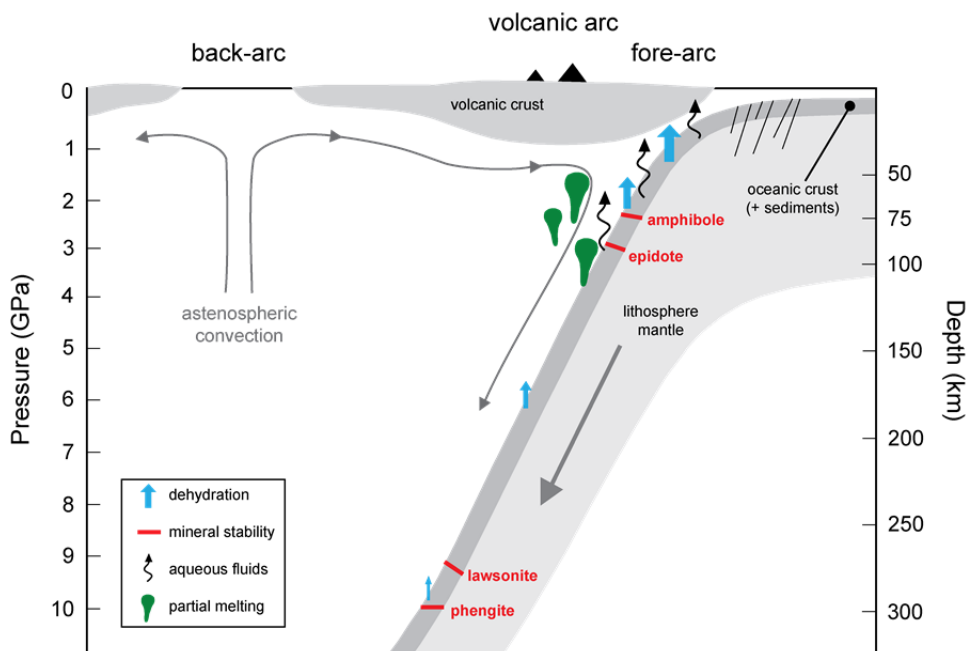


Figure 1.1 Schematic section through a subduction zone, showing hydrous mineral stabilities, fluid pathways and places of partial melting. Modified after Poli and Schmidt (2002), Stern (2002) and Spandler and Pirard (2013)

The subducting lithosphere is made up of various lithologies, each contributing its own, specific flavor to the overlying mantle wedge which is the dominant source for arc magmatism. The lithosphere base consists of partly hydrated upper mantle peridotites, several tens of kilometers thick, overlain by oceanic crust (only a few kilometers thick) composed of gabbroic intrusive and basaltic dike and extrusive rocks, at least partially covered by sediments of diverse provenance. Magmatic rocks either remain pristine or experience alteration by seawater or hydrothermal fluids on their journey from the location of formation to subduction. Major alteration often concerns only upper basaltic parts (pillow basalts and sheeted dykes), while gabbros remain largely unaltered (e.g. Kelley et al., 2003; Staudigel, 2003). Altered oceanic crust (AOC) is characterized by enrichment of volatiles (H_2O , CO_2 , Cl and S) and specific trace elements (e.g., K, Cs, Rb, B, Sr, Pb, and U). The uppermost lithologies of the oceanic lithosphere comprise a layer of sediments highly variable in composition and thickness but in general a few hundred meters thick (Plank and Langmuir, 1998) or almost absent (e.g. Izu-Bonin, Elliott et al., 1997). Average subducted sediments are dominated by terrigenous material over carbonates and opal (Plank and Langmuir, 1998). Despite their small fraction of the entire oceanic lithosphere, sediments contain the largest amounts of incompatible trace elements such as large ion lithophile elements (LILE, K, Cs, Rb, Ba, etc.), light rare earth elements (LREE, La-Nd), Th and U. It was the recognition of the correlation of sediment input into subduction zones and composition of arc rocks that excluded a solely mantle-derived source but suggested a considerable chemical influence from the slab (Morris et al., 1990). Bulk arc rocks are predominantly andesitic in composition, enriched in incompatible trace elements (LILE and LREE, e.g. Hawkesworth et al., 1993) relative to mid ocean ridge basalt (MORB) and display a pronounced LREE/HREE fractionation (McCulloch and Gamble, 1991; Elliott et al., 1997) as well as depletion of high field strength elements (HFSE, Tatsumi and Eggins, 1995). Furthermore, arc magmas are volatile-rich (H_2O , CO_2) which leads to explosive volcanism and the presence of hydrous minerals in arc-related igneous rocks. It is generally assumed that most of the water and the LILE, about 50% of CO_2 , and considerable amounts of LREE, Th and U dragged down in the slab are released and transported back to the arc crust (e.g. Wallace, 2005; John et al., 2011; van Keken et al., 2011).

The transfer processes of volatiles and elements from the slab to the crust are, however, far from being well resolved. Water as the dominant volatile phase is the key to generating mobile volatile phases capable in transporting solutes back to the surface. Besides constituting transfer agents, water-rich mobile phases from the slab trigger partial melting in the mantle wedge by lowering melting temperatures (e.g. Tatsumi and Eggins, 1995; Schmidt and Poli, 1998) and they influence the melting and crystallization behavior of silicates in general (e.g. Yoder and Kushiro, 1969; Sekine and Wyllie, 1982; Wyllie and

Ryabchikov, 2000). However, most of the free water (e.g. pore water) is lost during dehydration processes in the fore-arc region when the altered crust and sediments are compacted and water-rich lithologies (e.g. clay) dehydrate; therefore, only a limited amount of free water is present at sub-arc depths. It is almost exclusively structurally bound in hydrous minerals such as epidote-group minerals, amphibole or micas (biotite and phengite) and is released upon metamorphic mineral breakdown whereas the extended stability of e.g. phengite or lawsonite can transport water to even greater depths (Schmidt and Poli, 1998; Hermann et al., 2006; Hacker, 2008). The recognition that serpentine minerals (formed by hydration of olivine-rich gabbros and peridotite) in the mafic and ultramafic lithologies can retain up to 14 wt% H₂O (Ulmer and Trommsdorff, 1995), led to a widely accepted assumption that the water required for the generation of volatile phases in the slab might be externally-derived (Kessel et al., 2005a; Hermann et al., 2006; Spandler et al., 2008). However, the nature and composition of the generated volatile phases are crucial to element mobility and strongly vary as a function of pressure, temperature and rock composition. It is commonly assumed that aqueous fluids constitute the major mobile phase at the slab-mantle interface at sub-arc depths (Manning, 1998; Schmidt and Poli, 1998; Scambelluri and Philippot, 2001; Bebout, 2007). These fluids are relatively dilute and assumed to contain only 5 to 15 wt% of solutes mainly composed of Si, Al, alkali elements and some amount of LILE, while other trace element contents are thought to be generally low due to their retention in the host minerals (Manning, 2004; Kessel et al., 2005a; Spandler et al., 2007; Hermann and Rubatto, 2009). With increasing temperature and, to a lesser extent pressure, mineral solubilities in fluids generally increase and, therefore, fluid element concentrations increase accordingly (Manning, 2004). When the location of the wet solidus (onset of melting) is reached, aqueous fluids are replaced (or accompanied) by hydrous melts with distinctly increased solute contents. The presence of free fluids further promotes melting resulting in lowering of the wet solidus compared to the dry (fluid-absent) solidus at higher temperatures. Experimental studies have shown that the element capacity of hydrous melts compared to aqueous fluids is enhanced by up to more than one order of magnitude (e.g. Spandler et al., 2007; Hermann and Rubatto, 2009). In consideration of recent thermal models, water-saturated melting of the uppermost subducted lithologies is to be expected under common to warm geotherms (650-850°C top-slab temperatures at sub-arc depth) in present-day subduction zones (van Keken, 2002; Syracuse et al., 2010; Cooper et al., 2012). The wet solidus is suggested to be located at 700-750°C in AOC/sediments systems (Nichols et al., 1996; Hermann and Spandler, 2008; Skora and Blundy, 2010) and at 750 to 900°C for MORB systems (Lambert and Wyllie, 1972; Kessel et al., 2005b). In agreement with this and supported by geochemical analyses of natural arc rocks, the simplified, generally accepted view on element transport from the slab can be summarized as follows. Sediments melt

while the basaltic portion is rather flushed by fluids that leach out fluid-mobile elements (e.g. Elliott, 2003).

Next to fluids and melts, supercritical liquids have been proposed to represent potent transfer agents. With increasing pressure, supercritical liquids form above the critical curve, representing the hinge of the maximum fluid and melt solvus in P-T space (Stalder et al., 2000; Hermann et al., 2006). Above this curve, fluids and melts become physically indistinguishable i.e. a single-phase fluid is present across the entire range in temperature at given pressure. The intersection of critical curve and wet solidus is known as the second critical endpoint (Stalder et al., 2000; Manning, 2004; Schmidt et al., 2004a). Kessel et al. (2005a) have inferred that in the K-free MORB-water system the second critical endpoint is reached above 5 GPa, and they further showed that the supercritical liquid stable at these conditions carries elevated trace element concentrations of hydrous melt like flavor.

Over the last decades, many studies have been conducted attempting to characterize subduction-related mobile phase compositions produced at depths where eclogite is the main stable mineral assemblage in the subducted oceanic crust (> 60 km). Subduction of these rocks is suggested to promote the generation of basic to intermediate to acidic (basalt/tholeiite-andesite-dacite/rhyolite) plutonism and associated volcanism in supra-subduction arcs (e.g. Ringwood, 1974; Tatsumi et al., 1983; Kushiro, 1990; Gaetani et al., 1993; Schmidt and Poli, 1998; Ulmer, 2001). It became evident that the composition of the mobile phase strongly depends on the equilibrium phase assemblage of the slab. Therefore, when performing experiments on element mobility in subduction zones, it is crucial to design systems containing all potentially important residual phases in order to draw conclusions on arc-typical trace element patterns released from the slab. Typical eclogite-facies minerals, garnet and omphacite, incorporate and, therefore, control the mobility of HREE and possibly B, Li, V, Sr and Pb, respectively (e.g. Hermann, 2002; Spandler et al., 2003). However, they do not control important key elements in describing a slab component, such as LILE, LREE and HFSE. It is now a common assumption that mainly minor and accessory minerals exert the major control on these elements. The LILE (K, Rb, and Ba) are controlled by the white mica phengite (Domanik and Holloway, 1996; Schmidt, 1996; Sorensen et al., 1997; Zack et al., 2001; Scambelluri et al., 2008; Hermann and Rubatto, 2009; Skora and Blundy, 2010). Epidote-group minerals and monazite are the main host for LREE, Th and to a lesser extent U, while the HFSE are controlled by rutile and titanite (Ti, Nb and Ta; Brenan et al., 1994; Stalder et al., 1998; Klemme et al., 2005), zircon (Hf and Zr; Hermann, 2002), and apatite is the major host for P (e.g. Ayers et al., 1991; Johnson and Plank, 1999).

1.2 Previous experimental work

When high-pressure experimental and analytical methods to study processes in the deep Earth became available in the late 1960s, the view on arc rock genesis was still rather simplified. Many studies investigated the phase relations and melting behavior of subducted basalt in the presence of excess water assuming that these slab melts were the direct precursor of arc magmas (e.g. Green and Ringwood, 1968; Lambert and Wyllie, 1973; Stern and Wyllie, 1973; Stern et al., 1975; Stern and Wyllie, 1978; Sekine et al., 1981). However, these studies failed to reproduce melt compositions comparable to natural arc rocks (Stern and Wyllie, 1973). Additionally, geophysical models predicted common slab-top temperatures much colder than what is necessary to melt the basaltic slab component (Oxburgh and Turcotte, 1971; Anderson et al., 1978). When it became evident that hydrous minerals in the oceanic crust release water during prograde metamorphic devolatilization on their way down into the mantle (e.g. Ringwood, 1974), experiments with very little water, corresponding to the structurally bound water in the minerals, were performed (Rushmer 1991; Pawley and Holloway 1993; Poli 1993; Poli and Schmidt 1995; Rapp and Watson 1995; Liu et al. 1996; Kogiso et al. 1997; Poli and Schmidt 1997; Schmidt and Poli 1998; Vielzeuf and Schmidt 2001; Forneris and Holloway 2003; Schmidt et al. 2004a). Again, there was a discrepancy in the amount of fluid/melt produced in these experiments and the understanding of considerable element transport within subduction zones. The possibility of externally-derived water from underlying slab lithologies (Ulmer and Trommsdorff, 1995) lead to a shift in direction and many recent studies were performed under water-saturated conditions employing various chemical bulk systems (K-free MORB: Kessel et al. 2005a, 2005b; altered MORB: Klimm et al. 2008; pelite: Hermann and Spandler 2008; Skora and Blundy 2010).

While the determination of the melt phase is relatively straightforward due to transition to glass upon quenching, the analysis of aqueous fluids is a major challenge. Traditional methods often fail to quantify the entire fluid phase as they are either based on mass balance calculations or on the analysis of only quench solutes. The latter technique is critical at best because quenching of fluids results in extensive crystallization of solid quench phases accompanied by exsolution of unquenchable H₂O-rich fluid that contains some of the most fluid-mobile elements (alkali elements, alkaline earth elements, and LREE) in solution that are lost upon subsequent preparation such as piercing the experimental capsule to release the fluid (Stalder et al., 2002). To catch fluids at experimental P and T, one possibility is the use of diamond traps. The diamond trapping technique was originally developed by Ryabchikov and Boettcher (1980), Kushiro and Hirose (1992), and Baker and Stolper (1994) for anhydrous melting experiments. To apply the technique to hydrous melting and fluid-bearing sub-systems, it was modified by Stalder

et al. (1997; 1998). To prevent the loss of any elements prior to direct fluid analysis at room conditions, Kessel et al. (2004) developed the so-called “freezing” approach where fluid and melt phases in diamond traps are frozen in an external freezing stage (see also Aerts et al., 2010) prior to opening of the capsule and immediate analysis by LA-ICP-MS of the diamond + quench + predominantly ice assemblage. Because this technique is rather new, there is still a prominent lack in data on complex fluid-mineral systems which are urgently needed to obtain more realistic models of arc magma genesis.

1.3 Goals of this study

The prime goal of this PhD thesis is to determine the nature (aqueous fluid, hydrous melt or supercritical liquid) and compositions of the mobile phases leaving a subducting slab in equilibrium with an amphibolitic to eclogitic residue as a function of temperature, pressure and bulk composition corresponding to natural conditions relevant for arc magma generation below volcanic fronts. Two chemical systems are investigated, a K-free MORB and an AOC/sediment system. Especially the quantification of aqueous fluids is demanding, experimentally and analytically, and there is a considerable lack of experimental data. Next to the bulk volatiles (fluids and melts), the residual phase assemblage is examined in order to obtain a complete compositional dataset. In addition to the major element composition of all phases involved, trace element mobility needs to be evaluated for a large diversity of elements (REE, HFSE, LILE and transition metals) of which many constitute key elements in constraining the slab component in arc rocks. Therefore, we aim to determine trace element partition coefficients between all the phases in a specific chemical system for a series of P/T conditions. Special attention will be directed towards the hydrous solid phases zoisite and phengite, which are important providers of water during the course of dehydration of the slab with progressive subduction. Partition coefficients for stable slab-phases are urgently needed to model arc magma generation. Finally, the experimental results of this study will be compared to characteristic element contents and ratios measured in natural arc rocks and will be linked to the status quo in understanding how and by which transport agent elements are liberated from the slab in different subduction zone settings.

In order to optimize and improve the cryogenic LA-ICP-MS technique, we aim to design a new external freezing stage. Improvements will concern the gas flow in the ablation chamber, the sample holder and insulation of the entire device. The cryogenic LA-ICP-MS technique was originally developed to investigate K-free chemical systems. We, thus, will further refine the approach to apply it to systems containing potassium and will test a new element, bromine, as internal standard for LA-ICP-MS data quantification.

1.4 Organization of the thesis

This PhD thesis consists of six chapters of which chapters 3-5 are designed as publications in scientific journals. It is organized as follows:

Chapter 1 is the general introduction.

Chapter 2 details the experimental and analytical approach used for this study. Each following chapter will provide a methodology section but of very condensed nature. This chapter is particularly intended for readers interested in the detailed experimental procedures.

Chapter 3 outlines the importance and effect of epidote-group minerals in a K-free MORB system on the bulk volatiles escaping the slab at 2 and 3 GPa and 700 to 800°C. The results summarized here are part of the more extensive set of experiments presented in Chapter 4 and exclusively focus on the role of zoisite. This chapter documents the directly and completely analyzed trace element composition of the bulk volatiles (predominantly aqueous fluids) and provides zoisite-fluid partition coefficients, which are compared to previously published results in the literature. This chapter is to be submitted to "Geology".

Chapter 4 summarizes all experiments conducted in the K-free MORB system at 2 and 3 GPa and 700 to 1200°C. The major element content of all bulk volatiles is used to define the location of the wet solidus and discuss the nature of the mobile phase and trace element mobility in the presence of various stable mineral phases. Partition coefficients are provided for garnet, clinopyroxene and rutile/titanite. This chapter will be submitted to "Journal of Petrology".

Chapter 5 outlines the major and trace element compositions of bulk volatiles released from subducted altered MORB/sediments at 3 GPa and 700 to 900°C. First results and experimental/analytical issues when using Br as internal standard for LA-ICP-MS analyses are discussed for future applicability. A special focus is laid on the influence of phengite in the slab on the volatile phase and eventually the arc rock signature and differences compared to the K-free MORB system are pointed out. Partition coefficients are presented for phengite, garnet, rutile and clinopyroxene. The results of this chapter will be submitted to "Chemical Geology".

Chapter 6 gives a summary of the most relevant conclusions obtained in this PhD thesis. An outlook on the subject for further research is provided.

CHAPTER 2

Methodology

2.1 Experimental approach

Mobile phases (aqueous fluids and hydrous melts) and their coexisting mineral phase assemblages were produced experimentally using a piston cylinder apparatus at 2 and 3 GPa, a pressure range equivalent to subduction zone depths of 60-100 km. In order to determine the partitioning behavior within a particular system, it is crucial to analyze all generated phases quantitatively. Experimentally, this demands for effective separation of especially the bulk volatiles and the residues. We, therefore, employed diamond traps, placed in between two layers of powdered starting material, to capture the bulk volatiles in the interstices of the diamonds. The starting material was produced synthetically and spiked with a trace element mix contained in diopside glass.

The prime challenge in measuring mobile phases, especially very aqueous fluids, is complete quantification of their chemical composition. In order to prevent loss of any compounds during the analytical procedure, we froze the entire experimental charge with an external freezing device, cut it open and performed laser ablation ICP-MS analyses on the frozen bulk volatiles contained in the diamond trap. After defrosting, the trap was cut out and the residual solid phases were mounted and polished for subsequent electron probe microanalysis (EPMA). Provided the size of the solids allowed it, their trace element composition was determined by LA-ICP-MS employing beam sizes down to 5 μm diameter, and determined solid/volatile partition coefficients. All successful experiments conducted during this study are summarized in **Table 2.1**.

Table 2.1. Runtable summarizing all experiments during this thesis.

Run No.	starting material	Pressure [GPa]	Temp. [°C]	Duration [h]		H ₂ O ¹ [wt%]	Phases
				diamond trap	no trap		
SL2	TB-1	2	900	49		12.8	liq, grt, cpx, rut
SL3	TB-1	2	900		70	10.8	liq, grt, cpx, rut
SL4	TB-1	2	800	74		14.5	liq, grt, amph, zoi, rut
SL6	TB-1	2	800		71	11.6	liq, grt, amph, zoi, rut
SL7	TB-1	2	1000		28	12.9	liq, grt, cpx, rut
SL8	TB-1	2	1000		25 (static)	12.6	liq, grt, cpx, rut
SL10	TB-1	2	700		168	13.0	liq, grt, amph, zoi, rut
SL11	TB-1	2	1000	71		11.1	liq, grt, cpx
SL12	TB-1	2	700	163		11.0	liq, amph, zoi, rut, ttn
SL13	TB-1	2	1100	22		13.1	liq, cpx
SL14	TB-1	2	850	69		10.8	liq, grt, amph, cpx, rut
SL15	TB-1	2	750	163		11.6	liq, grt, amph, zoi, rut
SL17	TB-1	3	1000	26		10.6	liq, grt, cpx, rut
SL21	TB-1	3	700	167		10.5	liq, grt, cpx, zoi, stau, rut
SL23	TB-1	3	800	75		10.5	liq, grt, cpx, zoi, ky, rut
SL24	TB-1	3	900	39		10.6	liq, grt, cpx, rut
SL25	TB-1	3	1100	71		11.4	liq, grt, cpx
SL34	TB-1	3	1200	46		10.4	liq, grt, cpx
SL36	TB-1	2	900	70		10.7	liq, grt, cpx, rut
SL39	TB-1	2	700	167		11.0	liq, grt, amph, zoi, rut
SL40	TB-1	2	825		48	10.6	liq, grt, amph, cpx, rut
SLK1	TB-K5	3	900		136	10.8	liq, grt, phe, rut
SLK2	TB-K5	3	900	141		10.6	liq, grt, phe, rut
SLK3	TB-K5	3	800	165		10.4	liq, grt, cpx, phe, rut
SLK4	TB-K5	3	700	165		8.4	liq, grt, cpx, phe, stau, rut

¹ Water loaded in the capsule.

liq, liquid; grt, garnet; cpx, clinopyroxene; amph, amphibole; rut, rutile; ttn, titanite; zoi, zoisite; stau, staurolite; ky, kyanite; phe, phengite.

2.2 Starting materials and oxygen fugacity

Two different types of starting material were produced on the basis of synthetic powders; the potassium-free material (TB-1), originally investigated by Schmidt and Poli (1998), represents an average MOR basalt/gabbro. The second starting material (TB-K5) contains additionally 5 wt% of potassium and was used for the second series of experiments, representing a strongly altered MORB/sediment composition (see **Table 2.2**).

All mixtures were fabricated from reagent grade oxide powders. SiO₂, TiO₂, MgO, Fe₂O₃ were first fired in the oven at 1000°C, α -Al₂O₃, CaCO₃ or CaSiO₃, Na₂SiO₃ and K₂SiO₃ dried at 220°C and weighed in desired proportions. The mixes were subsequently homogenized in an agate mortar by gently grinding under ethanol for at least 30 minutes and then dried. To constrain oxygen fugacity, the ferric to ferrous ratio was fixed in the starting material by vitrification of the powders. They were placed in a high-temperature gas-mixing furnace

(CO₂-H₂ mixtures) and molten in a Pt-crucible at 1325°C for 2 hours before quenching rapidly by holding the crucible into cold water. The K-free starting material was fixed to a value corresponding to the NNO buffer equilibrium, while TB-K5 was fixed to the QFM buffer equilibrium. The obtained glasses were analyzed by EPMA to check for potential Fe-loss, which was negligible due to the employment of an iron pre-saturated Pt-crucible. After crushing the glass and grinding under ethanol to a fine powder it was stored under anhydrous conditions.

Table 2.2. Composition of the starting materials.

	TB-1		TB-K5	
	wt%	1 σ	wt%	1 σ
SiO ₂	51.78	0.99	53.23	0.53
TiO ₂	1.50	0.05	1.94	0.04
Al ₂ O ₃	16.36	0.59	21.70	0.20
FeO	9.99	0.27	6.70	0.17
MgO	6.83	0.28	5.11	0.10
CaO	10.30	0.38	4.69	0.11
Na ₂ O	3.19	0.11	1.97	0.06
K ₂ O	0.01	0.01	4.66	0.10
Total	100		100	
X _{Mg} ¹⁾	0.55		0.58	

¹⁾ X_{Mg} calculated with Fe²⁺ = Fe^{tot}

Trace elements were added as a pre-prepared spike (courtesy of Rohit Nandedkar, Diss. ETH No. 21411). A total of 30 trace elements, including all important groups of trace elements (LILE, REE, HFSE, transition metals), were added by complementary synthesis of a glass of diopside composition at a 2000 µg/g level, except U and Th at a 1000 µg/g level. The spiked and vitrified glass was analyzed by EPMA and laser ablation ICP-MS to check its composition and to ensure homogenization (**Table 2.3**). The glass was then ground under ethanol, dried, and 2 wt% of it were added to the initial starting material to obtain a 40 µg/g level for most trace elements and 20 µg/g for U and Th.

Inspection of initial experimental runs revealed that the low temperature experiment SL12 at 2 GPa/700°C was devoid of garnet, attributed to suppressed nucleation due to sluggish kinetics at this low temperature. The obtained assemblage does not correspond to natural systems (e.g. Zack et al., 2002 and references therein) where garnet is part of the mineral

assemblage at these conditions. We, therefore, added 0.5 wt% natural garnet seeds to the starting material, milled to a fine powder and sieved to a size $< 7 \mu\text{m}$. The composition of the garnet seeds ($x_{\text{alm}}: 0.324$, $x_{\text{pyr}}: 0.562$, $x_{\text{gross}}: 0.018$, $x_{\text{spess}}: 0.005$) strongly contrasts that of the garnet formed at higher temperatures in this study (see Chapter 4, **Figure 4.5**) in order to unequivocally locate run product garnet overgrowth rims on seed grains.

Table 2.3. Element concentrations in the diopside glass employed for doping as determined by LA-ICP-MS.

Major element composition			Trace element composition		
n=12	wt%	1 σ	n=9	[$\mu\text{g/g}$]	1 σ
SiO ₂	49.18	0.54	Li	1692	64
TiO ₂	1.47	0.05	Sc	1917	18
Al ₂ O ₃	0.15	0.02	V	1886	23
FeO	0.01	0.01	Rb	30.8	1.8
MgO	16.05	0.16	Sr	1971	39
CaO	24.12	0.29	Y	1992	39
Na ₂ O	0.02	0.03	Zr	1960	39
K ₂ O	0.21	0.03	Nb	2090	44
Total	91.21		Mo	1629	55
			Cs	29.3	1.8
			Ba	2099	35
			La	1920	25
			Ce	2023	21
			Nd	1728	8
			Sm	1822	16
			Eu	1883	13
			Gd	2005	30
			Tb	1860	29
			Dy	1951	39
			Ho	1875	39
			Er	1928	44
			Tm	1808	45
			Yb	2010	61
			Lu	1927	59
			Hf	1897	63
			Ta	2059	36
			W	1983	21
			Pb	170	8
			Th	935	29
			U	765	18

To simulate water-saturated systems, 10-15 wt% distilled water was weighed directly into the capsules by micro-syringe during preparation of the experimental charges. The water was additionally doped with 585 ppm CsOH. Cesium is a highly incompatible element and is assumed to partition strongly into the volatile phase which makes it an ideal candidate for the use as internal standard for quantification of the LA-ICP-MS analyses of the volatile phase in a K-free basaltic system. The same method was successfully applied in the study of Kessel et al. (2005a, b). Nevertheless, Cs cannot be used as internal standard when employing starting materials containing enough potassium so that a K-bearing mineral stably coexists with volatiles at run conditions. In such systems, white mica is expected to be a significant part of the mineral assemblage; the mica phase represents a sink for large ion lithophile elements such as Cs in its mineral structure even at very high pressures (e.g., Scambelluri et al., 2008). Hence, near complete incompatibility, which is an absolute prerequisite to successfully quantify the bulk volatile composition, is not guaranteed. We, therefore, chose the halogen bromine as internal standard, which is expected to behave incompatibly even in the presence of mica. Analogous to Cs, KBr (in H₂O) was added to the distilled water but on a 1180 ppm level to ensure proper detection during LA-ICP-MS analysis as Br⁺. Both, Cs- and Br-doped water were analyzed by ICP-MS (ThermoFinnigan Element XR) at ETH Zürich to determine doped concentrations.

2.3 Capsule design and diamond traps

Up to a temperature of 1000°C, gold was used to fabricate single capsules with the intention to reduce Fe-loss to the capsule walls (Gaetani and Grove, 1998). At temperatures in excess of the melting point of Au (1064°C), Au₉₀Pd₁₀ at 1100°C and Au₈₀Pd₂₀ at 1200°C were employed. All capsules had an inner and outer diameter of 2.7 and 3.0 mm, respectively.

First, 4 µl (corresponding to 10-15 wt% of the total system composed of H₂O and the solid starting material) of Cs- or Br-doped water was pipetted into the capsule by micro syringe and confirmed by weighing. Care was taken to place the water at the bottom of the capsules to minimize the danger of losing it during the subsequent filling process. In order to position the diamond trap in the middle of the capsule (see **Figure 2.1**), it was filled with a first layer of powdered starting material, followed by a thin layer of synthetic diamonds (~20 µm grain size in average). The amount of diamonds was adjusted to twice the weight of water. This 2:1 ratio has proven to work well for this type of experiments, providing sufficient void space to trap the fluid and/or melt and, at the same time, avoid the development of a pressure gradient within the trap during the experiment due to empty pore spaces between the diamonds (see also Aerts et al., 2010). On top of the diamond layer, the second half of the powdered starting material was placed and tightly packed

before crimping the edges and welding the capsule shut using a Tungsten arc-welder. Tightness of the capsule was tested by putting it into the furnace at 110°C for half an hour and then checking for weight-loss.

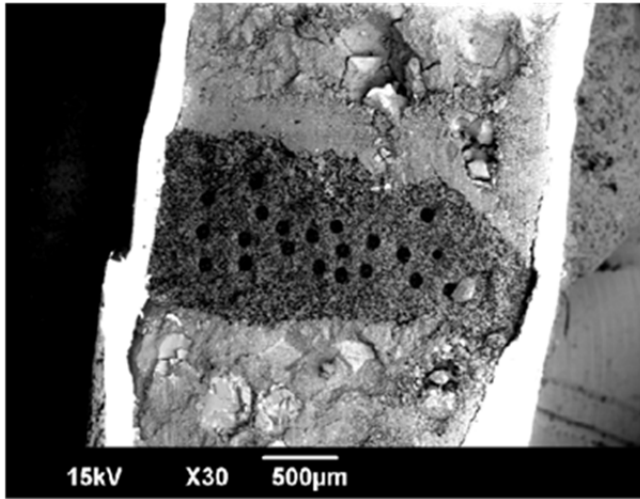


Figure 2.1: Backscattered electron (BSE) image of an experimental charge after LA-ICP-MS analysis showing a layer of diamonds sandwiched in between two layers of starting material. The black spots are the laser ablation craters.

2.4 Piston cylinder experiments

Most experiments (notably all experiments containing a diamond trap) were performed using a 600-ton end-loaded rocking piston cylinder apparatus with 14 mm bore size at the high pressure laboratory at ETH Zürich (**Figure 2.2**). The apparatus was designed at IGP, ETH Zürich (Schmidt and Ulmer, 2004) and can alternatively be fitted with a multi-anvil or a piston cylinder module allowing to cover the entire pressure range from 0.5 to 25 GPa. The entire apparatus is mounted on a rocking device that turns the entire equipment by 180° while applying pressure and temperature. Experiments were first pressurized cold (to ~4 kbars); followed by heating the charge at 50°C per minute. While heating up, the apparatus is turned constantly until run conditions are reached in order to generate homogeneous nucleation centers within the capsule. By rotating the apparatus every 15 minutes during the run, chemical zoning related to fluid concentrating towards the hotspot of the capsule as a result of Soret diffusion is eliminated (Schmidt and Ulmer, 2004). At the beginning of the project, a few experiments without diamond traps were conducted in a static, end-

loaded piston cylinder apparatus (Boyd and England, 1960) with the intention to generate solid charges that are more suitable for EPMA and LA-ICP-MS analysis. In the process of the project, this approach was found to be superfluous due to the satisfying results obtained by the diamond trap experiments. However, the principle functioning of both apparatus is identical.

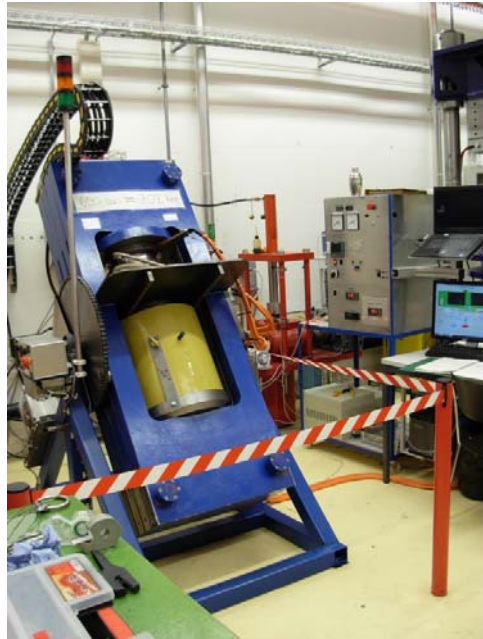


Figure 2.2: Rocking piston cylinder apparatus in the high pressure laboratory at ETH Zürich.

Heat (temperatures up to 2500°C) is generated by the resistance of a graphite furnace when running an electric current through it. Temperature was measured using a B-type Pt₉₄Rh₆/Pt₇₀Rh₃₀ thermocouple (contained in a mullite sleeve) with an estimated accuracy of $\pm 10^\circ\text{C}$. The capsule containing the sample powder and diamond trap was positioned inside the furnace in such a way that the trap was located at the hotspot of the entire assembly (see **Figure 2.3** for a sketch of an assembly). Hotspot and temperature distribution within the assembly were calculated using the numerical model of Hernlund et al. (2006). For my particular setup the geometry is crucial as growth of equilibrium minerals within the diamond trap, which would seriously falsify the quantification of the bulk volatile composition, can be strongly reduced. Quenching was done by cutting off the power supply, resulting in estimated quench rates in excess of 100°C/s.

The capsules were embedded in boron-nitride (BN) cylinders to prevent hydrogen loss (Truckenbrodt and Johannes, 1999; Truckenbrodt et al, 1997) and, therefore, oxidation of the charge (Stalder et al., 2001). An additional benefit of employing BN instead of MgO is its softness, allowing easy removal from the capsule after the experiment which is important for subsequent LA-ICP-MS analysis. However, because oxygen fugacity was not fixed during the experiment, the use of BN can potentially result in slightly reducing conditions (e.g. Truckenbrodt et al., 1997). MgO spacers above and below the BN-cylinder ensure separation between the capsule and the graphite furnace.

Pressures (0.5-4 GPa for a piston cylinder apparatus) are generated by pumping oil into a hydraulic reservoir that pressurizes a smaller surface (WC-piston) that is in contact with the assembly (see **Figure 2.4**). Near-hydrostatic pressure transfer onto the sample occurs by material that softens with increasing pressure and temperature. Pyrex glass and talc were employed in this study. The assembly was calibrated against the coesite-quartz transition (Bose and Gangluy, 1995) as well as the fayalite+quartz = ferrosilite reaction (Bohlen et al., 1980) resulting in a friction correction of +10% relative to the nominal pressure. On top of the assembly, a steel cylinder, surrounded by pyrophyllite, was inserted to hold the thermocouple in position and prevent extrusion of the assembly.

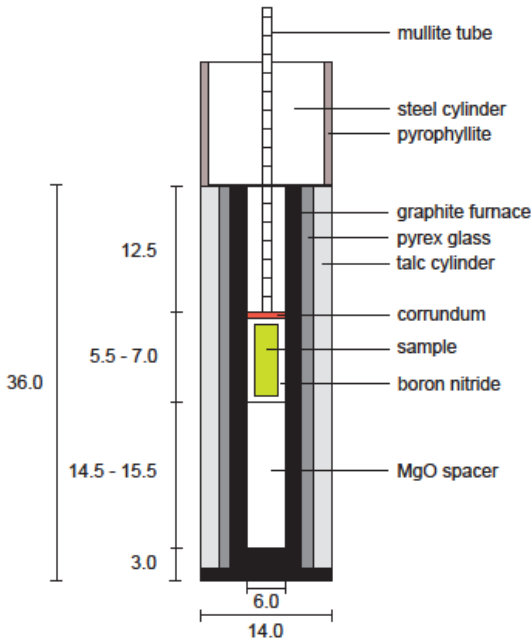


Figure 2.3: Talc-Pyrex-BN piston cylinder assembly (14 mm OD) employed in this study. Dimensions are given in mm.

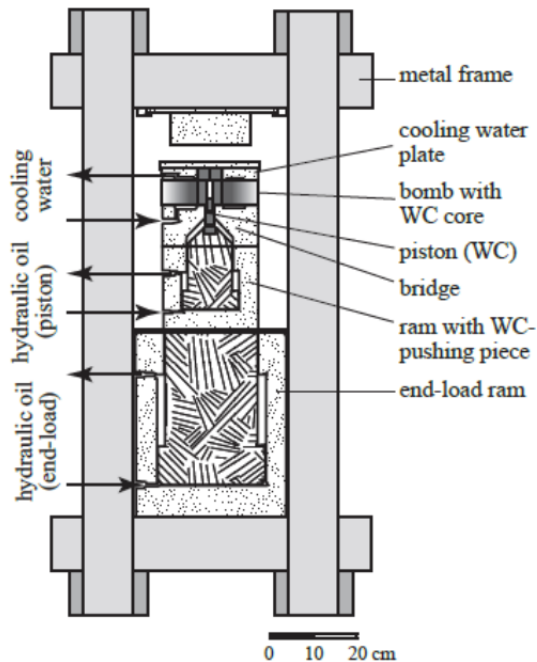


Figure 2.4: Schematic drawing of an end-loaded piston cylinder apparatus after Boyd and England (1960) (courtesy of Peter Ulmer).

2.5 Analytical methods

2.5.1 Diamond-trap experiments and the freezing stage

Analyzing volatiles that equilibrated with a solid phase assemblage at high P and T comes along with some analytical challenges. When quenching an experimental charge to ambient conditions, fluids and melts undergo extensive crystallization and/or exsolution; but solute precipitation from the volatile phase is not quantitative. Very soluble elements can remain dissolved in the residual aqueous fluid phase (e.g. potassium, Stalder et al., 2002) and by releasing the fluid from the capsule, these elements are lacking from the bulk volatile composition determined via quenched solutes. Due to the separation of fluids and quench solutes, the composition of the original fluid cannot be determined by conventional analytical methods. To eliminate these problems, Kessel et al. (2004) developed a novel technique to perform LA-ICP-MS analyses on the volatile-saturated diamond-trap. They designed a freezing stage where the sample capsule is frozen prior to

analyses, then cut open using a sharp razor blade and held in a frozen state during laser ablation ICP-MS analysis, allowing for complete quantification of the bulk volatile. The complex crystal-melt-fluid phase relations and trace element behavior of subducted MOR basalt at ultra-high-pressures were determined successfully using this new approach (Kessel et al, 2005a; Kessel et al., 2005b). The disadvantages of the original stage-design were the poor insulation and condensation of ice on the ablation window and in the tubes as liquid nitrogen was used to freeze the capsule.

To overcome these issues, Aerts et al. (2010) improved the freezing stage by replacing the liquid nitrogen cooling system by a stack of two (electronically controlled) Peltier elements and a more sophisticated insulation (see **Figure 2.5**). All LA-ICP-MS analyses in this study were conducted with this freezing stage.

Although this device provides easy handling and consistent results, we designed a new freezing stage (based on the same principle construction as the device of Aerts et al., 2010). A picture of the new stage is shown in **Figure 2.6**; all the construction drawings are provided in **Appendix A**. The following improvements were made:

- 1) Ablation chamber: The gas flow dynamics in the chamber can be optimized by an adequate geometry, thus strongly influencing signal stability (e.g. Bleiner and Günther, 2001). We, therefore, designed an ablation chamber that is rhombic in shape instead of the circular design of Aerts et al. (2010). Furthermore, we changed the position of the gas nozzles (that were the same size and position for both, inlet- and outlet nozzle for the earlier design); the gas inlet nozzle is smaller and positioned in the middle of the chamber in vertical extent, while the gas outlet nozzle is larger in diameter and positioned in the upper quarter of the chamber.
- 2) Sample holder: When frozen in the copper sample holder (lower part of the ablation chamber), the capsule is cut open using a sharp razor blade. For that purpose, the capsule needs to be fixed in the holder tightly so it is not bended or pulled out during cutting. We designed a new sample holder that provides much more stability due to an additional guiding rail.
- 3) Insulation and conductivity: For better insulation, we suggest to use Styrofoam around the stack of Peltier elements as well as on the sides of the sample holder. To remove the heat produced by the Peltier elements when cooling the sample, Aerts et al. (2010) employed a thermal paste in between the lower Peltier element and the cooling water plate. The paste has the disadvantage to dry out over time which prominently reduces its functionality; instead, it can be replaced by thermal foil.

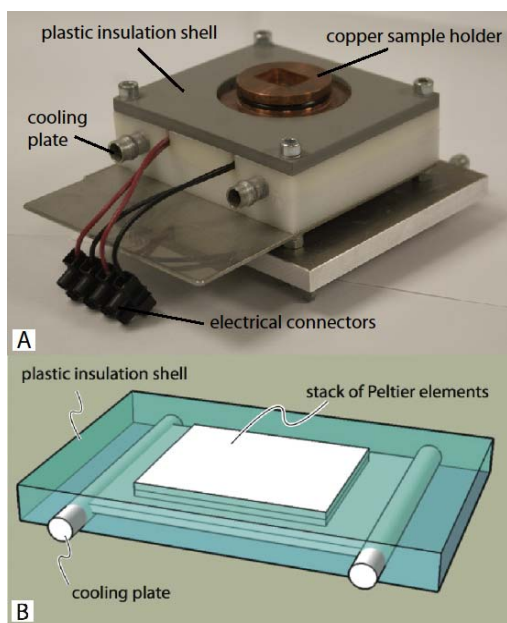


Figure 2.5: Peltier-cooled freezing stage designed by Aerts et al. (2010). All LA-ICP-MS analyses in this study were performed with this device.

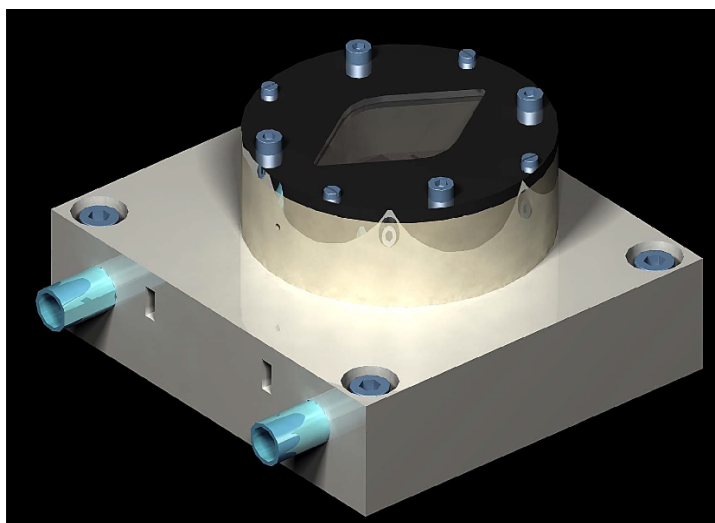


Figure 2.6: New design of the freezing stage. For explanations see text and Appendix A.

2.5.2 Laser ablation ICP-MS

Laser ablation ICP-MS analyses of (a) the bulk volatile in the diamond trap and (b) the stable residual minerals were performed at the Institute of Geological Sciences at the University of Bern. The laboratory accommodates a GeoLas-Pro 193 nm ArF Excimer laser system (Lambda Physik/Coherent) combined with an Elan DRC-e quadrupole mass spectrometer (Perkin Elmer). General operation procedures and optimization strategies are detailed in Pettke et al. (2012).

(a) After the capsule was frozen and cut open, the entire freezing stage was placed under the reflected light microscope and the diamond layer was located. Depending on the size and condition (coherence) of the diamond trap, 15-25 shots were done per sample with a spot size of 44-90 μm . The standard reference material used as external standard, NIST-SRM-610, was measured twice before and after one series of analyses. For the experiments containing potassium in the starting material and Br as internal standard, additionally the scapolite sample SCA-17 (Seo et al., 2011) was used as external standard and measured likewise. Ablated aerosols were transported to the ICP-MS by He-H₂ carrier gas mixture (1 and 0.008 l/min). Background was measured for 50 seconds, ablation intervals were in the range of 20-40 seconds at 8-10 Hz repetition rate. Dwell time was between 10-20 ms. Data reduction was carried out by using the software SILLS (Guillong et al., 2008). A problem with the diamond-trap technique is the potential growth of crystals within the trap due to incongruent dissolution of the starting material during the experiment (e.g. Keppler and Audétat, 2005). Already during ablating, care was taken to exclude analyses indicating mixed signals by element intensity ratio variations that would falsify the true composition of the bulk volatile phase. Additionally, ratios between mineral-compatible elements and elements, that either partition into the volatile phase or into a coexisting residual phase can be plotted. Data points plotting far off the vast majority are considered to be contaminated and were excluded. One example is shown in **Figure 2.7**. After defrosting, the diamond trap was furthermore examined visually using a scanning electron microscope (SEM) for the presence of mineral growth between the diamonds (see **Figure 2.8**).

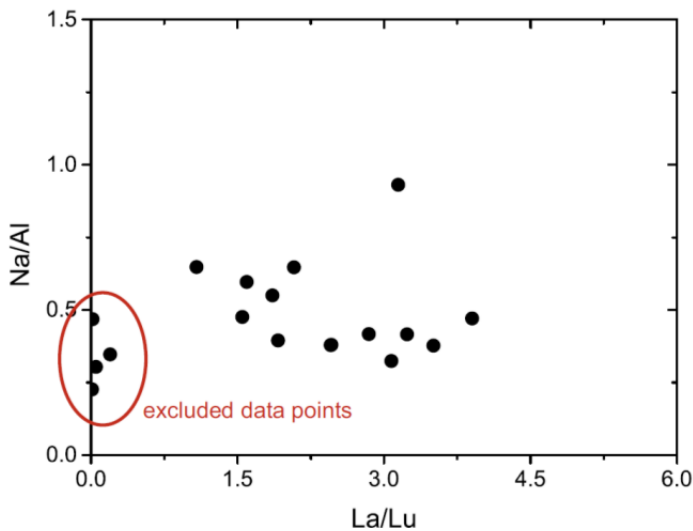


Figure 2.7: Na/Al vs. La/Lu of one diamond trap LA-ICP-MS analytical session showing excluded data points that imply garnet growth in the trap.

For the K-free experiments, Cs was used as internal standard. Cesium is expected to partition exclusively into the volatile phase. By knowing the initial H:Cs mass ratio, measured, apparent element concentrations can be recalculated into true values and the absolute concentrations of all elements in the volatile phase including H₂O can be quantified (see Kessel et al., 2004 and 2005b, for details). The same approach was used for the experiments using Br as the internal standard.

(b) For the analyses of the crystalline phases, the laser spot size had to be adapted to the size of the different crystals; beam sizes between 5 and 60 μm at 6-10 Hz repetition rate were employed. Background was measured for 50 seconds and external standards, NIST-SRM-610 and SCA-17, were measured twice before and after ablation. A strong increase in the counts of the incompatible elements (e.g. Cs) was taken as indicator for having shot through the crystal into interstitial material, and the integration interval was selected accordingly. As internal standards for SILLS, CaO, Al₂O₃ or TiO₂ concentrations previously determined by EPMA were used.

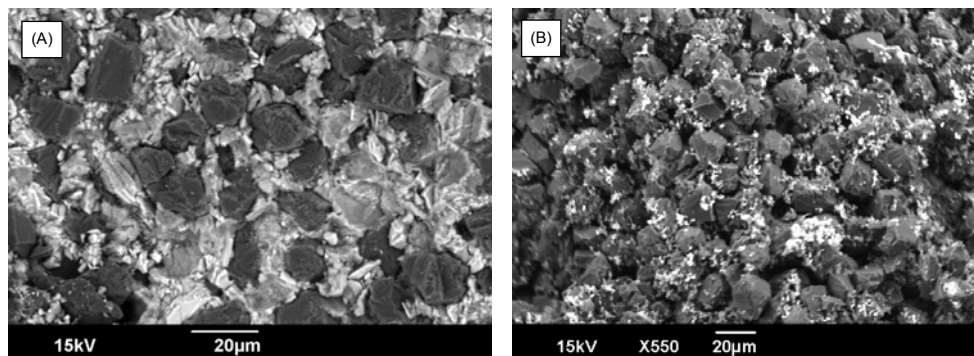


Figure 2.8: (A) Diamond-trap experiment at 2 GPa and 1100°C showing quenched melt within the interstices of the diamonds (black). (B) Diamond-trap experiment at 3 GPa and 700°C. At these conditions, a predominantly aqueous fluid containing low concentration of solutes is stable; therefore, the coherence of the trap is low. Note that in both traps no mineral growth could be detected.

2.5.3 Sample preparation for mineral analysis

The cut open and defrosted capsules were impregnated under vacuum with a low-viscosity Laromin resin for better mechanical coherence and the following additional reasons: First, the diamond trap had to be cut out of the experimental charge in order to polish the residual phase assemblage with diamond paste. Secondly, especially at low temperatures (700-800°C), where predominantly aqueous fluids with very low concentration of solutes are stable, the amount of potentially present quenched melt (glass) is insufficient to hold together the recovered run products. Therefore, they have to be fixed for subsequent treatment. Embedded in epoxy, the exposed sections were polished down to 1 μm and coated with 20 nm of carbon for EPMA analysis.

2.5.4 Electron probe micro-analysis

Major element concentration of minerals and glasses were determined with a five WDS (wavelength-dispersive) spectrometer JEOL JXA 8200 electron probe with attached secondary electron (SE) and backscattered electron (BSE) detectors at ETH Zürich. The employed standards were oxides or synthetic minerals (wollastonite, corundum, periclase, rutile, fayalite, K-feldspar and aegirine). Analyses were performed with an acceleration voltage of 15 kV and counting times of 40 seconds on peak and 20 seconds on the background. Beam current and beam size varied for minerals and glasses; for the former 20 nA and focused beam, for the latter 5 nA and 10 μm beam size were employed to minimize alkali migration.

CHAPTER 3

Zoisite in the subducting oceanic crust: Implications for the release of mobile phases during dehydration of the slab

Abstract

The typical geochemical signature of suprasubduction volcanic and plutonic arc rocks is inferred to be governed to a large degree by aqueous fluids and hydrous melts released from the subducting lithosphere. Nature and composition of these mobile phases depend on pressure, temperature and the trace element partitioning behavior with the residual phase assemblage of the slab. However, the latter properties remain poorly understood. Here we present the results of experiments conducted at 2 and 3 GPa and 700-800°C on a K-free and water-saturated MORB composition doped with 30 trace elements including important key elements, which are often used to decipher the subduction zone component in arc-related igneous rocks. Mobile phases were collected in diamond traps and subsequently analyzed by the cryogenic LA-ICP-MS technique (Kessel et al., 2004). This study provides new insights into the trace element composition of the bulk volatiles escaping the basaltic portion of the oceanic lithosphere based on direct LA-ICP-MS measurements. Furthermore, we present partition coefficients for the hydrous epidote-group mineral zoisite that were determined independently from mass balance constraints for the first time. Zoisite in the basaltic crust controls, among few other minerals, the LREE, Th (and U) budget of volatiles that are released into the mantle wedge and contribute to arc magma genesis. Our results testify that the respective bulk volatile only transports insignificant amounts of LREE and Th to the arc basalt source region. $D^{(zoisite/fluid)}$ values determined in this study are within the range of previously calculated $D^{(allanite/melt)}$ (Klimm et al., 2008) and provide a comparatively strong control on LREE and Th contents of low temperature subduction zone volatiles as REE-rich allanite does in equilibrium with hydrous melts.

Key words: Zoisite, eclogite, trace element partitioning, dehydration, subduction, experimental petrology

3.1 Introduction

The trace element signature of subduction zone magmas is mediated by several source lithologies: (1) hydrous slab mantle, (2) basaltic oceanic crust, (3) its sediment layer and (4) the peridotite in the depleted mantle wedge overlying the descending slab. While it is assumed that elements are predominantly transported from the sediments via hydrous melts, aqueous fluids are inferred as the preferred transport medium for elements originating from the (altered) oceanic crust (Elliott et al., 1997). Besides triggering flux-melting, those mobile phases further carry a trace element signature that can be directly linked to the distinct chemical features displayed by typical arc magmas, such as an overall enrichment of large ion lithophile elements (LILE) compared to rare earth elements (REE) (e.g. Hawkesworth et al., 1993) or a pronounced Light REE/Heavy REE fractionation (McCulloch and Gamble, 1991; Elliott et al., 1997). The trace element compositions of volatiles originating from the oceanic lithosphere are principally controlled by the trace element partitioning behavior between volatiles and the solid residual phases within the slab (Spandler et al., 2007). Detailed knowledge about the residual mineralogy and the pressure and temperature conditions they formed at is, therefore, crucial to decipher which elements are retained by the host rocks and which elements are released into the mantle wedge and eventually govern the chemical signature of arc magmas.

In subduction zone settings, hydrous minerals (e.g. amphibole, epidote-group minerals, lawsonite, talc) play an important role in providing volatiles, predominantly H₂O, and releasing volatile-mobile elements into the overlying mantle wedge during dehydration of the igneous oceanic crust (e.g. Schmidt and Poli, 1998; Forneris and Holloway, 2003). Epidote-group minerals are of particular importance as they may not only constitute rock-forming minerals in deeply subducted hydrous eclogites, but incorporate rare earth elements at weight percent levels and significant amounts of Sr, Pb, Th (Zack et al., 2002; Spandler et al., 2003). Experimental studies revealed the importance of epidote-group minerals as carriers for LREE, Th and to a lesser extent U, which represent key trace elements to determine and quantify the subduction component in arc lavas (e.g. McCulloch and Gamble, 1991; Hawkesworth et al., 1997). To date, however, experimentally determined element partitioning data between these hydrous minerals and their coexisting fluids or melts are scarce. Accurate analysis of the aqueous fluid phase coexisting with a solid residue has proven particularly difficult, both experimentally and analytically. Experimental $D(\text{mineral}/\text{fluid})$ values were computed for zoisite/fluid based on mass balance constraints (Feinemann et al., 2007; Martin et al., 2011) or were determined for zoisite/melt (Frei et al., 2003). Accessory allanite in subducting oceanic crust is an important and effective sink for LREE and Th, which are major constituents in its mineral structure. As far as allanite is concerned, so far only partition coefficients for the pair

allanite/melt were determined (Hermann, 2002; Klimm et al., 2008). It has been shown that the low solubility of allanite in silicate melts limits the LREE budget in arc magmas when allanite is part of the solid residue.

The aim of this study is to present the first experimentally determined partitioning coefficients between zoisite and bulk volatiles determined by direct measurement, i.e., independent from mass balance constraints.

3.2 Catching fluids: Experimental and analytical methods

To determine the partitioning of trace elements between eclogitic residual minerals in a subducting slab and the respective bulk volatile phase, piston cylinder experiments were conducted in a 'rocking' 600-ton press at 2 and 3 GPa and 700 to 800°C to prevent chemical zoning within the capsule and promote the constant homogenization of the volatile-rich mobile phase and the residual solid phases by turning the entire equipment by 180° every 15 min (Schmidt and Ulmer, 2004). To separate and quantify quenched solutes and solid mineral phases we employed diamond traps to collect the former in the interstices of the diamonds (e.g. Stalder et al., 1998, 2002; Kessel et al., 2004, Aerts et al., 2010). Oxygen fugacity of the starting material was pre-conditioned during vitrification in a gas-mixing furnace close to the Ni-NiO equilibrium, under the assumption that these conditions were maintained during the experiment. A synthetic starting material representing a pristine potassium-free MOR basalt/gabbro (TB-1, Schmidt and Poli, 1998) was employed; a total of 30 trace elements were added on a 40 µg g⁻¹ level (20 µg g⁻¹ for Th and U) by complementary synthesis of a diopside-glass. In experiment SL39 (2 GPa/700°C), the starting material was seeded with 0.5 wt% garnet to test the potential presence of garnet that was otherwise absent at these conditions. Prior to loading the starting material, 10-15 wt% H₂O were added to the Au-capsules, simulating the breakdown of hydrous phases in the slab during subduction and more importantly in terms of quantity, simulating the presence of external fluids as result of serpentine dehydration in the underlying slab lithologies (Ulmer and Trommsdorff, 1995). The water was doped with Cs (585 µg g⁻¹), which serves as internal standard for subsequent analysis. Due to its incompatible character Cs is employed for H₂O quantification in the laser-ablation inductive-coupled-plasma mass spectrometry (LA-ICP-MS) analyses of the diamond trap (Kessel et al., 2004, Aerts et al., 2010). In between two layers of starting material, we placed the diamond trap (synthetic diamonds, ~20 µm average grain size) in the center of the capsule corresponding to the hot-spot of the piston cylinder assembly.

Traditional methods (Stalder et al., 2001), such as piercing the capsule to release the fluid from the experimental charge for subsequent analysis, is prone to loss of ions dissolved at room temperature (e.g. K, Cs, Rb) and/or the formation of quench crystals in between the

solid residue. To prevent any loss of components, the recovered capsules were mounted into a freezing stage cooled with Peltier elements (Aerts et al., 2010). The capsules were cut open and analyzed (LA-ICP-MS spot analysis of the trap) while frozen. This allowed quantifying the composition of the entire pre-quench bulk volatile directly and completely. To eliminate overestimation of the concentration of compatible elements in the volatile phase, any analysis that indicated crystal growth in the diamond trap in the transient LA-ICP-MS signal, e.g. elevated HREE counts, was excluded from further investigation. After defrosting the capsule, the run products were mounted and polished. Major element composition and trace element concentrations of the residual zoisite were determined by electron probe microanalysis (EPMA) and LA-ICP-MS.

3.3 Bulk volatile composition

All experimental conditions, run products and modal phase proportions are summarized in **Table 3.1**. At 2 GPa and 700-800°C, the solid phase assemblage consists of garnet, amphibole, zoisite and accessory rutile (backscattered electron images of the experimental charges are shown in supplementary **Figure A1**). In the same temperature range but at 3 GPa garnet, clinopyroxene, zoisite and accessory rutile coexist with staurolite (700°C); at 800°C the eclogitic phase assemblage is complemented by kyanite and minor REE-rich zoisite, with the latter being a member of the epidote-group indicated by incorporation of several wt% of REE, however not an allanite.

The experimental results show a gradual decrease in the water content of the bulk volatiles from 40 to 33 wt% with increasing temperature from 700 to 800°C at 2 GPa and 45 to 42 wt% at 3 GPa (**Table 3.1**). While at 3 GPa/700°C the chemical composition of the volatile phase suggests an aqueous fluid to be stable, at 3 GPa/800°C and at all temperatures at 2 GPa the chemical composition indicates the presence of a subcritical mixed volatile phase (coexisting predominantly fluids with some melts). We, therefore, refer to the entire mixed volatile phases as bulk volatiles (see also Chapter 4).

The trace element partitioning of the bulk volatiles over the residual solids (**Figure 3.1**) reveals a strong volatile enrichment in incompatible LILE (Rb, Ba and Sr) and Pb, Li and B, represented by $D(\text{fluid/solid})$ ranging from 1 to 10 (see supplementary **Table A5**), with Rb and B displaying even higher D -values of up to 50. In general, $D(\text{bulk volatile/solid})$ for these elements reveal strong temperature dependence, with higher mobility at higher temperatures. For incompatible elements, partitioning trends at 2 and 3 GPa are identical, but lacking a clear pressure-dependence. Although LILE enrichment is a distinct feature of arc magmas discriminating them from MORB (Hawkesworth et al., 1993), it is noteworthy that we do not obtain a residual mineral such as phengite that preferentially incorporates these elements (Zack et al., 2001).

TABLE 3.1 RUN TABLE AND PHASE PROPORTIONS

Run	P (GPa)	T (°C)	Duration (h)	H ₂ O _m [*] (wt%)	CH ₂ O [†] (wt%)	P phase assemblages	Phase abundances [§] (wt%)	$\sum R^{2\theta}$	X _{ZOI}	$\sum REE_{-ZOI}$ (wt%)
SL39	2	700	67	110	40.1	liq, grt, amph, zoi, rut	22.7 (17), 17 (4.7), 56.6 (4.3), 7.3 (2.8), 17 (0.8)	0.91	0.70	0.37
SL 45	2	750	63	116	35.6	liq, grt, amph, zoi, rut	26.1 (0.4), 0.7 (1.1), 57.7 (10), 13.9 (0.6), 17 (0.2)	0.04	0.71	0.44
SL4	2	800	74	14.5	32.5	liq, grt, amph, zoi, rut	34.3 (3.7), 2.3 (9.3), 57.7 (10.0), 5.1 (5.7), 0.6 (1.4)	2.88	0.71	164
SL21	3	700	67	10.5	45.3	liq, grt, cpx, zoi, stau, rut	20.1 (2.8), 4.9 (7.6), 52.2 (7.1), 14.0 (6.9), 7.7 (4.5), 12 (1.4)	1.35	0.69	N.D. ^{**}
SL23	3	800	75	10.5	41.8	liq, grt, cpx, zoi, rut, ky	22.9 (2.9), 31.5 (7.5), 36 (5.9), 8.0 (5.3), 16 (1.4), tr	3.17	0.65	4.73

* Water loaded in the capsule.

† Water content of the fluid determined by dividing measured Cs in the fluid divided by added Cs to the starting material.

§ Modal phase abundances calculated by least squares mass balance. Numbers in parentheses indicate absolute one standard deviation.

Sum of residual squares obtained by mass-balance calculations.

** N.D. = not determined.

liq, liquid phase; grt, garnet; amph, amphibole; zoi, zoisite; cpx, clinopyroxene; stau, staurolite; ky, kyanite; rut, rutile; tr, trace amounts.

Therefore, bulk partitioning values for LILE represent maximum values and in the presence of phengite, the fractionation pattern for LILE, especially Cs, Rb and Ba, will be subject to change (e.g. Hermann et al., 2009).

Another distinct feature of arc magmas is a negative HFSE (high field strength elements) anomaly (Tatsumi and Eggins, 1995). Niobium, Tantalum and Titanium are strongly depleted relative to LILE and LREE as they are thought to be retained by Ti-rich phases such as rutile in the subducting oceanic lithosphere (e.g. Foley et al., 2000). In the present experiments, rutile is a ubiquitous phase of the residue throughout the experimental temperature range. It is the major host mineral for Nb and Ta, and to a lesser extent for Zr and Hf (Zack et al., 2002; Aulbach et al., 2008) in the absence of zircon (e.g. Hermann, 2002). Generally, our partitioning data reveal increasing volatile compatibility for Nb and Ta with increasing temperature from 700-800°C (**Figure 3.1**). $D_{Ta}^{(fluid/solid)}$ increases from 0.40 to 0.75 and $D_{Nb}^{(fluid/solid)}$ from 0.09 to 0.33 at 2 GPa. At 3 GPa, the increase is less pronounced with $D_{Ta}^{(fluid/solid)}$ varying from 0.01 to 0.18 and $D_{Nb}^{(fluid/solid)}$ from 0.07 to 0.22. Interestingly, the calculated bulk partition coefficients of the bulk volatile phase reveal contrasting fractionation behavior for Nb and Ta at 2 and 3 GPa. At lower pressure, $D_{Ta}^{(fluid/solid)} > D_{Nb}^{(fluid/solid)}$ indicates a preferred incorporation of Nb into rutile, while at 3 GPa, $D_{Ta}^{(fluid/solid)} < D_{Nb}^{(fluid/solid)}$. Literature rutile partitioning data reveal contrasting behavior for aqueous fluids and hydrous melts. Rutile in equilibrium with melt shows preferred incorporation of Ta over Nb (Schmidt et al., 2004b; Klemme et al., 2005; Klimm et al., 2008). The opposite is true when rutile is in equilibrium with aqueous fluids (Brenan et al., 1994; Stalder et al., 1998). The latter results, however, are less well constrained due to either large analytical errors or Nb/Ta values (in rutile) close to or equal to unity. The partitioning of Hf and Zr reveals identical fractionation behavior at 2 and 3 GPa and shows a strong positive temperature dependence but lower incompatibility at higher pressure with $D_{Hf}^{(fluid/solid)} < D_{Zr}^{(fluid/solid)}$. However, unlike anticipated for arc magmas, the compositions of the investigated bulk volatiles do not exhibit a strong depletion of HFSE relative to the other elements analyzed in this study.

REE, Th and U were identified as key elements characterizing the subduction component in arc magmas (McCulloch and Gamble, 1991; Elliott et al., 1997; Hawkesworth et al., 1997), but data highlighting the partitioning of these elements between volatiles and residual mineral assemblages are sparse. At 2 GPa and 700-750°C, REE are not volatile mobile and weakly fractionated (**Figure 3.1**). A distinct step of increasing volatile compatibility for LREE and partly MREE is observed in the temperature step from 750-800°C, resulting in a steep REE pattern. Because volatile-solid distribution coefficients at all temperatures are below ~0.1 (except Eu), resulting volatiles are always prominently depleted in REE.

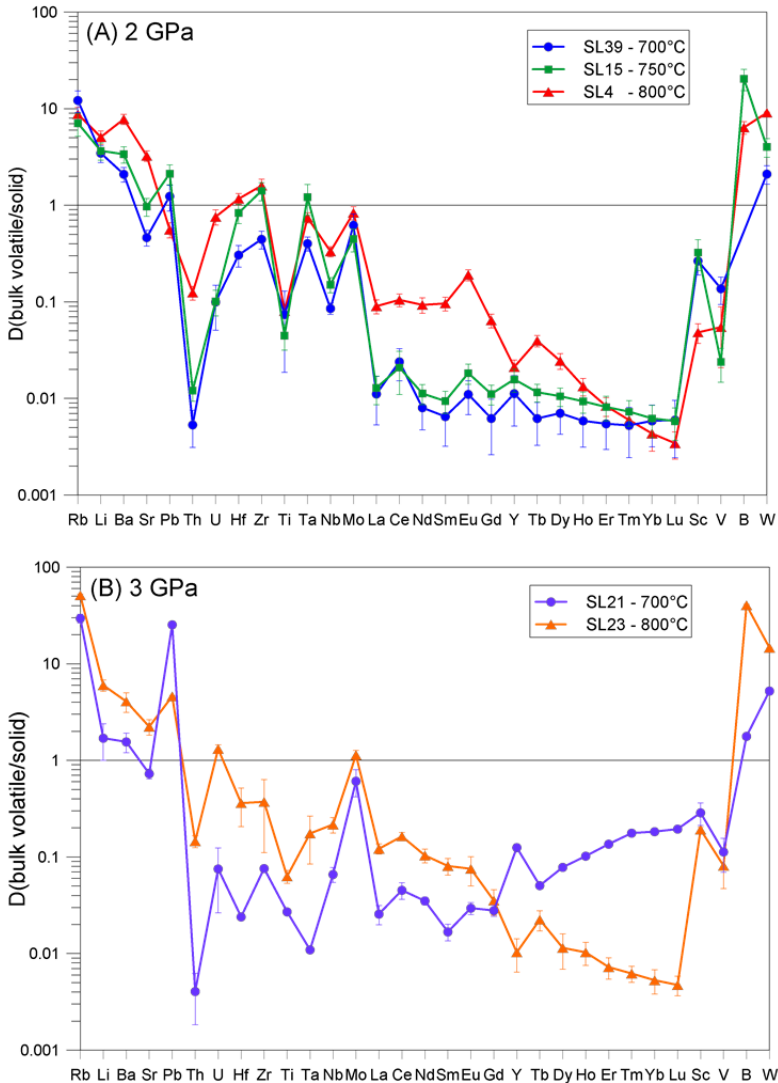


Figure 3.2. Bulk volatile-solid partition coefficients for (A) 2 GPa and (B) 3 GPa. Bulk solid residue was calculated by subtracting measured trace element composition in the volatile times its fraction from initial amount of trace elements in the starting material divided by solid residue fraction. Uncertainties are given as 1σ and were calculated by propagating uncertainties of elemental concentrations.

At 3 GPa/700°C, the partitioning pattern for the REE reveals fractionation with $D_{Lu}^{(fluid/solid)} > D_{La}^{(fluid/solid)}$, the inverse of the results at 2 GPa and 3 GPa/800°C, and contrary to what has

been published so far. At 800°C, the fractionation is similar to that at 2 GPa and 800°C. Increasing pressure mobilizes REE only moderately. It is well established that the strong depletion of the HREE is almost entirely due to residual garnet (e.g. Stalder et al., 1998; Kessel et al., 2005). Thus, the strong variability in fractionation behavior of HREE can be linked to the relative proportions of residual garnet and zoisite (**Table 3.1**). At 700°C and 750°C, the grt/zoi modal abundance ratio is between 0.05 and 0.1, with garnet amounting to only a few percent of the entire assemblage (1-2 wt%). Increasing the temperature to 800°C increases the modal proportion of garnet to 2.3 wt% (2 GPa) and 31 wt% (3 GPa) along with a distinct decrease in zoisite fraction. Consequently, the grt/zoi ratio increases to 0.4 and 4, respectively, and accounts for the steepening of the REE patterns of the bulk rock $D(\text{fluid/solid})$ data illustrated in **Figure 3.1**.

Several studies pointed out the importance of epidote-group minerals as carriers of LREE (La-Sm), Th (and U) in the subducting crust (e.g. Spandler et al., 2003). LREE, Th and U show increasing volatile mobility with increasing temperature. Thorium strongly fractionates from U with $D_{\text{Th}}^{(\text{fluid/solid})} < D_{\text{U}}^{(\text{fluid/solid})}$ indicating the preferred incorporation of Th into epidote-group minerals. We observe a distinct increase in the mobility from 700°C/750°C to 800°C with $D_{\text{Th}}^{(\text{fluid/solid})} = 0.12$ and $D_{\text{U}}^{(\text{fluid/solid})} = 0.76$ at 2 GPa/800°C, and $D_{\text{Th}}^{(\text{fluid/solid})} = 0.15$ and $D_{\text{U}}^{(\text{fluid/solid})} = 1.31$ at 3 GPa/800°C, revealing the stronger mobile character of U at higher temperatures compared to Th that remains clearly volatile-incompatible at all conditions. LREE partitioning is characterized by $D_{\text{LREE}}^{(\text{fluid/solid})}$ between 0.01 and 0.05 at low temperatures (700-750°C) and by a prominent increase in volatile mobility at 800°C, with $D_{\text{LREE}}^{(\text{fluid/solid})}$ between 0.1 and 0.2 at 2 and 3 GPa, respectively, displaying a similar partitioning behavior for LREE as for Th and U with increasing pressure and temperature. $D_{\text{La}}^{(\text{fluid/solid})} < D_{\text{Ce}}^{(\text{fluid/solid})} > D_{\text{Nd}}^{(\text{fluid/solid})} > D_{\text{Sm}}^{(\text{fluid/solid})}$ reveals that Ce is the most volatile-mobile of the LREE at all pressures and temperatures even though the difference in mobility for these elements becomes smaller with increasing temperature, leaving the partitioning pattern at 800°C flatter and the elements less fractionated from each other.

3.4 Zoisite composition

Epidote-group minerals form elongated crystals that are small in size, 10-20 μm by 5 μm at 700 and 750°C/2 GPa and <10 μm at all temperatures at 3 GPa. Only at 800°C/2 GPa, grains are exceptionally large up to 100 μm long at 30 μm diameter. Despite their fine-grained character, we obtained an almost complete dataset by adjusting beam size during LA-ICP-MS analyses. Only at 700°C/3 GPa, grains were too small for LA-ICP-MS analysis. Crystals display moderate zonation at low temperatures, which turns into a very pronounced

zonation at 800°C/2 GPa with HREE-enriched cores and LREE-enriched rims. We assume this is partly a result of retarded garnet nucleation, leading to an earlier formation of the epidote-group minerals and delayed nucleation of the garnets, promoting HREE incorporation into the cores of the epidote-group minerals prior to garnet saturation. Only rim compositions (i.e., the corresponding LA-ICP-MS transient signal sections) that are in equilibrium with the coexisting bulk volatile were used. Minerals were normalized to Si=3 and denote as zoisites ($x_{\text{zoi}} = 0.7$ at 700°C/2 GPa and 0.71 at 800°C/2 GPa). Distinctly higher REE concentrations are observed at 750°C to 800°C (**Table A3**). At 800°C/3 GPa, the phase assemblage consists of REE-poor and REE-rich zoisite (in minor amounts). Compared to 2 GPa, zoisites at 800°C/3 GPa are poorer in Al, Fe³⁺ and Ca ($x_{\text{zoi}} = 0.69$ and 0.65 at 700°C and 800°C). REE-rich zoisites at 800°C/3 GPa were analyzed by electron microprobe for Sr, Th, U and selected REE. The transition from zoisite to more REE-rich compositions is characterized by a distinct increase in total REE concentration (**Table 3.1**) to 4.7 wt% total LREE, 0.3 wt% Th and 0.2 wt% U. With total REE+Th+U = 0.15 a.p.f.u. they still belong to the clinozoisite subgroup, according to Armbruster et al. (2006).

The transition of REE-poor to REE-rich epidote-group minerals has been described in experimental studies (Hermann, 2002; Feineman et al., 2007; Klimm et al., 2008) where this change was found to occur between 800 and 900°C. Feineman et al. (2007) observed this compositional transition in their zoisite-fluid partitioning experiments at 2 GPa/900°C with an increase of the LREE by a factor of ~6. In contrast, Martin et al. (2011), who studied the partitioning between zoisite and aqueous fluids at 3 GPa, did not report this prominent change in mineral compositions with increasing temperature from 700°C to 850°C. REE-poor epidotes with $\sum\text{REE} = 0.45$ wt% at 750°C and allanite compositions with $\sum\text{REE} = 10.8$ wt% at 800°C were found by Klimm et al. (2008) at 2.5 GPa. In general, our result corresponds well with literature data, notably with the experimental stabilities of zoisite and allanite reported by Hermann (2002). Note, however, that all studies were performed with very different levels of trace element-doping of the starting material to enhance stability and abundance of allanite, thus partially accounting for discrepancies in composition of the epidote-group minerals reported in the different studies. While Martin et al. (2011) employed a relatively low doping level of 50-100 $\mu\text{g g}^{-1}$, Klimm et al. (2008) added 200 $\mu\text{g g}^{-1}$ (500 $\mu\text{g g}^{-1}$ total LREE). Compared with these values, the doping level adopted in this study (40 $\mu\text{g g}^{-1}$ for REE, 20 $\mu\text{g g}^{-1}$ for Th and U) is low and comparable to some natural MORB compositions (25-150 $\mu\text{g g}^{-1}$ LREE content) and, therefore, to the input into subduction zone environments.

3.5 Zoisite/fluid partitioning

Trace element partition coefficients of epidote-group minerals at 2 GPa/700-800°C (analyzed by LA-ICP-MS) and 3 GPa/800°C (analyzed by EPMA) are presented in **Figure 3.2**. The most striking features are the high (100-1700) $D^{(\text{zoisite}/\text{fluid})}$ for all REE and Th. They represent by far the most compatible elements in epidote-group minerals in the present experiments consistent with natural epidote compositions and other experimental partitioning studies.

Our data show generally $D_{\text{LREE}} (\text{La-Sm}) > D_{\text{MREE}} (\text{Eu-Ho}) \leq D_{\text{HREE}} (\text{Er-Lu})$ with a decrease from La to Sm by a factor of 0.4 to 2.6. LREE fractionate from each other especially at lower temperatures, e.g. $D_{\text{La}} > D_{\text{Ce}}$. D_{MREE} are always slightly lower than D_{HREE} , resulting in a relatively flat REE pattern. D_{Th} exceed D_{U} by about an order of magnitude at all temperatures. $D_{\text{Th}}/D_{\text{U}}$ decreases from 21 to 12 at 2 GPa from 700 to 800°C. Increasing temperature results in decreasing partitioning for D_{REE} , D_{Th} , and D_{U} . In natural samples, Sr and Pb are strongly enriched in epidote-group minerals (Zack et al., 2002; Spandler et al., 2003). In this study, D_{Sr} and D_{Pb} result between 3 and 12 at 700°C to 800°C and decrease with increasing temperature. An identical partitioning behavior with temperature is observed for HFSE. Niobium and Ta are incompatible in zoisite with $D_{\text{Nb}} > D_{\text{Ta}}$ while D_{Hf} and D_{Zr} reveal a slightly compatible character with preferred incorporation of Zr over Hf into zoisite.

The influence of pressure onto the trace element partitioning is obtained by comparing REE-rich zoisites at 3 GPa/800°C with zoisites at 2 GPa/800°C. All D-values display increased partitioning by a factor of 2-3 at higher pressure. Fractionation behavior is the same for most elements even though D_{Sm} shows relatively high values, being the most compatible of the LREE at 3 GPa/800 °C.

In the following, we compare our results with published partition coefficients for zoisite (Feineman et al., 2007; Martin et al., 2011) and allanite (Klimm et al., 2008). Compared to previous studies, three main differences of the zoisite partition behavior markedly stand out (**Figure 3.2b**). First, calculated D_{REE} , D_{Th} and D_{U} of Feineman et al. (2007) and Martin et al. (2011) are much lower than our values that result from directly measured zoisites and bulk volatile phases. Feineman et al.'s D_{LREE} at 2 GPa/750°C are lower by > 2 orders of magnitude at identical conditions. Martin et al. (2011) reported even lower D_{LREE} at 700°C/3 GPa ($D_{\text{La}} = 0.09$, compared to 1720 in this study at 2 GPa) which designates all REE as incompatible in zoisite in equilibrium with fluids. They suggest that increasing pressure reduces the compatibility of REE in zoisite, a conclusion that is contrary to our results ($D_{\text{LREE}}/3 \text{ GPa} > D_{\text{LREE}}/2 \text{ GPa}$ (**Figure 3.2a**)).

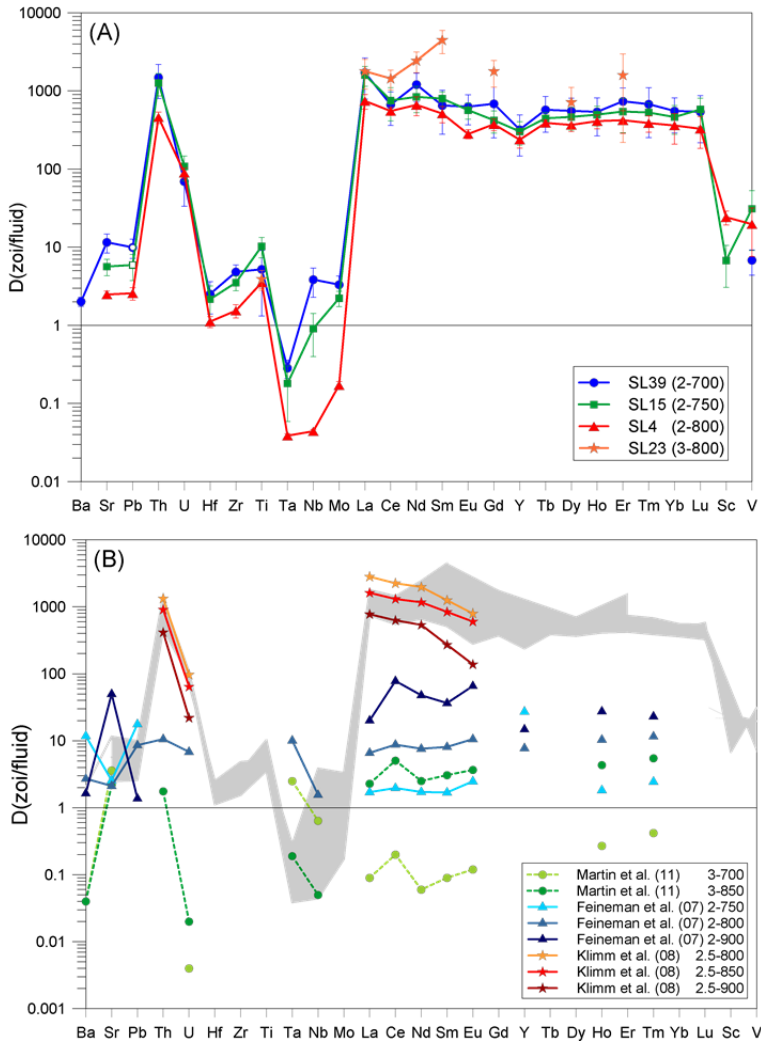


Figure 3.3. (A) Zoisite-fluid partition coefficients from this study. Empty symbols for Pb at 700 and 750°C and 2 GPa represent maximum values as LA-ICP-MS analyses of zoisites were below the limit of detection for Pb. (B) Zoisite-fluid partition coefficients from experiments of Martin et al. (2011) and Feineman et al. (2007), and allanite-melt partition coefficients from Klimm et al. (2008) compared with results from this study (grey shaded area) from (A).

Moreover, both studies suggest that HREE (and MREE) are more compatible than LREE at temperatures from 700-850°C. This is in contrast with our data and other experimental studies (Hermann, 2002) and with the fractionation observed in natural zoisites and allanites (e.g. Zack et al., 2002; Spandler et al., 2003; Frei et al., 2004). Our results suggest

that Th is incorporated into zoisite preferably over U, in agreement with Feineman et al. (2007) and Martin et al. (2011) although their D_{Th} and D_U are considerably lower than ours. We obtained $D_{Nb} > D_{Ta}$, whereas they calculated $D_{Nb} < D_{Ta}$, yet all the datasets reveal increasing compatibility for Nb and Ta with decreasing temperature.

The third striking difference between previous data and this study is the influence of temperature on the compatibility of REE. While our measurements at 2 GPa infer decreasing D-values with increasing temperature, Feineman et al. (2007) and Martin et al. (2011) calculated distinctly increasing compatibility with increasing temperature. The temperature dependence observed in our experiments is consistent with Klimm et al. (2008) for allanite-melt partitioning, resulting in a decrease of $D_{REE}^{(all/melt)}$ by a factor of ~ 3.6 with increasing temperature from 800°C to 900°C. Even though their experiments are at slightly higher pressure (2.5 GPa), our results are in good agreement with their partitioning behavior of LREE, Th and U. Assuming continuous solid-solution from epidote-clinozoisite to allanite-dissakisite with increasing temperature for a similar basaltic starting material, our $D(\text{zoisite}/\text{fluid})$ at lower temperatures complement their $D(\text{allanite}/\text{melt})$ for epidote-group mineral partitioning. We, therefore, conclude that the calculated D-values of Feineman et al. (2007) and Martin et al. (2011) significantly underestimate the compatibility of LREE, Th and U in zoisite.

3.6 Summary and conclusion

We present partition coefficients for 30 trace elements between zoisite and bulk volatiles corresponding to sub-arc conditions. In contrast to earlier experimental studies and for the first time, we obtained zoisite-fluid partitioning data independently from mass balance calculations by directly measuring volatile phases via the cryogenic LA-ICP-MS diamond trap approach. In the present experimental setup, epidote-group minerals are the major host for LREE, Th and U in eclogitic residues coexisting with a bulk volatile strongly depleted in REE, Th and to a lesser extent U. The results suggest continuous evolution towards allanitic compositions (assuming almost complete zoisite-allanite solid solution) + melt at the expense of zoisite with increasing temperature and pressure in the basalt-H₂O system. The determined $D(\text{zoisite}/\text{fluid})$ presented in this study extend previously published $D(\text{allanite}/\text{melt})$ to lower temperature conditions. The obtained dataset clearly confirms the importance of epidote-group minerals as carrier for LREE, Th, and U in the subducting slab, not only for REE-rich accessory epidote-group minerals but also for the low-temperature equivalent zoisite. Moreover, we demonstrate that measured $D(\text{zoisite}/\text{fluid})$ are in the range of previously published $D(\text{allanite}/\text{melt})$, much higher than

calculated $D(\text{zoisite}/\text{fluid})$ values reported in published experimental studies. Provided that zoisites occur more commonly than allanite in high-pressure terrains representing remnants of subducted crust (Enami et al., 2004), our new results broaden the applicability to more general settings. The trace element characteristics of a bulk volatile phase in equilibrium with epidote-group-bearing mineral assemblages result rather uniform irrespective of whether allanite-bearing mineral assemblages coexist with melts or zoisite-bearing mineral assemblages are in equilibrium with a volatile phase dominated by aqueous fluids.

The trace element composition of the bulk volatiles emerging from the slab simulated by our experiments does yet not fully explain the distinct features of arc magma signatures observed (e.g. enrichment of LREE over HREE) since very little LREE and Th are transported to the arc basalt source region when epidote-group minerals are present. Considering the low solubilities of zoisite and allanite in aqueous fluids and silicate melts at typical sub-arc conditions, it has been suggested previously that elimination of LREE-phases by melting of the oceanic crust and/or its sediment layer is the key to generate a REE-typical arc magma signature (e.g. Klimm et al., 2008; Hermann and Rubatto, 2009; Skora and Blundy, 2010). Our results for the basalt-H₂O system reinforce these findings and show that at low temperatures and in equilibrium with zoisite-bearing residues such a bulk volatile signature originating from the oceanic crust cannot be produced. This study, therefore, fills a gap in the low temperature assessment of the mobile phase escaping the descending slab in subduction zone environments.

3.7 Electronic appendix A1-A5

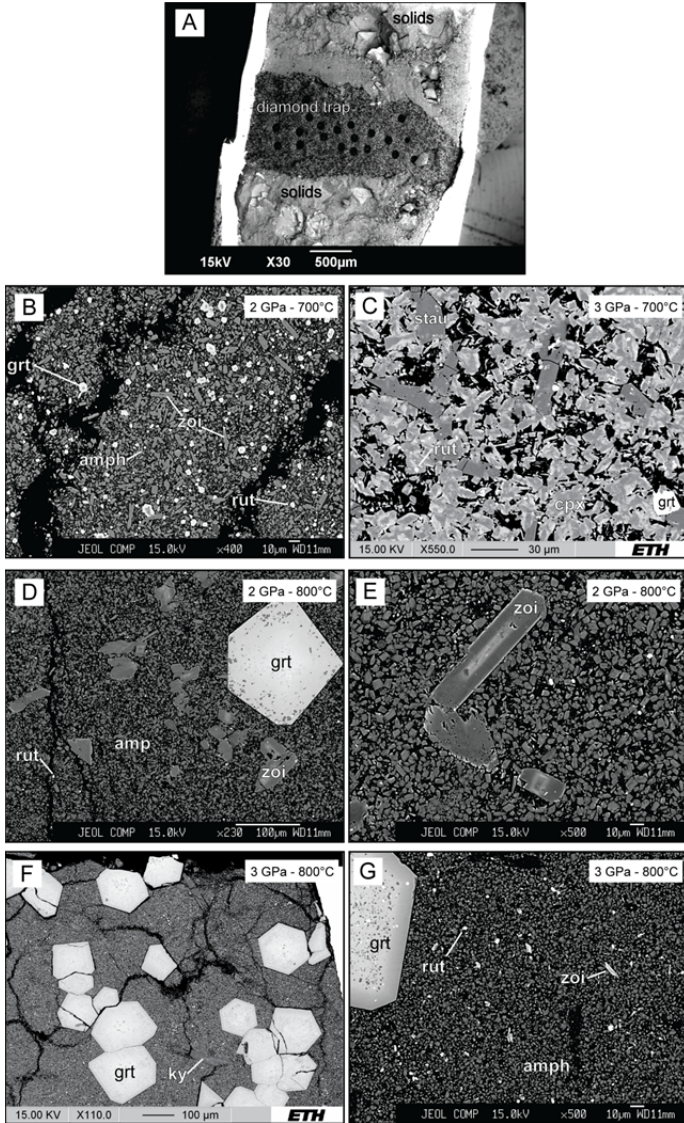


Figure A1. Backscattered electron images of representative run products at 2 and 3 GPa, 700 to 800°C. A: representative image of a cut open experimental capsule containing a diamond trap in between two layers of residual phases. The black holes in the trap are laser ablation pits. B and C: phase assemblage at 700°C with garnet, amphibole, zoisite and rutile. At 3 GPa, clinopyroxene replaces amphibole and staurolite is stable additionally. D and E: phase assemblage at 2 GPa/800°C. Note the strong zonation in zoisite shown in E. F and G: phase assemblage at 3 GPa/800°C. Kyanite was stable in this run.

TABLE A2. BULK VOLATILE COMPOSITION

Run	SL-39		SL-15		SL-4		SL-21		SL-23	
T (°C)	700		750		800		700		800	
P (GPa)	2		2		2		3		3	
	Average (ppm)	1 σ	Average (ppm)	1 σ	Average (ppm)	1 σ	Average (ppm)	1 σ	Average (ppm)	1 σ
n*	11		14		18		10		13	
Cs	236	25	206	36	195	21	276	14	245	45
Rb	3.68	0.84	2.90	0.58	2.46	0.35	4.72	0.31	4.41	156
Li	75	13	73	8	69	8	51	3	95	14
Ba	63	8	77	6	84	5	53	19	90	9
Sr	25.8	4.0	47.5	5.6	86.2	5.6	37.9	5.9	85.7	112
Pb	3.56	0.99	4.94	0.77	192	0.28	13.13	160	7.70	2.14
Th	0.11	0.05	0.27	0.04	2.84	0.36	0.08	0.03	3.03	0.92
U	190	0.91	199	0.48	12.04	175	141	0.33	18.63	2.64
Hf	12.2	2.8	29.2	4.1	35.8	2.8	10	0.3	14.4	2.5
Zr	17.8	3.1	44.2	5.5	44.4	5.5	3.3	0.8	15.2	3.1
Ti	1253	928	794	189	1509	78	452	56	1076	90
Ta	17.1	2.2	54.8	6.4	28.3	2.0	0.5	0.1	7.9	16
Nb	4.01	0.33	7.16	0.29	15.42	0.84	3.04	0.21	9.87	103
W	59	11	79	11	82	31	100	10	126	24
Mo	23.6	6.8	18.1	3.6	29.5	3.4	23.1	13	38.4	7.6
La	0.49	0.25	0.59	0.18	4.31	0.54	1.10	0.33	5.23	136
Ce	1.11	0.39	1.00	0.44	5.24	0.57	2.03	0.70	7.32	0.52
Nd	0.32	0.13	0.46	0.07	3.99	0.59	1.35	0.22	4.03	0.89
Sm	0.27	0.13	0.41	0.08	4.34	0.53	0.68	0.19	3.33	0.86
Eu	0.48	0.18	0.82	0.13	8.49	0.67	1.24	0.29	3.22	0.74
Gd	0.29	0.16	0.53	0.08	3.24	0.40	1.25	0.39	1.63	0.33
Y	0.51	0.27	0.75	0.15	1.08	0.16	5.42	1.66	0.47	0.27
Tb	0.26	0.12	0.51	0.06	1.88	0.15	2.08	0.70	0.96	0.48
Dy	0.32	0.12	0.49	0.06	1.23	0.19	3.35	1.04	0.52	0.25
Ho	0.25	0.11	0.42	0.07	0.65	0.11	4.18	1.51	0.45	0.33
Er	0.24	0.11	0.38	0.09	0.42	0.08	5.68	1.55	0.32	0.21
Tm	0.22	0.11	0.32	0.07	0.28	0.05	6.85	1.34	0.26	0.21
Yb	0.27	0.12	0.30	0.10	0.23	0.07	7.87	1.21	0.25	0.17
Lu	0.26	0.15	0.27	0.09	0.17	0.05	8.00	1.45	0.21	0.19
Sc	10.9	2.8	13.4	4.1	2.3	0.5	11.5	10	8.1	12
V	5.72	1.71	1.07	0.37	2.61	1.60	4.64	1.97	3.46	102
B	159	37	122	22	79	8	56	4	148	25

*Number of analyses.

CHAPTER 3

TABLE A3. ZOISITE COMPOSITION

Run	SL-39		SL-15		SL-4		SL-21		SL-23	
T (°C)	700		750		800		700		800	
P (GPa)	2		2		2		3		3	
	Average	1 σ	Average	1 σ	Average	1 σ	Average	1 σ	Average	1 σ
Major element composition (wt%)										
SiO ₂	38.05	0.50	38.66	0.70	38.59	0.75	39.12	0.67	39.31	0.52
Na ₂ O	0.32	0.18	0.16	0.21	0.14	0.14	0.17	0.09	N.D.	N.D.
CaO	22.53	0.32	22.72	0.49	22.51	0.73	20.53	0.64	20.14	0.58
FeO [*]	4.46	0.29	4.42	0.25	4.32	0.60	5.83	0.23	3.36	0.42
Al ₂ O ₃	29.04	0.44	29.28	0.70	28.31	1.42	28.97	0.81	28.92	0.43
MgO	0.65	0.18	0.65	0.23	1.17	0.66	1.07	0.20	1.10	0.10
Trace element composition (ppm)										
Cs	B.D.	B.D.	B.D.	B.D.	B.D.	B.D.	N.D.	N.D.	N.D.	N.D.
Rb	B.D.	B.D.	B.D.	B.D.	B.D.	B.D.	N.D.	N.D.	N.D.	N.D.
Li	B.D.	B.D.	B.D.	B.D.	B.D.	B.D.	N.D.	N.D.	N.D.	N.D.
Ba	127	-	B.D.	B.D.	B.D.	B.D.	N.D.	N.D.	N.D.	N.D.
Sr	298	68	269	55	214	18	N.D.	N.D.	N.D.	N.D.
Pb	35.5	-	<29 [†]	9.8	<4.9 [†]	0.56	N.D.	N.D.	N.D.	N.D.
Th	170	39	341	97	1069	292	N.D.	N.D.	3168	933
U	132	27	216	55	1078	49	N.D.	N.D.	2164	436
Hf	30.8	117	63.1	29.2	40.0	5.8	N.D.	N.D.	N.D.	N.D.
Zr	85.7	12.8	155.7	27.7	68.5	10.3	N.D.	N.D.	N.D.	N.D.
Ti	6542	686	8191	1355	5337	819	12902	10069	3509	331
Ta	4.84	1.10	7.58	4.56	1.11	-	N.D.	N.D.	N.D.	N.D.
Nb	15.4	6.17	6.51	3.66	0.68	-	N.D.	N.D.	N.D.	N.D.
W	216	2.09	2118	9.58	0.93	0.49	N.D.	N.D.	N.D.	N.D.
Mo	78.4	-	40.1	3.8	5.1	-	N.D.	N.D.	N.D.	N.D.
La	843	155	946	56	3204	563	N.D.	N.D.	9369	2996
Ce	742	220	760	83	2897	163	N.D.	N.D.	10554	2894
Nd	385	17	390	131	2647	607	N.D.	N.D.	9840	1954
Sm	177	50	326	30	2225	450	N.D.	N.D.	14922	3016
Eu	300	58	466	82	2386	255	N.D.	N.D.	N.D.	N.D.
Gd	196	54	224	62	1214	155	N.D.	N.D.	2910	910
Y	164	19	227	59	258	42	N.D.	N.D.	N.D.	N.D.
Tb	152	23	229	35	732	21	N.D.	N.D.	N.D.	N.D.
Dy	175	44	228	68	451	45	N.D.	N.D.	371	93
Ho	137	31	208	47	267	26	N.D.	N.D.	N.D.	N.D.
Er	179	32	205	84	176	45	N.D.	N.D.	516	283
Tm	148	51	167	40	109	18	N.D.	N.D.	N.D.	N.D.
Yb	150	23	138	33	817	217	N.D.	N.D.	N.D.	N.D.
Lu	144	21	156	36	56.3	18.2	N.D.	N.D.	N.D.	N.D.
Sc	B.D.	B.D.	90.7	415	56.8	0.5	N.D.	N.D.	N.D.	N.D.
V	39.0	7.7	33.3	20.6	515	2.4	N.D.	N.D.	N.D.	N.D.
B	B.D.	B.D.	B.D.	B.D.	B.D.	B.D.	N.D.	N.D.	N.D.	N.D.

* All Fe reported as FeO.

[†] LA-ICP-MS measurement below detection limit, therefore, this represents maximum value.

N.D. = no data; B.D. = below detection limit.

TABLE A4. PARTITION COEFFICIENTS (ZOISITE/FLUID)

Run	SL-39		SL-15		SL-4		SL-23	
T (°C)	700		750		800		800	
P (GPa)	2		2		2		3	
	D(zoi/fluid)	Error*	D(zoi/fluid)	Error	D(zoi/fluid)	Error	D(zoi/fluid)	Error
Cs	N.D. [§]	N.D.	N.D.	N.D.	N.D.	N.D.	N.D.	N.D.
Rb	N.D.	N.D.	N.D.	N.D.	N.D.	N.D.	N.D.	N.D.
Li	N.D.	N.D.	N.D.	N.D.	N.D.	N.D.	N.D.	N.D.
Ba	2.02	0.27	N.D.	N.D.	N.D.	N.D.	N.D.	N.D.
Sr	1156	3.17	5.66	132	2.48	0.26	N.D.	N.D.
Pb	9.96	2.75	5.93	2.18	2.58	0.47	N.D.	N.D.
Th	1487	688	1267	404	460	75	1047	442
U	69	36	109	38	90	14	116	29
Hf	2.52	1.12	2.16	105	1.12	0.18	N.D.	N.D.
Zr	4.83	1.12	3.52	0.76	154	0.30	N.D.	N.D.
Ti	5.22	3.91	10.31	2.99	3.54	0.57	3.93	1.12
Ta	0.28	0.07	0.18	0.12	0.04	0.002	N.D.	N.D.
Nb	3.85	157	0.91	0.51	0.04	0.002	N.D.	N.D.
Mo	3.32	0.95	2.22	0.49	0.17	0.02	N.D.	N.D.
La	1717	932	1609	458	744	161	1790	738
Ce	668	307	757	344	553	68	1442	409
Nd	1209	481	839	312	664	181	2439	724
Sm	651	372	799	172	512	121	4482	1468
Eu	629	261	569	134	281	37	N.D.	N.D.
Gd	685	434	422	134	375	66	1788	665
Y	320	173	303	101	238	53	N.D.	N.D.
Tb	574	278	446	84	390	34	N.D.	N.D.
Dy	555	255	465	150	368	67	717	395
Ho	541	274	498	141	411	83	N.D.	N.D.
Er	737	354	546	255	423	135	1594	1374
Tm	678	425	530	178	388	91	N.D.	N.D.
Yb	554	263	463	185	361	152	N.D.	N.D.
Lu	542	326	581	231	328	143	N.D.	N.D.
Sc	N.D.	N.D.	6.79	3.73	24	5	N.D.	N.D.
V	6.82	2.44	31	22	20	12	N.D.	N.D.
B	N.D.	N.D.	N.D.	N.D.	N.D.	N.D.	N.D.	N.D.

* Errors represent 1 σ uncertainties, calculated as a standard deviation.

[§]N.D. = not determined.

CHAPTER 3

TABLE A5. BULK PARTITION COEFFICIENTS (FLUID/SOLID)

Run	SL-39		SL-15		SL-4		SL-21		SL-23	
T (°C)	700		750		800		700		800	
P (GPa)	2		2		2		3		3	
	D(fluid/solid)	Error*	D(fluid/solid)	Error	D(fluid/solid)	Error	D(fluid/solid)	Error	D(fluid/solid)	Error
Cs	I.S.†	I.S.	I.S.	I.S.	I.S.	I.S.	I.S.	I.S.	I.S.	I.S.
Rb	12.20	3.08	7.09	1.89	8.80	1.56	29.49	2.44	51.11	20.38
Li	3.47	0.70	3.66	0.75	5.08	0.80	1.70	0.12	5.99	1.41
Ba	2.10	0.36	3.38	0.65	7.79	0.94	1.55	0.55	4.07	0.86
Sr	0.46	0.09	0.97	0.20	3.25	0.41	0.73	0.12	2.23	0.50
Pb	1.24	0.37	2.12	0.50	0.56	0.10	25.36	3.34	4.61	1.54
Th	0.005	0.002	0.012	0.003	0.12	0.02	0.004	0.001	0.15	0.05
U	0.10	0.05	0.10	0.03	0.76	0.14	0.08	0.02	1.31	0.31
Hf	0.31	0.08	0.83	0.19	1.17	0.15	0.024	0.006	0.36	0.09
Zr	0.44	0.09	1.41	0.30	1.60	0.26	0.08	0.02	0.37	0.10
Ti	0.07	0.06	0.045	0.013	0.08	0.01	0.027	0.004	0.06	0.01
Ta	0.40	0.07	1.22	0.43	0.75	0.09	0.011	0.002	0.18	0.05
Nb	0.09	0.01	0.15	0.03	0.33	0.04	0.07	0.01	0.22	0.05
W	2.10	0.45	4.02	0.89	9.09	0.11	5.23	0.56	14.66	3.90
Mo	0.62	0.19	0.45	0.12	0.84	0.13	0.61	0.05	1.13	0.31
La	0.011	0.006	0.013	0.004	0.09	0.01	0.026	0.008	0.12	0.04
Ce	0.024	0.009	0.021	0.010	0.10	0.02	0.045	0.015	0.15	0.03
Nd	0.008	0.003	0.011	0.003	0.09	0.02	0.035	0.006	0.10	0.03
Sm	0.006	0.003	0.009	0.002	0.10	0.02	0.017	0.005	0.08	0.03
Eu	0.011	0.004	0.013	0.004	0.19	0.03	0.030	0.007	0.08	0.02
Gd	0.006	0.004	0.011	0.003	0.064	0.010	0.028	0.009	0.035	0.010
Y	0.011	0.006	0.015	0.004	0.021	0.004	0.13	0.04	0.10	0.006
Tb	0.006	0.003	0.012	0.002	0.040	0.005	0.051	0.017	0.022	0.012
Dy	0.007	0.003	0.011	0.002	0.024	0.005	0.08	0.02	0.011	0.006
Ho	0.006	0.003	0.009	0.002	0.013	0.003	0.10	0.04	0.10	0.008
Er	0.005	0.003	0.008	0.002	0.008	0.002	0.14	0.04	0.007	0.005
Tm	0.005	0.003	0.007	0.002	0.006	0.001	0.13	0.04	0.006	0.005
Yb	0.006	0.003	0.006	0.002	0.004	0.001	0.13	0.03	0.005	0.004
Lu	0.006	0.004	0.006	0.002	0.003	0.001	0.19	0.04	0.005	0.004
Sc	0.27	0.08	0.32	0.11	0.048	0.011	0.29	0.03	0.19	0.05
V	0.14	0.04	0.024	0.009	0.055	0.034	0.11	0.05	0.08	0.01
B	N.D.§	N.D.	20.47	5.10	6.39	0.94	1.77	0.14	40.38	10.00

* Errors represent 1σ uncertainties, calculated as a standard deviation.

† I.S. = Internal standard. Cs was used as internal standard to calculate the composition of the fluid assuming that Cs is fluid-compatible by > 99%.

§ N.D. = no data.

CHAPTER 4

Composition and trace element partitioning of mobile volatile phases and solid mineral residues during water-saturated dehydration and melting of basalt

Abstract

Piston cylinder experiments in a pristine, K-free MORB-water system were performed at 2 and 3 GPa and 700 to 1200°C in order to determine the major and trace element composition and nature of mobile phases during dehydration and melting of subducting oceanic lithosphere. Results from runs at 700 to 800°C, including zoisite-bulk volatile partition coefficients, are reported in Chapter 3. 10-15 wt% H₂O was added to the basalt to simulate flushing by fluids from underlying lithologies. Mobile volatile phases were captured in diamond traps and measured by LA-ICP-MS following the freezing approach. The hydrous phase assemblage (amphibole, zoisite, garnet and rutile) is replaced by a typical anhydrous, eclogitic residue (clinopyroxene, garnet ±rutile) at ~850°C. We present trace element partition coefficients for garnet, clinopyroxene and rutile in equilibrium with hydrous melts and aqueous fluids with the latter being scarce in the literature up to date. The results display the strong control residual phases in the slab exert upon the composition of the mobile phase emanating from the slab and eventually governing the signature of arc magmas. While garnet controls heavy rare earth elements (HREE), rutile controls Ti, Nb and Ta and to a lesser extent Hf and Zr. We find that clinopyroxene has only little influence on the trace element budget in the investigated system. All $D(\text{mineral/volatile})$ are strongly temperature-dependent and decrease with increasing temperature. Our results show that for a K-free (i.e. mica-free) MOR basalt, distinct LREE/HREE fractionation typical for arc magmas can only be achieved by complete removal of any epidote-group mineral from the residue, leaving LREE and Th free to migrate into the mantle wedge. However, our findings suggest, consistent with earlier finding, that only significant degrees of melting of the basaltic portion of the slab produces a trace element signature typical for arc-related rocks.

4.1 Introduction

Igneous rock at convergent plate margins are generated from sources that result from complex interactions between depleted mantle wedge peridotites and the descending oceanic lithosphere in subduction zone environments. Arc magma, generated in the metasomatised mantle source region, is considered to be enriched with elements that were liberated from the slab either as hydrous partial melts of subducted sediments or as aqueous fluids originating from the mafic oceanic crust (e.g. Elliott et al., 1997). These processes ultimately lead to a distinct geochemical signature, which many arc rocks have in common. Compared to mid-ocean ridge (MOR) basalt, they are relatively enriched in large ion lithophile elements (LILE, e.g. Cs, Rb, Ba) and light rare earth elements (LREE, La-Sm) and depleted in heavy rare earth elements (HREE) and high field strength elements (HFSE, e.g. Nb and Ta; McCulloch and Gamble, 1991; Hawkesworth et al., 1993; Elliott et al., 1997). Element transfer from the slab to the mantle wedge is controlled, besides pressure and temperature, by the mineralogy of the oceanic crust. Knowing the residual phase assemblage is, therefore, crucial to comprehend under which conditions hydrous mobile phases, that can either be aqueous fluids, hydrous silicic melts or supercritical liquids, are generated at the slab-mantle interface. Moreover, if the P-T conditions of certain residual phase assemblages can be constrained, the trace element composition of arc rocks can be used to calculate slab-top temperatures (e.g. Klimm et al., 2008; Plank et al., 2009; Cooper et al., 2012).

Recently, phase relation and trace element partitioning studies in MORB/sediment-H₂O systems have pointed out the importance of several key (accessory) residual phases in the slab controlling solubility and accordingly the bulk partitioning behavior of various groups of trace elements. Epidote-group minerals and monazite control LREE and Th (e.g. Klimm et al., 2008; Hermann and Rubatto, 2009; Skora and Blundy, 2010), rutile controls HFSE (mainly Nb and Ta) (Foley et al., 2000; Zack et al., 2002; Lucassen et al., 2010) and white mica controls LILE (mainly Rb and K) (e.g. Scambelluri et al., 2008; Hermann and Rubatto, 2009). These studies have shown that at low temperatures (700-800°C) only negligible amounts of trace elements are transported to the mantle wedge through aqueous fluids since they are largely retained in key residual phases. Hence it was suggested that only melting of oceanic lithosphere can effectively mobilize enough trace elements to create the typical arc rock signatures and/or element ratios. Additionally, Kessel et al. (2005a, 2005b) presented evidence that supercritical liquids above the second critical endpoint in a MORB-H₂O system at 6 GPa and 800-1200°C reveal melt-like characteristics at any temperature implying similar element mobility compared to subcritical high temperature melts. In this study, we experimentally investigated the phase relations in a K-free MORB-H₂O system at 2 and 3 GPa and 700 to 1200°C. Furthermore, the starting material was

doped with all important trace elements groups (LILE, REE, HFSE, transition metals) to determine partition coefficients for garnet, clinopyroxene and rutile/titanite, representing a common eclogitic phase assemblage, in equilibrium with a volatile phase. While there exists a rather large data set for mineral partitioning in equilibrium with hydrous melts, D -values for aqueous fluids are scarce, especially in complex mineral assemblages (Green and Adam, 2003; Kessel et al., 2005a; Spandler et al., 2007). The principal reason for the lack of these data is the difficulty to quantify the composition of such fluids. In order to directly measure mobile volatile phases, we employed diamond traps to collect and subsequently analyze them by the cryogenic laser ablation ICP-MS technique (Kessel et al., 2004; Aerts et al., 2010). This approach allows for full quantification of the volatile phase independent from mass balance calculations. Low temperature (700-800°C) volatile phase compositions (as well as zoisite/volatile partition coefficients) are presented in Chapter 3 and used here to determine mineral/volatile partition coefficients for all other phases presented in this Chapter.

4.2 Experimental methods

4.2.1 Synthesis of the starting material

In order to simulate processes in a subduction zone environment, we used a synthetic starting material (TB-1; Schmidt and Poli, 1998) representing an average MOR basalt/gabbro. The potassium free starting composition was mixed from analytical grade oxide and carbonate powders, which were fired (1000°C: SiO_2 , TiO_2 , MgO , Fe_2O_3) and dried (220°C: Al_2O_3 , CaCO_3 , Na_2SiO_3) for 24 hours to remove any moisture before weighing and manually homogenizing the mix in an agate mortar under ethanol. Oxygen fugacity ($f\text{O}_2$) was constrained by fixing the ferric to ferrous ratio in the starting material. We equilibrated and vitrified the mixture in an iron pre-saturated Pt-crucible (to avoid Fe-loss) in an H_2 - CO_2 gas mixing furnace at 1325°C for 2 hours at fixed $f\text{O}_2$ value corresponding to the NNO buffer equilibrium. The homogeneity of the glass was checked after quenching with the electron probe (EPMA). The major element composition of TB-1 is listed in **Table 4.1**.

Trace elements were added to the starting material as a pre-synthesized spike (Rohit Nandedkar, Diss. ETH No. 21411) produced in the following way: First, a diopside glass was produced from synthetic compounds at ambient pressure and 1450°C. After grinding the glass to a fine powder, a total of 30 trace elements, including all important groups (LILE, REE, HFSE, transition metals), were added to the diopside mix at a 2000 $\mu\text{g/g}$ level, except U and Th, which were added at a 1000 $\mu\text{g/g}$ level. After vitrification at 1460°C for 3.5 hours, the glass composition was determined by laser-ablation inductively-coupled-plasma mass-

spectrometry (LA-ICP-MS, see **Table 4.2**) and ground to a fine powder before adding 2 wt% to the starting material to obtain a 40 µg/g level for most trace elements and 20 µg/g for U and Th. Pb and Rb were nearly completely lost during synthesis due to alloying with the Pt-crucible (Pb) and volatilization (Rb).

In low temperature runs at 2 GPa and 700°C, where slow nucleation kinetics prohibited garnet nucleation, the trace element-doped starting material was complemented with 0.5 wt% natural garnet seeds. These garnets (x_{alm} : 0.324, x_{pyr} : 0.562, x_{gross} : 0.018, x_{spess} : 0.005, see **Figure 4.5**) have a different composition from those formed at higher temperatures in this study. They were ground and sieved to a fine powder (< 7 µm) with the expectation that new, chemically distinct rims in equilibrium with the other residual phases, will grow during the experiment.

Table 4.1. Composition of the starting material.

n=20	TB-1	
	wt%	Std
SiO ₂	51.78	0.99
TiO ₂	1.50	0.05
Al ₂ O ₃	16.36	0.59
FeO	9.99	0.27
MgO	6.83	0.28
CaO	10.30	0.38
Na ₂ O	3.19	0.11
Total	100.00	
X_{Mg} ¹⁾	0.55	

¹⁾ X_{Mg} calculated with $\text{Fe}^{2+} = \text{Fe}^{\text{tot}}$

Table 4.2. Element concentrations in the diopside glass employed for doping as determined by LA-ICP-MS.

Major element composition			Trace element composition		
n=12	wt%	1 σ	n=9	[$\mu\text{g/g}$]	1 σ
SiO ₂	49.18	0.54	Li	1692	64
TiO ₂	1.47	0.05	Sc	1917	18
Al ₂ O ₃	0.15	0.02	V	1886	23
FeO	0.01	0.01	Rb	30.8	1.8
MgO	16.05	0.16	Sr	1971	39
CaO	24.12	0.29	Y	1992	39
Na ₂ O	0.02	0.03	Zr	1960	39
K ₂ O	0.21	0.03	Nb	2090	44
			Mo	1629	55
Total	91.21		Cs	29.3	1.8
			Ba	2099	35
			La	1920	25
			Ce	2023	21
			Nd	1728	8
			Sm	1822	16
			Eu	1883	13
			Gd	2005	30
			Tb	1860	29
			Dy	1951	39
			Ho	1875	39
			Er	1928	44
			Tm	1808	45
			Yb	2010	61
			Lu	1927	59
			Hf	1897	63
			Ta	2059	36
			W	1983	21
			Pb	170	8
			Th	935	29
			U	765	18

4.2.2 Experimental setup

For experiments up to 1000°C gold capsules (3.0 mm outer diameter, 2.7 mm inner diameter) were used to minimize Fe-loss to the capsule walls. At higher temperatures, 1100°C and 1200°C, Au₉₀Pd₁₀ and Au₈₀Pd₂₀ capsules were employed, respectively. In order to collect and separate the mobile volatile phase from the residual solid phase assemblage, we performed diamond trap experiments where the bulk volatiles were captured in the interstices of the diamonds (e.g. Stalder et al., 1998). At 2 GPa, a second series of experiments without diamond trap was conducted for better characterization of the residual eclogitic mineral phases.

In detail: First, 4 µl of water (corresponding to 10-15 wt% of the total H₂O and basalt system) was pipetted into the capsule by micro syringe. The water was additionally doped with 585 ppm Cs. Cesium is a highly incompatible element and is assumed to partition strongly into the volatile phase which makes it an ideal internal standard for the subsequent LA-ICP-MS analyses of the volatiles in a K-free basaltic system (see Kessel et al., 2004). For the experiments with diamond trap, half of the basaltic starting material was filled into the capsule, covered by a thin layer of synthetic diamonds (~20 µm average grain size), before filling up the capsule with the second half of the starting material. Capsules were welded shut using a tungsten arc-welder. By comparing the weight of the capsule before and after welding, water loss during welding could be excluded. Capsules were weighed and heated to 110°C to ensure tightness.

All capsules were embedded vertically into boron-nitride (BN) cylinders surrounded by a talc-pyrex piston cylinder assembly with straight graphite heaters and MgO spacers above and below the capsule. A friction correction of +10% to the nominal pressure was applied (calibrations based on the orthoferrosilite = fayalite + qtz reaction and the qtz – coesite transitions, Bohlen et al., 1980; Bose and Ganguly, 1995). Care was taken to place the capsule in the center of the assembly (where the hot spot is) to prevent mineral growth within the diamond trap. Oxygen fugacity was not controlled during the experiments but is estimated to stay approximately constant and close to the initial fO_2 fixed by the Fe^{3+}/Fe^{2+} ratio of the starting material. The use of BN around the capsule prevents oxidation due to hydrogen loss but can result in slightly reducing conditions (Truckenbrodt et al., 1997).

All experiments were performed in a 600-ton rocking piston cylinder apparatus with 14 mm bore size at ETH Zürich at 2 and 3 GPa and temperatures varying from 700°C to 1200°C. Pressure was kept constant during the runs and is estimated to deviate by less than 0.02 GPa from the nominal value. Temperature was controlled with a B-type Pt₉₄Rh₆/Pt₇₀Rh₃₀ thermocouple with an estimated accuracy of ±10°C. No corrections for the effect of pressure on the thermocouple (e.m.f.) were made. Experiments were first heated up to ~500°C to soften the Pyrex before increasing pressure and temperature simultaneously to the desired run conditions. During heating, the piston cylinder device

was turned by 180° constantly and subsequently every 15 minutes during the duration of the experiment to enhance reaction rates and reduce chemical zoning caused by thermal gradients along the capsule (Schmidt and Ulmer, 2004). Experiments were quenched by cutting power, with estimated quench rates exceeding 100°C/s.

4.3 Analytical methods

Upon quenching an experimental charge to ambient conditions, fluids or melts undergo extensive crystallization and/or exsolution; moreover, highly soluble elements remain in the fluid phase (e.g. potassium, Stalder et al., 2002). Using traditional methods to quantify the volatile phase composition, such as piercing the capsule and releasing the fluid, these soluble elements and potential quench crystals entrained in the fluid are lost and consequently lack from the bulk volatile composition. We, therefore, followed the "freezing" approach that allows for full quantification of the volatile phase (Kessel et al., 2004). Before opening, the capsule is mounted into an external freezing stage (Aerts et al., 2010), cooled below the freezing point of the volatile phase and then cut open to expose a longitudinal section of the capsule. The capsule remains frozen during the subsequent LA-ICP-MS analyses of the ice contained in the diamond trap.

4.3.1 LA-ICP-MS

Trace element compositions of the mobile volatile phases were measured with a 193 nm ArF Excimer laser system coupled to an ELAN DRC-e quadrupole mass spectrometer at the University of Bern. Depending on the size of the diamond trap, 15-25 shots were performed per sample with a spot size of 44-90 µm. The external standard NIST-SRM-610 was measured twice before and after one series of analyses. Background was measured for ~50 seconds, ablation intervals were in the range of 20-40 seconds at 8-10 Hz repetition rate.

Data reduction was done with the software SILLS (Guillong et al., 2008). Cesium was used as the internal standard to determine bulk volatile compositions under the assumption that all incompatible Cs partitions into the volatile phase; thus the known Cs:H ratio in the starting material and in the bulk volatile phase is identical. Therefore, absolute concentrations for all elements can be recalculated to quantify the entire mobile phase.

For the analyses of the crystalline residual phases, the laser spot size was adapted to the size of the different crystals in the range of 4 µm (for the very small phases, e.g. rutile) to 60 µm (e.g. garnet) at 5-10 Hz repetition rate, background was measured for ~50 seconds. A strong increase in the counts of incompatible elements (e.g. Cs) was taken as indicator

for having shot through the crystal and the integration interval was selected accordingly during off-line data reduction. CaO, Al₂O₃ or TiO₂ concentrations, previously determined by EPMA, were used as internal standards for quantification. Because of the sometimes very small beam sizes, stringent LOD calculations (Pettke et al., 2012) are critical to obtaining significant element concentrations at the 95% confidence level.

Table 4.3. Experimental results and calculated phase proportions.

Run No.	Pressure [GPa]	Temp. [°C]	Duration [h]		H ₂ O _{in} ^a [wt%]	cH ₂ O ^b [wt%]	Phase assemblage	Phase proportions ^c [wt%]	ΣR ² ^d
			diamond trap	no trap					
SL12	2	700		163	11.0	46.1	liq, amph, zoi, ttn, rut	22.8 (1.0), 57.3 (1.8), 18.2 (1.6), 1.7 (1.0), tr	0.50
SL39	2	700		167	11.0	40.1	liq, grt, amph, zoi, rut	22.7 (1.7), 1.7 (4.7), 56.6 (4.3), 17.3 (2.8), 1.7 (0.8)	0.91
SL10	2	700		168	13.0		liq, amph, zoi, rut	27.2 (0.7), 53.4 (1.1), 18.7 (1.0), 0.8 (0.3)	0.20
SL15	2	750		163	11.6	35.6	liq, grt, amph, zoi, rut	26.1 (0.4), 0.7 (1.1), 57.6 (1.0), 13.9 (0.6), 1.6 (0.2)	0.04
SL4	2	800		74	14.5	32.5	liq, grt, amph, zoi, rut	34.3 (3.7), 2.3 (9.3), 57.7 (10.0), 5.1 (5.7), 0.6 (1.4)	2.88
SL6	2	800		71	11.6		liq, grt, amph, zoi, rut	27.8 (3.3), 0.4 (7.6), 65.0 (8.7), 5.7 (5.1), 1.1 (1.3)	2.57
SL14	2	850		69	10.8	25.7	liq, grt, amph, cpx, rut	28.8 (2.2), 13.5 (8.8), 38.8 (13.4), 17.4 (4.9), 1.5 (0.83)	1.15
SL2	2	900		49	12.8	24.9	liq, grt, cpx, rut	47.8 (1.0), 33.6 (1.8), 18.5 (1.5), 0.1 (0.4)	1.45
SL3	2	900		70	10.8		liq, grt, cpx, rut	43.1 (1.5), 32.6 (2.5), 23.9 (2.1), 0.5 (0.5)	0.57
SL11	2	1000		71	11.1	22.9	liq, grt, cpx, rut	47.2 (2.1), 33.9 (3.2), 18.6 (2.6), 0.4 (0.7)	3.61
SL7	2	1000		28	12.9		liq, grt, cpx, rut	50.7 (0.8), 22.4 (1.2), 26.8 (1.1), tr	0.17
SL13	2	1100		22	13.1	20.5	liq, cpx	56.6 (10.9), 43.4 (9.4)	25.17
SL21	3	700		167	10.5	45.3	liq, grt, cpx, zoi, stau, rut	20.1 (2.8), 4.9 (7.6), 52.2 (7.1), 14.0 (6.9), 7.7 (4.5), 1.2	1.35
SL23	3	800		75	10.5	41.8	liq, grt, cpx, ky, zoi, rut	22.9 (2.9), 31.5 (7.5), 36 (5.9), tr, 8.0 (5.3), 1.6 (1.4)	3.17
SL24	3	900		39	10.6	33.1	liq, grt, cpx, rut	30.5 (2.5), 46.8 (5.0), 21.6 (4.3), 1.0 (1.0)	2.50
SL17	3	1000		26	10.6	30.3	liq, grt, cpx, rut	33.6 (3.2), 47.9 (6.0), 17.8 (5.0), 0.7 (1.2)	3.78
SL25	3	1100		71	11.4	19.6	liq, grt, cpx	39.9 (5.0), 44.3 (3.2), 15.8 (4.3)	3.24
SL34	3	1200		46	10.4	21.0	liq, grt, cpx	46.3 (1.2), 29.0 (1.7), 24.8 (1.8)	0.29

^a Water loaded in the capsule.^b Water content of the bulk volatile phase determined by dividing measured Cs in the bulk volatile divided by added Cs to the starting material.^c Modal phase abundances calculated by least squares mass balance. Numbers in parentheses indicate absolute one standard deviation.^d Sum of residual squares obtained by mass-balance calculations.

liq, bulk volatile phase; grt, garnet; amph, amphibole; zoi, zoisite; cpx, clinopyroxene; stau, staurolite; ky, kyanite; rut, rutile; ttn, titanite; tr, trace amounts.

4.3.2 Electron probe micro-analysis

After LA-ICP-MS analyses, the diamond traps in the defrosted capsules were visually examined using a scanning electron microscope (SEM) to exclude mineral growth within the trap. Then the capsules were impregnated with a low-viscosity Laromin resin, the diamond trap was cut out and the charges were embedded in epoxy and polished down to 1 μm . For EPMA analyses the samples were carbon coated (20 nm).

Major element composition of minerals and glasses were analyzed with wavelength-dispersive spectrometry (WDS) on a JEOL JXA-8200 electron probe micro-analyzer at ETH Zürich. Analyses were performed with counting times of 40 seconds on the peak and 20 seconds on the background using an acceleration voltage of 15 kV. Variable beam size and beam current of 10 $\mu\text{m}/5$ nA and focused beam/20 nA were used for glasses and minerals, respectively. Modal proportions of all the experiments were calculated using non-weighted least square regression based on the major element composition of the minerals and bulk volatiles (**Table 4.3**).

Table 4.4a. Bulk volatile major element composition at 2 GPa.

T (°C)	700		750		800		850		900		1000		1100	
Run	SL39	1 σ	SL15	1 σ	SL4	1 σ	SL14	1 σ	SL2	1 σ	SL11	1 σ	SL13	1 σ
# analyses	11		14		18		16		12		21		20	
Anhydrous (normalized to 100 wt%)														
SiO ₂	73.55	(1.11) ^a	73.13	(0.45)	70.83	(0.62)	68.48	(0.94)	65.11	(2.14)	61.89	(1.22)	58.38	(2.40)
Na ₂ O	8.83	(1.61)	7.33	(1.26)	5.96	(0.57)	7.06	(0.93)	6.85	(0.60)	5.59	(0.59)	4.72	(1.22)
CaO	2.17	(0.39)	2.65	(0.51)	3.45	(0.28)	3.09	(0.34)	4.70	(0.97)	5.91	(0.46)	8.51	(1.12)
FeO ^b	2.16	(0.42)	1.66	(0.49)	1.68	(0.23)	2.19	(0.66)	3.16	(0.50)	5.42	(0.39)	6.78	(1.11)
Al ₂ O ₃	12.36	(2.51)	14.63	(1.72)	17.01	(1.28)	17.77	(1.12)	17.80	(1.37)	17.32	(1.20)	14.79	(2.40)
MgO	0.81	(0.14)	0.47	(0.03)	0.84	(0.05)	1.10	(0.13)	1.82	(0.40)	2.56	(0.11)	5.69	(0.55)
TiO ₂	0.12	(0.02)	0.12	(0.03)	0.23	(0.01)	0.32	(0.01)	0.57	(0.04)	1.32	(0.07)	1.14	(0.13)
Hydrous (normalized to 100 wt% with H ₂ O)														
SiO ₂	43.82	(0.75)	47.25	(0.51)	47.86	(0.79)	51.31	(0.69)	48.87	(1.64)	48.59	(1.63)	46.41	(1.89)
Na ₂ O	5.42	(1.50)	4.69	(0.85)	3.87	(0.42)	5.13	(0.58)	5.14	(0.46)	4.37	(0.46)	3.57	(0.87)
CaO	1.44	(0.44)	1.60	(0.30)	2.43	(0.30)	2.29	(0.45)	3.80	(0.90)	4.58	(0.40)	6.83	(0.71)
FeO	1.43	(0.56)	1.07	(0.31)	1.16	(0.17)	1.64	(0.49)	2.37	(0.38)	4.31	(0.38)	5.32	(0.50)
Al ₂ O ₃	7.11	(1.84)	9.41	(1.10)	11.44	(0.85)	12.71	(1.40)	13.14	(1.26)	12.88	(1.52)	11.80	(1.97)
MgO	0.56	(0.17)	0.30	(0.02)	0.56	(0.04)	0.83	(0.10)	1.40	(0.29)	2.00	(0.09)	4.69	(0.36)
TiO ₂	0.13	(0.09)	0.08	(0.02)	0.15	(0.01)	0.24	(0.01)	0.43	(0.03)	1.03	(0.05)	0.91	(0.11)
H ₂ O	40.08		35.59		32.52		25.86		24.85		22.25		20.47	
P.I. ^c	1.25		0.82		0.56		0.66		0.64		0.56		0.50	
Al.I. ^d	0.62		0.89		1.06		1.01		0.86		0.83		0.65	

^a Numbers in parentheses indicate absolute standard deviation of the distribution of average compositions.

^b All Fe reported as FeO.

^c Peralkalinity index reported as Na₂O/Al₂O₃ molar.

^d Alumina index reported as Al₂O₃/(Na₂O+CaO).

Table 4.4b. Bulk volatile major element composition at 3 GPa.

T (°C)	700		800		900		1000		1100		1200	
Run	SL21	1 σ	SL23	1 σ	SL24	1 σ	SL17	1 σ	SL25	1 σ	SL34	1 σ
# analyses	10		13		14		17		16		17	
Anhydrous (normalized to 100 wt%)												
SiO ₂	76.20	(0.77) ^a	72.99	(1.36)	70.68	(1.22)	68.31	(1.40)	61.70	(2.21)	62.03	(3.34)
Na ₂ O	15.02	(0.49)	11.16	(2.87)	9.63	(1.35)	7.63	(1.13)	7.11	(0.81)	4.67	(1.01)
CaO	1.23	(0.29)	1.98	(0.59)	2.89	(0.56)	3.36	(0.61)	5.53	(0.74)	6.86	(1.39)
FeO ^b	4.14	(0.79)	2.17	(0.48)	2.97	(1.03)	3.99	(0.29)	3.76	(0.20)	5.37	(0.86)
Al ₂ O ₃	2.66	(0.41)	10.68	(1.92)	12.50	(3.33)	13.84	(2.23)	17.47	(1.85)	16.24	(1.22)
MgO	0.66	(0.10)	0.83	(0.17)	0.94	(0.17)	1.74	(0.17)	2.89	(0.14)	3.37	(0.95)
TiO ₂	0.08	(0.01)	0.18	(0.01)	0.40	(0.06)	1.13	(0.15)	1.53	(0.15)	1.46	(0.18)
Hydrous (normalized to 100 wt% with H ₂ O)												
SiO ₂	41.66	(1.00)	42.14	(1.04)	47.15	(1.17)	47.20	(1.17)	50.08	(1.75)	48.61	(2.33)
Na ₂ O	8.22	(0.28)	5.88	(1.09)	6.63	(1.36)	5.31	(0.76)	5.88	(0.73)	4.06	(1.22)
CaO	0.67	(0.16)	1.15	(0.35)	1.95	(0.37)	2.25	(0.41)	4.49	(0.58)	5.45	(1.22)
FeO	2.56	(0.53)	1.32	(0.35)	2.47	(0.94)	3.26	(0.54)	3.05	(0.16)	5.08	(1.27)
Al ₂ O ₃	1.18	(0.36)	6.96	(1.88)	7.84	(1.98)	9.70	(1.99)	13.35	(1.96)	11.74	(1.91)
MgO	0.35	(0.10)	0.61	(0.24)	0.63	(0.11)	1.22	(0.14)	2.34	(0.11)	2.91	(0.99)
TiO ₂	0.04	(0.01)	0.11	(0.01)	0.29	(0.02)	0.79	(0.11)	1.24	(0.12)	1.13	(0.15)
H ₂ O	45.31		41.83		33.06		30.27		19.56		21.02	
P.I. ^c	11.47		1.39		1.39		0.90		0.72		0.57	
Al.I. ^d	0.08		0.59		0.54		0.76		0.75		0.71	

^a Numbers in parentheses indicate absolute standard deviation of the distribution of average compositions.

^b All Fe reported as FeO.

^c Peralkalinity index reported as Na₂O/Al₂O₃ molar.

^d Alumina index reported as Al₂O₃/(Na₂O+CaO).

4.4 Results

4.4.1 Phase relations

Experimental conditions, phase assemblages and their modal proportions are summarized in **Table 4.3**. Average major element compositions of the bulk volatile and the mineral phases are reported in **Table 4.4** and **Table 4.5**; selected BSE-images of the experimental charges are depicted in **Figure 4.1**. At 2 GPa and up to 800°C, the phase assemblage commonly consists of garnet and the hydrous phases amphibole and zoisite with accessory rutile. It is replaced by the nominally anhydrous eclogitic minerals garnet, clinopyroxene (cpx) and rutile at 900°C and higher temperatures. Rutile is stable up to 1000°C and is melted out at 1100°C. In experiment SL12 (2 GPa, 700°C) garnet is absent, instead a second Ti-phase, titanite, is part of the assemblage. At 3 GPa, amphibole is no longer stable but zoisite coexists with garnet, cpx and rutile up to 800°C. From 900°C to 1200°C the phase

CHAPTER 4

assemblage contains garnet and cpx. Staurolite and kyanite join the residues at 700°C and 800°C, respectively. Rutile becomes exhausted from the residue at 1100°C. The composition of zoisite changes to relatively REE-rich epidote-group minerals at 800°C. Composition and trace element partitioning behavior of the epidote-group minerals and their coexisting bulk volatiles at 700°C to 800°C at 2 and 3 GPa are discussed elsewhere (Chapter 3), but we use the major and trace element composition of the volatiles at these conditions to calculate partition coefficients for the various minerals present in all the experiments discussed in this Chapter.

Table 4.5. Average major element composition of the run products in wt% (except zoisite).

Run	Phase	n	SiO ₂	1σ	Na ₂ O	1σ	CaO	1σ	FeO	1σ	Al ₂ O ₃	1σ	MgO	1σ	TiO ₂	1σ	Total
SL39	grt	5	38.00	(0.50) ^a	0.10	(0.05)	12.07	(0.44)	23.55	(0.34)	21.37	(0.32)	3.93	(0.26)	0.77	(0.08)	99.77
	amph	14	46.13	(0.92)	3.13	(0.28)	9.18	(0.18)	13.86	(0.35)	12.60	(0.79)	11.29	(0.41)	0.83	(0.16)	97.02
	rut ^b	10	0.80	(0.23)	0.11	(0.17)	0.60	(0.06)	1.66	(0.06)	0.71	(0.06)	0.11	(0.04)	94.18	(0.59)	98.18
SL12	amph	15	47.38	(0.51)	3.84	(1.05)	9.10	(0.30)	13.38	(0.35)	11.90	(0.94)	11.17	(0.62)	0.67	(0.11)	97.44
	rut	1	2.30	-	0.16	-	0.88	-	2.09	-	0.80	-	0.26	-	94.86	-	101.37
	ttn	9	31.01	(0.51)	0.11	(0.08)	27.82	(0.52)	1.13	(0.27)	2.89	(0.31)	0.22	(0.21)	35.33	(0.75)	98.52
SL15	grt	4	38.04	(0.27)	0.06	(0.02)	12.53	(0.53)	22.69	(0.60)	21.03	(0.25)	4.37	(0.45)	1.12	(0.23)	99.83
	amph	16	45.04	(1.73)	2.78	(0.33)	9.66	(0.50)	14.09	(0.84)	13.30	(0.83)	10.65	(1.12)	0.86	(0.26)	96.37
	rut	6	0.57	(0.36)	0.05	(0.03)	0.61	(0.13)	1.50	(0.29)	0.97	(0.13)	0.16	(0.14)	95.45	(0.38)	99.31
SL4	grt	3	38.58	(0.35)	0.13	(0.17)	12.86	(0.83)	19.39	(1.44)	21.09	(1.05)	6.61	(0.76)	1.31	(0.19)	99.99
	amph	22	43.10	(0.57)	2.95	(0.28)	10.41	(0.31)	13.08	(0.49)	15.72	(0.55)	10.82	(0.40)	1.09	(0.05)	97.16
	rut ^c	8	0.31	(0.22)	0.01	(0.01)	0.53	(0.11)	1.54	(0.04)	0.91	(0.07)	0.07	(0.05)	95.90	(0.50)	99.28
SL14	grt	5	39.05	(0.59)	0.07	(0.02)	12.12	(1.07)	18.76	(1.02)	21.25	(0.58)	7.55	(1.47)	1.44	(0.33)	100.24
	amph	31	42.11	(0.69)	3.31	(0.17)	10.35	(0.23)	12.41	(0.69)	16.68	(0.44)	10.99	(0.40)	1.34	(0.15)	97.19
	cpx	13	51.40	(1.53)	1.24	(0.17)	21.09	(0.54)	7.56	(0.93)	7.56	(0.54)	11.75	(0.68)	0.59	(0.16)	101.19
	rut	11	0.33	(0.16)	0.03	(0.03)	0.56	(0.07)	1.26	(0.05)	1.01	(0.08)	0.13	(0.08)	94.42	(0.40)	97.75
SL2	glass	17	56.35	(1.36)	4.48	(0.41)	3.62	(0.48)	0.79	(0.40)	15.63	(0.34)	0.21	(0.12)	0.61	(0.05)	81.68
	grt	8	39.73	(2.01)	0.14	(0.14)	12.27	(1.49)	17.62	(1.68)	19.37	(2.09)	8.91	(1.22)	2.13	(2.06)	100.18
	cpx	16	50.64	(0.73)	1.00	(0.11)	21.35	(0.20)	7.18	(0.65)	7.20	(0.59)	12.34	(0.26)	0.78	(0.14)	100.47
	rut	13	0.21	(0.11)	0.01	(0.01)	0.53	(0.09)	1.35	(0.04)	0.96	(0.02)	0.09	(0.03)	94.89	(0.52)	98.03
SL11	glass	18	54.62	(1.11)	2.57	(0.80)	6.07	(0.99)	1.96	(0.60)	16.81	(0.48)	1.18	(0.31)	1.46	(0.14)	84.67
	grt	3	39.49	(0.96)	0.16	(0.08)	10.94	(0.74)	17.11	(1.01)	19.64	(1.12)	10.48	(0.52)	2.02	(0.47)	99.85
	cpx	20	51.11	(0.52)	1.17	(0.24)	21.03	(0.60)	6.47	(0.50)	5.77	(0.92)	13.77	(0.58)	0.72	(0.10)	100.05
	rut ^d	16	0.18	(0.09)	0.01	(0.01)	0.51	(0.11)	1.64	(0.04)	1.11	(0.04)	0.06	(0.02)	94.81	(0.64)	98.32
SL13	glass	16	42.58	(1.91)	1.28	(0.20)	7.33	(0.80)	5.86	(0.75)	13.52	(0.79)	4.73	(0.82)	1.34	(0.08)	76.63
	cpx	6	52.15	(0.63)	0.54	(0.08)	22.07	(0.35)	4.24	(0.34)	4.18	(0.90)	16.29	(0.55)	0.46	(0.12)	99.95
SL21	grt	9	37.99	(0.96)	0.08	(0.18)	9.32	(1.02)	26.16	(1.37)	21.20	(0.79)	4.25	(0.47)	0.81	(0.45)	99.81
	cpx 1	8	54.10	(1.79)	5.86	(0.50)	11.56	(0.65)	7.67	(0.91)	12.52	(1.25)	7.14	(0.51)	0.71	(0.50)	99.54
	cpx 2	10	52.51	(1.36)	3.44	(0.50)	9.81	(4.31)	13.35	(1.53)	8.67	(2.41)	10.65	(0.93)	0.32	(0.16)	98.76
	rut	9	0.95	(0.32)	0.05	(0.03)	0.64	(0.13)	1.83	(0.11)	0.87	(0.20)	0.16	(0.05)	94.15	(0.68)	98.64
	stau	11	28.25	(0.83)	0.02	(0.02)	0.15	(0.08)	12.48	(0.19)	51.49	(0.72)	3.36	(0.16)	0.70	(0.34)	96.45
SL23	grt	7	39.11	(1.44)	0.21	(0.28)	10.37	(0.47)	21.05	(1.89)	21.07	(1.08)	7.17	(0.94)	1.36	(2.08)	100.35
	cpx	15	54.01	(0.68)	4.10	(0.40)	14.54	(0.78)	7.43	(1.99)	10.20	(0.84)	10.08	(0.46)	0.33	(0.08)	100.69
	rut	13	0.32	(0.19)	0.03	(0.05)	0.64	(0.09)	0.93	(0.07)	1.28	(0.10)	0.08	(0.04)	95.06	(0.79)	98.34
	ky	7	37.16	(0.25)	0.02	(0.01)	0.06	(0.01)	0.32	(0.03)	61.85	(0.66)	0.21	(0.04)	0.32	(0.20)	99.96
SL24	glass	16	60.67	(0.99)	6.25	(0.48)	2.42	(0.32)	0.59	(0.20)	13.19	(0.30)	0.28	(0.26)	0.37	(0.09)	83.78
	grt	4	40.37	(0.67)	0.42	(0.15)	11.30	(0.34)	18.48	(1.25)	19.88	(0.59)	8.34	(0.77)	1.79	(0.23)	100.59
	cpx	19	53.75	(0.78)	3.84	(0.52)	17.75	(0.95)	4.23	(0.30)	9.32	(0.85)	10.79	(0.61)	0.42	(0.08)	100.10
SL17	rut	17	0.35	(0.26)	0.02	(0.02)	0.51	(0.10)	1.20	(0.05)	1.15	(0.06)	0.08	(0.05)	95.57	(0.23)	98.89
	glass	26	47.66	(0.50)	3.55	(0.36)	3.80	(0.10)	2.48	(0.09)	12.73	(0.35)	1.43	(0.06)	1.14	(0.03)	72.79
	grt	6	40.13	(0.91)	0.36	(0.21)	11.01	(0.61)	17.42	(1.00)	19.67	(1.10)	9.30	(0.54)	2.20	(0.22)	100.09
SL25	cpx	27	52.49	(0.66)	2.71	(0.31)	18.92	(0.56)	4.88	(0.46)	7.18	(0.69)	11.85	(0.47)	0.64	(0.09)	98.67
	glass	28	47.69	(0.46)	3.89	(0.11)	5.94	(0.12)	2.84	(0.09)	14.23	(0.17)	2.71	(0.11)	1.55	(0.04)	78.86
	grt	7	39.90	(0.68)	0.16	(0.12)	10.65	(0.61)	16.11	(1.30)	20.70	(1.31)	10.85	(0.55)	1.64	(0.71)	100.00
SL34	cpx	21	52.41	(0.24)	2.67	(0.29)	19.18	(0.56)	3.71	(0.71)	8.71	(0.57)	12.54	(0.50)	0.75	(0.14)	99.97
	glass	22	57.56	(0.33)	4.29	(0.07)	6.44	(0.07)	3.58	(0.08)	14.18	(0.10)	2.04	(0.05)	1.97	(0.04)	90.06
SL12	grt	7	39.86	(0.49)	0.24	(0.12)	9.52	(1.61)	18.60	(1.18)	20.82	(0.68)	9.88	(1.13)	1.77	(0.47)	100.69
	cpx	12	51.97	(0.49)	3.80	(0.17)	14.98	(0.40)	5.88	(0.27)	13.52	(0.81)	8.86	(0.18)	0.86	(0.05)	99.87

^a Numbers in parentheses indicate absolute standard deviation of the distribution of average compositions.

^b Analyses for rutile from experiment SL10 (without diamond trap).

^c Analyses for rutile from experiment SL6 (without diamond trap).

^d Analyses for rutile from experiment SL7 (without diamond trap).

Abbreviations as in Table 4.3.

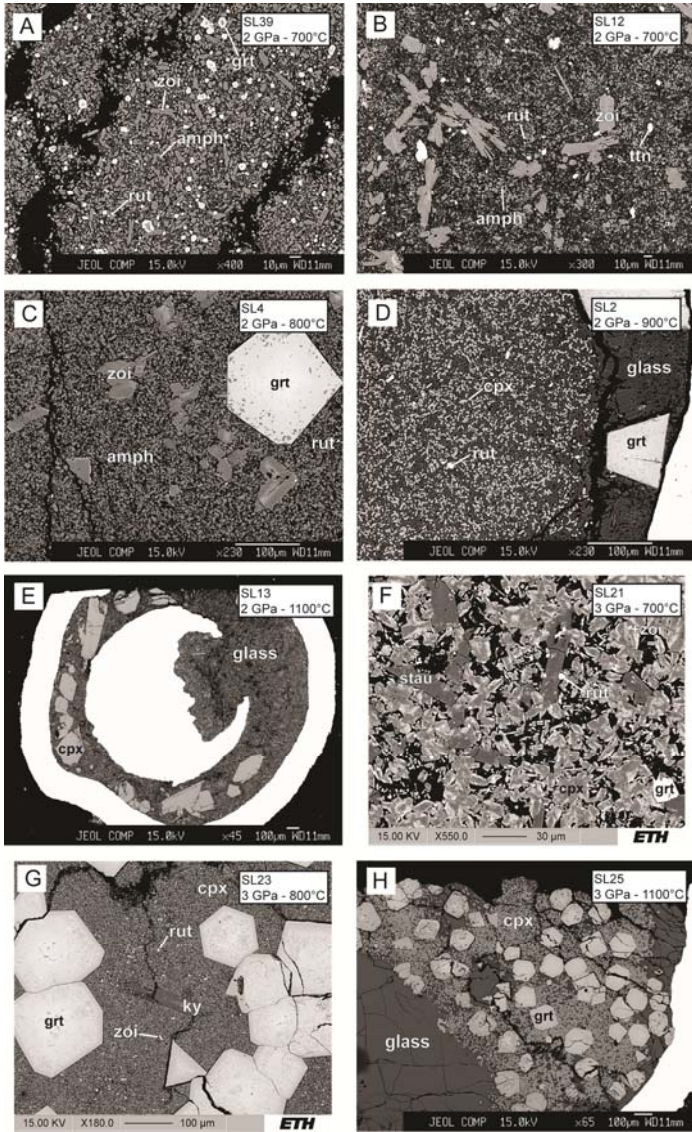


Figure 4.4. Backscattered electron images of representative run products at 2 and 3 GPa, 700 to 1100°C. A to C: water-saturated phase assemblage at 2 GPa with garnet, amphibole, zoisite and rutile. Note that B shows the run without garnet but with titanite in addition to rutile (SL-12). D: anhydrous phase assemblage with garnet, clinopyroxene, rutile and glass. E: glass and clinopyroxene as liquidus phase at 1100°C. F to H: phase assemblage at 3 GPa, F and G display garnet, clinopyroxene, zoisite, rutile. Additionally, staurolite and kyanite are stable at 700 and 800°C, respectively. Note that at 700°C two clinopyroxene compositions exist representing the effect of an intersection with a (metastable) solvus. H: anhydrous phase assemblage with garnet and clinopyroxene in a non-vesicular glass matrix. Rutile is molten out at these conditions.

Table 4.6. Average trace element composition (ppm) of the bulk volatile phase as determined by LA-ICP-MS.

P (GPa)	SL14		SL2		SL11		SL13		SL24		SL17		SL25		SL34	
	2	850	2	900	2	1000	2	1100	3	900	3	1000	3	1100	3	1200
# analyses	18	10	12	10	21	10	20	10	14	14	17	10	16	17	17	10
Cs	154.88 (23.53) ^a	147.78 (22.24)	130.07 (22.24)	130.07 (21.94)	123.50 (21.94)	123.50 (29.33)	227.93 (29.33)	227.93 (34.47)	174.85 (28.06)	112.95 (28.06)	112.95 (13.44)	124.78 (70.80)				
Rb	2.58 (0.53)	1.83 (0.49)	2.17 (0.49)	2.17 (0.25)	1.38 (0.25)	3.38 (0.31)	3.38 (0.31)	3.38 (0.31)	3.12 (0.56)	2.26 (0.56)	2.26 (0.27)	1.54 (0.49)				
Li	69.18 (7.05)	69.26 (8.25)	64.53 (8.39)	64.53 (8.39)	31.66 (8.39)	93.73 (15.36)	93.73 (15.36)	93.73 (15.36)	77.35 (14.31)	63.53 (14.31)	63.53 (7.27)	46.34 (6.66)				
Ba	75.00 (4.45)	71.01 (19.83)	68.55 (2.37)	68.55 (4.10)	41.02 (2.18)	65.76 (12.13)	65.76 (12.13)	65.76 (12.13)	63.21 (9.35)	62.40 (9.35)	62.40 (5.80)	72.93 (15.25)				
Sr	87.74 (7.89)	85.65 (13.81)	73.07 (3.85)	73.07 (3.85)	44.07 (4.47)	61.17 (9.73)	61.17 (9.73)	61.17 (9.73)	51.12 (10.73)	62.57 (10.73)	62.57 (7.30)	80.91 (15.13)				
Pb	3.29 (0.53)	2.39 (0.43)	4.25 (0.73)	4.25 (0.73)	0.14 (0.03)	5.76 (0.59)	5.76 (0.59)	5.76 (0.59)	1.13 (0.33)	0.71 (0.33)	0.71 (0.09)	0.31 (0.11)				
Th	22.39 (2.51)	25.84 (3.21)	20.56 (1.92)	20.56 (1.92)	13.33 (1.25)	18.52 (3.31)	18.52 (3.31)	18.52 (3.31)	16.48 (3.27)	18.28 (3.34)	18.28 (6.52)	23.11 (6.52)				
U	28.42 (3.54)	26.92 (0.97)	27.23 (2.46)	27.23 (2.46)	20.55 (5.02)	27.68 (3.21)	27.68 (3.21)	27.68 (3.21)	30.09 (4.44)	27.56 (2.89)	27.56 (2.89)	29.71 (7.12)				
Hf	36.09 (4.21)	40.74 (3.82)	31.14 (4.52)	31.14 (4.52)	24.07 (4.60)	19.62 (4.90)	19.62 (4.90)	19.62 (4.90)	22.82 (6.62)	32.16 (5.78)	32.16 (5.78)	31.97 (4.92)				
Zr	42.29 (5.78)	48.16 (4.47)	44.90 (6.24)	44.90 (6.24)	37.05 (8.86)	23.58 (6.43)	23.58 (6.43)	23.58 (6.43)	34.63 (9.11)	35.62 (19.77)	35.62 (19.77)	51.19 (8.80)				
Ti	2363 (95)	4321 (278)	10284 (518)	10284 (518)	9347 (1065)	2844 (249)	2844 (249)	2844 (249)	7773 (1072)	12263 (1072)	12263 (1057)	11465 (1453)				
Ta	27.52 (2.94)	41.52 (1.13)	68.13 (7.28)	68.13 (7.28)	50.71 (6.79)	28.73 (6.05)	28.73 (6.05)	28.73 (6.05)	59.35 (11.82)	62.78 (7.41)	62.78 (7.41)	58.53 (24.29)				
Nb	16.98 (0.69)	35.46 (2.99)	48.34 (2.72)	48.34 (2.72)	30.01 (2.40)	25.14 (3.46)	25.14 (3.46)	25.14 (3.46)	51.53 (5.07)	53.49 (4.03)	53.49 (4.03)	52.65 (11.81)				
Mn	35.89 (3.59)	45.34 (13.91)	53.81 (8.83)	53.81 (8.83)	43.84 (3.98)	73.33 (11.58)	73.33 (11.58)	73.33 (11.58)	44.13 (8.23)	29.71 (2.30)	29.71 (2.30)	64.45 (14.89)				
La	35.27 (4.83)	40.71 (14.28)	44.21 (2.83)	44.21 (2.83)	27.70 (2.15)	40.27 (8.69)	40.27 (8.69)	40.27 (8.69)	34.44 (9.08)	39.19 (7.66)	39.19 (7.66)	54.03 (12.58)				
Ce	35.28 (1.52)	51.69 (15.24)	48.99 (1.23)	48.99 (1.23)	33.04 (0.77)	49.29 (5.57)	49.29 (5.57)	49.29 (5.57)	46.33 (4.74)	51.29 (3.90)	51.29 (3.90)	61.44 (11.06)				
Nd	25.19 (2.11)	36.55 (2.52)	32.88 (2.23)	32.88 (2.23)	23.12 (1.98)	16.79 (3.55)	16.79 (3.55)	16.79 (3.55)	19.86 (4.38)	29.94 (5.83)	29.94 (5.83)	40.97 (8.89)				
Sm	13.00 (1.50)	17.11 (1.61)	24.74 (1.61)	24.74 (1.61)	23.70 (2.60)	7.37 (1.24)	7.37 (1.24)	7.37 (1.24)	11.71 (2.43)	26.28 (5.28)	26.28 (5.28)	34.09 (5.61)				
Eu	12.56 (1.23)	15.68 (1.21)	27.10 (1.61)	27.10 (1.61)	26.89 (3.60)	5.30 (1.18)	5.30 (1.18)	5.30 (1.18)	10.87 (1.99)	28.57 (4.80)	28.57 (4.80)	33.82 (4.69)				
Gd	3.35 (0.36)	5.83 (0.54)	14.61 (1.26)	14.61 (1.26)	24.30 (4.47)	5.03 (2.29)	5.03 (2.29)	5.03 (2.29)	7.83 (1.23)	21.78 (4.85)	21.78 (4.85)	30.42 (6.23)				
Y	0.84 (0.17)	1.93 (0.61)	3.44 (0.64)	3.44 (0.64)	23.59 (5.69)	0.59 (0.15)	0.59 (0.15)	0.59 (0.15)	5.58 (0.90)	14.94 (2.20)	14.94 (2.20)	14.26 (3.90)				
Tb	1.45 (0.21)	2.99 (0.22)	8.33 (0.61)	8.33 (0.61)	22.93 (4.09)	3.74 (2.36)	3.74 (2.36)	3.74 (2.36)	6.56 (1.25)	17.35 (3.93)	17.35 (3.93)	27.85 (8.36)				
Dy	0.90 (0.16)	1.93 (0.41)	5.35 (0.53)	5.35 (0.53)	23.83 (4.16)	3.52 (2.55)	3.52 (2.55)	3.52 (2.55)	5.97 (1.03)	15.34 (3.42)	15.34 (3.42)	25.22 (7.59)				
Ho	0.54 (0.14)	1.32 (0.09)	3.31 (0.33)	3.31 (0.33)	23.41 (4.26)	2.49 (1.76)	2.49 (1.76)	2.49 (1.76)	5.13 (0.85)	12.86 (2.89)	12.86 (2.89)	24.08 (9.36)				
Er	0.43 (0.14)	0.96 (0.18)	2.34 (0.32)	2.34 (0.32)	23.81 (4.29)	2.46 (1.97)	2.46 (1.97)	2.46 (1.97)	4.68 (0.82)	11.28 (2.57)	11.28 (2.57)	21.41 (8.23)				
Tm	0.26 (0.05)	0.69 (0.13)	1.62 (0.19)	1.62 (0.19)	23.11 (4.06)	2.31 (1.92)	2.31 (1.92)	2.31 (1.92)	4.07 (0.80)	9.42 (2.10)	9.42 (2.10)	20.57 (8.85)				
Yb	0.29 (0.09)	0.56 (0.08)	1.45 (0.20)	1.45 (0.20)	26.25 (4.47)	2.46 (2.16)	2.46 (2.16)	2.46 (2.16)	4.24 (0.86)	9.31 (1.95)	9.31 (1.95)	19.61 (8.24)				
Lu	0.18 (0.04)	0.56 (0.09)	1.10 (0.19)	1.10 (0.19)	24.43 (4.49)	2.33 (2.02)	2.33 (2.02)	2.33 (2.02)	3.64 (0.79)	8.17 (1.88)	8.17 (1.88)	18.86 (7.92)				
Sc	11.70 (2.32)	5.68 (2.21)	6.28 (0.48)	6.28 (0.48)	23.65 (4.08)	8.43 (1.94)	8.43 (1.94)	8.43 (1.94)	7.97 (1.36)	11.20 (1.21)	11.20 (1.21)	14.27 (2.69)				
V	3.55 (1.41)	5.05 (1.49)	9.14 (1.64)	9.14 (1.64)	35.28 (4.61)	9.30 (3.04)	9.30 (3.04)	9.30 (3.04)	15.09 (4.45)	15.51 (1.95)	15.51 (1.95)	29.75 (5.90)				
B	98.15 (13.53)	73.65 (6.05)	55.43 (8.24)	55.43 (8.24)	76.14 (14.76)	105.15 (12.63)	105.15 (12.63)	105.15 (12.63)	N.D. ^b	N.D.	N.D.	71.62 (15.06)				
W	89.28 (14.92)	113.84 (28.78)	70.95 (9.57)	70.95 (9.57)	38.75 (8.76)	185.26 (22.77)	185.26 (22.77)	185.26 (22.77)	101.20 (9.70)	81.08 (2.52)	81.08 (2.52)	61.50 (16.52)				

^a Numbers in parentheses indicate absolute standard deviation of the distribution of average compositions.^b N.D. = No data.

4.4.2 Nature of the volatile phase

Determining the nature of the mobile phase is not straightforward when employing the diamond trapping technique because it does not allow for visual characterization whether a pure aqueous fluid, hydrous melt, supercritical liquid or a mixture of them is present in the diamond trap. An additional complication arises when performing experiments in very water-rich systems such as the one examined in this study. A melt can only incorporate a certain amount of water at experimental pressures and temperatures (~35 wt% at 3 GPa). At low temperatures and 3 GPa, where the calculated water content exceeds 35 wt% (see **Table 4.3**), it has to be assumed that not all free water was dissolved in the melt phase during the experimental run. Due to lower water solubilities at lower pressures, the ability of melts incorporating water is considerably less than 35 wt%, but accurate data on H₂O-solubility in near-solidus granitic liquids are not available to date. Therefore, it has to be concluded that up to ~800°C at both pressures, the mobile phase captured in the trap is a mixture between both, fluids and melts; only at 3 GPa/700°C the chemical composition of the trap analysis designates the volatile to be a pure aqueous fluid (see below). We are thus referring to the mobile phase at these conditions as bulk volatile phase instead of aqueous fluid or hydrous melt. At all higher temperatures and determined water contents lower than the assumed or inferred H₂O solubility, the complete solubility of water in the melt during run conditions is to be expected. It is, therefore, safe to assume that a pure hydrous melt is stable.

Since it is impossible to recognize and analyze single mobile phases during LA-ICP-MS analyses of the trap, only the compositional information on the bulk volatiles can be used to determine whether it is composed of predominantly aqueous fluids or hydrous melts. Certain major element ratios can be employed to discriminate fluids from melts, such as SiO₂/Al₂O₃ or Na₂O/Al₂O₃ (e.g. Hermann and Spandler, 2008); aqueous fluids reveal very high values of these ratios whereas these values drop as soon as fluids are replaced by (hydrous) melts. **Figure 4.2** displays the evolution of SiO₂/Al₂O₃ and Na₂O/Al₂O₃ at 2 and 3 GPa as a function of temperature. The ratios at 3 GPa/700°C reveal distinctly higher values by almost an order of magnitude compared to all other temperatures where the ratios are more or less constant. At 2 GPa such a distinct step cannot be observed. Ratios at 700 and 800°C are elevated relative to higher temperature experiments but remain within the range we would typically attribute to melts. We, therefore, conclude that a pure aqueous fluid is only stable at 3 GPa and 700°C while up to ~800°C at both pressures a mixed bulk volatile phase is present that is replaced by pure hydrous melts at any higher temperature.

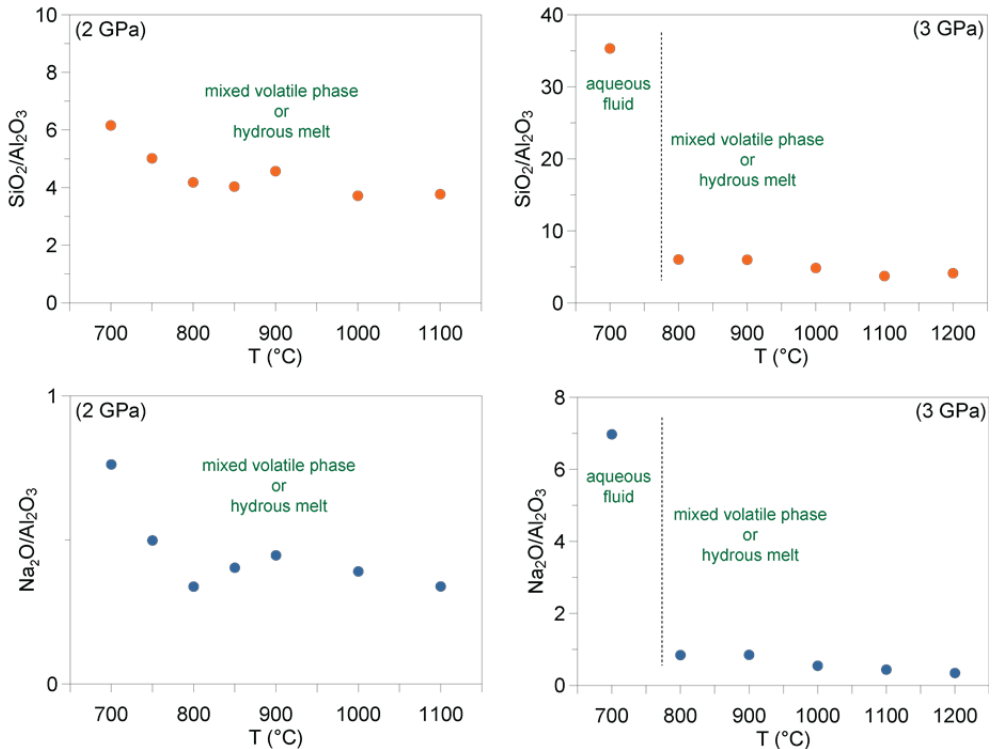


Figure 4.2. Evolution of SiO₂/Al₂O₃ and Na₂O/Al₂O₃ of the bulk volatile as a function of temperature at 2 (left side) and 3 GPa (right side). For explanations see text.

4.4.3 Major element composition

4.4.3.1 Bulk volatile phase

Bulk volatile compositions in the diamond trap were determined by LA-ICP-MS analyses using the "freezing" approach (see above) in a first step. At higher temperatures, the melts quenched to glass that we were able to analyze by EPMA in a second step. However, at lower temperatures (700–800°C at 2 GPa and 700°C at 3 GPa), the bulk volatile phase is very water-rich and contains only little solutes. Therefore, it does not quench well and no measurable glass pools could be detected in these experimental charges. Both, EPMA and LA-ICP-MS analyses of solid residual phases are reported in **Table 4.5** and **Table 4.7**; trace element composition of the bulk volatiles from 700 to 800°C at 2 and 3 GPa are reported in Chapter 3.

Quenched glass in high temperature runs has a vesicular texture (**Figure 4.1d**); this is a common feature in experimentally produced glasses which indicates that the bulk volatile phase separated into fluid or vapor and a hydrous melt (glass) upon quenching at the termination of the experiment. The amount and size of bubbles decreases with increasing temperature; at 2 GPa/900°C the bubbles (~8 μm) are frequent, whereas at 3 GPa/1100°C the glass contains no bubbles and is homogeneous. These textures are in good agreement with the determined water contents of the bulk volatiles that decrease successively with higher temperatures (**Table 4.3; Figure 4.3h**). Water contents of the bulk volatile phase were calculated according to the initial Cs:H ratio and measured Cs in the trap (see above). At 2 GPa, water contents decrease from 40 wt% at 700°C to 21 wt% at 1100°C; at 3 GPa the amount of water in the bulk volatiles is higher due to increasing solubility of H₂O at higher pressures (Botcharnikov et al., 2005 and references therein) and decreases from 45 wt% to 20 wt% within the investigated temperature range.

Figure 4.3 illustrates the evolution of the major element compositions of the bulk volatile phase as a function of temperature based on the LA-ICP-MS analyses of the trap. For better comparison and discussion of the volatile compositions at all temperatures, they were normalized to 100% without H₂O. The silica content at 2 and 3 GPa decreases gradually with increasing temperature due to the continuous consumption of coexisting low(er) silica phases and the increasing degree of melting (**Figure 4.3a**) approaching the bulk MOR-basalt composition. At higher pressure, silica contents of the mobile phase are higher. Within the same temperature range MgO reveals the opposite behavior with gradually increasing contents with increasing temperatures and lower solubilities at 3 GPa (**Figure 4.3b**). The FeO content displays a distinctive decrease from 700°C to 800°C followed by a gradual increase in concentration up to 1200°C at both pressures (**Figure 4.3c**). The prominent concentration change at the lowest investigated temperatures can be explained by poor nucleation and low modal proportions of garnet, leading to FeO liberation into the bulk volatile phase, instead of partitioning into garnet as it occurs at higher temperature. The disappearance of amphibole and onset of clinopyroxene crystallization at 2 GPa is best reflected in the Na₂O and CaO contents of the volatile phase (**Figure 4.3d and e**). Na₂O decreases whereas CaO increases with increasing temperatures but both oxides display a kink in evolution at 825°C. This highlights the change from a hydrous to a nominally anhydrous phase assemblage liberating Na₂O from peritectically decomposing amphiboles concomitantly forming higher CaO pyroxenes and garnet. The different liquidus phases present at different pressures (cpx at 2 GPa, garnet at 3 GPa) significantly influence the evolution of the Al₂O₃ concentration. While at 3 GPa aluminum increases continuously from 700°C to 1200°C, at 2 GPa the volatile phase reveals a bend in Al₂O₃ concentration at 1000°C and decreases towards 1100°C after an initial increase up to 900°C, reflecting the dissolution of garnet into the melt (**Figure 4.3f**).

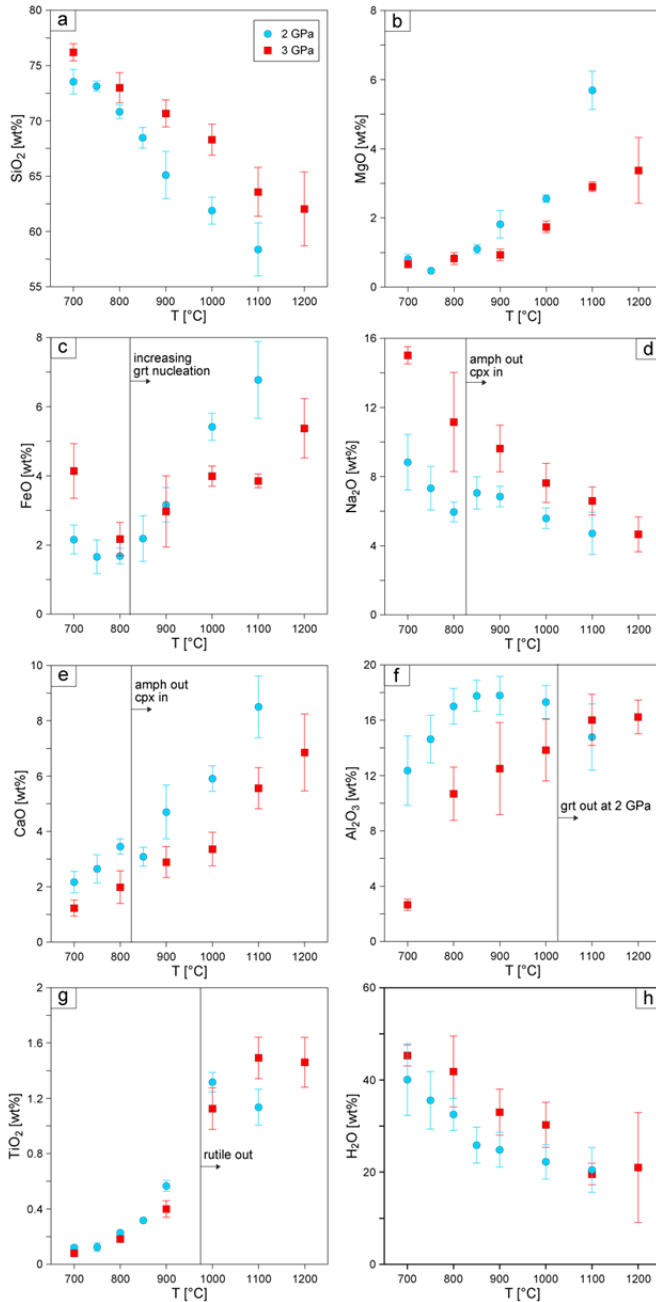


Figure 4.3. Concentrations of major element oxides (a-g) and water content (h) of the bulk volatile phase based on LA-ICP-MS analyses of the diamond trap (a-g normalized anhydrous to 100 wt%) as a function of temperature. Errors bars are 1 SD.

The pronounced step in TiO₂ content from 900°C to 1000°C marks the onset of melting out of rutile from the residual phase assemblage (**Figure 4.3g**).

Figure 4.4 shows the compositions of the bulk volatile phase as a function of temperature and pressure in a ternary ACF diagram (molar Al₂O₃+Fe₂O₃ - CaO+Na₂O - FeO+MgO) projected from SiO₂ and H₂O at 2 and 3 GPa. The calculated aluminum saturation index (ASI, molar Al₂O₃/CaO+Na₂O) reveals that volatile compositions at 3 GPa and up to 800°C exhibit peralkaline characteristics (strongly peralkaline at 700°C). At 2 GPa only the 700°C run results in slightly peralkaline volatiles. With increasing temperature at both pressures the volatile phases become metaluminous before at highest investigated temperatures they approach the initial bulk composition. At 2 GPa and 800-850°C they display slightly peraluminous characteristics (ASI>1) before shifting towards metaluminous compositions at higher temperatures. This is not observed at 3 GPa as the volatile phase is distinctly less aluminous at all temperatures except the highest ones approaching the bulk composition. The shift in composition is a consequence of increased modal abundances of garnet at 3 GPa and low temperatures (see **Table 4.3**) compared to lower pressures resulting in Al-poor bulk volatile phases. The presence of amphibole at 2 GPa furthermore depletes the volatile phase mainly in sodium, shifting the volatiles to more aluminous compositions.

A pronounced step in oxide or water concentration of the volatile phase is a strong indicator for the location of the solidus, i.e., the onset of melting where aqueous fluids are replaced by hydrous melts. For example, in the water-basalt system Kessel et al (2005b) determined the position of the wet solidus, indicated by distinct concentration steps in H₂O and oxides, at 4 and 5 GPa at 850-900°C and 1000-1050°C, respectively, whereas concentrations showed continuous evolution at all other temperatures. The smooth transition of water and oxides without pronounced step within the investigated temperature range at 6 GPa was taken as evidence for the existence of a supercritical liquid at these conditions. However, our data show a relatively continuous evolution of water (**Figure 4.3h**) and oxide (**Table 4.4**) concentrations over the entire temperature range at both pressures and, therefore, do not allow drawing conclusions about the location of the wet solidus based on these criteria alone. The comparatively very high SiO₂/Al₂O₃ and Na₂O/Al₂O₃ ratios (**Figure 4.2**) and the strong peralkaline character of the aqueous fluid at 3 GPa/700°C (**Figure 4.4**) provide nevertheless a clear indication on the location of the solidus. Textural evidence, such as the first appearance of glass at 800°C provide further strong support for our inference that the solidus in a K-free MORB-H₂O system occurs between 700 and 800°C at 3 GPa. Based on the same criteria, the results at 2 GPa suggest that the wet solidus lies at lower temperatures at around or even lower than 700°C. Clear evidence of glass (melt) was only observed at 800°C but very small amounts of glass, too little to analyze, might have been observed in experiment SL10 (2 GPa/700°C, no trap).

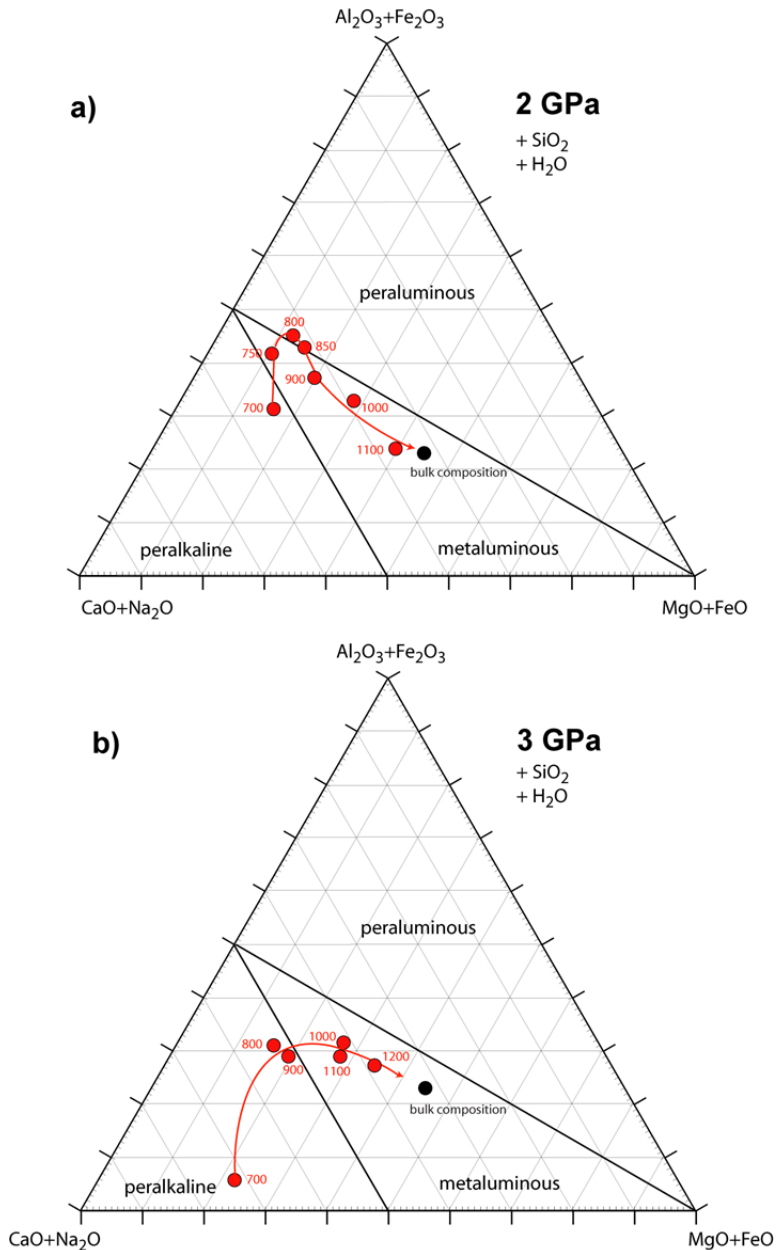


Figure 4.4. Molar projections of the volatile phase onto $\text{Al}_2\text{O}_3+\text{Fe}_2\text{O}_3$ - $\text{CaO}+\text{Na}_2\text{O}$ - $\text{FeO}+\text{MgO}$ ternary from $\text{SiO}_2+\text{H}_2\text{O}$ at a) 2 GPa and b) 3 GPa. Numbers adjacent to the symbols indicate the temperature. Black circles represent the bulk composition. For explanations see text.

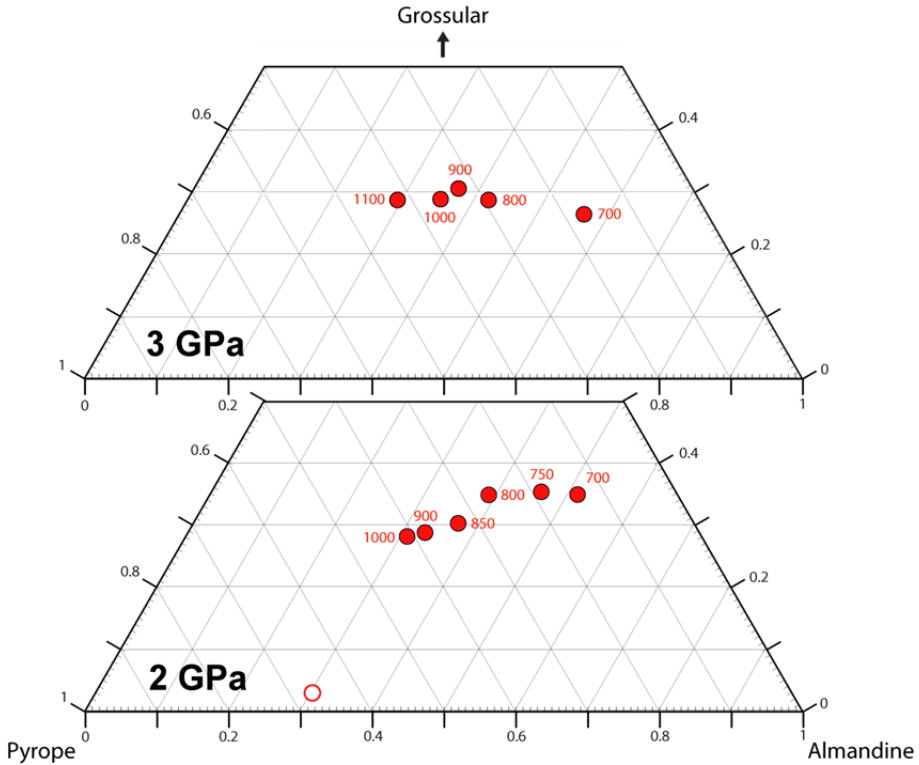


Figure 4.5. Ternary pyrope ($\text{Mg}_2\text{Al}_2\text{Si}_3\text{O}_{12}$) – almandine ($\text{Fe}_3\text{Al}_2\text{Si}_3\text{O}_{12}$) – grossular ($\text{Ca}_3\text{Al}_2\text{Si}_3\text{O}_{12}$) diagram for garnet compositions at 2 and 3 GPa and 700 to 1100°C. Numbers adjacent to the symbols indicate the temperature. For explanations see text. The composition of the seed garnets used in experiment SL39 is plotted for comparison (empty circle).

Thus, the findings of this study are in good agreement with the determined solidus in the water-basalt system by Kessel et al. (2005b) and references therein.

4.4.3.2 Garnet

Garnet is present in all but three experiments (SL12 and SL10, 2 GPa, 700°C, and SL13, 2 GPa, 1100°C) over the entire pressure and temperature range investigated in this study. At 3 GPa and 1200°C garnets show severe chemical modification resulting from quenching, therefore we did not consider the garnets at these conditions to represent true chemical equilibrium compositions. In general, garnet appears as large euhedral, porphyric crystals embedded in the fine grained matrix formed by the remaining residual phases (**Figure 4.1**). Grain size increases with temperature from 10 μm to several hundred μm . Analyses and

average compositions are provided in **Table 4.5**. Garnets are often zoned with Fe and Ti-rich cores while Mg is enriched in the rim. For mass balance calculations we used the average composition of the entire garnet grains. To quantify element partitioning we only considered rim compositions when grain size was sufficiently large. With increasing temperature the composition of garnet changes systematically. Mg-numbers ($\text{Mg}/(\text{Mg}+\text{Fe}^{2+})$) increase continuously from 0.2 at 700°C to 0.5 at 1200°C. No significant pressure dependence was detected. The increase in Mg-number corresponds to an overall increase of the pyrope component in all garnets at both pressures from ~15 mol% at 700°C to ~35-40 mol% at 1000°C (**Figure 4.5**). The almandine component decreases from ~50 mol% to ~32 mol% within the same temperature range at 2 GPa. The grossular component shows the least variation. At 2 GPa, there is a modest decrease from 35 mol% at 700°C to ~30 mol% at 850°C, followed by constant values with further increasing temperature. As an effect of pressure, the grossular component is significantly lower at 3 GPa (~28 mol% at all temperatures) compared to 2 GPa and low temperatures; the almandine component seems to be slightly higher at 3 GPa. The TiO_2 content increases with temperature from 0.5 to 1.6 wt%; Na_2O is detectable and ranges from 0.05 to 0.2 wt%.

4.4.3.3 Clinopyroxene

Clinopyroxene forms elongated crystals with sizes between 5 and 20 μm and starts crystallizing when amphibole and zoisite break down peritectically (**Figure 4.1**). At 2 GPa and 850°C cpx and amphibole coexist; at higher temperatures cpx is part of the anhydrous phase assemblage up to 1100°C, where cpx is the liquidus phase and forms crystals with several hundreds of μm in size (**Figure 4.1e**). At 3 GPa cpx is stable over the entire temperature range up to 1100°C. The experiment at 3GPa/1200°C produced a significant amount of cpx quench crystals that were not in equilibrium with the melt. We, therefore, will not consider these analyses as true cpx compositions.

EPMA analyses were normalized to 4 cations and 12 positive charges, average compositions are reported in **Table 4.5**. Similar to garnet, cpx shows increasing Mg-numbers with increasing temperature from 0.74 at 2 GPa/850°C to 0.91 at 1100°C. An increase of pressure leads to slightly higher Mg-numbers at 3 GPa for a given temperature. Clinopyroxenes have moderate to high Al-content (7-12 wt%). At both pressures, the Al content decreases whereas Ti and Mg contents increase with increasing temperature. Ti is most likely incorporated via the exchange $\text{TiAl}^{\text{IV}}\text{Al}^{\text{IV}} = (\text{Mg},\text{Fe}^{2+})\text{SiSi}$, evidenced by the positive correlation of Ti versus the calculated tetrahedrally coordinated Al (Al^{IV}) (**Figure 4.6a**). Compositional variations with temperature are depicted in **Figures 4.6b and c**. The jadeite component is strongly temperature and pressure sensitive. It systematically decreases with increasing temperatures. A strong increase in the jadeite content by a

factor of 2-5 at 3 GPa compared to 2 GPa is evident. Accordingly, Na correlates positively with calculated Al^{VI} confirming that the jadeite component substitutes for diopside and CaTs components (Ca-Tschermak end member, $\text{CaAl}_2\text{SiO}_6$) on the octahedrally coordinated M-sites of the clinopyroxene. Conversely, the enstatite component increases with temperature at both pressures. The Ca-Tschermak's content is low and displays contrasting behavior, at 2 GPa it decreases with increasing temperature whereas at 3 GPa the opposite is observed. Consistent with CaTs, Al^{IV} changes in the same fashion and with contrasting trends at 2 GPa (decrease with increasing temperatures) and 3 GPa (increase with increasing temperatures). At 3 GPa and 700°C two clinopyroxenes with very different compositions coexist. Cpx I displays high Al (12.5 wt%), Na (5.9 wt%) and low Fe^{2+} (7.7 wt%) and Mg (7.1 wt%) contents compared to cpx II (Al: 8.7 wt%, Na: 3.4 wt%, Fe^{2+} : 13.4 wt%, Mg: 10.7). We interpret the presence of these two distinct cpx compositions to represent the effect of an intersection with a (metastable) solvus in this experimental run and considered the higher Na-cpx as the stable one.

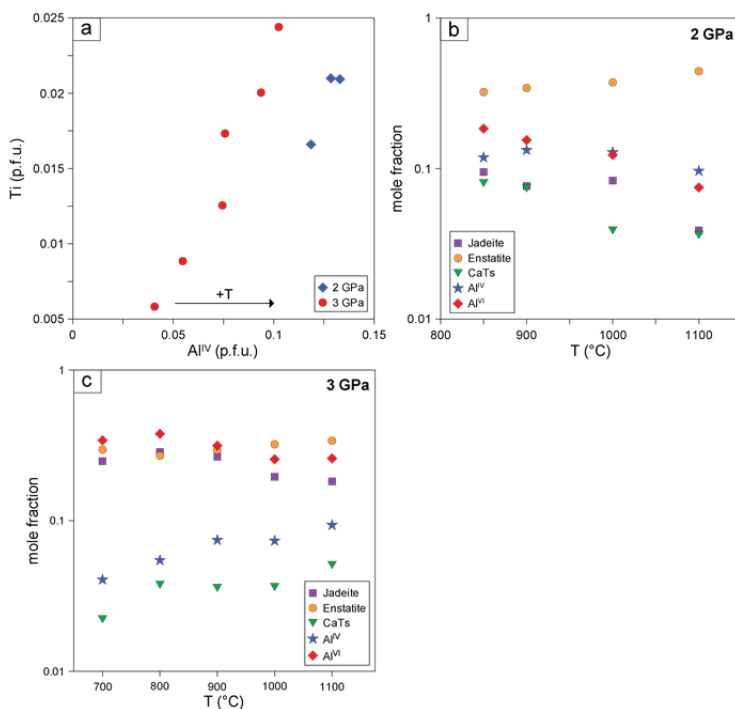


Figure 4.6. Compositions of clinopyroxene (p.f.u.) as a function of tetrahedrally coordinated Al (Al^{IV}) and Ti (Figure a) and temperature at 2 (Figure b) and 3 GPa (Figure c). Cations per formula unit (p.f.u.) were calculated on the basis of 4 cations and 12 positive charges. Results are average values based on all analyses at each temperature step.

4.4.3.4 Amphibole

Amphibole crystallizes only at 2 GPa and at temperatures between 700°C and 850°C forming elongated crystals, 2-15 μm in width, and becoming slightly larger with increasing temperature. Compositions were normalized based on the sum of cations = 13+Na+K+Ca, i.e. no Mg or Fe was assigned to the M4-site. According to this formula calculation, all amphiboles belong to the Ca-amphibole group (Leake et al., 1997; 2003) and range from magnesio-hornblende at low temperatures (700-750°C), tschermakites at 800°C to pargasite at 850°C. The silica content of the amphiboles correlates negatively with temperature from 6.7 at 700°C to 6.0 cations p.f.u. at 850°C (**Figure 4.7a**).

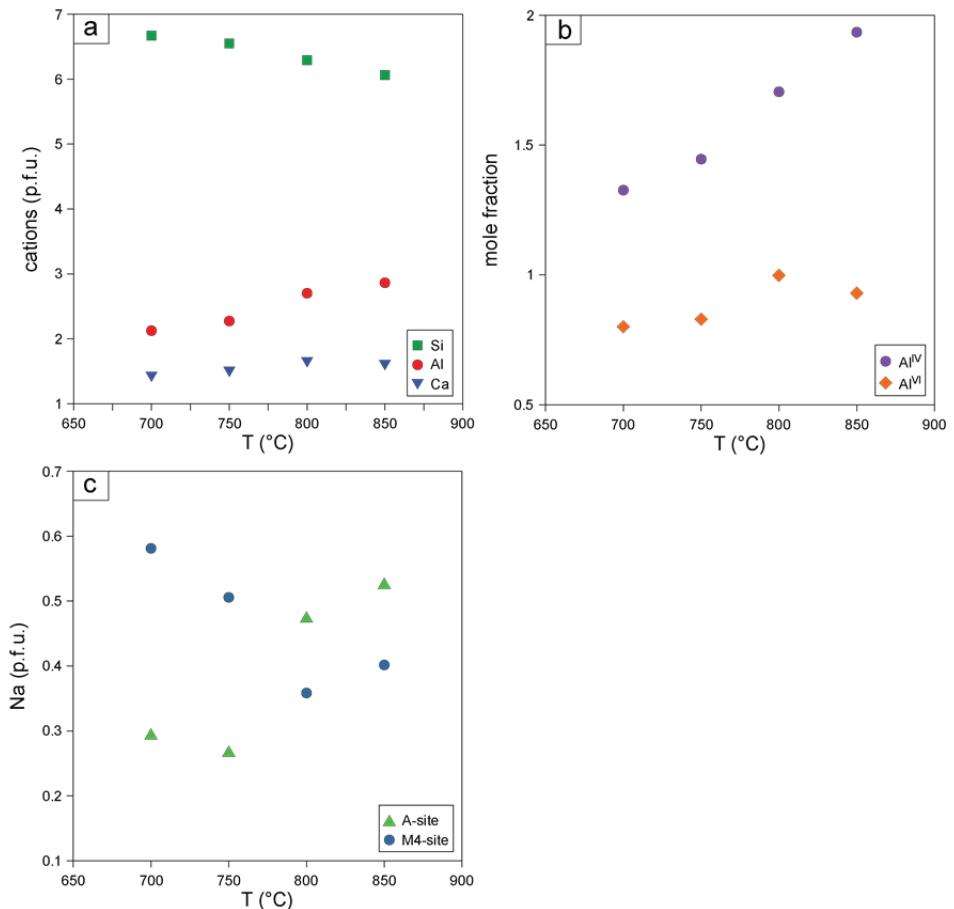


Figure 4.7. Composition of amphibole (p.f.u.) as a function of temperature at 2 GPa. Compositions were normalized based on the sum of cations = 13+Na+K+Ca, i.e. no Mg or Fe on the M4-site.

Al shows the opposite trend and increases with increasing temperature from 2.1 to 2.9 cations p.f.u. The calculated Al^{IV} (tetrahedrally coordinated) displays a relatively strong increase with temperature while Al^{VI} (octahedrally coordinated) increases only little (**Figure 4.7b**). The higher concentration on the Al^{IV}-site correlates well with the fact that Al^{IV} is highly temperature-sensitive under isobaric conditions. Titanium increases with temperature to a maximum of 0.15 p.f.u. at highest temperature (850°C). Fe_{tot} and Mg do not show much variation with temperature; Ca slightly increases at higher temperatures, reflecting a decreasing plagioclase (glaucofane, Na on M4-site) component. Sodium, similar to magnesium and iron, remains nearly constant with increasing temperature, but shows changing preference for incorporation on the A- or M4-sites (**Figure 4.7c**) respectively. At 700°C, Na preferably occupies M4 by 0.58 and A by 0.30. This ratio changes in favor of preferred incorporation into the A-site at 850°C by 0.53 (M4-site: 0.40) reflecting decreasing glaucofane (plagioclase) component with increasing temperature.

4.4.3.5 Ti-phases

Rutile is the dominant Ti-phase in our experiments. At both pressures, it is stable up to 1000°C. Rutiles are extremely small and thus difficult to analyze even with a focused beam. Apart from TiO₂, rutile also contains minor amounts of Al₂O₃, Fe⁽³⁺⁾₂O₃ and CaO. In experiment SL12 (2 GPa, 700°C) that was not doped with garnet seeds and where no garnet nucleated, an additional Ti-phase, titanite, was present with compositions of 31.0 wt% SiO₂, 27.8 wt% CaO, 35.3 wt% TiO₂ and minor amounts of Al₂O₃ and Fe⁽³⁺⁾₂O₃.

4.4.3.6 Other minerals

Staurolite is part of the phase assemblage at 3 GPa and 700°C with considerable FeO-content (12 wt%); this mineral has been observed in other experimental studies at similar conditions and starting material (e.g. Klimm et al., 2008). Staurolites have Mg-numbers of 0.32 and a TiO₂ content of around 0.7 wt%. At 3 GPa and 800°C kyanite completes the residual phase assemblage.

Table 4.7. Average trace element composition (ppm) of the run products determined by LA-ICP-MS.

Run	SL39			SL12			SL15			SL4					
	P (GPa)	T (°C)	phase	grt	1 σ	rut	1 σ	tn	1 σ	grt	1 σ	rut	1 σ	grt	1 σ
Cs	2	700		B.D. ^b	B.D.	B.D.	B.D.	B.D.	B.D.	0.32	B.D.	B.D.	B.D.	B.D.	B.D.
Rb				B.D.	B.D.	B.D.	B.D.	B.D.	B.D.	B.D.	B.D.	B.D.	B.D.	0.34	(0.04)
Li	20.05			-		B.D.	B.D.	B.D.	B.D.	4.89	(0.69)	B.D.	B.D.	5.64	(0.34)
Ba	B.D.	B.D.	B.D.	B.D.	B.D.	B.D.	B.D.	B.D.	B.D.	0.40	(0.07)	B.D.	B.D.	0.20	-
Sr	B.D.	B.D.	B.D.	B.D.	B.D.	B.D.	B.D.	B.D.	B.D.	0.36	(0.03)	B.D.	B.D.	0.58	(0.08)
Pb	B.D.	B.D.	B.D.	B.D.	B.D.	B.D.	B.D.	B.D.	B.D.	0.36	(0.03)	B.D.	B.D.	0.26	-
Th	B.D.	B.D.	B.D.	B.D.	B.D.	B.D.	B.D.	B.D.	B.D.	0.36	(0.03)	B.D.	B.D.	1.51	(0.19)
U	B.D.	B.D.	B.D.	B.D.	B.D.	B.D.	B.D.	B.D.	B.D.	0.36	(0.03)	B.D.	B.D.	1.51	(0.19)
Hf	25.52	(2.40) ^a	246	(19)	104.78	(14.63)	34.78	(1.09)	424	32.75	(1.19)	424	-	32.75	(1.19)
Zr	83.64	(18.06)	514	(15)	174.73	(0.26)	124.27	(0.26)	795	113.36	(4.82)	954.500	-	113.36	(4.82)
Ti	9659	(1057)	948600	-	354000	-	9249	(492)	5966	13356	(646)	5966	-	13356	(646)
Ta	4.84	(1.37)	2171	(386)	1207	(161)	13.17	(0.89)	5966	6.39	(0.28)	4161	-	6.39	(0.28)
Nb	5.41	(1.65)	4555	(543)	1377	(204)	3.80	(0.30)	4161	5.81	(0.71)	4161	-	5.81	(0.71)
Mo	B.D.	B.D.	B.D.	B.D.	B.D.	B.D.	B.D.	B.D.	B.D.	1.25	(0.48)	B.D.	B.D.	1.60	(0.09)
La	B.D.	B.D.	B.D.	B.D.	B.D.	B.D.	B.D.	B.D.	B.D.	B.D.	B.D.	B.D.	B.D.	0.14	(0.02)
Ce	B.D.	B.D.	B.D.	B.D.	B.D.	B.D.	B.D.	B.D.	B.D.	0.21	(0.05)	B.D.	B.D.	0.33	(0.08)
Nd	B.D.	B.D.	B.D.	B.D.	B.D.	B.D.	B.D.	B.D.	B.D.	B.D.	B.D.	B.D.	B.D.	2.59	(0.31)
Sm	B.D.	B.D.	B.D.	B.D.	B.D.	B.D.	B.D.	B.D.	B.D.	3.03	(0.75)	B.D.	B.D.	23.37	(1.20)
Eu	6.84	(0.66)	B.D.	B.D.	B.D.	B.D.	8.44	(1.48)	B.D.	48.13	(3.52)	B.D.	B.D.	48.13	(3.52)
Gd	23.74	(6.98)	B.D.	B.D.	B.D.	B.D.	16.52	(1.94)	B.D.	80.46	(10.16)	B.D.	B.D.	80.46	(10.16)
Y	125.45	(15.82)	B.D.	B.D.	B.D.	B.D.	102.06	(5.87)	B.D.	175.11	(15.87)	B.D.	B.D.	175.11	(15.87)
Tb	31.50	(7.79)	B.D.	B.D.	B.D.	B.D.	33.91	(2.20)	B.D.	106.57	(5.09)	B.D.	B.D.	106.57	(5.09)
Dy	52.20	(5.70)	B.D.	B.D.	B.D.	B.D.	60.76	(5.63)	B.D.	150.48	(9.50)	B.D.	B.D.	150.48	(9.50)
Ho	94.08	(15.93)	B.D.	B.D.	B.D.	B.D.	101.35	(8.31)	B.D.	108.59	(5.67)	B.D.	B.D.	108.59	(5.67)
Er	141.07	(23.98)	B.D.	B.D.	B.D.	B.D.	136.83	(4.55)	B.D.	155.39	(3.66)	B.D.	B.D.	155.39	(3.66)
Tm	237.16	(25.24)	B.D.	B.D.	B.D.	B.D.	170.86	(8.33)	B.D.	194.31	(15.41)	B.D.	B.D.	194.31	(15.41)
Yb	340.67	(58.68)	B.D.	B.D.	B.D.	B.D.	236.13	(27.56)	B.D.	237.43	(14.53)	B.D.	B.D.	237.43	(14.53)
Lu	450.08	(75.01)	B.D.	B.D.	B.D.	B.D.	241.09	(45.13)	B.D.	228.81	(11.88)	B.D.	B.D.	228.81	(11.88)
Sc	136.30	(19.42)	24.59	(4.76)	10.21	-	98.28	(8.05)	46.11	-	99.60	(12.01)	-	99.60	(12.01)
V	44.88	(6.55)	349.88	(24.00)	72.92	(7.80)	35.81	-	258.95	-	16.57	(1.12)	-	16.57	(1.12)
B	B.D.	B.D.	B.D.	B.D.	B.D.	B.D.	B.D.	B.D.	B.D.	B.D.	B.D.	B.D.	B.D.	B.D.	B.D.
W	16.28	(2.50)	B.D.	B.D.	B.D.	B.D.	1.65	(0.09)	B.D.	0.87	(0.09)	B.D.	B.D.	0.87	(0.09)

^a Numbers in parentheses indicate absolute standard deviation of the distribution of average compositions.

^b B.D. = Below detection limit.

Table 4.7. continued.

Run	SL6		SL14		SL2		SL3		SL11		SL13	
	P (GPa)	rut	2	850	grt	1 σ	900	rut	1 σ	grt	1 σ	2
T (°C)	800									1000		1100
phase												cpx
Cs	B.D.	B.D.	B.D.	B.D.	0.02	(0.14)	B.D.	B.D.	B.D.	0.03	(0.01)	B.D.
Rb	B.D.	B.D.	0.15	(0.03)	0.12	(0.01)	B.D.	B.D.	B.D.	0.09	(0.03)	0.02
Li	B.D.	B.D.	6.79	(0.27)	7.30	(0.88)	B.D.	B.D.	B.D.	4.03	(0.46)	5.23
Ba	B.D.	B.D.	0.12	-	0.17	(0.06)	B.D.	B.D.	B.D.	0.24	(0.17)	0.11
Sr	B.D.	B.D.	0.50	(0.10)	1.40	(0.03)	B.D.	B.D.	B.D.	0.48	(0.15)	5.61
Pb	B.D.	B.D.	B.D.	B.D.	0.24	(0.09)	B.D.	B.D.	B.D.			0.04
Th	B.D.	B.D.	0.33	(0.09)	0.49	(0.23)	B.D.	B.D.	B.D.	0.19	(0.06)	0.06
U	B.D.	B.D.	2.95	(0.52)	2.82	(0.23)	B.D.	B.D.	B.D.	1.08	(0.16)	0.06
Hf	490	(28)	23.82	(2.15)	28.04	(0.79)	318.78	-	-	14.76	(2.12)	7.62
Zr	837	(25)	68.95	(4.94)	61.21	(4.47)	443	-	-	48.14	(1.78)	6.10
Ti	965000	-	10032	(694)	16575	(2197)	948900	-	-	13561	(463)	5404
Ta	4621	(206)	6.40	(1.01)	5.76	(2.44)	5151	-	-	3.28	(0.98)	0.58
Nb	5244	(208)	2.70	(0.43)	1.39	(0.15)	4124	-	-	0.63	(0.31)	0.12
Mo	B.D.	B.D.	0.78	(0.23)	0.55	(0.31)	B.D.	B.D.	B.D.	0.63	(0.04)	0.76
La	B.D.	B.D.	0.25	(0.04)	1.09	(0.10)	B.D.	B.D.	B.D.	0.25	(0.09)	2.09
Ce	B.D.	B.D.	1.03	(0.13)	3.45	(0.60)	B.D.	B.D.	B.D.	0.90	(0.02)	4.13
Nd	B.D.	B.D.	11.39	(1.11)	18.04	(0.51)	B.D.	B.D.	B.D.	6.22	(0.79)	7.69
Sm	B.D.	B.D.	49.03	(1.84)	50.88	(1.10)	B.D.	B.D.	B.D.	27.96	(3.26)	12.78
Eu	B.D.	B.D.	69.63	(2.58)	58.21	(1.02)	B.D.	B.D.	B.D.	36.03	(5.42)	11.81
Gd	B.D.	B.D.	80.31	(0.77)	61.59	(3.23)	B.D.	B.D.	B.D.	55.60	(9.40)	16.64
Y	B.D.	B.D.	82.40	(7.09)	56.96	(3.70)	B.D.	B.D.	B.D.	59.60	(13.05)	18.04
Tb	B.D.	B.D.	74.62	(5.72)	62.20	(3.12)	B.D.	B.D.	B.D.	56.91	(10.30)	16.64
Dy	B.D.	B.D.	85.64	(3.31)	74.10	(9.48)	B.D.	B.D.	B.D.	53.28	(8.41)	18.64
Ho	B.D.	B.D.	81.67	(5.22)	75.92	(4.84)	B.D.	B.D.	B.D.	49.43	(7.09)	18.16
Er	B.D.	B.D.	82.84	(6.36)	76.91	(2.44)	B.D.	B.D.	B.D.	48.49	(5.37)	17.92
Tm	B.D.	B.D.	77.14	(7.12)	77.19	(3.72)	B.D.	B.D.	B.D.	42.71	(4.82)	15.27
Yb	B.D.	B.D.	80.56	(9.86)	78.41	(6.15)	B.D.	B.D.	B.D.	50.53	(12.88)	15.47
Lu	B.D.	B.D.	76.37	(8.68)	76.17	(4.75)	B.D.	B.D.	B.D.	43.04	(6.05)	14.05
Sc	32.69	(2.79)	77.26	(4.71)	109.99	(4.40)	19.16	-	-	68.78	(3.75)	81.81
V	412.44	(15.74)	45.31	(2.35)	83.73	(5.02)	412.71	-	-	54.44	(2.34)	204.36
B	B.D.	B.D.	132.86	(18.32)	0.47	-	B.D.	B.D.	B.D.	0.70	(0.15)	0.97
W	B.D.	B.D.	0.32	(0.11)	0.96	(0.65)	B.D.	B.D.	B.D.	0.17	(0.07)	0.06

Table 4.7. continued.

Run P (GPa) T (°C) phase	SL21			SL23			SL24		
	3 700 grt	3 800 grt	3 900 grt	3 800 grt	3 800 grt	3 900 grt	3 800 grt	3 800 grt	3 900 grt
Cs	B.D.	B.D.	B.D.	B.D.	B.D.	B.D.	B.D.	B.D.	B.D.
Rb	B.D.	B.D.	B.D.	0.13	-	B.D.	B.D.	B.D.	B.D.
Li	5.15	-	37.76	4.76	(1.12)	B.D.	B.D.	8.09	B.D.
Ba	1.72	-	B.D.	-	-	B.D.	B.D.	0.22	B.D.
Sr	1.79	(0.20)	20.63	0.37	(0.09)	B.D.	B.D.	1.20	B.D.
Pb	B.D.	B.D.	0.99	-	-	B.D.	B.D.	-	20.30
Th	B.D.	B.D.	0.54	0.40	(0.32)	B.D.	B.D.	5.03	10.73
U	0.93	(0.03)	0.47	4.10	(0.68)	B.D.	B.D.	15.68	2.79
Hf	21.28	-	20.21	40.81	(2.05)	267	(40)	37.67	11.72
Zr	54.95	-	16.83	77.08	(11.86)	271	(51)	79.57	12.80
Ti	5852	-	5599	9676	(1740)	950600	-	14439	3573
Ta	4.44	-	5.72	4.12	(1.63)	4272	(273)	11.36	10.43
Nb	4.57	-	7.62	3.10	(1.38)	3677	(248)	9.16	6.27
Mo	0.75	(1.40)	15.48	3.98	(1.77)	B.D.	B.D.	5.65	B.D.
La	1.25	(0.32)	0.85	0.17	-	B.D.	B.D.	3.53	16.28
Ce	4.28	(0.47)	B.D.	0.91	(0.31)	B.D.	B.D.	12.92	30.36
Nd	11.22	(0.75)	1.66	47.89	(6.02)	B.D.	B.D.	36.53	B.D.
Sm	21.57	(0.79)	1.97	64.89	(1.58)	B.D.	B.D.	63.94	B.D.
Eu	37.32	(2.50)	2.64	86.05	(7.17)	B.D.	B.D.	82.01	5.65
Gd	286.68	-	6.56	68.48	(4.59)	B.D.	B.D.	76.18	B.D.
Y	70.46	(7.06)	3.53	85.32	(9.96)	B.D.	B.D.	78.65	B.D.
Tb	144.53	(12.39)	3.55	77.10	(4.12)	B.D.	B.D.	74.25	9.62
Dy	237.32	(18.57)	3.42	74.60	(8.05)	B.D.	B.D.	77.95	5.30
Ho	395.47	(9.47)	5.93	68.88	(5.79)	B.D.	B.D.	76.65	4.64
Er	577.76	(9.60)	5.69	55.53	(5.43)	B.D.	B.D.	78.98	-
Tm	919.22	(78.61)	7.70	66.73	(5.17)	B.D.	B.D.	76.97	3.61
Yb	1056.69	(40.27)	8.23	55.67	(8.86)	B.D.	B.D.	80.59	16.56
Lu	103.59	(10.35)	33.62	83.87	(6.66)	69.69	-	74.74	4.71
Sc	27.69	(1.96)	30.48	26.59	(2.22)	367.68	(36.21)	61.00	56.92
V	B.D.	B.D.	B.D.	B.D.	B.D.	B.D.	B.D.	33.41	102.89
B	2.14	-	B.D.	0.93	(0.45)	B.D.	B.D.	3.55	B.D.
W									B.D.

Table 4.7. continued.

Run	SL17			SL25			SL34			
	SL24	3	1000	1000	1100	1200	grt	1σ	grt	1σ
P (GPa)	900	rut								
T (°C)										
phase										
Cs	B.D.	B.D.	0.11	(0.02)	B.D.	B.D.	0.02	(0.00)	B.D.	0.02
Rb	B.D.	B.D.	B.D.	B.D.	B.D.	B.D.	0.08	(0.01)	0.08	(0.01)
Li	B.D.	B.D.	9.28	(0.13)	B.D.	B.D.	7.05	(0.42)	26.85	(18.88)
Ba	B.D.	B.D.	B.D.	B.D.	B.D.	B.D.	0.09	-	6.95	-
Sr	B.D.	B.D.	0.90	(0.12)	13.51	(0.97)	0.54	(0.07)	11.25	(3.56)
Pb	B.D.	B.D.	B.D.	B.D.	B.D.	B.D.	B.D.	B.D.	B.D.	B.D.
Th	B.D.	B.D.	3.66	(1.18)	3.03	(0.54)	1.62	(0.09)	1.85	(0.39)
U	B.D.	B.D.	9.30	(0.26)	B.D.	B.D.	4.64	(0.15)	1.67	(0.56)
Hf	185	(24)	28.81	(1.82)	13.74	-	26.80	(0.56)	7.43	(0.82)
Zr	238	(24)	73.16	(2.56)	20.52	(5.01)	67.31	(1.89)	7.66	(1.21)
Ti	955700	-	18563	(250)	6064	(1095)	18109	(545)	6593	(782)
Ta	7148	(572)	15.77	(1.53)	2.26	-	13.98	(0.39)	2.86	(1.17)
Nb	4419	(250)	12.49	(1.24)	B.D.	B.D.	9.73	(0.23)	1.18	(0.70)
Mo	B.D.	B.D.	5.44	(0.68)	B.D.	B.D.	7.01	(0.81)	12.54	(3.41)
La	B.D.	B.D.	2.41	(0.28)	9.66	-	0.82	(0.09)	3.03	(0.85)
Ce	B.D.	B.D.	8.51	(0.94)	9.73	(4.20)	4.18	(0.29)	3.53	(1.52)
Nd	B.D.	B.D.	31.86	(4.48)	B.D.	B.D.	19.95	(0.64)	13.02	(2.84)
Sm	B.D.	B.D.	59.50	(1.99)	26.60	-	48.43	(1.21)	13.18	(3.67)
Eu	B.D.	B.D.	68.51	(5.93)	B.D.	B.D.	63.75	(2.88)	8.92	(2.13)
Gd	B.D.	B.D.	67.15	(7.78)	B.D.	B.D.	69.26	(1.92)	12.24	(1.31)
Y	B.D.	B.D.	80.76	(8.37)	B.D.	B.D.	93.09	(4.19)	8.35	(1.36)
Tb	B.D.	B.D.	64.89	(5.95)	5.34	(1.73)	73.34	(1.77)	5.91	(1.77)
Dy	B.D.	B.D.	77.13	(8.45)	8.79	-	78.96	(3.04)	9.55	(2.30)
Ho	B.D.	B.D.	82.29	(9.97)	3.06	(1.45)	76.52	(2.19)	4.90	(1.28)
Er	B.D.	B.D.	84.15	(10.44)	B.D.	B.D.	81.55	(6.03)	6.54	(1.69)
Tm	B.D.	B.D.	81.70	(10.05)	4.00	(0.04)	76.25	(1.66)	2.19	(1.16)
Yb	B.D.	B.D.	91.74	(10.16)	B.D.	B.D.	87.01	(2.72)	7.02	(1.62)
Lu	B.D.	B.D.	100.66	(16.14)	3.19	(1.56)	85.64	(2.18)	2.64	(0.88)
Sc	51.21	-	47.44	(3.96)	53.33	-	60.04	(9.84)	48.46	(6.58)
V	421.68	(55.40)	34.65	(5.93)	112.11	-	28.66	(2.96)	120.49	(24.67)
B	B.D.	B.D.	24.21	(4.78)	B.D.	B.D.	1.18	(0.43)	566.42	(0.56)
W	B.D.	B.D.	2.93	(0.57)	B.D.	B.D.	2.11	(0.23)	5.62	(224.46)

4.4.4 Trace element composition and partitioning

We measured trace element concentrations of garnets, cpx and Ti-phases by LA-ICP-MS. **Table 4.7** summarizes all average analyses and corresponding standard deviations. Partition coefficients $D^{(\text{mineral/volatile})}$ are listed in **Tables 4.8-4.10**. Zoisite trace element compositions and partitioning from low temperature runs are reported in Chapter 3. Most garnets are sufficiently large for analyses except for those formed in low temperature experiments ($\leq 10 \mu\text{m}$). Additionally, garnets are, similar as for major elements, trace element-zoned and often inclusion-rich in the core. Zonation in garnets (experimental and natural) results most likely from fast growth when only few nuclei are present. As intracrystalline diffusion is too slow, garnets cannot fully re-equilibrate during the experiment (Van Orman et al., 2002) resulting in zoned crystals. When size permitted, we measured the homogenous inclusion-free rims. Analyses affected by contamination from inclusions (mainly melt and rutile) were excluded.

At 2 GPa, Ti-phases (rutile and titanite) and cpx are extremely small (see above) and generally did not allow accurate characterization by LA-ICP-MS analyses except for cpx in experiment SL-13 at 2 GPa/1100°C. In the case of rutile and titanite, we will focus only on trace elements that are significantly incorporated into these minerals (HFSE, V and Sc) and in the case of HFSE almost exclusively controlled by them in the absence of zircon, which would control Hf and Zr to the largest extent (e.g. Hermann, 2002; Klemme et al., 2005). Cpx trace element partitioning data are reported only for the high temperature run at 2 GPa, 1100°C, and at 3 GPa from 700°C to 1100°C.

All reported trace element partitioning data ($D^{(\text{mineral/volatile})}$) were calculated on the basis of the LA-ICP-MS analyses of the hydrous bulk volatile phase contained in the trap (**Table 4.6**).

4.4.4.1 Garnet

Figure 4.8 depicts the partitioning behavior of garnet in equilibrium with volatile phases at 2 GPa from 700°C to 1000°C and at 3 GPa from 700°C to 1200°C. Generally, LILE (Cs, Rb, Ba, and Sr), Li, Pb and B behave strongly incompatible and do not change much with increasing pressure and/or temperature. REE are strongly fractionated from Light REE (LREE) to Heavy REE (HREE) by up to 5 orders of magnitude with the latter being the most compatible elements in garnet. At higher pressure, the fractionation pattern is less extreme resulting in slightly flatter MREE to HREE patterns. A distinct effect of increasing pressure is reduced compatibility for MREE and HREE while LREE are slightly more compatible but show commonly incompatible character at both pressures. Apart from REE, HFSE (Ti, Zr, Hf, Nb, and Ta) are incorporated into garnet by considerable amounts (**Table 4.7**). With increasing

CHAPTER 4

temperature generally both, $D_{REE}^{(grt/volatile)}$ and $D_{HFSE}^{(grt/volatile)}$ decrease consistently at 2 and 3 GPa, apart from experiment SL4 (2/800), which reveals slightly enhanced compatibility for HREE and experiment SL21 (3/700) that results in lowered MREE and HREE partition coefficients.

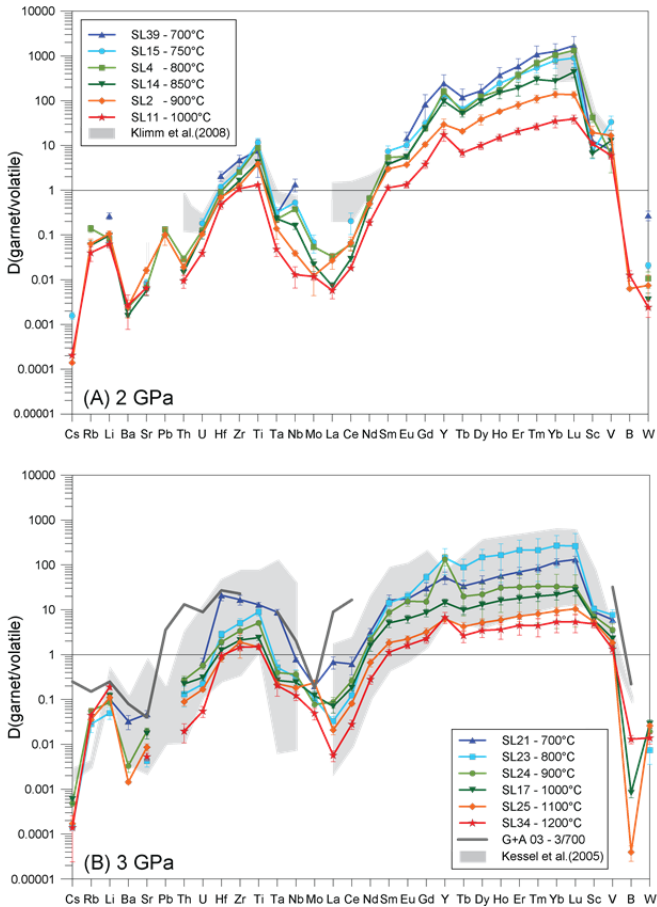


Figure 4.8. (A) Garnet-volatile (bulk volatile up to 800°C, 850-1000°C hydrous melt) partition coefficients at 2 GPa and 700 to 1000°C. Garnet-melt partition coefficients from experiments of Klimm et al. (2008) (grey shaded region) at 2.5 GPa and 800 to 900°C are compared with results from this study. (B) Garnet-volatile (fluid at 700°C, bulk volatile at 800°C, 900-1200°C hydrous melt) coefficients at 3 GPa and 700 to 1200°C. Garnet-liquid partition coefficients from experiments of Kessel et al. (2005a) (grey shaded region) at 4 GPa and 700 to 1100°C and Green and Adam (2003) (solid grey line) at 3 GPa and 700°C are compared with results from this study. For discussion see text. Error bars are 1 SD.

Zr and Hf are fractionated from Nb and Ta by more than an order of magnitude at low temperatures; at higher temperature this fractionation increases. While $D_{\text{Nb}}/D_{\text{Ta}} < 1$ at all conditions, D_{Zr} is always larger than D_{Hf} at all temperatures and pressures with weighted mean values of $D_{\text{Zr}}/D_{\text{Hf}}$ of 2.2 ± 0.18 at 2 GPa and 1.3 ± 0.19 at 3 GPa. Generally, D_{Ta} is less temperature-sensitive than D_{Nb} at both pressures, D_{Nb} varies within almost two orders of magnitude at 2 GPa. $D_{\text{Nb}}/D_{\text{Ta}}$ is constrained to a weighted mean value of 0.83 ± 0.09 by our experiments at 3 GPa. Interestingly, $D_{\text{Nb}}/D_{\text{Ta}}$ reveals opposite behavior at low compared to higher temperatures at 2 GPa: From 850°C to 1000°C $D_{\text{Nb}}/D_{\text{Ta}}$ yields ratios close to those at 3 GPa with decreasing $D_{\text{Nb}}/D_{\text{Ta}}$ from 0.7 to 0.3 with increasing temperature. At lowest temperatures this ratio seems to change in favor of $D_{\text{Nb}} > D_{\text{Ta}}$, testified by $D_{\text{Nb}}/D_{\text{Ta}}$ of 1.7 at 800°C and $D_{\text{Nb}}/D_{\text{Ta}}$ of 4.7 at 700°C. D_{U} and D_{Th} are below unity (incompatible) at both pressures and all temperatures; D_{U} is always higher but fractionates slightly stronger from D_{Th} at lower pressure. The overall partitioning of U and Th increases with increasing pressure by about one order of magnitude. D_{Sc} and D_{V} plot in the range of D_{HFSE} but analytical uncertainties are substantial and no clear trend can be established.

4.4.4.2 Clinopyroxene

Only experiment SL-13 at 2 GPa and 1100°C produced large enough cpx crystals for reliable analysis for all trace elements above detection limit. Additionally, results from the 700°C, 900°C, 1000°C and 1100°C experiments at 3 GPa are shown. Average compositions for 2 and 3 GPa are given in **Table 4.7** and D-values are plotted in **Figure 4.9**.

With the exception of Sc and V (and HFSE, MREE and HREE at 3 GPa/700°C) all $D^{(\text{cpx}/\text{volatile})}$ plot below unity constraining all other determined trace elements to be incompatible in cpx in our study. At 3 GPa, $D_{\text{REE}}^{(\text{cpx}/\text{volatile})}$ do not reveal any significant internal fractionation within error except for the LREE (La-Nd) that yield lower values by almost one order of magnitude compared to the other REE. The latter show a tendency of $D_{\text{MREE}} > D_{\text{LREE}}$ and D_{HREE} . HFSE are fractionated from each other as well as from the REE. Nb and Ta reveal a distinct negative anomaly with values close to or below 0.1 and $D_{\text{Nb}} < D_{\text{Ta}}$. In contrast, Zr and Hf are more compatible in cpx and plot above the range of the LREE with $D_{\text{Zr}} < D_{\text{Hf}}$. Li and Sr are incorporated into cpx by about the same degree as Zr and Hf while all remaining elements (Rb, Ba, Th and U) display strongly incompatible character and $D_{\text{U}} < D_{\text{Th}}$. The influence of pressure and temperature is difficult to define due to analytical limitations of the cpx composition at 3 GPa; nevertheless, cpx analyses suggest decreasing D's with increasing temperature and display a negative pressure correlation for most $D^{(\text{cpx}/\text{volatile})}$.

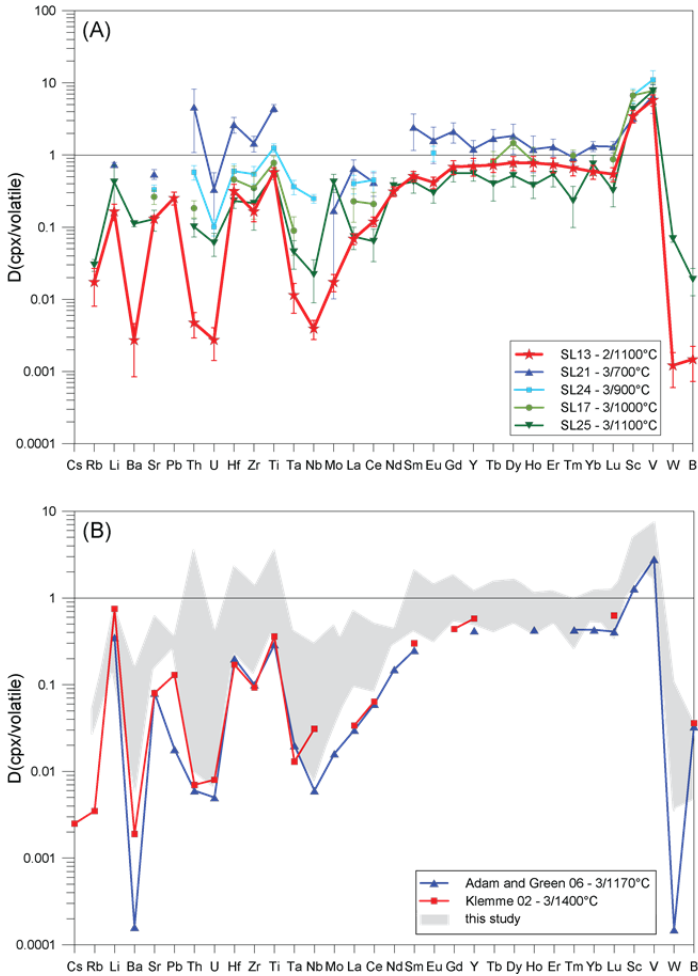


Figure 4.9. (A) Cpx-volatile (aqueous fluid at 3 GPa/700°C, bulk volatile at 3 GPa/800°C and hydrous melt at all other temperatures) partition coefficients at 2 and 3 GPa and 700 to 1100°C. Error bars are 1 SD. (B) Cpx-melt partition coefficients from Klemme (2002) and Adam and Green (2006) at 3 GPa for comparison to the results from this study (grey shaded area). For explanations see text.

4.4.4.3 Ti-Phases

Rutile trace element partitioning data were obtained by LA-ICP-MS from 700°C to 900°C at 2 GPa and 800°C to 900°C at 3 GPa, average compositions are reported in **Table 4.7**. Additionally, titanite compositions from run SL-12 (2 GPa, 700°C) were determined and compared to the rutile data (**Figure 4.10**). TiO₂ values, determined by EPMA, were used as internal standard to quantify trace element compositions.

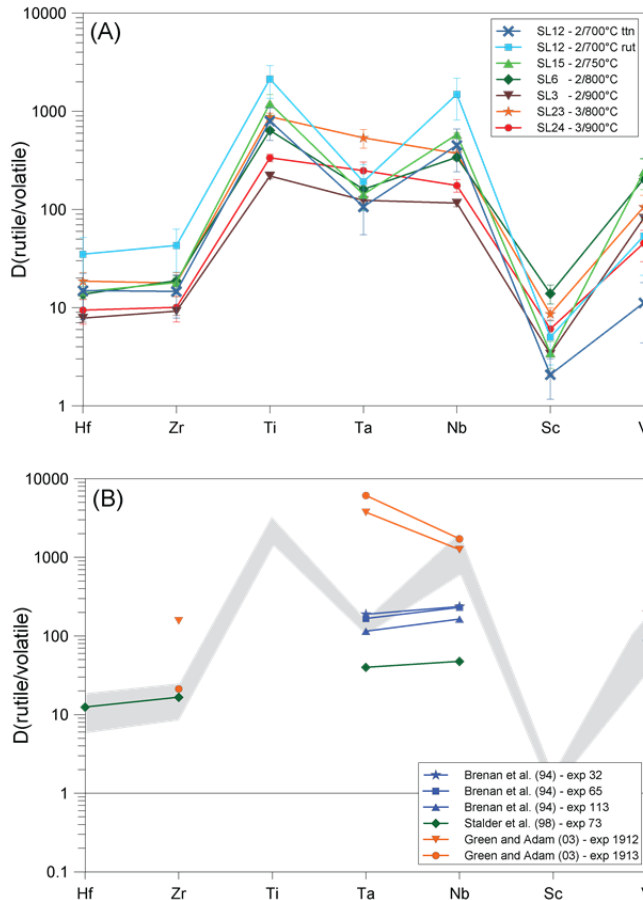


Figure 4.10. (A) Rutile-volatile (bulk volatile up to 800°C and melt at 900°C) partition coefficients at 2 and 3 GPa and 700 to 900°C of this study. Error bars are 1 SD. (B) Rutile-fluid partition coefficients from Brenan et al. (1994) at 1 GPa and 900°C, Stalder et al. (1998) at 5 GPa and 1000°C and Green and Adam (2003) at 2 GPa/700°C and 3 GPa/650°C compared to rutile partition coefficients for volatiles dominated by aqueous fluids from this study at 700 and 750°C (grey shaded area, SL12, SL15.). For explanations see text.

Figure 4.10a reveals decreasing $D_{\text{HFSE}}^{\text{(rut/volatile)}}$ with increasing temperature for both investigated pressures. D_{Zr} and D_{Hf} fractionate only insignificantly (within error) from each other with slightly higher values for D_{Zr} at 2 GPa and plot around one order of magnitude above unity at both pressures. D_{Nb} and D_{Ta} reveal contrasting behavior at low and high temperatures. At 700° and 2 GPa D_{Nb} fractionates from D_{Ta} with $D_{\text{Nb}}/D_{\text{Ta}} = 7.8$. This value decreases continuously with increasing temperatures to 0.9 at 900°C. At 3GPa

and 800°C and 900°C, the results suggest $D_{Nb} < D_{Ta}$ with constant mean values of 0.67 ± 0.01 . The fractionation pattern resembles that at equivalent temperatures at 2 GPa. D_{Ti} and D_{Nb} are independent of pressure whereas D_{Ta} increases with increasing pressure to a larger extent. Sc and V are both compatible at both pressures and fractionate by one order of magnitude with $D_{Sc} < D_V$. Partition coefficients for titanite display basically the same fractionation behavior as for $D^{(rut/volatile)}$ at low temperatures and 2 GPa but with constantly lower D-values for all elements compared to rutile data at the same pressure and temperature conditions.

Table 4.8. Mineral-volatile partition coefficients of garnet.

Run	SL39	SL15	SL4	SL14	SL2	SL11
	D(grt/liq)	Error ^a	D(grt/liq)	Error	D(grt/liq)	Error
Cs	N.D. ^b	N.D.	N.D.	N.D.	0.0001	0.0002
Rb	N.D.	N.D.	0.14	(0.02)	0.06	(0.01)
Li	0.27	(0.05)	0.08	(0.01)	0.11	(0.02)
Ba	N.D.	N.D.	0.002	(0.0001)	0.002	(0.0011)
Sr	N.D.	N.D.	0.007	(0.001)	0.02	(0.003)
Pb	N.D.	N.D.	0.13	(0.02)	0.10	(0.04)
Th	N.D.	N.D.	0.03	(0.006)	0.02	(0.01)
U	N.D.	N.D.	0.13	(0.05)	0.10	(0.01)
Hf	2.09	(0.52)	0.92	(0.17)	0.69	(0.07)
Zr	4.71	(1.31)	2.55	(0.33)	1.27	(0.15)
Ti	7.71	(5.77)	8.85	(2.84)	3.84	(0.57)
Ta	0.28	(0.09)	0.31	(0.10)	0.23	(0.06)
Nb	1.35	(0.43)	0.53	(0.05)	0.16	(0.03)
Mo	N.D.	N.D.	0.05	(0.007)	0.02	(0.007)
La	N.D.	N.D.	0.03	(0.006)	0.01	(0.001)
Ce	N.D.	N.D.	0.06	(0.02)	0.03	(0.004)
Nd	N.D.	N.D.	0.65	(0.12)	0.45	(0.06)
Sm	N.D.	N.D.	5.38	(0.71)	3.77	(0.48)
Eu	14.36	(5.46)	5.67	(0.61)	5.54	(0.58)
Gd	82.93	(53.12)	31.10	(6.01)	23.95	(2.61)
Y	244.17	(132.64)	161.48	(28.20)	98.20	(21.51)
Tb	119.02	(62.11)	56.78	(5.34)	51.33	(8.31)
Dy	165.57	(65.73)	123.74	(19.48)	95.67	(17.63)
Ho	372.06	(180.33)	242.86	(46.06)	151.78	(41.64)
Er	582.45	(277.55)	364.12	(83.36)	192.33	(66.27)
Tm	1083.04	(580.34)	542.17	(131.15)	297.03	(66.87)
Yb	1259.55	(606.15)	791.44	(270.62)	273.32	(93.16)
Lu	1699.35	(1030.93)	898.25	(337.38)	436.03	(108.08)
Sc	12.55	(3.74)	7.36	(2.32)	6.60	(1.37)
V	7.84	(2.60)	33.51	(11.45)	12.76	(5.11)
B	N.D.	N.D.	N.D.	(0.002)	0.006	(0.0003)
W	0.27	(0.07)	0.02	(0.003)	0.01	(0.001)

^a Errors represent 1σ uncertainties, calculated as a standard deviation.^b N.D. = no data.

Table 4.8. continued.

Run	SL21	SL23	SL24	SL17	SL25	SL34
	D(grt/liq)	Error	D(grt/liq)	Error	D(grt/liq)	Error
Cs	N.D.	0.0001 (0.00003)	0.0005 (0.00008)	0.0006 (0.0001)	0.0002 (0.00004)	0.0001 (0.0001)
Rb	N.D.	N.D.	0.06 (0.008)	N.D.	0.04 (0.01)	0.04 (0.02)
Li	0.10 (0.005)	0.05 (0.01)	0.09 (0.02)	0.12 (0.02)	0.11 (0.01)	0.19 (0.03)
Ba	0.03 (0.01)	N.D.	0.003 (0.001)	N.D.	0.001 (0.0001)	N.D.
Sr	0.05 (0.01)	0.004 (0.001)	0.02 (0.004)	0.02 (0.004)	0.01 (0.002)	0.005 (0.001)
Pb	N.D.	N.D.	N.D.	N.D.	N.D.	N.D.
Th	N.D.	0.13 (0.06)	0.27 (0.06)	0.22 (0.08)	0.09 (0.02)	0.02 (0.01)
U	0.66 (0.16)	0.22 (0.05)	0.57 (0.10)	0.31 (0.05)	0.17 (0.02)	0.05 (0.02)
Hf	21.00 (5.19)	2.84 (0.51)	1.92 (0.49)	1.26 (0.37)	0.83 (0.15)	0.95 (0.16)
Zr	16.77 (4.14)	5.06 (1.28)	3.37 (0.96)	2.11 (0.56)	1.89 (0.48)	1.46 (0.25)
Ti	12.93 (1.61)	8.99 (1.78)	5.08 (0.54)	2.39 (0.33)	1.48 (0.15)	1.50 (0.20)
Ta	8.82 (1.36)	0.52 (0.23)	0.40 (0.14)	0.27 (0.06)	0.22 (0.03)	0.20 (0.09)
Nb	0.79 (0.05)	0.31 (0.14)	0.36 (0.07)	0.24 (0.03)	0.18 (0.01)	0.12 (0.03)
Mo	0.20 (0.06)	0.10 (0.05)	0.08 (0.03)	0.12 (0.03)	0.24 (0.03)	0.05 (0.01)
La	0.68 (0.21)	0.03 (0.01)	0.09 (0.02)	0.07 (0.02)	0.02 (0.005)	0.006 (0.002)
Ce	0.62 (0.26)	0.12 (0.04)	0.26 (0.05)	0.18 (0.03)	0.08 (0.01)	0.03 (0.01)
Nd	3.18 (0.63)	2.28 (0.52)	2.18 (0.54)	1.60 (0.42)	0.67 (0.13)	0.28 (0.06)
Sm	16.45 (4.63)	14.38 (4.12)	8.68 (1.65)	5.08 (1.07)	1.84 (0.37)	1.13 (0.19)
Eu	17.44 (4.15)	20.13 (4.63)	15.47 (3.51)	6.30 (1.28)	2.23 (0.39)	1.62 (0.26)
Gd	29.97 (9.62)	52.88 (11.51)	15.16 (6.99)	8.58 (1.68)	3.18 (0.71)	2.26 (0.47)
Y	52.92 (16.24)	144.41 (84.21)	133.56 (37.37)	14.49 (2.78)	6.23 (0.96)	6.79 (1.92)
Tb	33.83 (11.92)	88.81 (45.43)	19.86 (12.61)	9.90 (2.10)	4.23 (0.96)	2.65 (0.82)
Dy	43.09 (13.87)	149.02 (73.55)	22.12 (16.22)	12.91 (2.64)	5.15 (1.16)	3.45 (1.06)
Ho	56.75 (20.91)	167.14 (126.61)	30.82 (22.15)	16.06 (3.29)	5.95 (1.35)	3.63 (1.44)
Er	69.67 (19.14)	212.98 (142.55)	32.06 (25.91)	17.98 (3.86)	7.23 (1.73)	4.48 (1.76)
Tm	84.31 (16.54)	213.42 (170.74)	33.39 (28.24)	20.09 (4.67)	8.10 (1.81)	4.44 (1.95)
Yb	116.74 (20.56)	270.21 (182.92)	32.82 (29.04)	21.63 (4.99)	9.35 (1.98)	5.40 (2.32)
Lu	132.09 (24.45)	263.39 (235.31)	32.12 (28.01)	27.63 (7.46)	10.49 (2.43)	5.40 (2.30)
Sc	9.03 (1.18)	10.39 (1.80)	7.23 (1.90)	5.96 (1.13)	5.36 (1.05)	4.83 (0.92)
V	5.97 (2.57)	7.69 (2.35)	3.59 (1.22)	2.30 (0.78)	1.85 (0.30)	1.33 (0.28)
B	N.D.	N.D.	N.D.	0.001 (0.0002)	0.0004 (0.00001)	0.01 (0.003)
W	0.02 (0.00)	0.007 (0.004)	0.02 (0.005)	0.03 (0.006)	0.03 (0.003)	0.01 (0.004)

Table 4.9. Mineral-volatile partition coefficients of clinopyroxene.

Run	SL13		SL21		SL24		SL17		SL25	
	D(cpx/liq)	Error ^a	D(cpx/liq)	Error	D(cpx/liq)	Error	D(cpx/liq)	Error	D(cpx/liq)	Error
Cs	N.D. ^b	N.D.	N.D.	N.D.	N.D.	N.D.	N.D.	N.D.	N.D.	N.D.
Rb	0.02	(0.01)	N.D.	N.D.	N.D.	N.D.	N.D.	N.D.	0.03	(0.01)
Li	0.17	(0.04)	0.75	(0.04)	N.D.	N.D.	N.D.	N.D.	0.42	(0.30)
Ba	0.003	(0.00)	N.D.	N.D.	N.D.	N.D.	N.D.	N.D.	0.11	(0.01)
Sr	0.13	(0.01)	0.54	(0.08)	0.33	(0.05)	0.26	(0.06)	0.13	(0.04)
Pb	0.25	(0.05)	N.D.	N.D.	0.22	(0.04)	N.D.	N.D.	N.D.	N.D.
Th	0.005	(0.00)	4.63	(3.55)	0.58	(0.13)	0.18	(0.05)	0.10	(0.03)
U	0.003	(0.00)	0.33	(0.23)	0.10	(0.03)	N.D.	N.D.	0.06	(0.02)
Hf	0.32	(0.08)	2.66	(0.66)	0.60	(0.15)	0.46	(0.24)	0.23	(0.05)
Zr	0.16	(0.05)	1.46	(0.36)	0.54	(0.15)	0.35	(0.22)	0.22	(0.12)
Ti	0.58	(0.09)	4.47	(0.56)	1.26	(0.17)	0.78	(0.18)	0.54	(0.08)
Ta	0.01	(0.01)	N.D.	N.D.	0.36	(0.08)	0.09	(0.05)	0.05	(0.02)
Nb	0.004	(0.00)	N.D.	N.D.	0.25	(0.03)	N.D.	N.D.	0.02	(0.01)
Mo	0.02	(0.00)	0.17	(0.16)	N.D.	N.D.	N.D.	N.D.	0.42	(0.12)
La	0.07	(0.01)	0.66	(0.20)	0.40	(0.12)	0.23	(0.11)	0.07	(0.03)
Ce	0.12	(0.02)	0.42	(0.15)	0.45	(0.15)	0.21	(0.09)	0.06	(0.03)
Nd	0.31	(0.05)	N.D.	N.D.	N.D.	N.D.	N.D.	N.D.	0.38	(0.10)
Sm	0.51	(0.08)	2.43	(1.28)	N.D.	N.D.	N.D.	N.D.	0.43	(0.13)
Eu	0.42	(0.08)	1.59	(0.83)	1.07	(0.26)	N.D.	N.D.	0.30	(0.08)
Gd	0.68	(0.15)	2.12	(0.67)	N.D.	N.D.	N.D.	N.D.	0.56	(0.14)
Y	0.70	(0.19)	1.21	(0.38)	N.D.	N.D.	N.D.	N.D.	0.56	(0.12)
Tb	0.73	(0.15)	1.69	(0.57)	N.D.	N.D.	0.81	(0.31)	0.40	(0.17)
Dy	0.78	(0.18)	1.84	(0.82)	N.D.	N.D.	1.47	(0.25)	0.52	(0.16)
Ho	0.78	(0.18)	1.20	(0.63)	N.D.	N.D.	0.82	(0.46)	0.38	(0.13)
Er	0.74	(0.17)	1.30	(0.36)	N.D.	N.D.	N.D.	N.D.	0.54	(0.18)
Tm	0.66	(0.15)	0.93	(0.18)	N.D.	N.D.	0.98	(0.19)	0.23	(0.13)
Yb	0.59	(0.13)	1.33	(0.20)	N.D.	N.D.	N.D.	N.D.	0.75	(0.23)
Lu	0.55	(0.12)	1.31	(0.24)	N.D.	N.D.	0.88	(0.47)	0.32	(0.13)
Sc	3.46	(0.68)	3.27	(0.42)	5.30	(0.88)	6.70	(1.14)	4.33	(0.75)
V	5.79	(1.02)	6.57	(2.82)	7.40	(2.42)	7.75	(2.33)	7.77	(1.87)
W	0.001	(0.00)	N.D.	N.D.	N.D.	N.D.	N.D.	N.D.	0.05	(0.01)
B	0.01	(0.00)	N.D.	N.D.	N.D.	N.D.	N.D.	N.D.	0.02	(0.01)

^a Errors represent 1 σ uncertainties, calculated as a standard deviation.^b N.D. = no data.**Table 4.10.** Mineral-volatile partition coefficients of rutile and titanite (2 GPa/700°C).

Run	SL12		SL15		SL6		SL3		SL23		SL24			
	D(ttn/liq)	Error ^a	D(rut/liq)	Error	D(rut/liq)	Error	D(rut/liq)	Error	D(rut/liq)	Error	D(rut/liq)	Error		
Hf	14.93	(7.41)	35.07	(16.92)	14.50	(2.04)	13.70	(1.34)	7.82	(0.73)	18.63	(4.21)	9.43	(2.66)
Zr	14.64	(6.82)	43.08	(20.12)	17.99	(2.23)	18.83	(2.40)	9.20	(0.85)	17.80	(4.91)	10.08	(2.93)
Ti	797.80	(292.40)	2137.82	(783.54)	1201.58	(286.52)	639.44	(33.11)	219.59	(14.13)	883.33	(74.04)	336.06	(29.44)
Ta	106.71	(51.36)	191.95	(95.10)	142.45	(43.76)	160.70	(11.70)	124.05	(3.36)	537.41	(116.49)	248.77	(56.05)
Nb	451.46	(208.91)	1493.39	(678.55)	581.16	(23.48)	340.17	(23.00)	116.30	(9.80)	372.67	(46.21)	175.78	(26.13)
Sc	2.08	(0.92)	5.01	(2.41)	3.45	(1.05)	13.93	(3.06)	3.38	(1.31)	8.63	(1.33)	6.07	(1.39)
V	11.21	(6.82)	53.79	(32.44)	242.28	(82.83)	204.98	(125.52)	81.76	(24.06)	106.30	(32.95)	45.33	(15.98)

^a Errors represent 1 σ uncertainties, calculated as a standard deviation.

4.5 Discussion

One of the main purposes of this study is to quantify the partitioning behavior between all residual solid phases and their coexisting volatile phase, either representing an aqueous fluid, hydrous melt or a mixed bulk volatile phase, in a hydrous MOR basalt system below its second critical endpoint (Kessel et al., 2005b). A large data set exists for trace element partitioning in equilibrium with hydrous melts, however, only few experimental studies attempted to evaluate complex mineral-volatile systems for aqueous fluids (Green and Adam, 2003; Kessel et al., 2005a; 2005b; Spandler et al., 2007). We, therefore, compare our new data with results from previous studies and put special emphasis on the different behavior at low and high temperatures and dominating aqueous fluids or hydrous melts, respectively. All mineral partition coefficient data is referring to $D(\text{mineral}/\text{volatile})$.

4.5.1 Garnet

Garnet partition coefficients from this study are compared with data from previous studies in **Figure 4.8**. Our D_{HREE} and D_{MREE} reveal relatively high values (up to almost 1000 or even higher for low temperature experiments) which is in good agreement with other water-saturated high-pressure experiments employing a basaltic starting material (Green and Adam, 2003; Kessel et al., 2005a; Klimm et al., 2008). While Klimm et al.'s D -values (at 2.5 GPa) plot within the range of values determined in this study for HREE and MREE at 2 GPa, D_{HREE} and D_{MREE} of Kessel et al. (2005a) at 4 GPa and Green and Adam (2003) at 3 GPa/700°C are consistently higher. Given the difficulties to measure rim-compositions exclusively when analyzing small stable phases in low temperature runs our results at 3 GPa and 700°C have to be regarded with caution. In contrast to HREE and MREE, discrepancies for D_{LREE} are more pronounced for the various studies and vary within the range of 0.01-1. LREE are strongly controlled by minor and accessory phases such as epidote-group minerals (e.g. Hermann 2002; Frei et al., 2003; Spandler et al., 2003; Feineman et al., 2007; Klimm et al., 2008). Compared to (other) studies that report epidote-group minerals in their residues, our results display lower values for D_{LREE} than Klimm et al. (2008) and to some extent Kessel et al. (2005a) (see results in Klimm et al., 2008) at identical temperatures while the latter cover a larger range within the investigated temperature range than ours. The high variability for D_{LREE} in the literature can probably be ascribed to contamination by either melt inclusions or matrix contamination. Van Westrenen et al. (2001) have shown that the $D_{\text{Zr}}/D_{\text{Hf}}$ ratio correlates positively with the grossular content in garnets in garnet/melt partitioning experiments. In

a similar fashion as in the study of Klimm et al. (2008), our D_{Zr}/D_{Hf} vary little with temperature but display lower values in general with weighted means of 2.2 ± 0.18 at 2 GPa and 1.3 ± 0.19 at 3 GPa compared to their 3.11 ± 0.18 at 2.5 GPa at same grossular contents (24 mol%). Results from anhydrous experiments in a MORB system (Pertermann et al., 2004) at 3 GPa/1340-1360°C and identical grossular content (24 mol%) are in very good agreement with our data at higher pressure ($D_{Zr}/D_{Hf} \sim 1.25$). Although with slightly lower grossular content (14-16 mol %) but at similar pressure-temperature conditions and similar bulk system as Pertermann et al. (2004), Klemme et al. (2002) obtained $D_{Zr}/D_{Hf} = 1.29$ for garnet at 3 GPa and 1400°C which fits our results well at 3 GPa. Generally, D_{Zr} and D_{Hf} , which show a slightly negative temperature-correlation from 700°C to 1100°C in our study, nicely complement the values found between 1340°C and 1400°C at anhydrous conditions determined in the studies mentioned above. We, therefore, conclude that, next to the grossular content, pressure plays a more important role in determining D_{Zr}/D_{Hf} rather than temperature.

Our D_{Nb} and D_{Ta} show $D_{Nb} < D_{Ta}$ at 3 GPa over the investigated temperature range and are thus consistent with published data, even if the latter show considerable variation for absolute values and retention of Nb and Ta in garnets. Kessel et al. (2005a) determined D_{Nb} and D_{Ta} of up to almost 100 at 4 GPa/700°C, followed by a continuous decrease with increasing temperature down to < 0.01 at 1100°C. It cannot be excluded that these analyses were contaminated by rutile inclusions that resulted in overestimated Nb and Ta partitioning data as natural garnets generally show very low D_{Nb} and D_{Ta} (~ 0.001 , e.g. Fulmer et al., 2010). Results from anhydrous studies (Klemme et al., 2002; Pertermann et al., 2004) report consistently low D_{Nb} and D_{Ta} values of ~ 0.01 or lower. D_{Nb} and D_{Ta} at 3 GPa/700°C from studies using comparable basaltic starting materials under hydrous conditions (Green and Adam, 2003) are higher than ours by more than one order of magnitude at the same conditions, whereas Klimm et al. (2008) obtained D_{Nb} and D_{Ta} that are in the range of those from this study. They calculated a tightly constrained weighted mean for D_{Nb}/D_{Ta} of 0.72 ± 0.04 , whereas Green and Adam (2003) report $D_{Nb}/D_{Ta} = 0.22$. At 3 GPa, D_{Nb}/D_{Ta} in the present study amounts to 0.83 ± 0.09 from 800°C to 1100°C, which exceeds values obtained at anhydrous conditions (Pertermann et al., 2004)? It has been suggested that the partitioning behavior of Nb and Ta largely depends on the melt composition and structure; D_{Nb} and D_{Ta} for rutile show a positive correlation with melt polymerization (i.e. increasing Si-content, Schmidt et al., 2004b, and references therein). Our bulk volatile compositions reveal higher D-values along with SiO_2 -contents decreasing from 76 to 63 wt% from 700°C to 1100°C than Klimm et al. (54 to 60 wt% at 2.5 GPa) and Adam and Green (42 wt% at 3 GPa). We, therefore, suggest that our elevated D_{Nb}/D_{Ta}

values are a consequence of higher melt polymerization compared to the other water-saturated studies. At 2 GPa and 850°C to 1000°C the partitioning behavior of Nb and Ta is identical with the results obtained at higher pressure in this study. At 2 GPa, however, the results suggest $D_{Nb} > D_{Ta}$. From 700°C to 1000°C D_{Nb}/D_{Ta} decreases continuously from 4.75 to 0.27. The favored retention of Nb at low temperatures does not result from preferred incorporation of Nb over Ta in garnet but rather from the composition of the bulk volatile phase. While at low temperatures Nb is depleted strongly compared to Ta, this ratio evens out with increasing temperature (see Chapter 3). In general, pressure has only limited influence on the Nb and Ta partitioning of garnets, increased pressure seems to lead to slightly increased D_{Nb} and D_{Ta} . This is in good agreement with previous observations for D_{Nb} and D_{Ta} at 1000°C and 3 to 5.7 GPa in the study of Stalder et al. (1998) in a simplified CMAS-system; their data do rather suggest stronger retention of Nb and Ta with increasing temperature while no clear pressure-dependence could be established.

D_U/D_{Th} of garnets have been determined experimentally for different anhydrous basaltic magma and mantle lithologies mainly; for a high-Al basalt at 2.5 GPa/1430°C (Hauri et al., 1994), for garnet peridotite at 3-3.5 GPa/1300-1565°C (Beattie, 1993), for pyroxenites at 2.5 GPa/1420-1450°C (Elkins et al., 2008) and for dry eclogites at 2.9-3 GPa/1340-1390°C (Pertermann et al., 2004). All studies determined weighted mean values for D_U/D_{Th} of 4-5.5 revealing a clear preference of garnet to incorporate U over Th. In contrast, studies in a hydrous MORB-system (Green and Adam, 2003; Klimm et al., 2008) show the opposite trend and obtain $D_U/D_{Th} < 1$ for garnets. In general, our results display $D_U > D_{Th}$ at both investigated pressures but with different magnitudes; at 2 GPa fractionation is much stronger and results in a weighted mean of 4.43 ± 0.40 while at 3 GPa $D_U/D_{Th} = 1.83 \pm 0.27$. Additionally, increasing pressure seems to increase preferentially the compatibility of Th by an order of magnitude while U is less affected. Compared to the data of Kessel et al. (2005a), who performed experiments using the same starting material and experimental and analytical techniques at higher pressures, our results are in good agreement but our D_U and D_{Th} at low temperatures (700°C to 800°C) reveal lower values by more than an order of magnitude. D_U and D_{Th} of Klimm et al. (2008) and Green and Adam (2003) are elevated by one and two orders of magnitude, respectively, while all D_U and D_{Th} determined under anhydrous mantle conditions are much lower than ours. Klimm et al. (2008) argued that the contrasting partitioning behavior of D_U/D_{Th} in their study compared to results at mantle conditions (Beattie, 1993; Hauri et al., 1994; Pertermann et al., 2004; Elkins et al., 2008) is caused by different oxygen fugacities established in the different studies. Their experiments were buffered to NNO while the others were

performed under more reducing conditions. Higher fO_2 leads to formation of U^{5+} and U^{6+} species while U is present as the predominantly and more compatible U^{4+} species at more reducing conditions which in turn leads to elevated D_U/D_{Th} . The fO_2 of our starting material was constrained close to NNO but not buffered during the experiments. The use of diamonds for the trap (see methods) and the employment of BN around the capsules might result in slightly reducing conditions (Truckenbrodt et al., 1997). However, we did not observe any detectable dissolution of the diamonds after the experiment and, therefore, do not expect significant influence of the fO_2 by dissolution. Even though we do indeed observe a modest Eu-anomaly (due to formation of more incompatible Eu^{2+} under somewhat more reducing conditions) in the partitioning pattern for garnets at 2 GPa, it is completely absent at 3 GPa where $D_U/D_{Th} > 1$ still persists, however, at lower values than at 2 GPa. We, furthermore, do not observe essentially higher D_U at 3 GPa but rather more varying D_{Th} that affect D_U/D_{Th} next to the composition of the bulk volatile phase. Based on our results, we conclude that D_U/D_{Th} might be overestimated at 2 GPa but the overall trend of $D_U^{grt/volatile} > D_{Th}^{grt/volatile}$ is valid for more oxidizing environments likewise.

4.5.2 Clinopyroxene

While an extensive set of cpx-volatile partitioning data exists in the literature, the variability of determined $D^{(cpx/volatile)}$ is significant (see Bédard (2014) for an excellent compilation of all published data up to date). Even though studies were conducted under various conditions in diverse chemical systems (natural and synthetic), it became clear that the partitioning behavior of different trace elements is very complex and depends most likely on several parameters. Some studies point out the importance of the mineral composition influencing the incorporation of trace elements into different sites with changing mineral chemistry (e.g. Gaetani and Grove, 1995; Lundstrom et al., 1998; Green et al., 2000; Hill et al., 2000). Others draw attention to the importance of the melt composition that controls $D^{(cpx/volatile)}$ to some extent (e.g. Bennett et al., 2004; Gaetani, 2004). Nevertheless, pressure and temperature may be the parameters affecting $D^{(cpx/volatile)}$ the most (e.g. Stalder et al., 1998; Hill et al., 2011).

Most of the studies were carried out in mafic magmatic and mantle systems (see Bédard, 2014) while only few determined $D^{(cpx/volatile)}$ for felsic melts (containing > 60 wt% SiO_2 , < 3 wt% MgO) at high pressures. Moreover, there is very limited data available for low-temperature experiments ($< 1000^\circ C$) in complex mineral-volatile systems, and most partitioning studies focused on a small number of trace elements only and did not include all important trace element groups within one set of experiments. Apart from the variety

of employed starting materials and experimental conditions in the various studies, the general trace element pattern obtained in this study is in excellent agreement with previously published results (Hauri et al., 1994; Green et al., 2000; Klemme et al., 2002; Adam and Green, 2006; Hill et al., 2011). Sc and V are the most compatible elements in cpx in this study with D_{Sc} and D_V between 2 and 11, which is consistent with values determined by Hill et al. (2011) for Sc and Barth et al. (2002) for V.

There is a general consensus that $D^{(cpx/volatile)}$ for HFSE and REE decrease with increasing pressure and temperature (e.g. Stalder et al., 1998; Green et al., 2000; Hill et al., 2011). Our results support these findings; at 3 GPa, D_{Zr} , D_{Hf} , D_{Nb} and D_{Ta} show a clear negative temperature correlation from 700°C to 1100°C and $D_{Nb} < D_{Ta}$ as well as $D_{Zr} < D_{Hf}$ with Zr and Hf resulting in higher D-values than Nb and Ta by about one order of magnitude at higher temperatures (**Figure 4.9**). Absolute D-values (see **Table 4.9**) for these elements are in the same range as those determined by Klein et al. (2000) and Barth et al. (2002) for andesitic and tonalitic melts, which are comparable in composition (high SiO₂-content) with our bulk volatile phase in a eclogitic bulk system but are in general higher than many D_{HFSE} determined in previous studies for mafic systems.

Temperature-dependence for D_{REE} at 3 GPa is less clear and errors are rather large but in general show the same trend, however, D_{HFSE} vary more than D_{REE} within the investigated temperature-range. Again, D_{REE} determined in this study are at the high end of the results presented in previous studies but always < 1 at all investigated conditions, except from experiment SL21 (3 GPa/700°C). Analogous to temperature, we observe lower D-values for REE, Hf and Zr with increased pressure, which is in line with previous results in the literature (e.g. Green et al., 2000). Partitioning of HFSE and REE with melts is thought to be controlled by clinopyroxene composition (Hill et al., 2000), resulting in a positive correlation of D_{HFSE} and D_{REE} against Al^{IV} and accordingly, against the CaTs component. In contrast, our data display decreasing D_{HFSE} and D_{REE} with increasing Al^{IV} and CaTs content (**Figure 4.11**). However, our data do not allow drawing conclusions on compositional effects as experiments were not conducted under isothermal conditions. Our results, therefore, illustrate the strong temperature control, which dominates over compositional effects in this study (see also Hill et al., 2011). To visualize the influence of temperature on the activity of the different sites, Al^{IV} and Al^{VI}, Al-content of cpx was plotted against Si (**Figure 4.12**). Total aluminum content increases with increasing Si and decreases with temperature. Concentration of Al^{VI} behaves in the same manner but diverges more from total Al at lower temperatures. This is directly related due to higher concentration of Al^{IV} at lower temperatures.

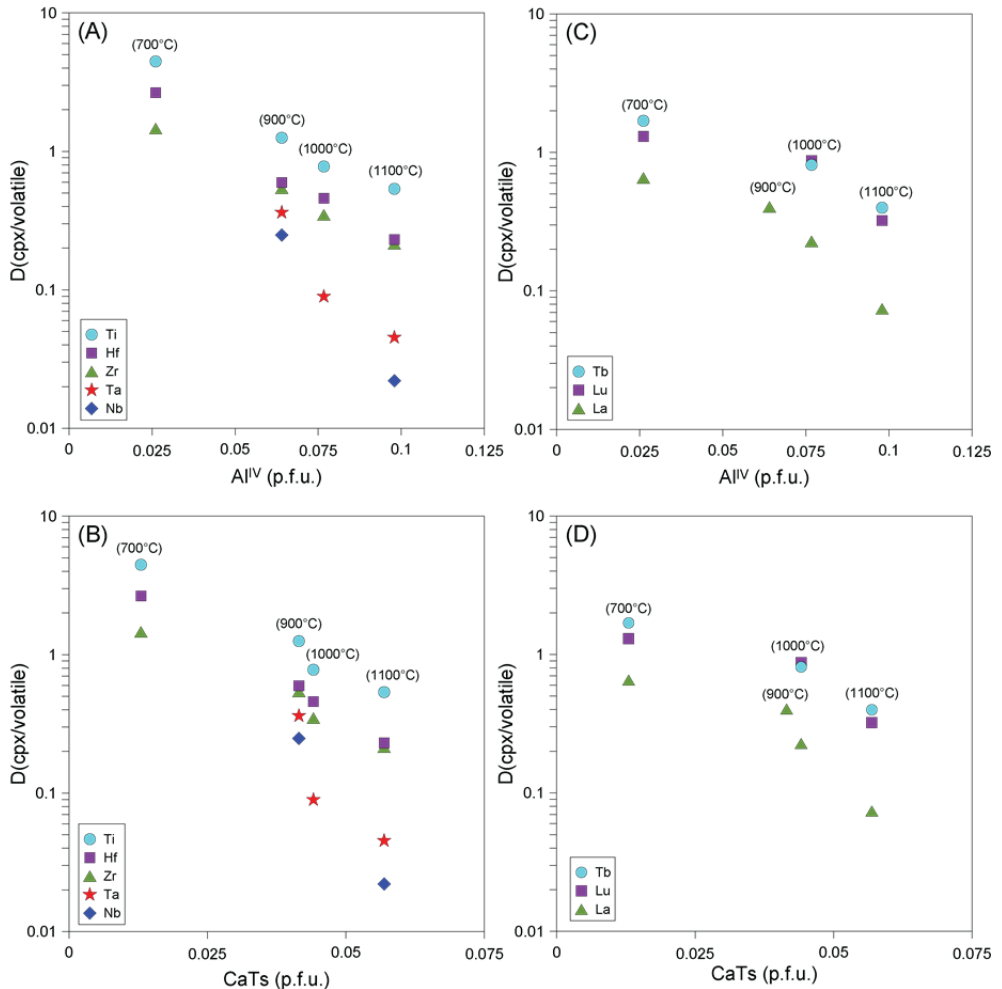


Figure 4.11. Trace element partition coefficients (HFSE and REE) of clinopyroxene at 3 GPa and 700 to 1100°C as a function of Al^{IV} (A and C) and CaTs content (B and D). Explanations see text.

Next to pressure, temperature and melt composition also affect trace element partitioning. Bennett et al. (2004) demonstrated that the sodium content of silicate melts has a significant effect on trace element partitioning in the NCMAS system compared to Na-free systems, resulting in higher D -values in NCMAS by one order of magnitude for tri- and tetravalent cations. **Figures 4.13a and b** depict $D(\text{cpx/volatile})$ for selected HFSE and REE plotted against the Na content of the coexisting bulk volatile. We do indeed observe a distinct increase of D -values with increasing Na content, which is more pronounced for

HFSE than for REE in general. As in the study of Bennett et al. (2004) higher charged (+5) Nb and Ta seem to be more affected than the tetravalent Hf and Zr in this study.

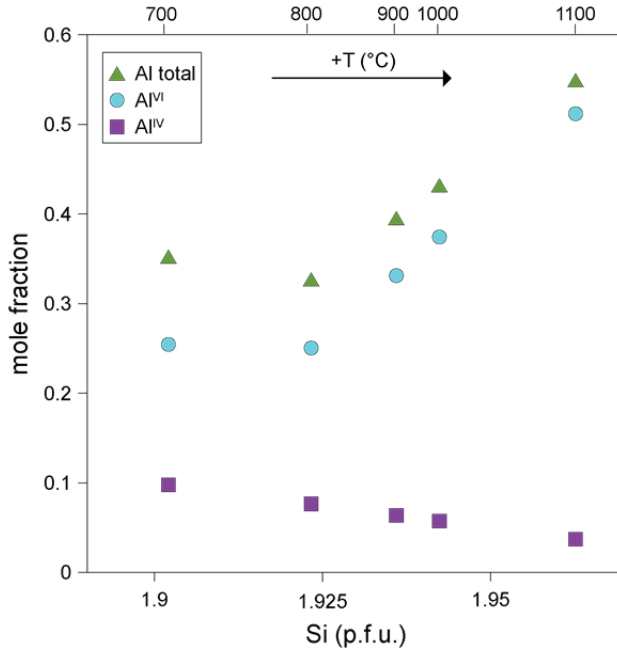


Figure 4.12. Change of Al-content and site occupancy of the Al^{IV}- and Al^{VI} with Si content (p.f.u.) of clinopyroxene. Corresponding temperatures are labeled at the top.

One has to keep in mind, however, that our D-values are subject to varying temperatures and the pure effect of Na in the bulk volatile phase cannot be quantified on the basis of our results.

Gaetani (2004) showed that the degree of polymerization of the melt is another effect that influences trace element partitioning significantly. Degree of polymerization can be expressed as NBO/T (non-bridging oxygens over tetrahedral cations). They suggest that for NBO/T < 0.49 melt structure plays a crucial role in affecting trace element partitioning near the peridotite solidus while for higher NBO/T (i.e. smaller degree of polymerization) this effect diminishes. We observe a clear positive correlation for D_{REE} and D_{HFSE} and Si-content of the coexisting bulk volatile (**Figure 4.13c and d**). Analogous to the effect of sodium content in a volatile, +5 elements (Nb and Ta) are more affected than +4 Zr and Hf with inferred increasing degree of polymerization. Again, similar to the effect of Na in a

volatile, temperature might still be the control dominating over degree of polymerization. In contrast to Gaetani et al. (2004), our data do not reveal any obvious correlation between NBO/T and the trace element partitioning.

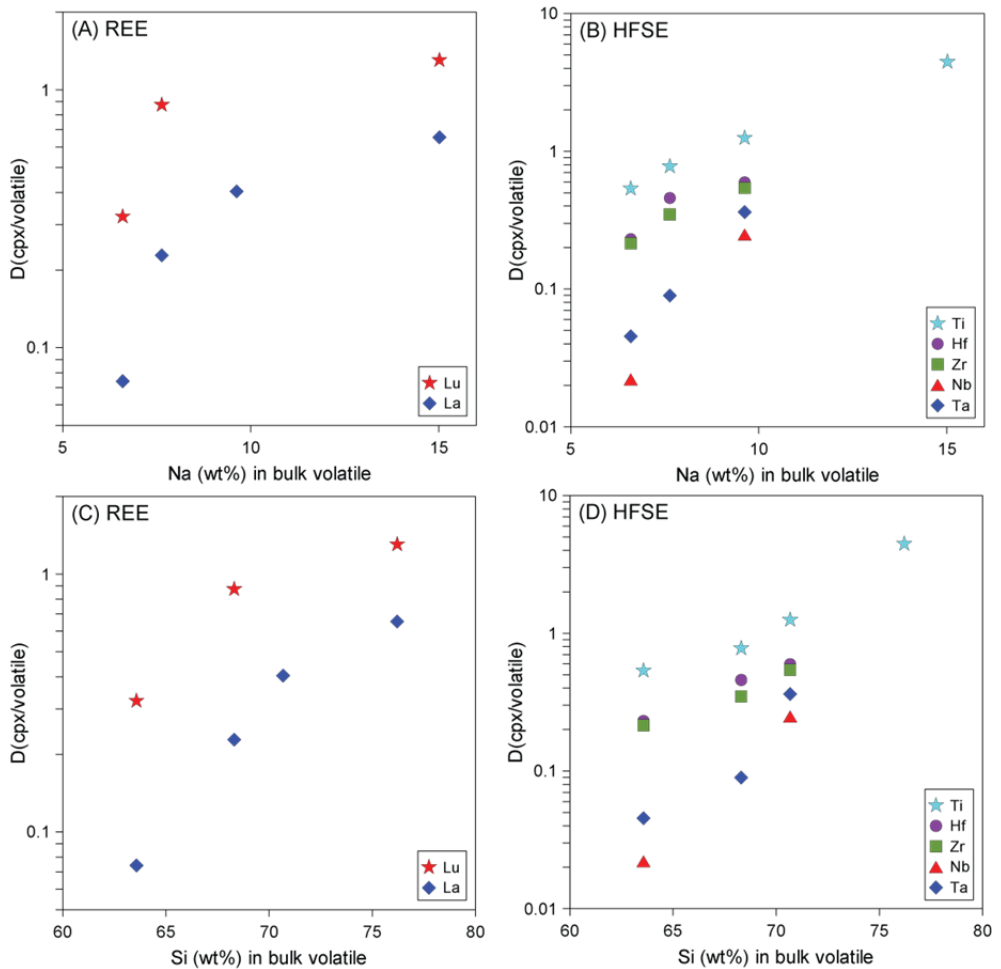


Figure 4.13. Variations of trace element partition coefficients (HFSE and REE) of clinopyroxene at 3 GPa and 700 to 1100°C as a function of bulk volatile composition. (A) and (B) with Na-content (wt%) of the bulk volatile. (C) and (D) with Si-content (wt%) of the bulk volatile. Explanations see text.

4.5.3 Ti-phases

Rutile is the major Ti-phase in eclogites, incorporating significant amounts of HFSE, especially Nb and Ta (e.g. Foley et al., 2000; Zack et al., 2002; Xiong et al., 2005; Schmidt et al., 2009). Many studies suggested that the presence of rutile in eclogites and associated rocks is supposedly responsible for the distinct negative anomalies of Ti, Nb and Ta with respect to LILE and LREE (e.g. McCulloch and Gamble, 1991; Brenan et al., 1994; Stalder et al., 1998; Klemme et al., 2002), a characteristic feature of many volcanic arc rocks (Tatsumi and Eggins, 1995). It has been shown that rutile controls the Nb and Ta budget during dehydration/melting of the subducting oceanic lithosphere almost entirely (e.g. Lucassen et al., 2010).

Most experimental partitioning studies agree on the fact that rutile is able to fractionate Nb from Ta, and there is a general consensus that Ta is preferably incorporated into rutile compared to Nb leading to $D_{\text{Nb}}/D_{\text{Ta}} < 1$ in equilibrium with melt (e.g. Schmidt et al., 2004b; Klemme et al., 2005; Xiong et al., 2005; Bromiley and Redfern 2008). Tiepolo et al. (2000) concluded on the basis of a positive correlation between $D_{\text{Nb}}/D_{\text{Ta}}$ and the M1-O bond length of amphiboles that Ta has a marginally smaller effective ionic radius than Nb which results in favored incorporation of the former into these specific lattice sites. Horng and Hess (2000) assumed identical ionic radii for both, Nb and Ta, but different molecular electronic polarizability; higher polarizability of Nb causes stronger distortion of the rutile structure due to stronger covalent bonds with O, which leads to facilitated incorporation of Ta. Our results at 3 GPa and 2 GPa/900°C are in good agreement with literature $D_{\text{Nb,Ta}}$ and reveal average $D_{\text{Nb}}/D_{\text{Ta}}$ of 0.71 and 0.94, respectively. However, with decreasing temperature from 800 to 700°C and in equilibrium with a bulk volatile that is dominated by aqueous fluids at 2 GPa, $D_{\text{Nb}}/D_{\text{Ta}}$ shows increasing values of up to 7.8 at 700°C; $D_{\text{Nb}}/D_{\text{Ta}} > 1$ is in clear contrast with the values determined for $D_{\text{Nb}}/D_{\text{Ta}}$ in equilibrium with melts at 900°C. Due to the experimental challenge of quantifying aqueous fluids there are very few rutile/fluid partitioning data up to date, notably for low temperatures. Nevertheless, the results for $D_{\text{Nb,Ta}}$ suggest higher D_{Nb} than D_{Ta} in the studies of Brenan et al. (1994) and Stalder et al. (1998) who determined values in the range comparable to this study or lower but with less significant fractionation of Nb and Ta (see **Figure 4.10b**). In contrast, Green and Adam (2003) found $D_{\text{Nb}}/D_{\text{Ta}} < 1$ for rutiles in equilibrium with aqueous fluids at 650 and 700°C. While their D_{Nb} values are similar to ours, D_{Ta} are higher by more than one order of magnitude resulting in a contrasting fractionation behavior. D_{Nb} values in this study reveal a continuous decrease with increasing temperatures at both pressures. D_{Ta} at 2 GPa on the other hand, displays reverse behavior when the composition of the bulk

volatile phase changes from predominantly fluid to predominantly melt characteristics around 800°C, changing $D_{\text{Nb}}/D_{\text{Ta}}$ to melt characteristics; $D_{\text{Nb}}/D_{\text{Ta}}$ thus seems to be influenced largely by D_{Ta} . Bromiley and Redfern (2008) suggested that pressure has a more pronounced effect on D_{Ta} than on D_{Nb} based on rutile/melt partitioning experiments, which is also the case for our data; while for D_{Nb} no change can be determined at identical temperatures at 2 and 3 GPa, D_{Ta} is higher by a factor of 2-3 at 3 GPa. Next to pressure, temperature and compositional effects related to melt composition have a strong influence on the partitioning of Nb and Ta (e.g. Linnen and Keppler, 1997; Horng and Hess, 2000; Schmidt et al., 2004b). Schmidt et al. (2004b) showed that D-values for Nb and Ta as well as $D_{\text{Nb}}/D_{\text{Ta}}$ increase with increasing degree of polymerization, e.g. basaltic to rhyolitic melts, approaching 1 for $D_{\text{Nb}}/D_{\text{Ta}}$ in the most differentiated melts. Since the melt composition is also a function of temperature (and pressure), its effect is not easily discriminated on the basis of our data. However, Linnen and Keppler (1997) suggested that the solubility for Ta in melts is higher than for Nb based on solubility experiments of columbite and tantalite in subaluminous to peraluminous granitic melts. If different activity coefficients for Nb and Ta are indeed an important control on the partitioning behavior of these elements, this might explain the changing of $D_{\text{Nb}}/D_{\text{Ta}}$ at 2 GPa with changing bulk volatile characteristics.

D_{Zr} and D_{Hf} of this study plot consistently lower compared to D_{Nb} and D_{Ta} by about one order of magnitude. Fractionation between D_{Zr} and D_{Hf} is small and not well constrained but reveals $D_{\text{Zr}}/D_{\text{Hf}} = 1-1.4$ and $1-1.1$ at 2 and 3 GPa, respectively. While D-values generally decrease with increasing temperature, no pressure effect can be observed. Most previous rutile/volatile partitioning studies focused on Nb and Ta and only some determined Zr and Hf partitioning (Brenan et al., 1994; Stalder et al., 1998; Green and Adam, 2003; Klemme et al., 2005; Xiong et al., 2005); most of them agree that D_{Hf} is preferably retained by rutile and calculated $D_{\text{Zr}}/D_{\text{Hf}} < 1$. Our data are in good agreement with most previously measured values and show that rutile controls Zr and Hf only to a minor extent. In contrast to the clear correlation of $D_{\text{Nb}}/D_{\text{Ta}}$ with bulk volatile composition and the resulting reverse fractionation behavior observed at low and higher temperatures, such a trend cannot be documented for $D_{\text{Zr}}/D_{\text{Hf}}$.

Two studies additionally measured the partitioning of V into rutile but obtained rather varying results for D_{V} (Klemme et al., 2005; Xiong et al., 2005). Xiong et al. (2005) concluded, based on their relatively high D_{V} (average ~69), that vanadium is present mainly as V^{4+} and, therefore, estimated the oxygen fugacity during their experiments to be between NNO and FMQ. This is somehow in contrast with the results of Klemme et al. (2005) who measured D_{V} between 0.15 and 17.8 and observed the highest D_{V} under the

most reducing conditions in their set of experiments. They interpreted their higher D_V as a consequence of V^{5+} as dominant species. Our fO_2 is constrained close to NNO (see methods) and we measure D_V in the range of those of Xiong et al. (2005) or even higher; following their argumentation we conclude that V is present predominantly as V^{4+} in our experiments.

In experiment SL12 (2 GPa/700°C) titanite, another potentially important Ti-phase in addition to rutile, was stable, which offers a direct comparison between the two in terms of trace element partitioning. In contrast to rutile, titanite incorporates not only large amounts of HFSE but also REE (e.g. Prowatke and Klemme, 2005). Unfortunately, the crystal size in our experiment was extremely small ($< 10 \mu\text{m}$) and LA-ICP-MS analyses could have been performed with $4 \mu\text{m}$ beam size only. Therefore, detection limits for REE (and most other elements) were high and we obtained significant values only for HFSE and V. Previous studies have shown that the HFSE (Nb, Ta, Zr, Hf) fractionation pattern for titanite is generally the same as for rutile but magnitude of fractionation differs (Tiepolo et al., 2002; Prowatke and Klemme, 2005; John et al., 2009). For example, $D_{\text{Nb}}/D_{\text{Ta}}$ between rutile and melt can reach values close to 1 (as mentioned above) while Prowatke and Klemme (2005) found $D_{\text{Nb}}/D_{\text{Ta}}$ between titanite and melt as low as 0.07. As for rutile in equilibrium with aqueous fluids-dominated bulk volatiles (2 GPa/700-800°C), $D_{\text{Nb}}/D_{\text{Ta}}$ exceeds 1 for titanite in our experiment, which is the opposite from what was determined in all other studies. D_{HFSE} are lower by a factor of 2-4 compared to rutile and $D_{\text{Nb}}/D_{\text{Ta}}$ by a factor of 2 resulting in 4.2 (rutile 7.8) in the experiment containing both, titanite and rutile.

4.5.4 Implications for subduction zone dehydration

Volcanic arc rocks often represent the only witnesses one has at hand to infer how elements were transported within subduction zone settings. Their chemical composition might reveal under what pressure and temperature conditions magmas were generated and which mineral phases and metasomatic components were present in order to induce certain element ratios typical for arc magmas provided the volcanic rocks are primary or near-primary mantle melts and not significantly modified by differentiation and assimilation processes. The trace element signature and the concentration of some specific elements observed in arc volcanic rocks are thereby often inherited from a descending slab. Thus, the aim of many recent studies was to experimentally reproduce these ratios by investigating fluid-rock equilibria exemplary for dehydration and melting of subducted oceanic lithosphere. It has been shown that the extent of mobilization of various trace

elements depends not only on pressure and temperature, but also on the nature of the mobile phase (aqueous fluid, hydrous melt or supercritical liquid) and the residual mineral assemblage in the slab (e.g. garnet, epidote-group minerals, monazite, rutile, zircon), which strongly influences trace element mobility and partitioning. It is, therefore, fundamental to quantify the efficiency of element transport in different transport agents and in equilibrium with different residual slab lithologies potentially present.

We have calculated the trace element bulk volatile/solid partition coefficients to determine which elements are retained in the slab residues and which ones are more efficiently liberated and migrate upwards into the mantle wedge where they potentially contribute to arc magma genesis. **Figure 4.14 a and b** show the results of these calculations at 2 and 3 GPa and 850-1200°C; additionally, we have plotted the results from the experiments at 700-800°C for comparison (grey shaded areas, Chapter 3). At 2 GPa, the most volatile-mobile elements are LILE (Rb, Ba, Sr) as well as Pb, Li and B with $D(\text{volatile/solid})$ between 1 and 25 while Rb displays values of up to 85 at 3 GPa. From 850-1100°C, also Th and U, as well as HFSE (Hf, Zr, Ta) and LREE (La-Nd) show increasing volatile-compatible character, while HREE, Sc, V and W are clearly volatile-incompatible and remain in the eclogitic portion of the slab. The pattern at 1100°C is relatively flat and slightly below 1, which confirms that cpx, which is the liquidus phase at these conditions, has only minor impact on the trace element budget and that the MREE and HREE are mainly controlled by garnet that is no longer stable at 2 GPa/1100°C. The results at 3 GPa reveal basically the same bulk-D pattern but with slightly higher values especially at higher temperatures consistent with increased melt solubilities and lower melt fractions in line with a positive slope of the solidus and liquidus curves in P-T-space at higher pressures.

Compared to the results at lower temperatures (shaded areas), one distinct difference can be pointed out: from 700-800°C, LREE (La-Sm), Th and U are clearly and to a much larger extent depleted in the bulk volatile compared to high-T melts. This difference coincides with a distinct change in the residual host rock composition of the slab and the disappearance of the hydrous phases amphibole and zoisite at around 850°C, leaving a nominally anhydrous phase assemblage at higher temperatures.

We have shown that zoisite is the main control on LREE, Th and U in our low-T experiments (Chapter 3). The efficient retention of these elements by epidote-group minerals and monazite in the oceanic crust and its overlying sediment layer has been demonstrated also by other studies (Hermann, 2002; Feinemann et al., 2007; Klimm et al., 2008; Hermann and Rubatto, 2009; Skora and Blundy, 2010). The consequence of epidote-group minerals present in the slab is demonstrated impressively in **Figure 4.14**. For example, D_{La} at 900°C are increased compared to 700°C by a factor of 136 and 50 at 2 and 3 GPa, respectively. An even more pronounced difference reveals Th at 900°C compared to 700°C with D_{Th} higher by factors of 642 and 287 at 2 and 3 GPa, respectively.

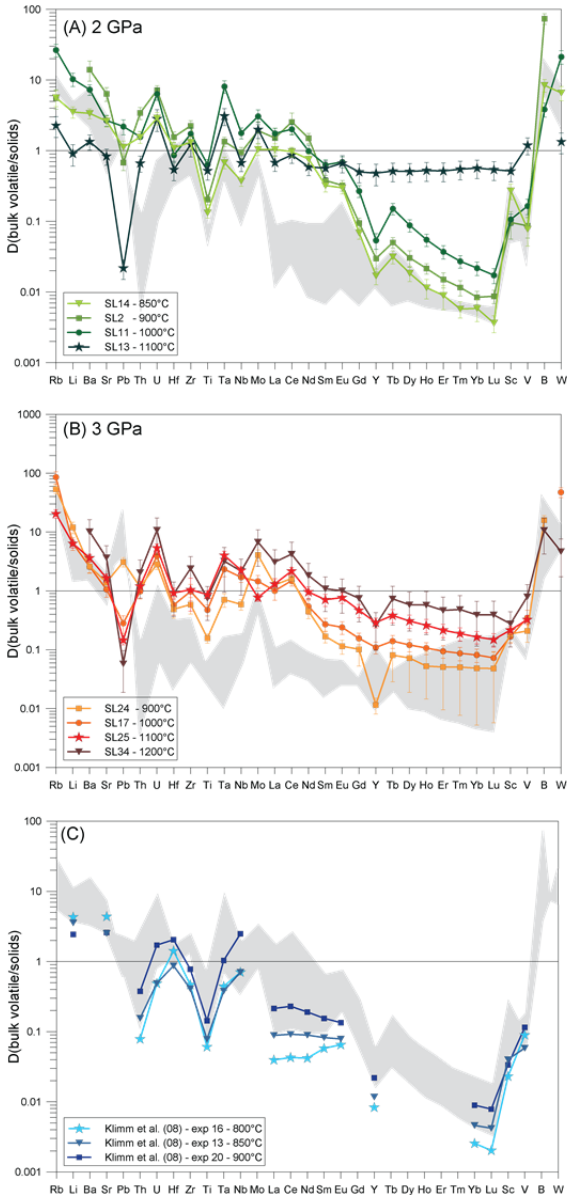


Figure 4.5. Bulk volatile-solid partition coefficients of this study at 2 GPa (A) and 3 GPa (B). Grey shaded areas show results at 700 to 800°C (from Chapter 3). Bulk solid residue was calculated by subtracting measured trace element composition in the volatile times its fraction from initial amount of trace elements in the starting material divided by solid residue fraction. Uncertainties are given as 1σ and were calculated by propagating uncertainties of elemental concentrations. (C) Melt-bulk solid partition coefficients from Klimm et al. (2008) at 2.5 GPa compared with data from this study and Chapter 3 at 2 GPa and 800 to 1000°C (grey shaded area).

In general, LREE, Th and U become volatile-compatible in the mobile bulk volatile phase as soon as epidote-group minerals have molten out, therefore, become nearly completely mobile to be transported into the mantle wedge. Hydrous melting often has been proposed to be the mechanism to efficiently transport elements such as REE (Klimm et al., 2008; Hermann and Rubatto, 2009; Skora and Blundy, 2010). However, they have also shown that the solubility of certain REE-phases (allanite, monazite) in the melt phase is low so that only elimination of these phases leads to a trace element pattern in the melt that is consistent with the observed LREE budget of arc rocks, consistent with the results from this study emphasizing that only the removal of epidote-group minerals results in a strong LREE/HREE fractionation typical for arc magmas. **Figure 4.14c** compares the bulk partition coefficients of Klimm et al. (2008) for basalt at 2.5 GPa and 800-900°C with our results at 2 GPa (grey shaded area). At these conditions, they find allanite to be stable in equilibrium with melt while our experiments suggest that an aqueous fluid-dominated bulk volatile at 800°C is replaced by hydrous melts at 850°C. While for most elements our D -values are in good agreement with theirs, not surprisingly, the differences for LREE, Th and U are considerable above 800°C. For example, our $D_{\text{LREE,Th,U}}$ at 850°C plot higher by more than one order of magnitude with values above unity, whereas both studies suggest values in a similar range at 800°C. Our results confirm earlier findings that for common epidote-group mineral bearing basaltic compositions and at typical sub-arc conditions, only complete removal of epidote-group minerals in the oceanic lithosphere mobilizes LREE, Th and U efficiently. Nonetheless, the presence of allanite in the descending oceanic crust is not a prerequisite and might be strongly dependent on a sufficient input of LREE into subduction zones to enhance allanite stability. Most previous experiments have been doped with LREE, Th and U at unrealistic high levels to stabilize allanite deeply into the melting regime (see Skora and Blundy, 2010) and might, therefore, only be relevant for extraordinary natural settings.

Elliott et al. (1997; 2003) have proposed that interpretation and modeling of arc magma generation requires consideration of (at least) two different physical components from the slab; an aqueous fluid from the basaltic portion and a hydrous melt as main transport agent from the sediments if the latter are present. In the following we compare the experimentally derived bulk volatile phase compositions with the trace element signature of typical sediment-starved arcs, such as Izu-Bonin or parts of the Mariana arc. Common features of dominantly to exclusively basalt-derived components are PUM-normalized La/Sm of around 1, Ba/Th ratios in excess of 1000 and excess ^{238}U over ^{230}Th (Elliott et al., 1997; Elliott 2003). In contrast, addition of sediment melts would result in increased La/Sm ratios and much lower Ba/Th ratios in the arc source region due to the input of LREE and Th, which are highly enriched in the sediments. However, the trace element doping of our starting composition does not correspond to natural values as it is generally too high,

especially for Th. In order to compare to natural settings, we applied a correction factor for Ba, Th, La and Sm in the bulk volatile compositions based on N-MORB values in natural basaltic lithologies (Sun and McDonough, 1989). Most mobile volatile phases of this study reveal PUM-normalized La/Sm of 0.4-1.2 (corrected for N-MORB) within the investigated temperature range at 2 and 3 GPa. When correcting for E-MORB, La/Sm reveals slightly higher values of average 2.2. Highest Ba/Th ratios (corrected for N-MORB) are determined for fluids at 700°C with values of 9500 and 11000 at 2 and 3 GPa, respectively. With increasing temperature, Ba/Th drops down to around 500 at 800°C at both pressures; it then stays at ~60 for all melts at higher temperatures due to the breakdown of zoisite and the resulting enhanced mobility of Th. Correction for E-MORB results in even higher Ba/Th of 17000 and 20000 at 700°C and 2 and 3 GPa, respectively. Based on recent thermal models, predicted slab-top temperatures amount to about 750-850°C for most subduction zones (e.g. Syracuse et al., 2010; Van Keken et al. 2011). With the exception of unusually hot subduction zones, this implies that the basaltic crust does not undergo significant melting and if it occurs, then only its uppermost parts are involved. Consequentially, only fluid-dominated bulk volatiles from our 700-800°C experiments represent realistic transport agents that might migrate upward; their composition and key element ratios are in good agreement with natural arc rocks (e.g. Elliott 2003). Elevated U/Th measured in rocks of sediment-starved settings was suggested to be the result of fractionation in equilibrium with aqueous fluids rather than melts (Elliott 2003). **Figure 4.14** reveals that at both pressures and over the entire temperature range of this study, U efficiently fractionates from Th. This effect is not restricted to low-temperature bulk volatiles but also observed at conditions where no epidote-group mineral causes high U/Th ratios in the melts. The same relationship was observed in melts in the sediment-H₂O system examined by Hermann and Rubatto (2009). They already pointed out that excess U might not be necessarily a criterion to determine the nature of the mobile phase released from the slab. A reason for high U/Th in melts might be the oxidation state of U. While both, U and Th normally occur as tetravalent elements, the supposedly oxidizing environment in subduction zones leads to formation of more incompatible U⁶⁺ which preferably enters a fluid or melt phase.

4.6 Summary and concluding remarks

The purpose of this study was the full characterization of mobile slab components over a wide range of temperatures at 2 and 3 GPa, conditions representative for sub-arc conditions in subduction zones. Most of the results presented here cover supra-solidus temperature conditions where hydrous melts (< 35 wt% water) serve as transfer agent from the oceanic crust to the mantle wedge; the low-temperature bulk volatile regime is

presented mostly in Chapter 3. The change from fluid- to melt-dominated compositions coincides with a distinct change in the residual host rock composition of the slab and the disappearance of the hydrous phases amphibole and zoisite at around 850°C at 2 GPa, leaving an anhydrous eclogitic residue at higher temperatures. At 3 GPa, this change can be observed between 800 and 900°C. We present partition coefficients for most of the residual phases (garnet, cpx and rutile/titanite) in equilibrium with their bulk volatile phases. While there exists an extensive set of mineral-melt partition coefficients in the literature for various minerals, mineral-fluid D-values are sparse and, therefore, our results at low temperatures provide new constraints for element transfer during dehydration of the descending slab. The results confirm the strong control garnets exerts on HREE, rutile and titanite on Nb and Ta, while cpx has only little impact on the trace element release or retention when coexisting with the phases found in our experiments. In agreement with conclusions drawn by earlier studies, we found that only significant degrees of melting of the basaltic portion of the slab produces a trace element signature that is typical for arc-related rocks such as high LREE/HREE. In contrast, the composition of low-temperature bulk volatiles with respect to their LREE and Th concentrations are strongly controlled by the presence of zoisite. We show enhanced mobility for these elements at generally lower temperatures than suggested by results from allanite-bearing residues in a MORB-H₂O system at similar P-T conditions (e.g. Klimm et al., 2008). These conclusions are somewhat different from the results of the study by Kessel et al. (2005a) who inferred that at higher pressures where the fluid-melt solidus ceases to exist, a supercritical liquid phase is present that spans a continuum from low to high temperature conditions with geochemical characteristics typical for arc magmas. Thus, the modes of dehydration and melting and, as a consequence, the nature and composition of the metasomatic agent emanating from the subducting oceanic lithosphere are inferred to be sensitive to pressure (depth) and most likely change from a two phase regime involving aqueous fluids and hydrous silicic melts to a higher pressure regime where a single supercritical mobile phase moderates the trace element characteristic of the metasomatic agent.

CHAPTER 5

The influence of phengite in subducted crust: implications for arc magmatism

Abstract

Subducted sediments are the lithologies hosting the largest amount of key elements for understanding subduction zone processes, such as large ion lithophile elements (LILE) and rare earth elements (REE), compared to other parts of a subducting oceanic lithosphere. These elements are considered to be liberated from the slab mainly by melting of the sediments before being transported to the source region of arc magmas. Here we report the results of piston cylinder experiments conducted at conditions prevailing in the upper part of subducted lithosphere (3 GPa and 700 to 900°C) employing a trace element-doped starting material representing strongly altered oceanic crust (AOC)/sediments. Approximately 10 wt% of water was added to the system to simulate flushing by fluids originating from underlying lithologies. In order to determine nature and quantitative composition of the mobile phase (aqueous fluid or hydrous melt), we used diamond traps to catch the volatiles and adapted the "freezing" method to systems containing potassium by the use of bromine as internal standard. We find an aqueous fluid being stable at 700°C whereas melting starts at around 800°C in coexistence with a phase assemblage composed of garnet, clinopyroxene, phengite and rutile. Phengite and rutile occur at all conditions, whereas clinopyroxene is exhausted at 900°C. Our results furthermore suggest an epidote-group mineral being stable at 700 and 800°C. We present partition coefficients for garnet, rutile, clinopyroxene and phengite with the latter being rare in the literature up to date but essential to understand LILE transport in subduction zones. Resulting bulk volatile-solid partition coefficients reveal trace element pattern very similar to those obtained in studies in MORB systems when epidote-group minerals and phengite coexist. Above the breakdown of the former at 900°C, the melt reveals enrichment of LREE compared to LILE due to the presence of phengite, which is the major host and control for LILE. This study confirms the importance of residual phases in the slab in monitoring key elements used to describe the slab component in arc magmatic rocks.

5.1 Introduction

Subduction zone settings are one of the most important environments in terms of element (re)cycling on Earth. When oceanic lithosphere is being subducted, slabs experience progressive dehydration and/or melting which in turn liberates elements that are able to travel upwards into the mantle wedge and eventually govern the trace element signature of arc magmas. Despite the importance of these processes, little is still known about the nature (aqueous fluid, hydrous melt, supercritical fluid) and composition of the element transport agents. It is evident that primitive arc rocks differ from mid ocean ridge basalts (MORB) in their composition as a result of addition of a slab-derived mobile volatile phase that modifies the depleted mantle region where arc magmas are generated. The water-rich, slab-derived mobile phase is suggested to be composed mainly of silica and incompatible elements such as large ion lithophile elements (LILE), Th, U and to a lesser extent light rare earth elements (LREE), based on geochemical studies on arc rocks (e.g. Hawkesworth et al., 1993; Tatsumi and Eggins, 1995). Subducted sediments are thought to play a key role as they are the dominant host of LILE in the oceanic lithosphere (Plank and Langmuir, 1993; Plank and Langmuir, 1998). Based on distinct element ratios and in agreement with proposed slab-top temperatures relevant to magma generation (750-850°C, e.g. Syracuse et al., 2010; van Keken et al., 2011), it is inferred that elements are transported from the slab by melting of the sediment lithologies, while the basaltic portion of the slab is rather flushed by extremely water-rich fluids from underlying hydrous mantle lithologies (e.g. Ulmer and Trommsdorf, 1995) that filter fluid-mobile elements out (Elliott et al., 1997; Johnson and Plank, 1999; Pearce et al., 2005; Spandler and Pirard, 2013).

The release of elements is strongly controlled by the individual minerals that form and decompose in the subducted slab. It is well established that rutile is the main control on most of the high field strength elements (HSFE, Brennan et al., 1994; Zack et al., 2002; Klemme et al., 2005) which results in a distinct negative Nb-anomaly in arc rocks (e.g. McCulloch and Gamble, 1991; Hawkesworth et al., 1993). Garnet is stable over a wide temperature range and is preventing the heavy rare earth elements (HREE) from leaving the slab efficiently (e.g. Stalder et al., 1998; Green et al., 2000; Kessel et al., 2005a). It became evident in recent years that LREE plus Th and LILE are mainly controlled by accessory and minor phases. The mobility of the former is strongly dependent on the presence or absence of epidote-groups minerals (e.g. Hermann, 2002; Klimm et al., 2008; Chapter 3) or monazite (e.g. Hermann and Rubatto, 2009; Skora and Blundy, 2010). The white mica phengite is suggested to be the major host and primary control for LILE (Domanik and Holloway, 1996; Schmidt, 1996; Sorensen et al., 1997; Melzer and Wunder, 2000; Zack et al., 2001; Schmidt et al., 2004a; Scambelluri et al., 2008; Hermann and Rubatto, 2009). However, experimentally determined partition coefficients between

phengite and fluids or melts are rare (Melzer and Wunder, 2000; Green and Adam, 2003) but urgently needed to quantify and understand LILE-transport in subduction zones. In this study we have conducted high pressure and temperature experiments (3 GPa, 700-900°C) on a water-saturated, Ca-rich sediment composition in order to determine the quantitative composition of the mobile volatile phase as well as to analyze individual residual phases (garnet, phengite, rutile, clinopyroxene) and calculate partition coefficients. We have adapted the "freezing method", developed by Kessel et al. (2004) for K-free MORB-systems, to systems containing potassium by using a different internal standard (incompatible Br) for LA-ICP-MS analysis. This approach allows for full and direct quantification of any mobile volatile phase independent from mass-balance calculations. The results are compared to MORB-systems to address the question on how phengite influences LILE mobility and the geochemical signature of arc rocks.

5.2 Methods

5.2.1 Synthesis of the starting material

The starting material, TB-K-5, employed in this study was composed from synthetic compounds and was chosen to represent strongly altered MOR basalt/sediment. It was mixed from reagent grade oxide and carbonate powders after they were fired (1000°C: SiO₂, TiO₂, MgO, Fe₂O₃) and dried (220°C: Al₂O₃, CaCO₃, Na₂SiO₃, K₂SiO₃) for 24 hours to remove any moisture and subsequently homogenized in an agate mortar under ethanol. In order to constrain oxygen fugacity (fO₂) of the starting material, the ferric to ferrous ratio was fixed by vitrifying the mixture in an iron pre-saturated Pt-crucible (to avoid Fe-loss) in an H₂-CO₂ gas mixing furnace at 1325°C for 2 hours. The resulting fO₂ corresponds to the QFM buffer equilibrium. After quenching the glass was checked with electron probe microanalysis (EPMA); major element composition of TB-K-5 is listed in **Table 5.1**.

Trace elements were added to the starting material as a pre-mixed spike (Rohit Nandedkar, Diss. ETH No. 21411). A previously produced diopside glass was ground to a fine powder and complemented by a total of 30 trace elements, including all important groups of trace elements (LILE, REE, HFSE, transition metals), at a 2000 µg/g level, except for U and Th, which were added at a 1000 µg/g level. After vitrification of the mixture at 1460°C for 3.5 hours, the glass composition was checked by laser-ablation inductive-coupled-plasma mass-spectrometer (LA-ICP-MS) analysis and ground to a fine powder. 2 wt% were added to the starting material to obtain a 40 µg/g level for most trace elements and 20 µg/g for U and Th (see **Table 5.2**). Lead, Rb and Cs were nearly completely lost during synthesis due to alloying with the Pt-crucible (Pb) and volatilization (Rb, Cs).

Table 5.1. Composition of the starting material.

n=28	TB-K-5	
	wt%	Std (1σ)
SiO ₂	53.13	0.76
TiO ₂	1.94	0.04
Al ₂ O ₃	21.77	0.41
FeO	6.71	0.17
MgO	5.14	0.18
CaO	4.69	0.11
Na ₂ O	1.97	0.06
K ₂ O	4.65	0.11
Total	100.00	
$X_{\text{Mg}}^{1)}$	0.58	

¹⁾ X_{Mg} calculated with $\text{Fe}^{2+} = \text{Fe}^{\text{tot}}$

5.2.2 Experimental methods

The experimental method is basically identical to that presented in Chapters 3 and 4. We performed diamond trap experiments in order to separate the volatile phase from the residual solid phase assemblage and catch it in the interstices of the diamonds (e.g. Stalder et al., 1998). For all experiments, annealed gold capsules (3.0 mm outer diameter, 2.7 mm inner diameter) were employed with the attempt to minimize Fe-loss to the capsule walls. To obtain water-saturated systems, 4 μl distilled water was filled into the capsule by micro syringe first, which corresponds to 8-12 wt% of the total H₂O plus altered basalt system. The water was additionally doped with 1180 $\mu\text{g g}^{-1}$ Br, which serves as internal standard for the subsequent LA-ICP-MS data quantification of the volatile phase (see Kessel et al., 2004). For more details see **section 5.2.3.1**. In a next step, half of the starting material was filled into the capsule, followed by a layer of synthetic diamonds (~20 μm grain size on average). On top of the diamonds, the second half of starting material was placed and tightly packed before welding the capsule shut using a Tungsten arc-welder. Capsules were weighed before and after welding to ensure that no water loss occurred during welding; they were heated to 110°C after welding to check for tightness of the capsules.

Table 5.2. Trace element concentrations in the starting material as determined by LA-ICP-MS.

Trace element glass		
n=10	[$\mu\text{g/g}$]	1σ
Li	33.28	1.25
B	42.88	7.11
Sc	29.82	0.31
V	39.74	1.90
Rb	5.98	0.61
Sr	44.07	0.38
Y	28.00	0.40
Zr	46.65	0.53
Nb	36.03	0.80
Mo	54.00	3.62
Cs	1.12	0.10
Ba	40.81	1.03
La	37.01	1.75
Ce	32.77	0.35
Nd	25.13	0.42
Sm	26.12	0.50
Eu	29.20	0.57
Gd	26.42	0.32
Tb	25.91	0.32
Dy	26.69	0.31
Ho	26.75	0.37
Er	26.09	0.40
Tm	25.55	0.33
Yb	27.93	0.35
Lu	26.46	0.39
Hf	26.75	0.35
Ta	30.09	0.39
W	57.43	6.27
Pb	4.32	0.08
Th	13.48	0.16
U	12.55	0.21

The experimental assembly consisted of a boron-nitride (BN) cylinder surrounding the capsule, spacers of MgO above and below the capsule, a graphite furnace and outer sleeves of talc and Pyrex. This assembly requires a friction correction of 10% based on calibrations employing the orthoferrosilite = quartz + fayalite and quartz = coesite reaction curves (Bohlen et al., 1980; Bose and Ganguly, 1995). To prevent mineral growth within the diamond trap during the experiment, it is crucial to place the capsule in the center of the experimental cell where the hotspot is located. No attempt was made to monitor fO_2 , but it is assumed to stay approximately constant and close to the value initially imposed by the Fe^{3+}/Fe^{2+} ratio of the starting material, and no significant gain or loss of H_2 occurred during the experiment. The use of BN around the capsule prevents oxidation due to hydrogen loss on one hand but can result in slightly reducing conditions on the other hand (Truckenbrodt et al., 1997).

Experiments were run in a 600-ton rocking piston cylinder apparatus with 14 mm bore size at ETH Zürich at 3 GPa and temperatures from 700°C to 900°C using the 'hot-piston-in' method. Pressure was kept constant during the runs and is estimated to fluctuate no more than ± 0.02 GPa. Temperature was controlled with a B-type $Pt_{94}Rh_6/Pt_{70}Rh_{30}$ thermocouple with an estimated accuracy of $\pm 10^\circ C$. No corrections for the effect of pressure on the thermocouple (e.m.f.) were made. During heating, the piston cylinder apparatus was constantly turned by 180° , and then every 15 minutes during the experiment to enhance reaction rates and reduce chemical zoning caused by thermal gradients along the capsule (Schmidt and Ulmer, 2004). Experiments were quenched by turning off the power.

5.2.3 Analytical methods

To prevent loss of any fluid-soluble elements, such as potassium (e.g. Stalder et al., 2002), and potential quench crystals entrained in the escaping fluid when opening the experimental charge, we followed the "freezing" approach introduced by Kessel et al. (2004). Before opening, the capsule was mounted into an external freezing stage (Aerts et al., 2010), frozen and then cut open to expose a longitudinal section of the capsule. The capsule stays frozen during the subsequent LA-ICP-MS analyses of the ice plus solute mixture in the interstices of the diamond trap. This approach allows for full quantification of the volatile phase.

5.2.3.1 Internal standard solution

The freezing approach, originally developed by Kessel et al. (2004), is dependent on elements that behave completely incompatible, i.e. partition quantitatively into the volatile phase and not into mineral phases. Such an element is Cesium in K-free systems where

mica is not a stable phase incorporating Cs (among other LILE) in its mineral structure (e.g. Zack et al., 2001). In that case, an internal standard in the form of Cs-doped water with known concentration is added to the experimental system (see Chapter 3 and 4). By knowing the initial H:Cs mass ratio, measured, apparent element concentrations can be recalculated into true values; hence, the absolute concentrations of all elements in the volatile phase, including H₂O, can be quantified (see Kessel et al., 2004, 2005a and 2005b, for details). However, in this study we employed a starting material containing a considerable amount of potassium to ensure detectability of the white mica phengite, which is a common stable phase in a subducting oceanic lithosphere and is, therefore, assumed to be crucial in controlling the LILE budget in subduction zones (Domanik and Holloway, 1996; Schmidt, 1996; Zack et al., 2001; Hermann 2002; Hermann and Rubatto, 2009; Skora and Blundy, 2010). Accordingly, an alternative, incompatible element that could be used as internal standard needed to be found; halogens, such as bromine, behave incompatibly and are thus predicted to partition near-completely into the volatile (e.g. Beyer et al., 2012; Joachim et al., 2014). Analogous to Cs in K-free experiments, Br (in H₂O) was added to the distilled water on a 1000 $\mu\text{g g}^{-1}$ level to ensure proper detection during LA-ICP-MS analysis as Br⁺. The Br-doped water was analyzed by ICP-MS (ThermoFinnigan Element XR) at ETH Zürich to determine the accurate doping concentrations (1181 \pm 15 $\mu\text{g g}^{-1}$ Br, error is 2 standard deviation of 11 measurements).

To test the applicability of Br as an internal standard, we performed an experiment using the potassium-free starting material TB-1 (see Chapter 3 and 4) at 2 GPa and 900°C (SL36). The bulk volatile phase of this experiment was successfully quantified with the employment of Cs as internal standard (SL2); therefore, when using Br instead of Cs under identical experimental conditions, these two experiments allow for direct comparison of the composition of the volatile phase since the resulting phase assemblage was identical. Surprisingly, LA-ICP-MS analysis of the bulk volatile of SL36 reveals a strongly elevated average concentration of ⁷⁹Br of 3500 \pm 800 $\mu\text{g g}^{-1}$, exceeding the doped Br concentration of 1180 $\mu\text{g g}^{-1}$ by a factor of \sim 3. Moreover, analysis of the glass phase in SL36 reveals average values for Br of 156 \pm 60 $\mu\text{g g}^{-1}$, which is about a factor of 10 lower than what was measured in the trap. As the internal standard is crucial in quantifying the hydrous composition of the volatile phase, this issue needs to be evaluated and discussed in detail. Similar to experiment SL36, experiment SL-K-1 (without trap) conducted at 3 GPa and 900°C produced a melt that quenched to a glass, which was analyzed by LA-ICP-MS and used to calculate partition coefficients at these conditions (see below). At identical conditions (3 GPa, 900°C) and starting material, experiment SL-K-2 was performed containing a diamond trap, which was analyzed employing the freezing approach. Again, the glass of SL-K-1 revealed a Br-content of a factor of 10 lower (Br = 320 \pm 80 $\mu\text{g g}^{-1}$) than the trap measurement of SL-K-2 (Br = 3900 \pm 300 $\mu\text{g g}^{-1}$). It turned out that all other trap

measurements in this study returned Br values of the same magnitude as SL36 and SL-K-2, revealing that the deviation is consistent throughout all experiments.

Figure 5.1 depicts a comparison of determined bulk D-values of experiment SL36 and SL2 (Chapter 4). Note that for both experiments, the exact same trace-element doped, K-free starting material was used, but the former contained Br, the latter Cs as internal standard. In order to determine bulk partition coefficients of SL36, we applied a correction factor of 10 as discussed above. Apart from an almost identical trace element pattern for both experiments, calculated water contents (based on internal standards Cs and Br) of the melt are very consistent as well (29.4 wt% and 30.4 wt% water in SL36 and SL2, respectively).

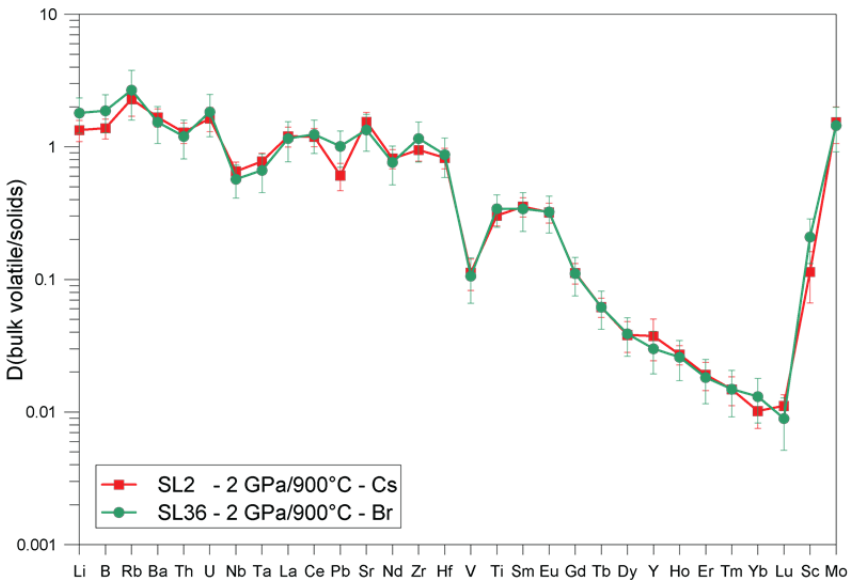


Figure 5.1. D(bulk volatile/solids) of experiment SL36 (this study) using Br as internal standard compared to experiment SL2 (Chapter 4) using Cs as internal standard. Both experiments employed the same K-free, trace element-doped starting material TB1 (Chapter 3 and 4).

These results corroborate our working hypothesis that the use of Br as internal standard for LA-ICP-MS data quantification works in principle and should be applicable to other chemical systems. In this work, we applied a correction factor of 10 for Br in experiments SL-K-3 and SL-K-4 at 3 GPa, 800°C and 700°C, respectively. The resulting trace element bulk-D patterns and D(mineral/volatile) at 3 GPa and 700 to 900°C for a K-rich system are internally consistent.

What exactly the cause is for the observed about one order of magnitude increase of Br in the diamond trap volatile remains obscure (an in-depth examination of potential causes is beyond the scope of this work). Once this problem is solved, we are confident that the use of Br (or I) as internal standard for LA-ICP-MS volatile data quantification will constitute a reliable method for K-rich bulk compositions stabilizing white mica. The results of this study should, therefore, be considered as a first attempt and should be interpreted with caution. Note, however, that the spider diagram patterns remain unaffected by the documented uncertainty in Br volatile concentrations, because element abundance ratios are exclusively calibrated by the use of external standardization only in LA-ICP-MS.

5.2.3.2 LA-ICP-MS

Trace element compositions of the bulk volatile phase were measured with a 193 nm ArF Excimer laser system coupled to an ELAN DRC-e quadrupole mass spectrometer at the University of Bern. Daily optimization routines ensured robust plasma condition, thus minimizing problems related to element fractionation. Depending on the coherence of the diamond trap, 10-20 shots were done per sample with a spot size of 60-90 μm . Two standard reference materials were used as external standard; the scapolite sample, Sca17 (Seo et al., 2011), was employed to calibrate the Br-concentration of the sample, while NIST-SRM-610 was used for all other elements. Both external standards were measured twice before and after one series of analyses. Background was measured for 40 seconds, ablation intervals were in the range of 20-40 seconds at 6-10 Hz repetition rate. For the analyses of the crystalline residual phases and melt pools, the laser spot size was adapted to the size of the different crystals in the range of 4 μm (for the very small phases, e.g. rutile) to 24 μm (e.g. garnet) at 5-10 Hz repetition rate, background was measured for 30 seconds. A strong increase in the counts of mineral-incompatible elements was taken as indicator for having drilled through the crystal and provided a decisive criterion to set integration intervals accordingly. Data reduction was done using the software SILLS (Guillong et al., 2008). CaO, Al₂O₃ or TiO₂ concentrations, previously determined by electron microprobe, were used as internal standards for quantification. Stringent, IUPAC-recommended procedures to calculate the limits of detection (LOD) for low-intensity analyte signals returns significant element concentrations calculated for each element in every analysis at 95% confidence (Pettke et al., 2012).

5.2.3.3 Electron probe micro-analysis (EPMA)

Polished and carbon-coated run products (minerals and glass) were analyzed with wavelength-dispersive spectrometers (WDS) on a JEOL JXA-8200 electron probe micro-

analyzer at ETH Zürich. Analyses were performed with an acceleration voltage of 15 kV and counting times of 40 seconds on peak and 20 seconds on the backgrounds. Beam current and beam size varied for minerals and glasses; 20 nA and focused beam were used for minerals, glasses were analyzed with 5 nA and defocused beam in order to minimize alkali migration losses.

5.3 Results

5.3.1 Phase relations

Experimental conditions, phase assemblages and their modal proportions are summarized in **Table 5.3**. Modal proportions were determined by least-squares regression based on the recalculated hydrous major element composition. The eclogitic mineral assemblage at 3 GPa at 700 and 800°C consists of garnet, phengite, clinopyroxene (cpx) and accessory rutile. Staurolite is additionally present at 700°C. Furthermore, mass balance calculations and bulk-D trace element patterns (see below) at 700 and 800°C reveal that a LREE- and Th-rich phase, most probably an epidote-group mineral, likely was present. Unfortunately, we were not able to detect this phase, probably due to very small crystal sizes and/or low abundances. At 900°C, cpx is no longer stable and disappears from the residue. Selected BSE-images of the experimental charges are provided in **Figure 5.2**. In the experiments at 700 and 800°C all phases are uniformly fine grained (2-30 µm) except for some larger euhedral garnets (50 µm). Phengite appears mostly as fine, elongated sheets, up to 30 µm long and only a few µm thick at 800°C. Clinopyroxene grew as large as garnet but with a very patchy appearance, due to the coexistence of two chemically distinct compositions at 800°C, which is interpreted to result from an intersection with a (metastable) solvus in the diopside-jadeite systems. At 700°C all phases are only 10-20 µm in size. Glass (quenched melt) is observed in the 800 and 900°C experiment² only. At 800°C very little glass could be detected while at 900°C, it is homogeneously distributed between the solid phases and contains micro-vesicles (up to 2 µm). Vesicles are a common feature in water-rich experiments when the amount of water during run conditions exceeds the amount that can be quenched into a glass at its glass transition temperature (e.g. Klimm et al., 2008). Garnets tend to be larger at 900°C (~80 µm) as well as phengite, that often appears as sheets (~75 and 25 µm thickness); clinopyroxene is molten out at these conditions. Rutile occurs in all runs, its size increases with increasing temperature (1-10 µm).

Table 5.3. Run table

Run No.	Pressure [GPa]	Temp. [°C]	Duration [h]		H ₂ O _{in} ^a [wt%]	cH ₂ O ^b [wt%]	Phase assemblage	Phase proportions ^c [wt%]	ΣR ² ^d
			diamond trap	no trap					
SL-K-1	3	900		136	10.8	N.D.	liq, grt, phe, rut	39.8 (2.0), 30.8 (2.6), 28.4 (2.8), 1.0 (0.6)	1.35
SL-K-2	3	900	141		10.6	27.6	liq, grt, phe, rut	36.2 (2.2), 33.0 (3.0), 29.6 (3.1), 1.2 (0.7)	1.63
SL-K-3	3	800	166		10.4	39.6	liq, grt, phe, cpx, rut	21.2 (3.0), 23.3 (5.9), 44.8 (4.4), 10.1 (5.8), 0.6 (1.2)	3.57
SL-K-4	3	700	165		8.4	39-45 ^e	liq, grt, phe, cpx, stau, rut	18.3 (4.7), 11.4 (8.5), 37.9 (11.0), 23.5 (10.3), 7.2 (6.6)	3.32
SL36	2	900		70	10.7	31.0	liq, grt, cpx, rut	N.D.	N.D.

^a Water loaded in the capsule.

^b Water content of the fluid determined by dividing measured Br in the fluid divided by added Br to the starting material.

^c Modal phase abundances calculated by least squares mass balance. Numbers in paratheses indicate absolute one standard deviation.

^d Sum of residual squares obtained by mass-balance calculations.

^e minimal to maximal values, see text for explanation.

N.D. = Not determined

liq, liquid phase; grt, garnet; phe, phengite; cpx, clinopyroxene; stau, staurolite; rut, rutile; tr, trace amounts.

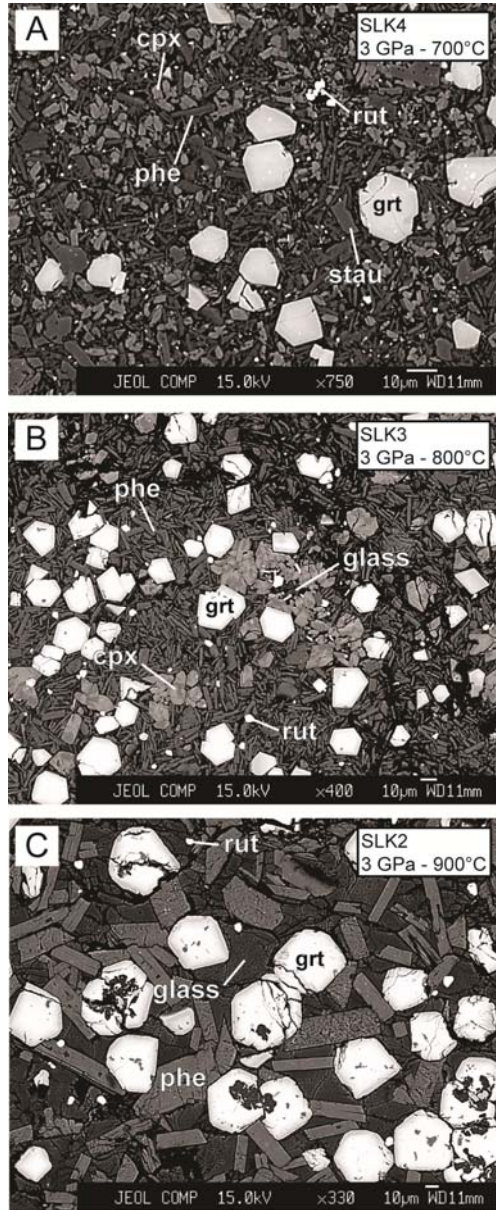


Figure 5.2. Backscattered electron images of representative run products at 3 GPa and 700 to 900°C. (A): subsolidus phase assemblage at 700°C with garnet, clinopyroxene, phengite, staurolite and rutile. (B) and (C): phase assemblage at suprasolidus conditions at 800 and 900°C with garnet, clinopyroxene, phengite, rutile and glass (B). Note that at 800°C two clinopyroxene compositions exist, representing intersection with a (metastable) solvus. At 900°C (C) clinopyroxene is no longer part of the phase assemblage.

5.3.2 Water content of the volatile phase

In order to calculate the water content of the volatile phase and based on that, to recalculate apparent element volatile concentrations into true values, the use of an appropriate internal standard is essential (see above). While the approach using Cs as standard is well established (Kessel et al., 2005a; 2005b; Chapters 3 and 4), employment of Br in systems containing potassium still needs further investigation, as described above. **Figure 5.3** shows the calculated water content of the volatile phase from 700 to 900°C. Water contents at same P-T conditions obtained in the K-free system (Chapter 4) are plotted for comparison. Generally, water contents in this study are slightly lower but reveal the same decreasing trend with increasing temperature even though the value at 700°C (23 wt% H₂O), based on measured Br content in the trap, does not follow this trend. This run is located below the water-saturated solidus (see discussion below); we would expect water contents in the range between minimum 39 wt% and maximum 45 wt% according to the data obtained in both studies; hence, we suspect that the water concentration of the volatile phase in this experiment is wrong. Therefore, we recalculated maximal and minimal hydrous trace element compositions of the volatile phase based on 39 and 45 wt% H₂O, respectively (**Table 5.4**). Accordingly, bulk-D partition coefficients (**Figure 5.11 and Table 5.7**) are calculated based on the hydrous data. It turns out, however, that the deviations relative to expected maximal and minimal volatile water concentrations are small; hence, the pattern based on 23 wt% H₂O (originally calculated based on measured Br in the trap) is shown only.

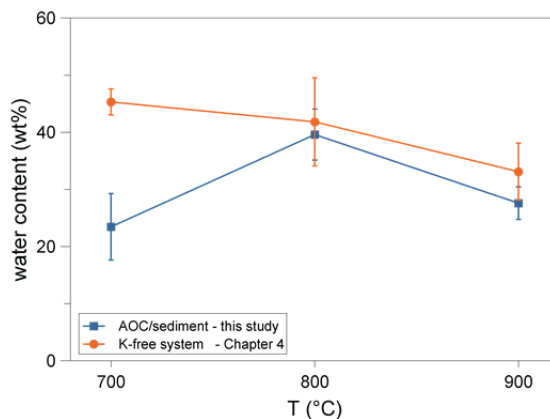


Figure 5.3. Water content of the volatile phase based on LA-ICP-MS analyses of the diamond trap and calculated with using Br as internal standard plotted against temperature (squares). For comparison, determined water contents in the K-free MORB system at same P-T conditions are shown (circles). Error bars are 1 SD based on Br and Cs analyses of the trap.

CHAPTER 5

Table 5.4. Anhydrous and hydrous liquid major element composition at 3 GPa.

T (°C)	700		700		800		900	
Run	SLK4	1 σ	SLK4	1 σ	SLK3	1 σ	SLK2	1 σ
# analyses	10		10		17		15	
Anhydrous (normalized to 100 wt%)								
SiO ₂	71.84	(0.67) ^a			72.53	(0.90)	68.29	(0.67)
Na ₂ O	15.87	(1.08)			8.79	(0.92)	4.63	(0.19)
CaO	0.28	(0.07)			0.99	(0.32)	1.90	(0.12)
FeO ^b	0.77	(0.05)			1.62	(0.27)	0.81	(0.12)
Al ₂ O ₃	1.20	(0.35)			8.58	(1.31)	18.09	(0.22)
MgO	0.24	(0.07)			0.88	(0.07)	0.64	(0.10)
TiO ₂	0.12	(0.02)			0.25	(0.02)	0.41	(0.02)
K ₂ O	9.69	(0.80)			6.36	(0.69)	5.23	(0.21)
Hydrous (normalized to 100 wt% with H ₂ O)								
	minimal H ₂ O ^e		maximal H ₂ O ^e					
SiO ₂	43.99	0.77	39.66	0.69	43.79	(0.53)	48.97	(0.93)
Na ₂ O	9.59	0.72	8.65	0.65	5.31	(0.54)	4.79	(0.89)
CaO	0.16	0.05	0.14	0.04	0.60	(0.19)	1.00	(0.20)
FeO	0.52	0.08	0.47	0.07	0.98	(0.16)	1.35	(0.37)
Al ₂ O ₃	0.90	0.36	0.81	0.32	5.18	(0.77)	10.71	(2.10)
MgO	0.17	0.05	0.15	0.04	0.53	(0.04)	0.61	(0.21)
TiO ₂	0.08	0.02	0.07	0.02	0.15	(0.01)	0.25	(0.05)
K ₂ O	5.59	0.79	5.04	0.71	3.84	(0.41)	4.73	(0.69)
H ₂ O	39.00		45.00		39.62		27.59	
P.I. ^c	24.15		24.15		2.49		0.67	
Al.I. ^d	0.04		0.04		0.37		1.05	

^a Numbers in parentheses indicate absolute standard deviation of the distribution of average compositions.

^b All Fe reported as FeO.

^c Peralkalinity index reported as Na₂O/Al₂O₃ molar.

^d Alumina index reported as Al₂O₃/(Na₂O+CaO).

^e See text for explanation.

5.3.3 Major element composition

5.3.3.1 Bulk volatile phase

The anhydrous major element composition of the bulk volatile phase, based on the LA-ICP-MS analyses of the trap, is shown as a function of temperature in **Figure 5.4**. The composition of the volatile phase is a strong function of the residual mineral assemblage.

Since it remains constant except for the disappearance of cpx at 900°C, the evolution of the composition of the volatile is continuous, and most elements show well-defined trends. With increasing temperature SiO₂ decreases slightly while Al₂O₃ increases strongly from 1 wt% to almost 15 wt%. The alkalis, Na₂O and K₂O, decrease at higher temperatures, which is in good agreement with higher solubility in aqueous fluids compared to higher-T hydrous melts (e.g. Green and Adam, 2003; Chapter 4). FeO, MgO, CaO and TiO₂ contents are low (< 2 wt% at all temperatures) and all show systematic increase with increasing temperature. The increase of Fe, Mg and Ca is a consequence of the gradual consumption of clinopyroxene and garnet during melting until the former disappears between 800°C and 900°C. Titanium is primarily controlled by residual rutile. Even though rutile is stable at all temperatures in this study, TiO₂ increases from 700°C to 900°C due to enhanced solubility at higher temperatures (e.g., Antignano and Manning, 2008, and references therein). Volatiles are extremely peralkaline at 700°C and evolve towards metaluminous to peraluminous compositions at 900°C, approaching the initial bulk compositions which itself is peraluminous in composition (**Figure 5.5**). The calculated aluminum saturation index (ASI, Al₂O₃/CaO+Na₂O) reveals values of 0.06 to 1.1 from 700 to 900°C and calculated peralkaline index (PI, Na₂O /Al₂O₃) from 17.5 to 0.74 within the same temperature range.

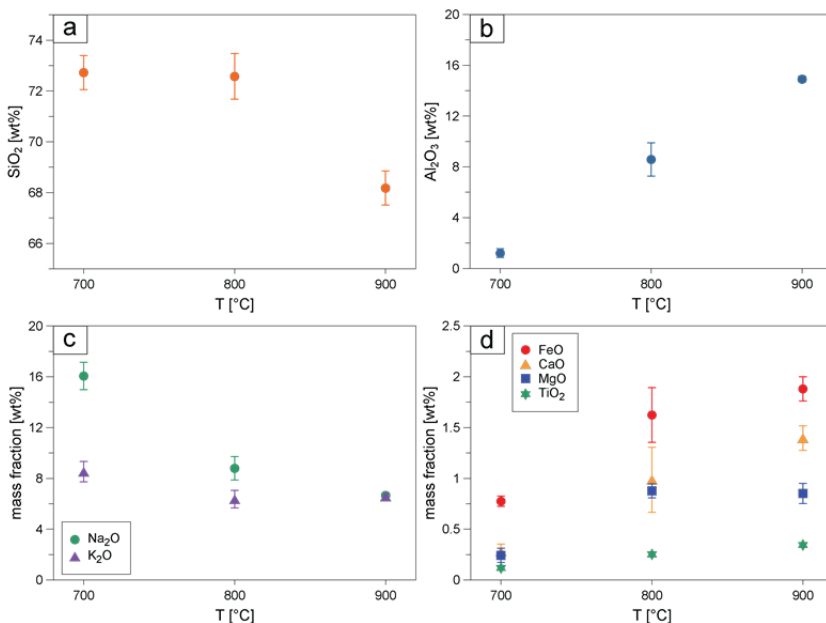


Figure 5.4. Concentrations of major oxides of the bulk volatile phase based on LA-ICP-MS analyses of the diamond trap (normalized anhydrous to 100 wt%) as a function of temperature. (a) SiO₂; (b) Al₂O₃; (c) K₂O and Na₂O; (d) FeO, MgO, CaO and TiO₂.

Only the chemical composition of the volatile phase allows drawing conclusions about the nature (aqueous fluids or hydrous melts) of the volatile phase since textural characterization of the glass (quenched melt) or other solutes, resulting from quenching an aqueous fluid, is not possible when using the diamond trapping technique (see also Chapter 4). Based on the results shown in **Figure 5.5** and **Figure 5.13**, we conclude that at 700°C an aqueous fluid (highly peralkaline, high $\text{SiO}_2/\text{Al}_2\text{O}_3$ and $\text{Na}_2\text{O}/\text{Al}_2\text{O}_3$ ratios) is stable. At 800°C, where we calculated a water content of almost 40 wt% in the volatile phase, it has to be assumed that a mixed bulk volatile phase exists, composed of fluids and hydrous melts. At these conditions we clearly observe a melt (glass) but a melt phase at 3 GPa is expected to incorporate less than 35 wt% of water, therefore, it has to be concluded that additionally a very water-rich fluid is stable at the same time. At 900°C (with <30 wt% of water in the volatile phase) we assume a hydrous melt being stable exclusively. These results are in very good agreement with the results obtained in the K-free MORB-system at same P-T conditions (Chapter 4).

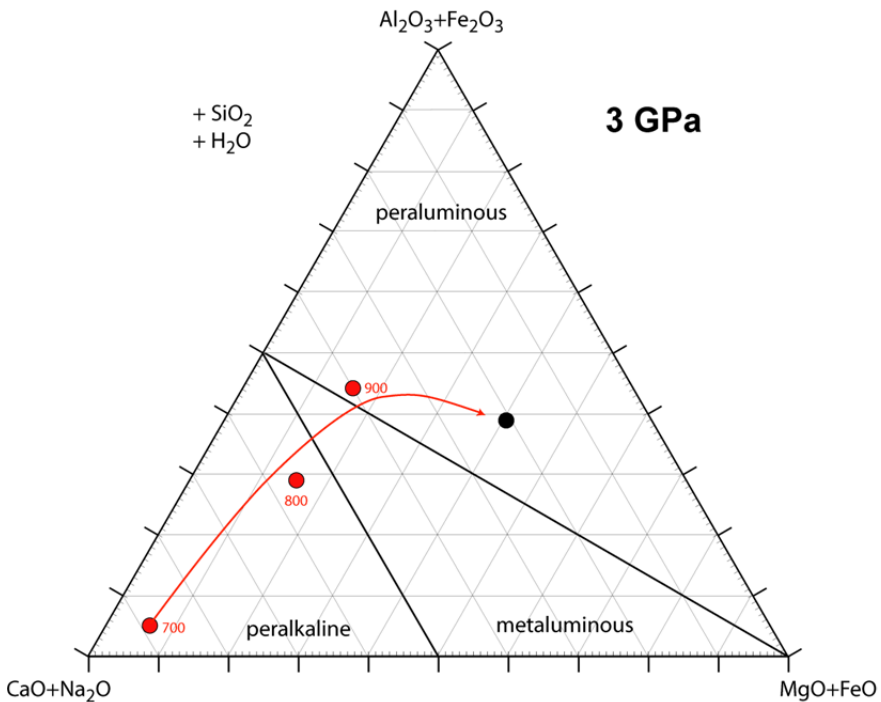


Figure 5.5. Bulk volatile compositions as a function of temperature in a ternary ACF diagram (molar $\text{Al}_2\text{O}_3 + \text{Fe}_2\text{O}_3 - \text{CaO} + \text{Na}_2\text{O} - \text{FeO} + \text{MgO}$) projected from SiO_2 and H_2O at 3 GPa. Numbers adjacent to the symbols indicate the temperature. Black circle represents the bulk composition.

5.3.3.2 Garnet

Garnet is present at all investigated temperatures; it is often inclusion-rich (mainly rutile and cpx) and zoned with increasing Mg and decreasing Fe and Ti from core to rim. Average compositions are presented in **Table 5.5**. For mass balance calculations we used the average composition of the entire garnet grains.

With increasing temperature, garnet composition changes systematically; the pyrope and grossular component increase with increasing temperature in the interval 700 to 900° from 18 to 27 mole% and 25 to 32 mole%, respectively. In contrast, the almandine component decreases from 47 to 34 mole% within the same temperature range. Mg-numbers ($\text{Mg}/(\text{Mg}+\text{Fe}^{2+})$) increase continuously from 0.26 at 700°C to 0.45 at 900°C. As an effect of increasing temperature, TiO_2 content of garnets increases from 0.8-1.6 wt%. Comparison of garnet data of the experiments in a K-free system (see Chapter 4) with those obtained in this study reveals very similar compositions for both sets of experiments.

5.3.3.3 Clinopyroxene

Clinopyroxenes analyses were normalized to 4 cations and 12 positive charges, average compositions are listed in **Table 5.5**. They are omphacitic at both temperatures and relatively Al-rich (12-13 wt% Al_2O_3), and tend to decrease in Al from 700 to 800°C whereas Mg and Ti increase. Similar to garnet, cpx shows increasing Mg-numbers with increasing temperature from 0.62 to 0.88. As mentioned above, at 800°C two compositionally different cpx are present. Cpx I displays lower Si (52.5 wt%), Na (4.5 wt%) and higher Fe^{2+} (6.4 wt%) and Ti (0.77 wt%) compared to cpx II (Si: 54.2 wt%, Na: 5.5 wt%, Fe^{2+} : 2.4 wt% and Ti: 0.29 wt%). In general, clinopyroxene exhibit a dominant jadeite component (32-39 wt%), moderate enstatite component (19-26 wt%) and a small eskolaite component of 4-10 wt%. The Ca-Tschermak's content is very low with 2.4-3.6 wt%.

5.3.3.4 Phengite

EPMA analyses (average compositions are given in **Table 5.5**) of phengite were normalized to 11 oxygen atoms ($10\text{O}^{2-} + 2\text{OH}^-$ per formula unit). Following the argumentation of Auzanneau et al. (2006), Fe^{3+} was fixed to 50% of the total iron. **Figure 5.6** shows the systematic compositional change of phengite with temperature. From 700 to 900°C Si (p.f.u.) decreases whereas the Al-, Mg- and K-content (p.f.u.) increases with increasing temperature. Titanium increases from 0.02 to 0.08 within the same temperature range and in equilibrium with rutile. The paragonite component in phengite is generally low, with Na-contents (p.f.u.) of 0.04 to 0.07. These compositional trends are generally in good agreement with other studies (e.g. Hermann and Spandler, 2008; Skora and Blundy, 2010).

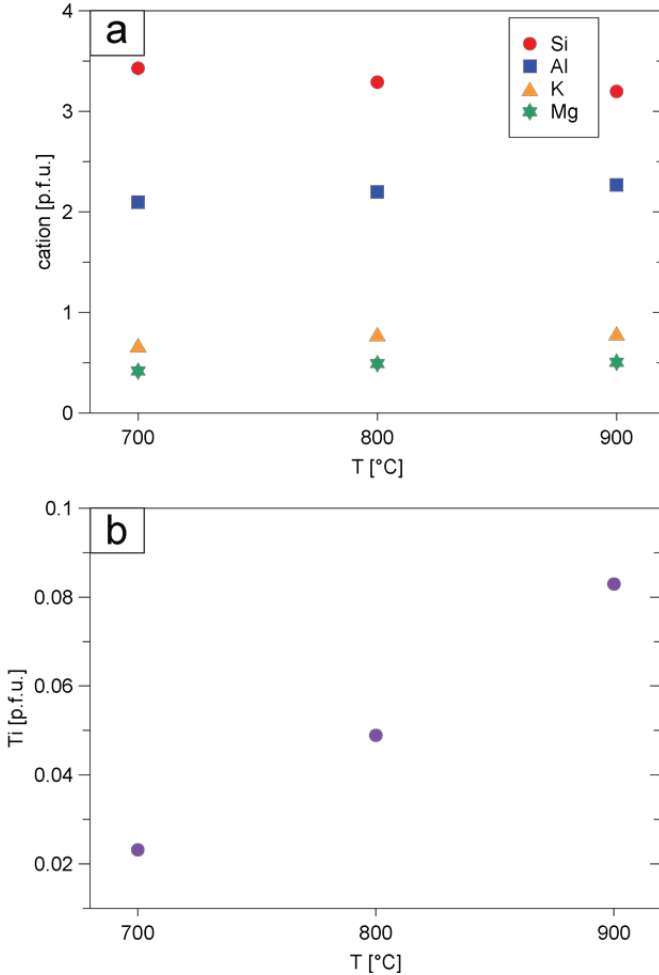


Figure 5.6. Si, Al, Mg and K (a) and Ti (b) (a.p.f.u.) in phengite as a function of temperature.

5.3.3.5 Minor minerals

Rutile is the dominant Ti-phase controlling the Ti-budget in our experiments. It additionally contains minor amounts of Al_2O_3 (1-1.5 wt%) and $Fe^{3+}_2O_3$ (0.7-1.5 wt%).

Staurolite occurs in the 700°C run and exhibits a considerable amount of FeO with around 9 wt% and a Ti-content of 0.7 wt%; it has a Mg-number of 0.46. The presence of staurolite at these conditions and starting material is not surprising and was observed in other studies similar to this (e.g. Klimm et al., 2008; Skora and Blundy, 2010, Chapter 4).

Table 5.5. Average major element composition of the run products in wt%.

Run	Phase	n	SiO ₂	1σ	Na ₂ O	1σ	CaO	1σ	FeO	1σ	Al ₂ O ₃	1σ	MgO	1σ	TiO ₂	1σ	K ₂ O	1σ	Total
SLK4	grt	12	37.06	(0.83) ^a	0.05	(0.02)	9.69	(0.52)	24.90	(1.22)	21.28	(0.32)	5.01	(0.93)	0.76	(0.17)	0.04	(0.01)	98.79
	cpx	15	53.77	(0.86)	5.40	(0.27)	12.25	(1.20)	7.57	(0.40)	13.27	(1.12)	6.98	(0.73)	0.52	(0.23)	0.24	(0.31)	100.00
	phe	8	51.00	(0.68)	0.33	(0.05)	0.05	(0.01)	2.45	(0.19)	26.45	(0.47)	4.16	(0.10)	0.46	(0.06)	7.88	(0.58)	92.77
	rut	1	1.45	-	0.07	-	0.37	-	1.58	-	1.03	-	0.37	-	93.14	-	0.13	-	98.12
	stau	4	30.47	(0.20)	0.02	(0.00)	0.04	(0.01)	9.34	(0.13)	55.03	(0.54)	4.45	(0.19)	0.73	(0.16)	0.07	(0.02)	100.14
SLK3	grt	14	38.38	(0.77)	0.08	(0.02)	11.02	(0.29)	21.51	(1.00)	21.35	(0.35)	6.26	(0.68)	1.30	(0.16)	0.04	(0.01)	99.92
	cpx I	28	52.48	(0.74)	4.48	(0.21)	13.73	(1.18)	6.43	(0.62)	12.54	(0.43)	8.33	(0.47)	0.77	(0.30)	0.05	(0.02)	98.81
	cpx II	7	54.21	(1.12)	5.54	(0.43)	14.39	(0.50)	2.42	(0.35)	12.21	(0.49)	9.54	(0.33)	0.29	(0.11)	0.05	(0.01)	98.65
	phe	10	48.85	(0.67)	0.57	(0.08)	0.03	(0.03)	1.43	(0.40)	27.70	(0.50)	4.89	(0.62)	0.97	(0.19)	9.14	(0.25)	93.57
	rut	12	0.23	(0.28)	0.02	(0.02)	0.13	(0.05)	0.84	(0.07)	1.21	(0.20)	0.03	(0.01)	95.62	(0.32)	0.17	(0.03)	98.26
	SLK2	grt	7	39.17	(0.47)	0.12	(0.02)	12.76	(0.60)	17.46	(1.56)	21.70	(0.69)	7.86	(1.16)	1.61	(0.26)	0.02	(0.01)
phe	21	47.17	(0.76)	0.34	(0.03)	0.04	(0.04)	1.51	(0.12)	28.40	(0.52)	5.01	(0.51)	1.63	(0.18)	9.16	(0.23)	93.25	
rut	13	0.14	(0.03)	0.03	(0.02)	0.10	(0.06)	0.72	(0.05)	1.47	(0.03)	0.05	(0.01)	96.77	(0.43)	0.15	(0.03)	99.42	

^a Numbers in parentheses indicate absolute standard deviation of the distribution of average compositions. Abbreviations as in Table 3.

5.3.4 Trace element partitioning

5.3.4.1 Garnet

As for major elements, garnets are suspected to show zoning in trace elements too, most likely due to slow intracrystalline diffusion rates (e.g. Orman et al., 2002). We were, however, not able to analyze rim compositions only (due to their small size); therefore, our analyses are supposedly contaminated by elements enriched in the core. This results in relatively large errors for LREE and HREE, which are the elements mostly accounting for zoning in garnets.

Garnet-volatile partition coefficients are given in **Figure 5.7** and **Table 5.6**. Generally, the trace element pattern is characterized by a steep fractionation of the LREE to HREE with the latter showing values of >1000 for the lowest temperature runs. This is in good agreement with results from high-pressure studies employing similar water-saturated bulk compositions (Green and Adam, 2003; Kessel et al., 2005a; Klimm et al., 2008; Skora and Blundy, 2010; Chapter 4). Our results reveal $D_{La}^{grt/volatile} > D_{Ce}^{grt/volatile}$ which is contrary to what is determined for garnet in the above mentioned studies and also in Chapter 4 (Figure 4.8). We conclude that this results from matrix contamination resulting in too high values for incompatible La.

For REE, but also for most other elements, partition coefficients are strongly influenced by temperature; D-values typically decrease with increasing temperature, consistent with the findings of Van Westrenen et al. (2001) and Kessel et al. (2005a).

The HFSE (Hf, Zr, Nb, and Ta) partitioning reveals identical temperature dependence as REE but generally less internal fractionation. Niobium and Tantalum plot around 1 or slightly lower, while Zr and Hf reveal values between 1 and 10 (~60 at 700°C). D_{Zr}/D_{Hf} result a weighted mean value of 1.55 ± 0.15 . Van Westrenen et al. (2001) have shown that the D_{Zr}/D_{Hf} ratio correlates positively with the grossular content in garnets. Compared with $D_{Zr}/D_{Hf} = 1.3 \pm 0.19$ determined for garnets at the same pressure in Chapter 4, this is in good agreement based on the slightly lower grossular content of the latter. Literature results at identical pressure conditions are consistent with our findings; in anhydrous MORB systems, Pertermann et al. (2004) found $D_{Zr}/D_{Hf} \sim 1.25$ at 24 mol% grossular contents, Klemme et al. (2002) obtained $D_{Zr}/D_{Hf} = 1.29$ for garnet at 3 GPa and 1400°. D_{Nb} is slightly lower than D_{Ta} but fractionation is insignificant in our data, which results in a weighted mean of $D_{Nb}/D_{Ta} = 0.95 \pm 0.17$. The high value from this study compared to $D_{Nb}/D_{Ta} = 0.72$ (Klimm et al., 2008) or 0.22 (Green and Adam, 2003) might be a consequence of the higher polymerization of the volatile phase in this study as suggested by e.g. Schmidt et al. (2004b).

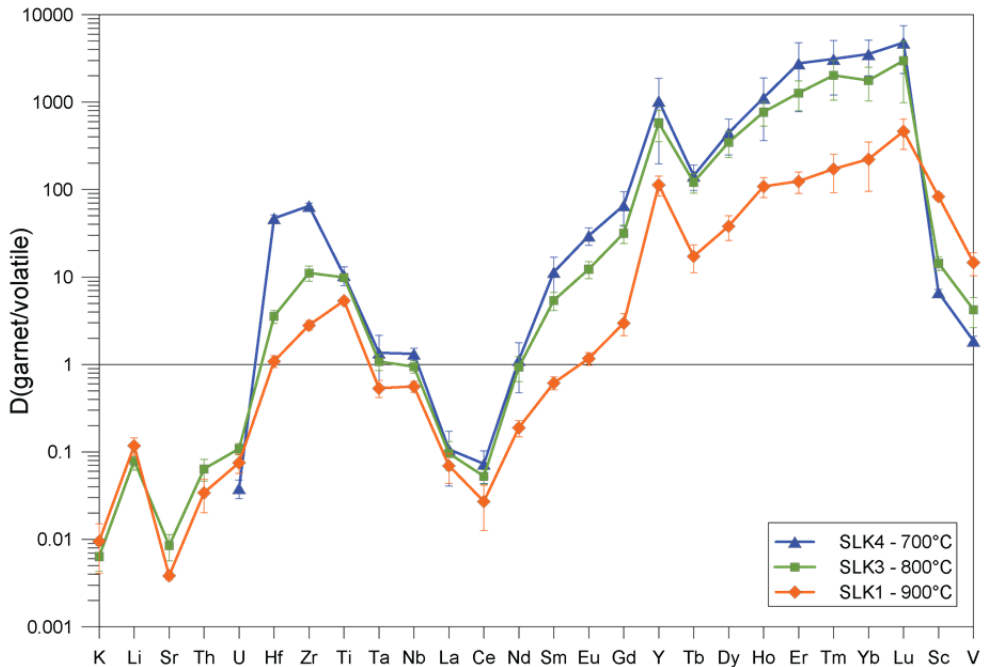


Figure 5.7. Garnet-volatile (fluid at 700°C, mixed phase at 800°C and melt at 900°C) partition coefficients at 3 GPa and 700 to 900°C. For discussion see text. Error bars are 1 SD.

They have shown that $D_{\text{Nb}}/D_{\text{Ta}}$ increase with increasing Si-content in the melt. D_{Th} and D_{U} are less well constrained by our results but suggest strongly incompatible behavior of U with values between 0.03 and 0.1. Lithium and Sr reveal consistently low values between 0.004-0.1; most LILE (e.g. Cs, Rb, and Ba) were below LOD (limit of detection); hence, partition coefficients could not be determined.

5.3.4.2 Phengite

Phengite LA-ICP-MS analyses were challenging due to small mineral thickness especially at 700°C, but data show relatively consistent patterns even though some contamination with matrix cannot be excluded. D-values are plotted in **Figure 5.8a** and values given in **Table 5.6**. We were able to determine LILE (Cs, Rb, K, Ba, Sr and Li) and at 800 and 900°C HFSE (Nb, Ta, Hf and Zr) as well as Mo, Th, U, La and Ce. Note that Rb at 700°C and Cs at 700 and 800°C were below LOD and D-values, therefore, have to be considered as maximum values.

As expected from natural samples (e.g. Zack et al., 2001), phengite is the major host for LILE and shows strongest enrichment in Ba with D_{Ba} of up to 24 at 700°C. Generally, partitioning behavior for LILE can be summarized as follows: $D_{Ba} > D_K > D_{Rb} > D_{Li} > D_{Cs} > D_{Sr}$ while only Rb, K and Ba are compatible in phengite and plot between 1 and 24. Rb fractionates from Cs with a weighted mean value of 5.3 ± 0.1 . The HFSE, REE, Th and U generally plot below 1 with the HFSE being the most compatible of them at 800°C with values around 1 or slightly higher. Fractionation behavior of HFSE at 800 and 900°C is consistent and reveals $D_{Hf} > D_{Zr}$ and $D_{Nb} > D_{Ta}$. D-values for all elements show temperature dependence and decrease with increasing temperature.

In the following, results from this study are compared with previously published data for phengite trace element partitioning. To our knowledge, only few studies have determined partition coefficients up to date, their results are shown in **Figure 5.8b**. Melzer and Wunder (2000) performed exchange experiments at 2 GPa/600°C and 4 GPa/700°C in order to calculate K_D - and D-values for Rb and Cs in equilibrium with an aqueous fluid. Green and Adam (2003) measured partition coefficients for phengite in equilibrium with aqueous fluid at 3 GPa and 650 to 700°C. Finally, Green et al. (2000) presented phlogopite/basanite coefficients at 3 GPa/1200°C, which can be compared to phengite data as LILE substitute for potassium on the same lattice site. Our results are generally in good agreement with literature data. D_{Rb} and D_{Cs} of Melzer and Wunder (2000) are in the range of our results and display the same fractionation behavior defining Cs to be incompatible in equilibrium with aqueous fluids. Even though at higher temperature (1200°C) D-values of Green et al. (2000) for Ba and Sr match our determined D_{Ba} and D_{Sr} extremely well in terms of absolute values and fractionation. Results of Green and Adam (2003) differ slightly from all these studies, including ours, in that their D-values plot around one magnitude higher for all elements. It has to be noted though, that their measurements resulted in partition coefficient pattern between phengite and aqueous fluid and not absolute values; they determined D-values by measuring phengite and the quench solutes in their experimental charge. Assuming that LILE are extremely soluble in water, it could well be that by releasing the water from the capsule after the experiment, a significant fraction was lost and is lacking from the fluid composition (compare Stalder et al., 2002). Thus, D-values of Green and Adam (2003) might be overestimated. Nevertheless, their trace element pattern for LILE is in line with the results from the other mentioned studies.

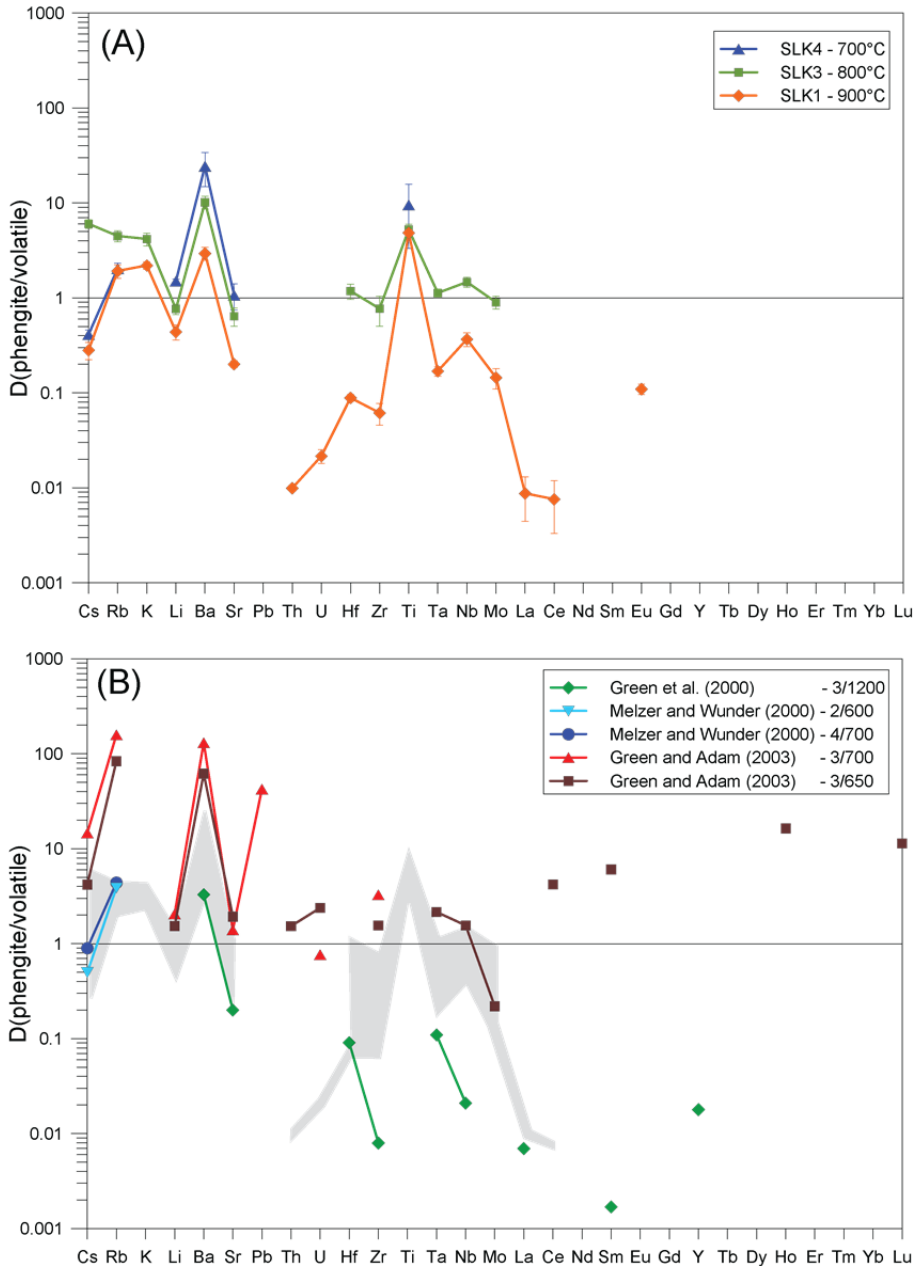


Figure 5.8. (A) Phengite-volatile (fluid at 700°C, mixed phase at 800°C and melt at 900°C) partition coefficients at 3 GPa and 700 to 900°C. Error bars are 1 SD. (B) Phengite-fluid partition coefficients from experiments of Green et al. (2000); Melzer and Wunder (2000); Green and Adam (2003) are plotted for comparison with the results from this study (grey shaded area).

Table 5.6. Mineral-volatile partition coefficients of garnet, phengite, rutile and clinopyroxene in ppm.

Phase	Garnet				Phengite				Rutile				Clinopyroxene			
	Run	T (°C)	700 SLK4 D(gf/lig)	800 SLK3 D(gf/lig)	900 SLK1 D(gf/lig)	700 SLK4 D(pha/lig)	800 SLK3 D(pha/lig)	900 SLK1 D(pha/lig)	800 SLK3 D(rut/lig)	900 SLK2 D(rut/lig)	800 SLK3 D(cpx/lig)	900 SLK3 D(cpx/lig)	Error	800 SLK3 D(cpx/lig)	Error	
Cs			B.D. ^b	B.D.	B.D.	0.41	6.02	0.28	(0.06)	N.D.	N.D.	N.D.	N.D.	N.D.		
Rb			B.D.	B.D.	B.D.	2.04	4.48	1.92	(0.31)	N.D.	N.D.	N.D.	N.D.	N.D.		
K			B.D.	B.D.	B.D.	(1.24)	(0.12)	4.18	(0.64)	2.20	(0.20)	N.D.	N.D.	(0.008)		
Li			0.05	(0.01)	0.12	1.50	(0.08)	0.76	(0.10)	0.44	(0.08)	N.D.	N.D.	(0.19)		
Ba			B.D.	B.D.	B.D.	24.42	(9.61)	10.17	(1.58)	2.94	(0.46)	N.D.	N.D.	B.D.		
Sr			0.02	(0.01)	0.04	1.07	(0.33)	0.64	(0.14)	0.20	(0.02)	N.D.	N.D.	(0.03)		
Pb			B.D.	B.D.	B.D.	N.D.	N.D.	N.D.	N.D.	N.D.	N.D.	N.D.	N.D.	N.D.		
Th			B.D.	0.06	(0.02)	B.D.	B.D.	B.D.	(0.001)	B.D.	B.D.	N.D.	N.D.	(0.15)		
U			0.04	(0.01)	0.11	(0.02)	0.08	(0.02)	(0.004)	N.D.	N.D.	N.D.	N.D.	(0.002)		
Hf			46.97	(4.15)	3.56	(0.60)	1.09	(0.17)	B.D.	1.18	(0.22)	0.09	(0.01)	24.98		
Zr			65.13	(4.88)	11.16	(2.20)	2.82	(0.35)	B.D.	0.77	(0.27)	0.06	(0.02)	5.60		
Ti			10.51	(2.56)	9.90	(0.93)	5.37	(0.46)	9.54	(6.22)	5.25	(0.73)	4.85	(0.38)		
Ta			1.36	(0.79)	1.08	(0.23)	0.54	(0.12)	B.D.	1.13	(0.11)	0.17	(0.02)	692.06		
Nb			1.32	(0.21)	0.95	(0.15)	0.56	(0.08)	B.D.	1.47	(0.18)	0.37	(0.06)	309.26		
Mo			N.D. ^c	N.D.	N.D.	N.D.	N.D.	N.D.	(0.03)	0.90	(0.14)	0.15	(0.03)	N.D.		
La			0.11	(0.07)	0.10	(0.03)	0.07	(0.03)	B.D.	B.D.	B.D.	0.01	(0.004)	N.D.		
Ce			0.07	(0.03)	0.05	(0.01)	0.03	(0.01)	B.D.	B.D.	B.D.	0.01	(0.004)	N.D.		
Nd			1.12	(0.65)	0.94	(0.30)	0.19	(0.04)	B.D.	B.D.	B.D.	B.D.	B.D.	0.23		
Sm			11.39	(5.49)	5.42	(1.28)	0.62	(0.10)	B.D.	B.D.	B.D.	B.D.	B.D.	0.23		
Eu			29.75	(6.80)	12.31	(2.71)	1.17	(0.19)	B.D.	B.D.	B.D.	0.11	(0.01)	0.82		
Gd			66.24	(28.07)	31.77	(7.62)	2.98	(0.85)	B.D.	B.D.	B.D.	B.D.	B.D.	1.43		
Y			1032	836	579	226	114	29	(0.85)	B.D.	B.D.	B.D.	B.D.	0.89		
Tb			144	47	122	31	17	6	(0.85)	B.D.	B.D.	B.D.	B.D.	2.83		
Dy			446	197	348	114	38	12	(0.85)	B.D.	B.D.	B.D.	B.D.	20.32		
Ho			1124	761	771	239	109	28	(0.85)	B.D.	B.D.	B.D.	B.D.	4.09		
Er			2773	1998	1273	475	125	34	(0.85)	B.D.	B.D.	B.D.	B.D.	12.42		
Tm			3124	1920	2026	970	172	81	(0.85)	B.D.	B.D.	B.D.	B.D.	16.68		
Yb			3548	1542	1774	743	223	127	(0.85)	B.D.	B.D.	B.D.	B.D.	16.68		
Lu			4802	2680	2986	1998	465	176	(0.85)	B.D.	B.D.	B.D.	B.D.	33.04		
Sc			6.67	(0.55)	14.43	(2.55)	83.65	(8.26)	N.D.	N.D.	N.D.	2.59	(0.96)	26.66		
V			1.86	(0.24)	4.25	(1.61)	14.70	(4.34)	4.65	(1.25)	15.98	(6.96)	(12.05)	36.91		
B			N.D.	N.D.	N.D.	N.D.	N.D.	N.D.	0.36	(0.03)	B.D.	B.D.	B.D.	29.49		
W			N.D.	N.D.	N.D.	N.D.	N.D.	N.D.	N.D.	N.D.	N.D.	N.D.	N.D.	5.67		
														10.19		
														4.12		
														B.D.		
														0.03		

^a Errors represent 1σ uncertainties, calculated as a standard deviation.

^b B.D. = below detection limit

^c N.D. = no data.

5.3.4.3 Rutile

Rutile-volatile partition coefficients could only be determined for experiments at 800°C and 900°C and only for HFSE; values are given in **Figure 5.9** and **Table 5.6**. Determined D_{HFSE} at 800°C in this study are in good agreement with the results from Chapter 4 and literature values (e.g. Klemme et al., 2005; Xiong et al., 2005; Klimm et al., 2008). D_{Nb} is lower than D_{Ta} with $D_{\text{Nb}}/D_{\text{Ta}} = 0.45$, D_{Zr} and D_{Hf} reveal no fractionation with $D_{\text{Zr}}/D_{\text{Hf}} = 1.01$. The former value is consistent with the suggested positive dependence of $D_{\text{Nb}}/D_{\text{Ta}}$ and polymerization of the melt (Linnen and Keppler, 1997; Schmidt et al., 2004b) compared to $D_{\text{Nb}}/D_{\text{Ta}} \approx 0.71$ obtained in Chapter 4 where the silica-content of the bulk volatile is slightly higher than in this study. Results at 900°C display similar fractionation behavior ($D_{\text{Nb}}/D_{\text{Ta}} = 0.40$) but partition coefficients seem rather low compared to literature data (but see Bromiley and Redfern, 2008, even though at higher temperature).

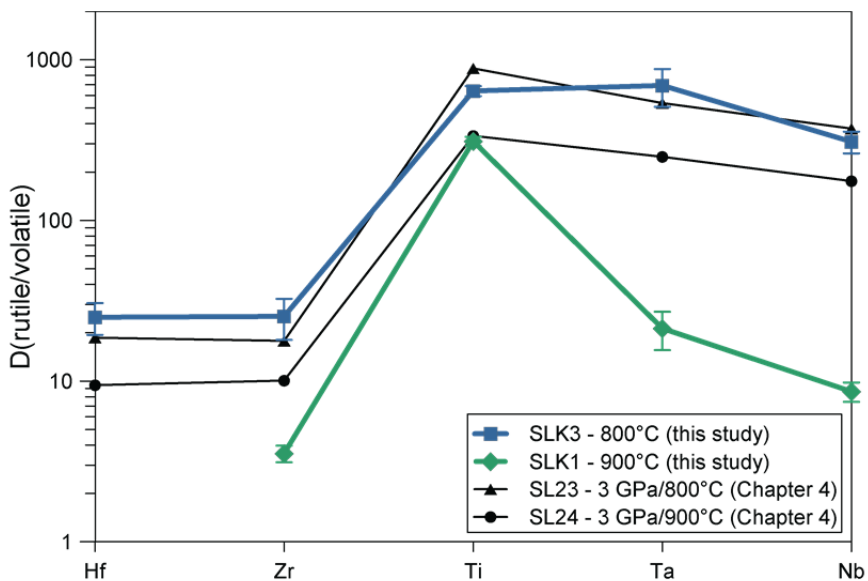


Figure 5.9. Rutile-volatile (fluid at 700°C, mixed phase at 800°C and melt at 900°C) partition coefficients of this study (blue and green) compared with values obtained in Chapter 4 at identical P-T conditions (black circles and triangles). Error bars are 1 SD.

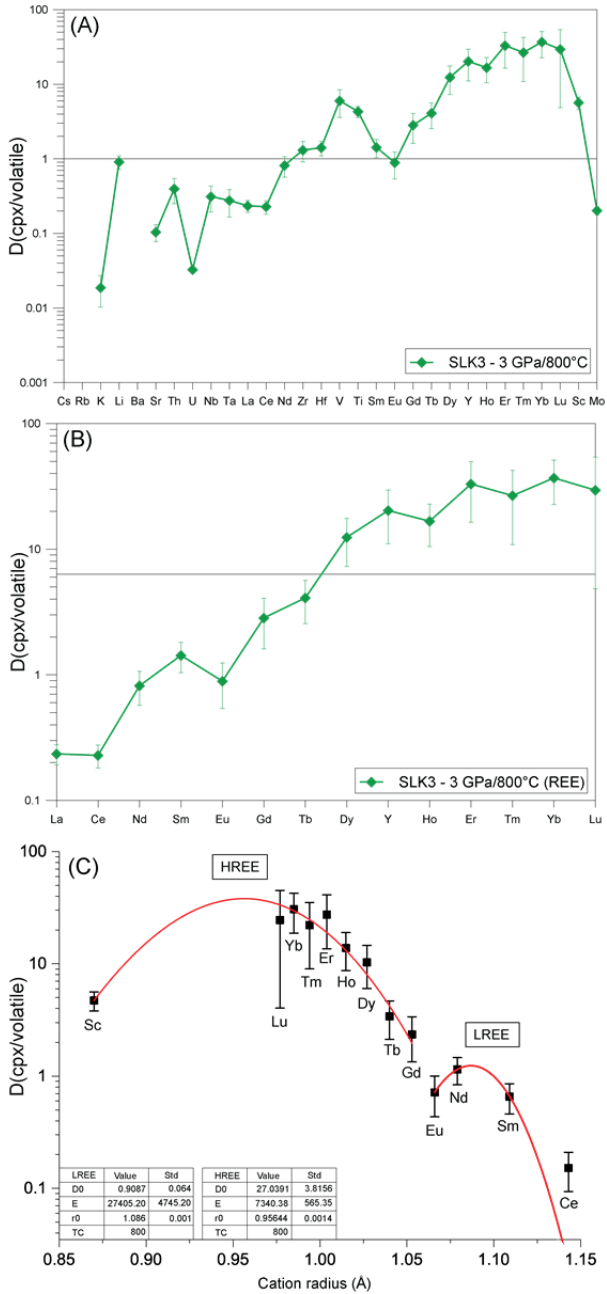


Figure 5.10. Clinopyroxene-volatile partition coefficients at 3 GPa and 800°C for a full range of elements (A) and REE (B). Error bars are 1 SD. (C) Partition coefficients (HREE + Sc and LREE) against cation radius. Red lines are fitted parabola using the equation of Blundy and Wood (1994).

5.3.4.4 Clinopyroxene

Clinopyroxene could only be analyzed by LA-ICP-MS in experiment SL-K-3 at 800°C at smallest-possible spot size (4 μm); therefore, one must be aware that contamination by surrounding mineral phases cannot be excluded. Moreover, we have shown in Chapter 4 (K-free system) that cpx does not incorporate significant amounts of trace elements, resulting in D-values for most elements <1 . We have also shown in this study and Chapters 3 and 4, that garnet and zoisite are part of the phase assemblage at these P-T conditions. The former strongly controls HREE while the latter incorporates and controls LREE. In nature, with these two phases present, cpx will not exert a strong control on REE in general. **Figure 5.10a** shows the trace element pattern obtained at 800°C. Note that absolute values might be overestimated, notably for incompatible elements. Most elements determined are incompatible except of MREE, HREE, V, Sc, Zr and Hf, which plot between 1 and 36; LREE (La-Sm) reveal values between 0.2 and 1.4. D_{Sc} and D_{V} display values in the range of those determined for cpx in the K-free system (Chapter 4). While in the latter REE D-values result in a relatively flat partitioning pattern, MREE and HREE show a more parabolic pattern in this study (**Figure 5.10b**), implying moderate control of cpx for these elements. The shape of the LREE (Ce-Sm) + Eu pattern is distinctly different from that for MREE and HREE and suggests incorporation onto different lattice sites for both groups. With the cpx being relatively omphacitic, the M2-site, where Na and very minor K are incorporated, should be larger than in cpx with higher diopside content. With LREE having larger ionic radii than HREE, the former are assumed to occupy the M2-site, while HREE might reside on the smaller M1-site resulting in two overlapping parabola in an Onuma diagram (Onuma et al., 1968) as suggested in **Figure 5.10c**.

5.3.4.5 Bulk residues

Partition coefficients between the bulk volatile phase and the solid bulk residue are shown in **Figure 5.11a** (and **Table 5.7**). The solid bulk residue was calculated from the bulk volatile fraction and initial trace element starting composition divided by the solid fraction. Bulk volatile fraction was determined from initially added water and calculated water in the volatile phase (see above). Generally, $D^{\text{volatile/solids}}$ increase with increasing temperature due to increased solubility of the minerals and as a result the release of trace elements into the mobile volatile phase at higher temperatures. At 700 and 800°C, the only incompatible trace elements are Cs, Sr, Rb, Li and U; all other elements are suggested to be retained within minerals in the slab.

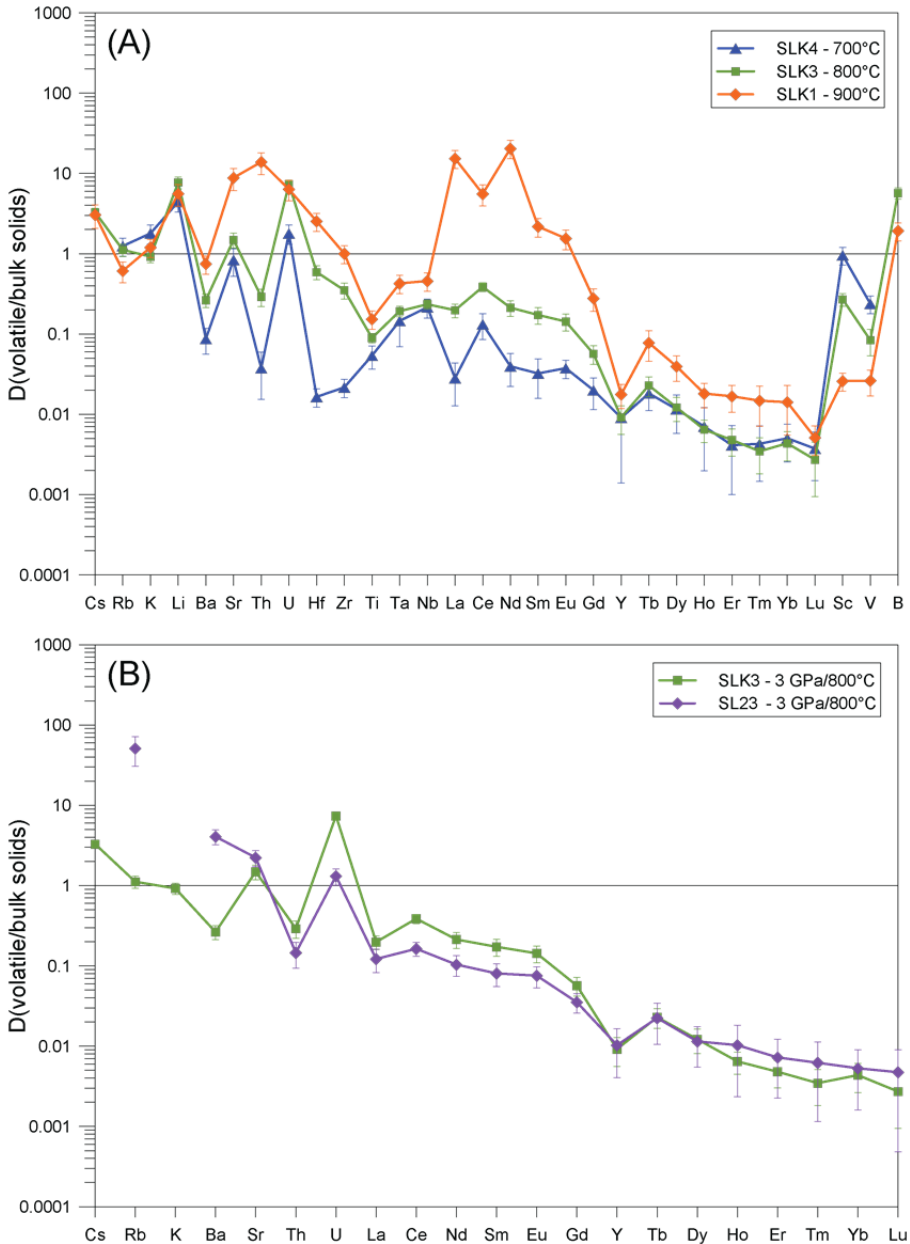


Figure 5.11. Volatile-bulk solid partition coefficients at 3 GPa and 700 to 900°C from this study (A). (B) Comparison between experiment SLK3 (this study) and SL23 (Chapter 4, K-free system) to show the influence of potentially coexisting epidote-group minerals in the residue on mobility of selected elements. Uncertainties are given as 1σ and were calculated by propagating uncertainties of elemental concentrations.

Incompatibility of these elements was implied as well by other studies with similar starting composition (Hermann and Rubatto, 2009; Skora and Blundy, 2010). Heavy REE are the most volatile-incompatible elements with values around or even below 0.01. It is well established, that garnet acts as host for REE, especially the HREE (e.g. Brenan et al., 1995; Stalder et al., 1998; Kessel et al., 2005a) and is, therefore, responsible for their depletion in the mobile volatile phase. Niobium, Tantalum and Titanium are buffered by accessory rutile, which itself is solubility-controlled (e.g. Ryerson and Watson, 1987). This means that these elements are released into the volatile phase only when rutile becomes exhausted from the residue. As rutile is stable within the investigated temperature range in this study, Nb and Ta remain volatile-incompatible at all temperatures. It has to be noted though, that compared to natural Ti-input into subduction zones (for example GLOSS, average Global Oceanic Subducted Sediments, 0.69 wt% TiO₂), our doping level is high (1.94 wt% TiO₂), thus further enhancing stability of rutile. Hafnium and Zr are slightly more volatile-compatible and are, in contrast to Nb and Ta, partly controlled by garnet. Interestingly, results at 700°C reveal D-values lower by more than one magnitude. This can be partly explained by the high $D_{\text{Hf,Zr}}^{\text{grt/volatile}}$ determined at 700°C (see **Figure 5.7**). The influence of rutile cannot be entirely assessed as they were too small for LA-ICP-MS analysis. In contrast to lower temperature runs, the trace element pattern at 900°C differs to some extent for LREE (La-Sm) and Th. While at 700 and 800°C internal REE fractionation is moderate ($D_{\text{La}}/D_{\text{Lu}} = 8-73$), extreme fractionation can be observed at 900°C ($D_{\text{La}}/D_{\text{Lu}} = 3000$) which results in the liberation of the LREE into the mobile volatile phase. The same can be observed for Th; while incompatible at lower temperatures, D_{Th} is elevated at 900°C by a factor of 50 compared to D_{Th} at 800°C. As for REE, $D_{\text{Th}}/D_{\text{U}}$ is subject to major change and increases from 0.02 to 2.2 from 700 to 900°C. This drastic change for LREE and Th must be due to a change in the residue; as mentioned above, these results suggest, that an epidote-group mineral is stable at 700 to 800°C even though we were unable to detect it. Epidote-group minerals incorporate significant amounts of LREE and Th (Chapter 3; e.g. Zack et al., 2002; Spandler et al., 2003) and are expected to be host for these elements in the chemical system used in this study. To illustrate this assumption for the behavior of REE, Th and U we compare $D^{\text{volatile/solids}}$ from this study (SL-K-3) to the results of Chapter 4 (SL23, K-free system) at identical P-T conditions in **Figure 5.11b**. Note that both experiments are trace element doped on the same level. It is obvious that generally the trace element pattern is very similar even though absolute values differ slightly. In the case of HREE this is most likely due to higher modal proportions of garnet in experiment SL23 (31.5 wt%) compared to SL-K-3 (23.3 wt%). Unlike for rutile (i.e. Ti, Nb and Ta), HREE bulk partitioning is not controlled by solubility of the mineral but by the abundance of its host mineral in the

residue. Same should be valid for LREE and zoisite. According to this and since we could not measure zoisite in SL-K-3, we can only assume that a lower proportion of zoisite crystallized in run SL-K-3, resulting in higher $D^{\text{volatile/solids}}$. Difference in $D_{\text{U}}^{\text{volatile/solids}}$ is considerable but nonetheless, $D_{\text{Th}}^{\text{volatile/solids}}$ suggest retention of Th to a similar extent, again pointing towards the presence of an epidote-group mineral at 800°C in this study.

D-values for LILE generally reveal volatile-compatible character except for Ba, which plots below 1 at all temperatures. LILE are assumed to be controlled by phengite which is part of the phase assemblage in this study and is shown to incorporate mainly Ba and Rb. Naturally, this is reflected in the bulk $D^{\text{volatile/solids}}$ pattern with D_{Ba} and D_{Rb} being the least volatile-compatible elements of all the LILE. Inspection of **Figure 5.11b** reveals the influence of phengite being part of the residue in that D_{Ba} and D_{Rb} from experiment SL23 (no phengite in the residue and no other host for Ba) plot one magnitude (or more) higher than D_{Ba} and D_{Rb} from experiment SL-K-3 (this study). Unfortunately, we were not able to determine bulk-D values in the K-free system for Cs as it was used as internal standard in these experiments and added in large amounts.

Table 5.7. Volatile-bulk solid partition coefficients at 3 GPa.

T (°C)	700		800		900	
Run	SLK4		SLK3		SLK1	
	D(liq/solid)	Error ^a	D(liq/solid)	Error	D(liq/solid)	Error
Cs	N.D.	N.D.	3.29	(0.38)	3.06	(0.99)
Rb	1.25	(0.32)	1.12	(0.20)	0.61	(0.18)
K	1.79	(0.48)	0.92	(0.15)	1.20	(0.30)
Li	4.45	1.13	7.74	(1.33)	5.60	(1.69)
Ba	0.09	(0.03)	0.26	0.05	0.75	(0.19)
Sr	0.84	(0.32)	1.49	(0.309)	8.84	(2.7139)
Pb	N.D.	N.D.	N.D.	N.D.	N.D.	N.D.
Th	0.04	(0.02)	0.29	(0.07)	13.89	(4.19)
U	1.79	(0.48)	7.39	(0.86)	6.36	(1.81)
Hf	0.02	(0.004)	0.59	(0.12)	2.54	(0.64)
Zr	0.02	(0.01)	0.35	(0.08)	1.01	(0.25)
Ti	0.05	(0.02)	0.09	(0.01)	0.15	(0.04)
Ta	0.15	(0.08)	0.19	(0.03)	0.43	(0.11)
Nb	0.22	(0.06)	0.23	(0.03)	0.46	(0.12)
Mo	N.D.	N.D.	N.D.	N.D.	N.D.	N.D.
La	0.03	(0.02)	0.20	(0.04)	15.36	(3.88)
Ce	0.13	(0.05)	0.39	(0.05)	5.58	(1.64)
Nd	0.040	(0.02)	0.21	(0.05)	20.47	(5.26)
Sm	0.032	(0.02)	0.17	(0.04)	2.18	(0.57)
Eu	0.038	(0.01)	0.14	(0.03)	1.55	(0.43)
Gd	0.020	(0.01)	0.057	(0.01)	0.28	(0.09)
Y	0.009	(0.01)	0.009	(0.00)	0.02	(0.01)
Tb	0.018	(0.01)	0.023	(0.01)	0.08	(0.03)
Dy	0.012	(0.01)	0.012	(0.00)	0.04	(0.01)
Ho	0.007	(0.005)	0.006	(0.002)	0.018	(0.01)
Er	0.004	(0.003)	0.005	(0.002)	0.017	(0.01)
Tm	0.004	(0.003)	0.003	(0.002)	0.015	(0.01)
Yb	0.005	(0.002)	0.004	(0.002)	0.014	(0.01)
Lu	0.004	(0.002)	0.003	(0.002)	0.005	(0.002)
Sc	0.96	(0.24)	0.27	(0.05)	0.026	(0.01)
V	0.24	(0.06)	0.08	(0.03)	0.026	(0.01)
B	N.D.	N.D.	5.70	(0.89)	1.93	(0.48)
W	N.D.	N.D.	N.D.	N.D.	N.D.	N.D.

^a Errors represent 1 σ uncertainties, calculated as a standard deviation.

^b N.D. = no data.

5.4 Discussion

5.4.1 Position of the wet solidus

The position of the wet (fluid saturated) pelite solidus has been a matter of debate in recent years and several studies resulted divergent suggestions for its location at pressures relevant for arc magmatism (2.5-4.5 GPa, Syracuse and Abers, 2006). The wet solidus in red clay sediments up to 3 GPa is located just below 700°C (Nichols et al., 1994), which is in good agreement with the solidus of 700-750°C for average global subducting sediments at 3.5 GPa (Hermann and Spandler, 2008) and the 750°C of radiolarian clay at 3 GPa (Skora and Blundy, 2010). In contrast, Auzanneau et al. (2006) reported the location of the wet solidus for a metagreywacke composition, similar to the composition of the starting material of Hermann and Spandler (2008), slightly higher than 800°C at 3 GPa. Likewise, the solidus in red clays was placed between 800 and 825°C at 3 GPa, based on the observed transition from fluid to melt (Johnson and Plank, 1999). **Figure 5.12** summarizes the findings of the studies mentioned above.

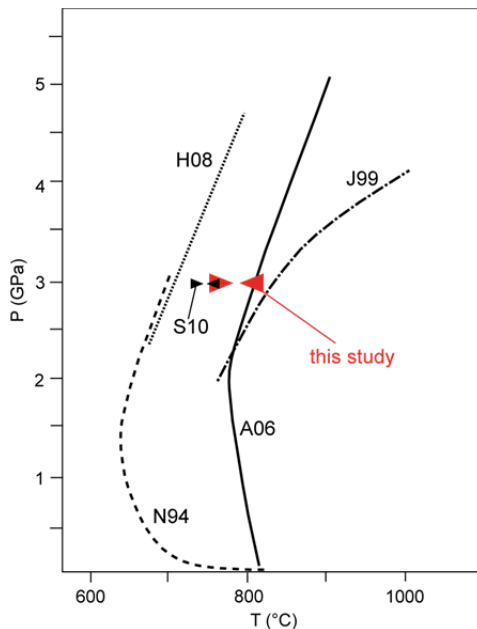


Figure 5.12. Compilation of positions of the wet solidus in experimental sediment composition systems. Red triangles, this study; N94, Nichols et al. (1994); J99, Johnson and Plank (1999); A06, Auzanneau et al. (2006); H08, Hermann and Spandler (2008); S10, Skora and Blundy (2010). After Hermann and Spandler (2008).

These considerable differences could be a result of variations in the starting composition employed or expose difficulties in detecting the appearance of glass in the residual phase assemblage. Determination of the change from an aqueous fluid to a hydrous melt, i.e., location of the solidus, at high pressures can be challenging but mostly goes along with the first appearance of glass (quenchable melt). In the case of Auzanneau et al. (2006), who added only 0.4 wt% of excess water to their starting material (in contrast to the above mentioned studies, which were all performed under water-saturated conditions), detection of glass is difficult given that melt fractions are very low, and the water-saturated solidus may thus escape recognition. Our study was not primarily designed to determine the exact position of the wet solidus; temperature steps (100°C) are too large. Nevertheless, we can put some constraints. We observe small glass pools between solid phases at 800°C (see **Figure 5.2**) while at 700°C no glass can be detected. At 900°C glass pools are large enough for LA-ICP-MS analyses. On the basis of our experiments, we can locate the wet solidus somewhere between 700 and 800°C. According to the extremely low abundance of glass at 800°C, the wet solidus in our system probably lies closer to 800°C than 700°C. Next to the appearance of glass, certain major element ratios could help defining the nature of the mobile phase (see e.g. Hermann and Spandler, 2008). They showed that $\text{SiO}_2/\text{Al}_2\text{O}_3$ and $\text{Na}_2\text{O}/\text{Al}_2\text{O}_3$ ratios reveal significantly higher values in aqueous fluids compared to hydrous melt compositions. The same can be observed in our experiments (**Figure 5.13**), even though with substantially larger values at 700°C than those of Hermann and Spandler (2008; and also compared to data at 3 GPa/650-700°C from Green and Adam, 2003). This further confirms that at 700°C an aqueous fluid is stable, which is then changing its nature towards hydrous melts around 800°C.

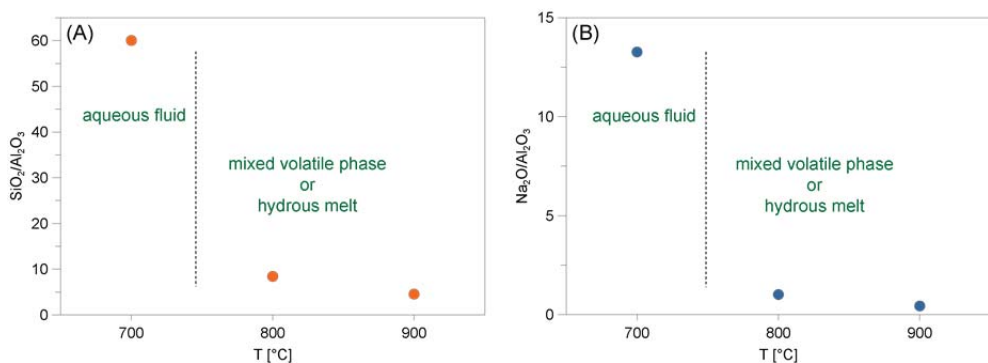


Figure 5.13. Evolution of $\text{SiO}_2/\text{Al}_2\text{O}_3$ (A) and $\text{Na}_2\text{O}/\text{Al}_2\text{O}_3$ (B) of the bulk volatile phase as a function of temperature reveals distinctly different ratios for aqueous fluids and hydrous melts.

5.4.2 Element transport from subducted AOC/sediment compositions

The starting material employed in this study represents a very strongly altered MORB and resembles in many aspects that of Ca-rich sediment compositions used in previous studies (e.g. pelagic red clay, Johnson and Plank, 1999; radiolarian clay, Skora and Blundy, 2010). In the following, results from this study are compared to features typically observed in arc lavas inheriting a subduction component which clearly stems from subducting sediments. Studies of arc lavas as well as experiments imply that elements from the sediment portion of the slab are transported by (hydrous) melts while very dilute aqueous fluids leach elements from the basaltic portion, which leads to trace element signatures often determined in sediment-starved arcs (e.g. Elliott et al., 1997; 2003). Even though much less quantitatively abundant, the former is responsible for the substantial enrichment of certain elements (e.g. LILE, REE, Th) in arc lavas due to the initially high trace element abundance relative to subducted mafic lithologies or the mantle wedge (e.g. Lesser Antilles arc, Plank and Langmuir, 1998). Fluids and melts from the slab collectively contribute to the distinct geochemical signature of arc magmatic rocks such as enrichment of LILE (e.g. Hawkesworth et al., 1993; Tatsumi and Eggins, 1995; Pearce et al., 2005) and LREE, and depletion of HREE and HFSE (e.g. McCulloch and Gamble, 1991; Hawkesworth et al., 1993) compared to N-MORB. It became evident in recent years that the signature of arc lavas strongly depends on the residual phases stable in the slab. Phengite is the primary control of LILE (e.g. Domanik and Holloway, 1996; Schmidt, 1996; Sorensen et al., 1997; Melzer and Wunder, 2000; Zack et al., 2001; Schmidt et al., 2004a; Hermann and Rubatto, 2009; this study); LREE and Th (and to a lesser extent U) in Ca-rich systems are controlled by epidote-group-minerals (Hermann et al., 2002; Klimm et al., 2008; Chapter 3) or monazite (Hermann and Rubatto, 2009; Skora and Blundy, 2010) in Ca-poor systems. Garnet is a major host for the HREE and exerts strong control on their partitioning behavior (e.g. Stalder et al., 1998; Kessel et al., 2005a; Chapter 4), and the behavior of HFSE is governed by rutile (e.g. Brenan et al., 1994; Zack et al., 2002; Klemme et al., 2005). It is, therefore, important in experimental studies that these phases are present in order to interpret the composition of the mobile volatile phase correctly, which is the case in this study. Plank and Langmuir (1993) presented strong evidence on the clear correlation between the composition of the subducting sediment pile and their associated arc lavas. As is assumed that melting of the sediments is the main process in transporting elements from the slab to the surface (e.g. Elliott et al., 1997; Plank, 2005), this implies that initial element ratios in the sediments should be inherited in the mobile volatile phase and eventually in the arc volcanic rocks as well. An example is the Th/Rb ratio; Johnson and Plank (1999) showed in their experiments on pelagic red clay that Th/Rb normalized to their starting material approaches 1 only when the solidus is exceeded at around 800°C and 2 GPa, i.e., when melting starts. However, they did not report monazite or zoisite/allanite in their residue

which would control the mobility of Th. In contrast, in our study phengite is stable at all temperatures and an epidote-group mineral coexists up to 800°C. **Figure 5.14a** shows Th/Rb normalized to our starting material (Th/Rb_N) and plotted against temperature. It is important to mention that the doping level of Th in this study is not essentially much higher than what is measured for natural sediments, Rb is lower in this study (GLOSS, Plank and Langmuir, 1998; $\text{Rb} = 64 \mu\text{g g}^{-1}$, $\text{Th} = 7.7 \mu\text{g g}^{-1}$). At 700 and 800°C, Th/Rb_N clearly remains below 0.5 before abruptly increasing to ~ 2 at 900°C. This value implies an enrichment in Th compared to the initial Th/Rb ratio of the starting material since part of the Rb is fixed in phengite and an epidote-group mineral is not stable at 900°C. In any case it is important to note that in this study the presence or absence of an epidote-group mineral is the major control (next to phengite being stable at all temperatures) on Th/Rb and not melting primarily, since our data suggest the wet solidus to be located somewhere below 800°C where we still assume an epidote-group mineral being stable. These results emphasize earlier findings with regard to the importance of the residual phase assemblage of the slab.

Ba/Th is another element ratio used to discriminate a fluid or melt signature. Elliott et al. (1997; 2003) showed that in sediment-starved arcs (fluid signature) a common feature are Ba/Th ratios exceeding 1000 while addition of sediment melts would result in much lower Ba/Th ratios. We have shown in the K-free MORB-H₂O system (Chapter 4) that for predicted slab-top temperatures of 750-850°C (e.g. Syracuse et al., 2010; van Keken et al., 2011), aqueous fluids-dominated volatiles, rather than hydrous melts, represent realistic transport agents that thus account for the high Ba/Th ratio of natural rocks, since hydrous melts reveal Ba/Th ratios that are substantially lower (by more than two orders of magnitude). The ratios obtained there, however, cannot be applied to natural systems directly because addition of trace elements to the starting material does not correspond to natural values for MORB. These are considerably lower to what we added. But as we doped both systems with the same amount for all trace elements, it allows, nevertheless, directly illustrating the effect of phengite in the residue. **Figure 5.14b** highlights the difference between the K-free system and that representative for AOC/sediment used in this study. In the sediment-system Ba/Th does not exceed values of 10 from 700 to 900°C with $\text{Ba/Th} = 7$ at 700°C, which is two orders of magnitude lower than in the K-free system at same temperature ($\text{Ba/Th} \sim 620$ at 700°C). The $D_{\text{Ba}}^{\text{phe/volatile}}$ obtained in this study clearly show that Ba is the most compatible element in phengite and is, therefore, responsible for lower Ba/Th in a sediment-system.

Finally, we want to stress another arc geochemical signature in the light of our results, the depletion of HFSE with respect to LREE and Th. The La/Nb evolution, relative to PUM, as a function of temperature is displayed in **Figure 5.14c**. Results reveal that only at 900°C,

when epidote-minerals are exhausted, La is distinctly enriched when compared to Nb. Note that La/Nb of the starting material used in this study is 1 (see **Table 5.2** and **Figure 5.14c**), which means that fractionation of Nb and La does occur during sediment melting based on the results presented here. This is in contrast with many previous studies on aqueous fluids and hydrous melts in pelite and basalt systems as pointed out by Hermann and Rubatto (2009) and references therein (see **Figure 5.14c**). They all reported allanite or monazite and rutile in their residue in the investigated temperature range but in contrast to this study, their doping level was relatively high and mostly exceeded natural concentrations. At least in the case of allanite, where LREE and Th are major structural components, doping leads to enhanced stability of the mineral (see e.g. Skora and Blundy, 2010; Chapter 3), possibly beyond the solidus into the melting regime (e.g. Klimm et al., 2008). This could be a reason for the discrepancies when comparing this study to the previous ones since our doping level for LREE is much lower. It was often argued that the typical negative Nb-anomaly in arc rocks could be inherited from the subducted sediments, which themselves display a high Nb-depletion prior to subduction (Plank and Langmuir, 1998). However, this is not true for all arcs; the Mariana arc for example is dominated by volcanoclastic sediments which have no initial negative Nb-anomaly (Elliott et al., 1997). Martindale et al. (2013) observed in their phase relation study on these trace element-undoped volcanoclastics that the resulting $D(\text{glass-bulk solids})$ show indeed a distinct Nb fractionation from La (about one order of magnitude) due to rutile in their residue. This is in very good agreement with the results of this study at 900°C.

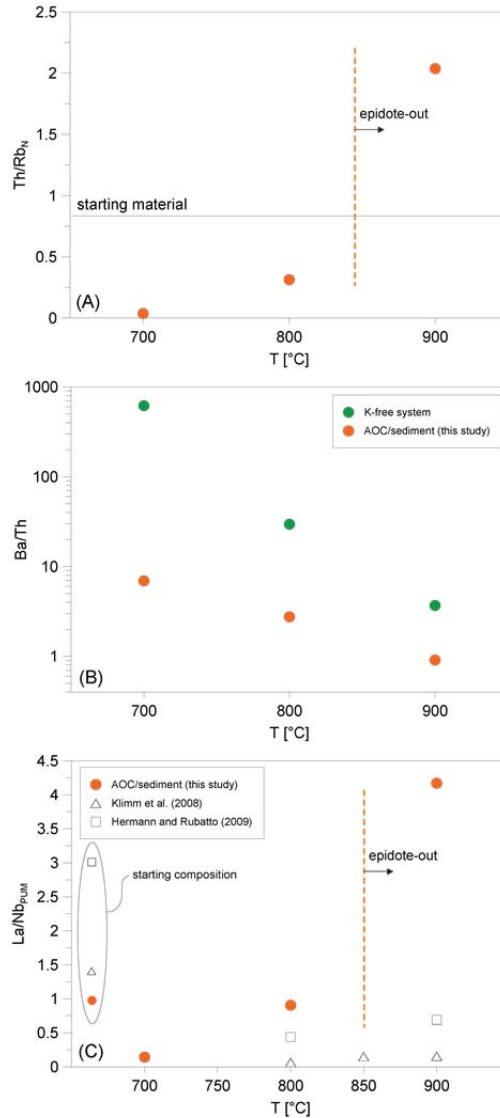


Figure 5.14. Element ratios in the bulk volatile phase as a function of temperature from 700 to 900°C. (A) Th/Rb normalized to initial starting composition (N) displays enrichment of Th compared to Rb at 900°C when epidote-group minerals are exhausted but phengite is still stable. (B) Comparison of results from this study (orange circles) and results of Chapter 4 (green circles, K-free system) shows the influence of phengite on Ba/Th ratios in keeping Ba/Th low when phengite is part of the residue. (C) PUM-normalized La/Nb implies depletion of Nb at 900°C compared to LREE in this study. Results from Klimm et al. (2008) and Hermann and Rubatto (2009) are additionally shown, they did not observe fractionation. The starting compositions of the mentioned studies are shown to illustrate the effect of enrichment/depletion.

5.4.3 Comparison to MORB and the influence of phengite

In the following, results from this study are compared to the results obtained in the K-free MORB-H₂O system to discuss the possible consequences for arc magmatism in sediment-starved settings (K-free, Chapter 3 and 4) and settings with high sediment input (K-rich, this study). For both systems, the residual phase assemblage is almost identical with the exception of phengite, which is only present in the K-rich system. This is consistent with the findings of e.g. Schmidt et al. (2004a) who showed that at > 100 km depth in subduction zones, MORB-, greywacke- and pelite-lithologies produce an identical residue in the slab. Consequently, we should find differences in bulk-D behavior and, therefore, element mobility only in the elements that are controlled by phengite, most prominently LILE. As we doped the same amount of trace elements in both studies, we can directly compare the outcome for both systems. We have already shown in **Figure 5.11b** (for LILE, REE, Th and U at 800°C) that bulk-D trace element patterns are most similar for K-rich and K-free compositions and that differences in absolute D-values arise because of varying modal proportions of the residual minerals and melt fractions; hence, the most interesting question is whether and how phengite might influence the overall arc signature, namely the characteristic enrichment of LILE compared to REE. **Figure 5.15** gives the bulk-D trace element pattern for both systems over the investigated temperature range. It is evident that in the K-free system, LILE are by far the most incompatible elements at all temperatures and, therefore, reproduce the arc signature well (Chapter 4). Interestingly, the same is true for the AOC/sediment system investigated in this study up to 800°C; at 900°C the release of LREE due to the breakdown of epidote-group minerals changes the ratio LILE/LREE in favor of the LREE. This puts important constraints on the release of fluids and/or melts with an arc-typical signature, notably since phengite breakdown is not reached for the proposed slab-top temperatures (e.g. Hermann and Rubatto, 2009). As an overall conclusion, this study shows that phengite is the most important host and control on the LILE. Its influence is limited in terms of strong depletion of LILE compared to LREE when residual mineral assemblages include epidote-group minerals that control LREE. Therefore, the difference in trace element patterns (not absolute values) of the mobile phase between a K-free system and systems with large sediment-input might be negligible at P-T conditions relevant to the generation of arc magmas.

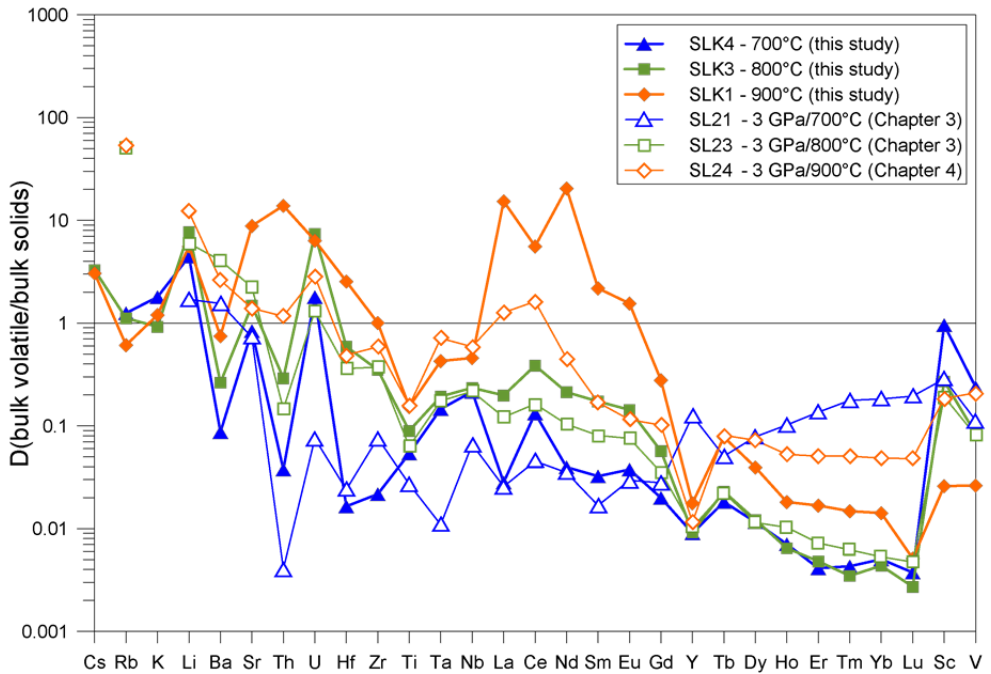


Figure 5.15. Bulk volatile-bulk solid partition coefficients from this study (filled symbols) compared to that from Chapter 4 (open symbols) in a K-free system reveal differences in element mobility in subducted AOC/sediment and MOR basalt.

5.5 Summary and concluding remarks

The aim of this study was to determine the effect of the white mica phengite in subducted AOC/Ca-rich sediment at P-T conditions (3 GPa, 700 to 900°C) relevant to subduction zone settings. We quantified the composition of the slab-escaping volatile phase by adapting the "freezing" method for K-free systems (Kessel et al., 2004) to systems containing potassium. This requires an internal standard different than Cs, which does not behave completely incompatible in the presence of phengite and can, therefore not be used for the chemical system used in this study. We found that incompatible bromine as internal standard could be a reliable option in the future even though some issues remain unresolved at this point and require further investigation. The results of this study suggest that sediment melting starts below 800°C at 3 GPa which is in line with most previous studies that investigated the position of the wet solidus in sediment systems. Determined partition coefficients for garnet and rutile confirm the strong control on HREE and HFSE, respectively. It is also shown that phengite, being stable beyond the wet solidus, is the most important host for

LILE and K. We provide partition coefficients for phengite and bulk volatiles (fluids, melts or a mixture of both at 800°C), which are rare up to date but urgently needed to model subduction zone processes. Mass balance calculations and the composition of the volatile phase imply that at 700 and 800°C, an epidote-group mineral was stable additionally. Epidote-group minerals have previously been shown to control key elements (LREE and Th) relevant to subduction zone processes. This study confirms the importance of accessory and minor phases (rutile, phengite, epidote-group minerals) in the slab as they govern distinct element ratios (e.g. Ba/Th, Th/Rb, La/Nb) that are used to assess the nature of the element transport agent (aqueous fluid or hydrous melt) leaving the slab. When comparing to K-free MORB systems, our results reveal that the trace element pattern of bulk volatiles in sediment systems astonishingly resembles that observed in sediment-starved subduction zone settings at low temperatures up to the point where epidote-group minerals are exhausted. We find that in the presence of the latter, the LILE are depleted compared to LREE, which illustrates a trace element signature not typically displayed by arc magmas

CHAPTER 6

Conclusions and outlook

6.1 Synthesis

The objective of this thesis was to determine and quantify the slab components that leave distinct fingerprints in igneous arc rocks and are responsible for the prominent trace element (re)cycling within subduction zones. The geochemical trace element signature of arc rocks is mediated by up to four different source lithologies. (1) Hydrous slab mantle, (2) variably altered basaltic oceanic crust, (3) its potential sediment layer, and (4) the peridotites in the depleted mantle wedge overlying the descending slab. The basaltic and sediment portions of the slab, however, constitute the major lithologies in hosting the largest amounts of trace elements. At pressure and temperature conditions examined in this work (2 and 3 GPa, 700 to 1200°C), these trace elements are carried by aqueous fluids, hydrous melts or a mixture of both coexisting (bulk volatile) as main transport agents. Especially the quantification of the former comes along with major experimental and analytical challenges and, therefore, data on transport capacities of aqueous fluids are rare up to date. Bulk volatiles were collected in diamond traps and subsequently analyzed by the recently developed cryogenic laser ablation ICP-MS technique (Kessel et al., 2004; Aerts et al., 2010), which allows for direct and complete compositional quantification of the bulk volatile at experimental P and T. We have designed a new external freezing stage wherein the capsule is fixed, frozen and subsequently analyzed. The following improvements were implemented. (i) The ablation chamber was adapted to optimize gas flow by changing to a rhombic shape and by adjusting the position of the gas nozzles, (ii) a new, more stable sample holder was designed, and (iii) insulation of the entire freezing stage was improved. Two water-saturated, chemically different systems were investigated in the course of this work: (1) a K-free basalt system and (2) a strongly altered basalt/Ca-rich sediment system.

6.2 K-free MORB system

High P- and T-experiments resulted in the formation of aqueous fluids (at 3 GPa /700°C) or fluid-dominated bulk volatiles from 700 to 800°C at 2 and at 800°C at 3 GPa; at higher temperatures a hydrous melt was stable. The major element composition of the volatile

phase reflects the presence of the various residual minerals and evolves from extremely peralkaline fluids towards metaluminous compositions with a water content decreasing from up to 45 wt% to 20 wt% as a function of temperature. The wet solidus is located around 700°C and between 700 and 800°C at 2 and 3 GPa, respectively. The change from fluid-dominated volatiles to pure melts goes along with a prominent change in the residual phase assemblage. It is dominated by the mainly hydrous minerals amphibole and zoisite at low-temperature conditions next to garnet and accessory rutile/titanite. At suprasolidus conditions, typically, nominally anhydrous eclogitic minerals (garnet, clinopyroxene and rutile) dominate the residue. Trace element partition coefficients are determined for garnet, clinopyroxene, zoisite and rutile/titanite. The results show that garnet is the principal control for the heavy REE with $D(\text{mineral/volatile})$ of up to 1000 or higher at lowest temperatures. Rutile incorporates significant amounts of HFSE, primarily Nb and Ta, whereas Hf and Zr are jointly controlled by rutile and garnet. Light REE, Th and, to a lesser extent, U are almost exclusively controlled by zoisite. It has been shown that clinopyroxene exerts only little control on the trace element partitioning with Sc and V being the only cpx-compatible elements in our experimental study. Generally, mineral/volatile partition coefficients of all phases decrease with increasing temperature. Special emphasis was laid on the partitioning behavior of zoisite because (i) they control key elements in describing a characteristic arc signature pattern and (ii) only very limited data are available on the partitioning of epidote-group minerals in general. We have determined zoisite partition coefficients in equilibrium with fluids or fluid-dominated volatiles independent from mass balance calculations for the first time. Compared to previous studies, several striking differences can be observed. Zoisite mineral/fluid partition coefficients for LREE and Th obtained in this work are higher by at least two orders of magnitude compared to previous results. Light REE are the most compatible elements compared to MREE and HREE with $D(\text{zoi/fluid})$ of up to 1000; this value is in the range of determined D -values for Th, which strongly fractionates from U. In contrast to earlier findings, the results presented here suggest that D -values increase with increasing pressure and decreasing temperature. Allanite, the REE-rich epidote-group mineral, was not observed in the experiments of this work. We conclude that the stability of allanite depends largely on the concentrations of LREE and Th in the bulk system, i.e. the trace element doping level in experiments is critical, as REE and Th constitute major structural components in allanite. Therefore, the presence of allanite might not be a prerequisite in a slab in nature. However, $D(\text{zoi/fluid})$ values presented here imply similar compatibility for LREE and Th as literature $D(\text{allanite/melt})$ data, broadening the influence of epidote-group minerals to more general settings. Overall, the composition of the volatile phase has been proven to be strongly dependent on the residual phase assemblage. At low-temperature conditions, LILE are the only elements concentrated in the volatile phase and are, therefore, free to be transported

into the mantle wedge. This is a direct consequence of the absence of a potential host like white mica. All other elements are fixed in residual minerals and variably strongly remain in the slab. Only when zoisite is exhausted, the LREE concentrate in the mobile volatile phase and produce the typical LREE/HREE fractionation observed in natural arc rocks. Furthermore, the results of this work reinforce the usefulness of key element ratios, such as Ba/Th, in identifying natural arc rocks from sediment-starved subduction zones. We show that merely fluid-dominated volatiles reproduce the observed signature originating from the basaltic portion of the slab. This is in excellent agreement with predicted slab-temperatures which suggest that the slab-basalts do not undergo melting except for specific conditions (such as slab-breakoff).

6.3 Altered MORB/sediment system

This part of the work focused on the uppermost portion of a slab, the sediment layer associated with underlying, potentially strongly altered basaltic lithologies. Even though subordinate by mass compared to the pristine basaltic section, the sediments constitute the major hosts for trace elements within the subducting oceanic lithosphere. At 3 GPa and 700 to 900°C, the residue is made up of mainly garnet, phengite, clinopyroxene (up to 800°C) and accessory rutile. Additionally, the resulting trace element systematics suggest that at 700 and 800°C, an epidote-group mineral was stable, which was, however, not detected. The presence of mica demands for adaption of the cryogenic LA-ICP-MS technique to systems containing potassium. We found that bromine (replacing Cs for K-free systems) might be a reliable internal standard element for LA-ICP-MS analysis because it remains incompatible even in the presence of mica. However, some issues concerning the behavior of Br in diamond trap experiments and following cryogenic LA-ICP-MS analysis remain unresolved and need further investigation. By applying a correction factor we, nevertheless, obtained an internally consistent dataset that allows for drawing first conclusions on the composition of the mobile phase escaping from the subducted sediments. First appearance of melt was observed in the experiment at 800°C placing the wet solidus in sediment systems to be somewhere between 700 and 800°C. This textural observation is supported by specific major element ratios (e.g. $\text{SiO}_2/\text{Al}_2\text{O}_3$) that decrease drastically when changing from aqueous fluids to hydrous melts. Generally, volatile phases are very peralkaline at low temperatures and tend towards peraluminous compositions with increasing temperature; the water content decreases from 700 to 900°C. Trace element partition coefficients were determined for garnet, phengite, clinopyroxene and rutile. As for zoisite in the K-free MORB system, a major goal of this part was to characterize phengite/volatile element partitioning and its influence on arc rock signatures as there are virtually no experimental data available in the literature. Phengite is the only

host for LILE in our experiments. Partition coefficients reveal that Ba is the most compatible element in phengite with $D(\text{phe}/\text{fluid})$ up to 24, followed by Rb and Cs with the latter two showing preference for the volatile phase. The resulting bulk (bulk volatile/bulk solids) trace element patterns display that, despite the presence of phengite, most LILE (Cs, Rb, K, Li) behave incompatibly and are liberated from the slab via fluids and melts. Due to residual garnet (strongly depleting the volatile phase in HREE next to clinopyroxene that exhibits minor control), rutile (retaining HFSE) and the epidote-group minerals that control LREE and Th, LILE are still the most incompatible elements. The resulting bulk trace element patterns are surprisingly similar to those determined in the K-free MORB system. Only when epidote-group minerals are exhausted at 900°C, LILE/LREE fractionation changes in favor of LREE due to phengite coexisting with hydrous melt. This puts tight constraints on the mobile phase being liberated from the slab that can explain a given arc signature. We also found that at 900°C, Nb sufficiently fractionates from La producing the Nb-anomaly characteristic of arc rocks.

In summary, the two most potent systems in terms of trace element content and with the potential to release most of them during subduction, MOR-basalt and AOC/sediment, have been investigated. The nature and composition of the bulk volatile phases released during dehydration and melting of the slab have been analyzed quantitatively, and partition coefficients between those mobile phases and most (except amphibole) residual phases are determined.

6.4 Outlook

The development of the cryogenic LA-ICP-MS technique enabled the study of aqueous fluids by a completely new approach. The advantage of being able to analyze fluids directly and completely and not being dependent on mass balance calculations or the analysis of only quench solutes is considerable, and it has proven to constitute a reliable experimental and analytical technique for the future. While limited to K-free hydrous systems at the beginning, we attempted to adapt the method to systems containing potassium and hydrous minerals. As described above, we are confident that in general bromine (or alternatively iodine) could be used as internal standard in such systems but certain issues need to be investigated. The cause for the elevated Br-signals during cryogenic LA-ICP-MS trap analysis remains unclear and has to be examined. A possible reason could be an influence of the diamonds used for the trap or a Br artifact resulting from the cryogenic measurement conditions, since conventional analyses of the glass pools returned plausible results. However, only a serious experimental effort, yet to be devised, can possibly solve this issue. Once this is understood, more experiments are desirable in an altered MORB/sediment system to for example investigate the influence of K on the wet solidus at

various pressures or to improve the understanding of the partition behavior of phengite. Generally, the method can be applied to other systems too; the key point is to find a suitable internal standard for LA-ICP-MS data quantification for the specific system. For example, it would be interesting to quantify the exact composition of fluids released from the serpentinites within a slab as they most likely provide substantial amounts of water into overlying lithologies and host some important elements, such as Li, B, As, Sb and halogens.

An important issue that was discussed to some extent in this thesis is the "problem" of doping experiments with high amounts of trace elements to ensure analytical detectability in reaction products. Our results have implied that for some key solid-solution minerals (e.g. epidote-group minerals), doping at unnaturally high levels might stabilize minerals into P-T regions uncommon in nature. Future experiments thus need to be designed towards naturally relevant compositions, notably since analytical techniques have prominently improved in recent years.

Bibliography

- Adam, J. & Green, T. (2006). Trace element partitioning between mica- and amphibole-bearing garnet Iherzolite and hydrous basanitic melt: 1. Experimental results and the investigation of controls on partitioning behaviour. *Contributions to Mineralogy and Petrology* **152**, 1-17.
- Aerts, M., Hack, A. C., Reusser, E. & Ulmer, P. (2010). Assessment of the diamond-trap method for studying high-pressure fluids and melts and an improved freezing stage design for laser ablation ICP-MS analysis. *American Mineralogist* **95**, 1523-1526.
- Anderson, R. N., Delong, S. E. & Schwarz, W. M. (1978). Thermal model for subduction with dehydration in the downgoing slab. *Journal of Geology* **86**, 731-739.
- Antignano, A. & Manning, C. E. (2008). Rutile solubility in H₂O, H₂O-SiO₂, and H₂O-NaAlSi₃O₈ fluids at 0.7-2.0 GPa and 700-100°C: Implications for mobility of nominally insoluble elements. *Chemical Geology* **255**, 283-293.
- Armbruster, T., Bonazzi, P., Akasaka, M., Bermanec, V., Chopin, C., Giere, R., Heuss-Assbichler, S., Liebscher, A., Menchetti, S., Pan, Y. M. & Pasero, M. (2006). Recommended nomenclature of epidote-group minerals. *European Journal of Mineralogy* **18**, 551-567.
- Aulbach, S., O'Reilly, S. Y., Griffin, W. L. & Pearson, N. J. (2008). Subcontinental lithospheric mantle origin of high niobium/tantalum ratios in eclogites. *Nature Geoscience* **1**, 468-472.
- Auzanneau, E., Vielzeuf, D. & Schmidt, M. W. (2006). Experimental evidence of decompression melting during exhumation of subducted continental crust. *Contributions to Mineralogy and Petrology* **152**, 125-148.
- Ayers, J. C. & Watson, E. B. (1991). Solubility of apatite, monazite, zircon, and rutile in supercritical aqueous fluids with implications for subduction zone geochemistry. *Philosophical Transactions of the Royal Society of London Series a-Mathematical Physical and Engineering Sciences* **335**, 365-375.
- Baker, M. B. & Stolper, E. M. (1994). Determining the composition of high-pressure mantle melts using diamond aggregates. *Geochimica et Cosmochimica Acta* **58**, 2811-2827.
- Barth, M. G., Foley, S. F. & Horn, I. (2002). Partial melting in Archean subduction zones: constraints from experimentally determined trace element partition coefficients between eclogitic minerals and tonalitic melts under upper mantle conditions. *Precambrian Research* **113**, 323-340.
- Beattie, P. (1993). Uranium thorium disequilibria and partitioning on melting of garnet peridotite. *Nature* **363**, 63-65.
- Beattie, P. (1994). Systematics and energetics of trace-element partitioning between olivine and silicate melts: Implications for the nature of mineral/melt partitioning. *Chemical Geology* **117**, 57-71.
- Bebout, G. E. (2007). Metamorphic chemical geodynamics of subduction zones. *Earth and Planetary Science Letters* **260**, 373-393.
- Bédard, J. H. (2014). Parameterizations of calcic clinopyroxene-melt trace element partition coefficients. *Geochemistry Geophysics Geosystems* **15**, 303-336.

BIBLIOGRAPHY

- Bennett, S. L., Blundy, J. & Elliott, T. (2004). The effect of sodium and titanium on crystal-melt partitioning of trace elements. *Geochimica et Cosmochimica Acta* **68**, 2335-2347.
- Beyer, C., Klemme, S., Wiedenbeck, M., Stracke, A. & Vollmer, C. (2012). Fluorine in nominally fluorine-free mantle minerals: Experimental partitioning of F between olivine, orthopyroxene and silicate melts with implications for magmatic processes. *Earth and Planetary Science Letters* **337**, 1-9.
- Bleiner, D. & Günther, D. (2001). Theoretical description and experimental observation of aerosol transport processes in laser ablation inductively coupled plasma mass spectrometry. *Journal of Analytical Atomic Spectrometry* **16**, 449-456.
- Blundy, J. D. & Wood, B. J. (1994). Prediction of crystal-melt partition coefficients from elastic moduli. *Nature* **372**, 452-454.
- Blundy, J. D. & Wood, B. J. (2003a). Partitioning of trace elements between crystals and melts. *Earth and Planetary Science Letters* **210**, 383-397.
- Blundy, J. D. & Wood, B. J. (2003b). Mineral-melt partitioning of uranium, thorium and their daughters. *Reviews in Mineralogy and Geochemistry* **52**, 39-123.
- Bohlen, S. R., Essene, E. J. & Boettcher, A. L. (1980). Reinvestigation and application of olivine-quartz-orthopyroxene barometry. *Earth and Planetary Science Letters* **47**, 1-10.
- Bose, K. & Ganguly, J. (1995). Quartz-coesite transition revisited - reversed experimental-determination at 500-1200°C and retrieved thermochemical properties. *American Mineralogist* **80**, 231-238.
- Botcharnikov, R., Freise, M., Holtz, F. & Behrens, H. (2005). Solubility of C-O-H mixtures in natural melts: New experimental data and application range of recent models. *Annals of Geophysics* **48**, 633-646.
- Boyd, F. R. & England, J. L. (1960). Apparatus for phase-equilibrium measurements at pressures up to 50 kilobars and temperatures up to 1750°C. *Journal of Geophysical Research* **65**, 741-748.
- Brenan, J. M., Shaw, H. F., Phinney, D. L. & Ryerson, F. J. (1994). Rutile-aqueous fluid partitioning of Nb, Ta, Hf, Zr, U and Th - Implications for high-field strength element depletions in island-arc basalts. *Earth and Planetary Science Letters* **128**, 327-339.
- Brenan, J. M., Shaw, H. F., Ryerson, F. J. & Phinney, D. L. (1995). Mineral-aqueous fluid partitioning of trace elements at 900°C and 2.0 GPa - Constraints on the trace element chemistry of mantle and deep-crustal fluids. *Geochimica et Cosmochimica Acta* **59**, 3331-3350.
- Bromiley, G. D. & Redfern, S. A. T. (2008). The role of TiO₂ phases during melting of subduction-modified crust: Implications for deep mantle melting. *Earth and Planetary Science Letters* **267**, 301-308.
- Cooper, L. B., Ruscitto, D. M., Plank, T., Wallace, P. J., Syracuse, E. M. & Manning, C. E. (2012). Global variations in H₂O/Ce: 1. Slab surface temperatures beneath volcanic arcs. *Geochemistry Geophysics Geosystems* **13**, 1-27.
- Domanik, K. J. & Holloway, J. R. (1996). The stability and composition of phengitic muscovite and associated phases from 5.5 to 11 GPa: Implications for deeply subducted sediments. *Geochimica Et Cosmochimica Acta* **60**, 4133-4150.

- Elkins, L. J., Gaetani, G. A. & Sims, K. W. W. (2008). Partitioning of U and Th during garnet pyroxenite partial melting: Constraints on the source of alkaline ocean island basalts. *Earth and Planetary Science Letters* **265**, 270-286.
- Elliott, T., Plank, T., Zindler, A., White, W. & Bourdon, B. (1997). Element transport from slab to volcanic front at the Mariana arc. *Journal of Geophysical Research-Solid Earth* **102**, 14991-15019
- Elliott, T. (2003). Geochemical tracers of the slab. In: Eiler, J. (ed) *Geophysical Monograph Series* **138**. AGU, 23-45.
- Enami, M., Liou, J. G. & Mattinson, C. G. (2004). Epidote minerals in high P/T metamorphic terranes: Subduction zone and high- to ultrahigh-pressure metamorphism. *Epidotes* **56**, 347-398.
- Feineman, M. D., Ryerson, F. J., DePaolo, D. J. & Plank, T. (2007). Zoisite-aqueous fluid trace element partitioning with implications for subduction zone fluid composition. *Chemical Geology* **239**, 250-265.
- Foley, S. F., Barth, M. G. & Jenner, G. A. (2000). Rutile/melt partition coefficients for trace elements and an assessment of the influence of rutile on the trace element characteristics of subduction zone magmas. *Geochimica et Cosmochimica Acta* **64**, 933-938.
- Forneris, J. F. & Holloway, J. R. (2003). Phase equilibria in subducting basaltic crust: implications for H₂O release from the slab. *Earth and Planetary Science Letters* **214**, 187-201.
- Frei, D., Liebscher, A., Wittenberg, A. & Shaw, C. S. J. (2003). Crystal chemical controls on rare earth element partitioning between epidote-group minerals and melts: an experimental and theoretical study. *Contributions to Mineralogy and Petrology* **146**, 192-204.
- Frei, D., Liebscher, A., Franz, G. & Dulski, P. (eds.) (2004). Trace element geochemistry of epidote minerals. In: *Reviews in Mineralogy and Geochemistry* **56**, 553-604.
- Fulmer, E. C., Nebel, O. & van Westrenen, W. (2010). High-precision high field strength element partitioning between garnet, amphibole and alkaline melt from Kakanui, New Zealand. *Geochimica et Cosmochimica Acta* **74**, 2741-2759.
- Gaetani, G. A., Grove, T. L. & Bryan, W. B. (1993). The influence of water on the petrogenesis of subduction-related igneous rocks. *Nature* **365**, 332-334.
- Gaetani, G. A. & Grove, T. L. (1995). Partitioning of rare-earth elements between clinopyroxene and silicate melt - Crystal-chemical controls. *Geochimica et Cosmochimica Acta* **59**, 1951-1962.
- Gaetani, G. A. & Grove, T. L. (1998). The influence of water on melting of mantle peridotite. *Contributions to Mineralogy and Petrology* **131**, 323-346.
- Gaetani, G. A. (2004). The influence of melt structure on trace element partitioning near the peridotite solidus. *Contributions to Mineralogy and Petrology* **147**, 511-527.
- Green, T. H. & Ringwood, A. E. (1966). Origin of the calc-alkaline igneous rock suite. *Earth and Planetary Science Letters* **1**, 307-316.
- Green, T. H., Blundy, J. D., Adam, J. & Yaxley, G. M. (2000). SIMS determination of trace element partition coefficients between garnet, clinopyroxene and hydrous basaltic liquids at 2-7.5 GPa and 1080-1200°C. *Lithos* **53**, 165-187.

BIBLIOGRAPHY

- Green, T. H. & Adam, J. (2003). Experimentally-determined trace element characteristics of aqueous fluid from partially dehydrated mafic oceanic crust at 3.0 GPa, 650-700°C. *European Journal of Mineralogy* **15**, 815-830.
- Grove, T. L., Chatterjee, N., Parman, S. W. & Medard, E. (2006). The influence of H₂O on mantle wedge melting. *Earth and Planetary Science Letters* **249**, 74-89.
- Guillong, M., Meier, D. L., Allan, M. M., Heinrich, C. A. & Yardley, B. W. D. (2008). Appendix A6: SILLS: Matlab-based program for the reduction of laser ablation ICP-MS data of homogeneous materials and inclusions. *Mineralogical Association of Canada Short Course. Vancouver B. C.*, 328-333.
- Hacker, B. R. (2008). H₂O subduction beyond arcs. *Geochemistry Geophysics Geosystems* **9**, 1-24
- Hauri, E. H., Wagner, T. P. & Grove, T. L. (1994). Experimental and natural partitioning of Th, U, Pb and other trace-elements between garnet, clinopyroxene and basaltic melts. *Chemical Geology* **117**, 149-166.
- Hawkesworth, C. J., Gallagher, K., Hergt, J. M. & McDermott, F. (1993). Mantle and slab contribution in arc magmas. *Annual Reviews Earth and Planetary Science* **21**, 175-204.
- Hawkesworth, C., Turner, S., Peate, D., McDermott, F. & vanCalsteren, P. (1997). Elemental U and Th variations in island arc rocks: Implications for U-series isotopes. *Chemical Geology* **139**, 207-221.
- Heinrich, C. A., Pettke, T., Halter, W. E., Aigner-Torres, M., Audétat, A., Günther, D., Hattendorf, B., Bleiner, D., Guillong, M. & Horn, I. (2003). Quantitative multi-element analysis of minerals, fluid and melt inclusions by laser-ablation inductively-coupled-plasma mass-spectrometry. *Geochimica et Cosmochimica Acta* **67**, 3473-3497.
- Hermann, J. (2002). Allanite: thorium and light rare earth element carrier in subducted crust. *Chemical Geology* **192**, 289-306.
- Hermann, J., Spandler, C., Hack, A. & Korsakov, A. V. (2006). Aqueous fluids and hydrous melts in high-pressure and ultra-high pressure rocks: Implications for element transfer in subduction zones. *Lithos* **92**, 399-417.
- Hermann, J. & Spandler, C. J. (2008). Sediment melts at sub-arc depths: An experimental study. *Journal of Petrology* **49**, 717-740.
- Hermann, J. & Rubatto, D. (2009). Accessory phase control on the trace element signature of sediment melts in subduction zones. *Chemical Geology* **265**, 512-526.
- Hernlund, J., Leinenweber, K., Locke, D. & Tyburczy, J. A. (2006). A numerical model for steady-state temperature distributions in solid-medium high-pressure cell assemblies. *American Mineralogist* **91**, 295-305.
- Hill, E., Wood, B. J. & Blundy, J. D. (2000). The effect of Ca-Tschemak's component on trace element partitioning between clinopyroxene and silicate melt. *Lithos* **53**, 203-215.
- Hill, E., Blundy, J. D. & Wood, B. J. (2011). Clinopyroxene-melt trace element partitioning and the development of a predictive model for HFSE and Sc. *Contributions to Mineralogy and Petrology* **161**, 423-438.

- Hornig, W. S. & Hess, P. C. (2000). Partition coefficients of Nb and Ta between rutile and anhydrous haplogranite melts. *Contributions to Mineralogy and Petrology* **138**, 176-185.
- Joachim, B., Pawley, A., Lyon, I., Henkel, T., Clay, P. L., Ruzié, L., Burgess, R. & Ballentine, C. J. (2014). Partial separation of halogens during the subduction of oceanic crust. In: Abstract, C. (ed.) EGU General Assembly, Conference Abstract. Vienna.
- John, T., Klemd, R., Klemme, S., Pfander, J. A., Hoffmann, J. E. & Gao, J. (2011). Nb-Ta fractionation by partial melting at the titanite-rutile transition. *Contributions to Mineralogy and Petrology* **161**, 35-45.
- Johnson, M. C. & Plank, T. (1999). Dehydration and melting experiments constrain the fate of subducted sediments. *Geochemistry Geophysics Geosystems* **1**, 1-26.
- Kelley, K. A., Plank, T., Ludden, J. & Staudigel, H. (2003). Composition of altered oceanic crust at ODP Sites 801 and 1149. *Geochemistry Geophysics Geosystems* **4**, 1-21.
- Keppler, H. & Audétat, A. (2005). Fluid-mineral interaction at high pressure. In: Miletich, R. (ed.) Mineral behavior at extreme conditions. Budapest: *EMU notes in Mineralogy*, Eötvös University Press, 225-252.
- Kessel, R., Ulmer, P., Pettke, T., Schmidt, M. W. & Thompson, A. B. (2004). A novel approach to determine high-pressure high-temperature fluid and melt compositions using diamond-trap experiments. *American Mineralogist* **89**, 1078-1086.
- Kessel, R., Schmidt, M. W., Ulmer, P. & Pettke, T. (2005a). Trace element signature of subduction-zone fluids, melts and supercritical liquids at 120-180 km depth. *Nature* **437**, 724-727.
- Kessel, R., Ulmer, P., Pettke, T., Schmidt, M. W. & Thompson, A. B. (2005b). The water-basalt system at 4 to 6 GPa: Phase relations and second critical endpoint in a K-free eclogite at 700 to 1400°C. *Earth and Planetary Science Letters* **237**, 873-892.
- Klein, M., Stosch, H. G., Seck, H. A. & Shimizu, N. (2000). Experimental partitioning of high field strength and rare earth elements between clinopyroxene and garnet in andesitic to tonalitic systems. *Geochimica et Cosmochimica Acta* **64**, 99-115.
- Klemme, S., Blundy, J. D. & Wood, B. J. (2002). Experimental constraints on major and trace element partitioning during partial melting of eclogite. *Geochimica et Cosmochimica Acta* **66**, 3109-3123.
- Klemme, S., Prowatke, S., Hametner, K. & Günther, D. (2005). Partitioning of trace elements between rutile and silicate melts: Implications for subduction zones. *Geochimica et Cosmochimica Acta* **69**, 2361-2371.
- Klimm, K., Blundy, J. D. & Green, T. H. (2008). Trace element partitioning and accessory phase saturation during H₂O-saturated melting of basalt with implications for subduction zone chemical fluxes. *Journal of Petrology* **49**, 523-553.
- Kogiso, T., Tatsumi, Y. & Nakano, S. (1997). Trace element transport during dehydration processes in the subducted oceanic crust. 1. Experiments and implications for the origin of ocean island basalts. *Earth and Planetary Science Letters* **148**, 193-205.
- Kushiro, I. (1990). Partial melting of mantle wedge and evolution of island-arc crust. *Journal of Geophysical Research-Solid Earth and Planets* **95**, 15929-15939.

BIBLIOGRAPHY

- Kushiro, I. & Hirose, K. (1992). Experimental determination of composition of melt formed by equilibrium partial melting of peridotite at high-pressures using aggregates of diamond grains. *Proceedings of the Japan Academy Series B-Physical and Biological Sciences* **68**, 63-68.
- Lambert, I. B. & Wyllie, P. J. (1972). Melting of gabbro (quartz eclogite) with excess water to 35 kilobars, with geological applications. *Journal of Geology* **80**, 693-708.
- Leake, B. E., Woolley, A. R., Arps, C. E. S., Birch, W. D., Gilbert, M. C., Grice, J. D., Hawthorne, F. C., Kato, A., Kisch, H. J., Krivovichev, V. G., Linthout, K., Laird, J., Mandarino, J. A., Maresch, W. V., Nickel, E. H., Rock, N. M. S., Schumacher, J. C., Smith, D. C., Stephenson, N. C. N., Ungaretti, L., Whittaker, E. J. W. & Guo, Y. Z. (1997). Nomenclature of amphiboles: Report of the subcommittee on amphiboles of the International Mineralogical Association, commission on new minerals and mineral names. *American Mineralogist* **82**, 1019-1037.
- Leake, B. E., Woolley, A. R., Birch, W. D., Burke, E. A. J., Ferraris, G., Grice, J. D., Hawthorne, F. C., Kisch, H. J., Krivovichev, V. G., Schumacher, J. C., Stephenson, N. C. N. & Whittaker, E. J. W. (2003). Nomenclature of amphiboles: Additions and revisions to the International Mineralogical Association's 1997 recommendations. *Canadian Mineralogist* **41**, 1355-1362.
- Linnen, R. L. & Keppler, H. (1997). Columbite solubility in granitic melts: consequences for the enrichment and fractionation of Nb and Ta in the Earth's crust. *Contributions to Mineralogy and Petrology* **128**, 213-227.
- Liu, J., Bohlen, S. R. & Ernst, W. G. (1996). Stability of hydrous phases in subducting oceanic crust. *Earth and Planetary Science Letters* **143**, 161-171.
- Longerich, H. P., Jackson, S. E. & Günther, D. (1996). Laser ablation inductively coupled plasma mass spectrometric transient signal data acquisition and analyte concentration calculation. *Journal of Analytical Atomic Spectrometry* **11**, 899-904.
- Lucassen, F., Dulski, P., Abart, R., Franz, G., Rhede, D. & Romer, R. L. (2010). Redistribution of HFSE elements during rutile replacement by titanite. *Contributions to Mineralogy and Petrology* **160**, 279-295.
- Lundstrom, C. C., Shaw, H. F., Ryerson, F. J., Williams, Q. & Gill, J. (1998). Crystal chemical control of clinopyroxene-melt partitioning in the Di-Ab-An system: Implications for elemental fractionations in the depleted mantle. *Geochimica et Cosmochimica Acta* **62**, 2849-2862.
- Manning, C. E. (1998). Fluid composition at the blueschist - eclogite transition in the model system Na₂O-MgO-Al₂O₃-SiO₂-H₂O-HCl. *Schweizerische Mineralogische und Petrographische Mitteilungen* **78**, 225-242.
- Manning, C. E. (2004). The chemistry of subduction-zone fluids. *Earth and Planetary Science Letters* **223**, 1-16.
- Martin, L. A. J., Wood, B. J., Turner, S. & Rushmer, T. (2011). Experimental measurements of trace element partitioning between lawsonite, zoisite and fluid and their implication for the composition of arc magmas. *Journal of Petrology* **52**, 1049-1075.
- Martindale, M., Skora, S., Pickles, J., Elliott, T., Blundy, J. & Avanzinelli, R. (2013). High pressure phase relations of subducted volcanoclastic sediments from the west pacific and their implications for the geochemistry of Mariana arc magmas.

- Chemical Geology* **342**, 94-109.
- McCulloch, M. T. & Gamble, J. A. (1991). Geochemical and geodynamical constraints on subduction zone magmatism. *Earth and Planetary Science Letters* **102**, 358-374.
- Melzer, S. & Wunder, B. (2000). Island-arc basalt alkali ratios: Constraints from phengite-fluid partitioning experiments. *Geology* **28**, 583-586.
- Morris, J. D., Leeman, W. P. & Tera, F. (1990). The Subducted component in island-arc lavas - Constraints from Be isotopes and B-Be systematics. *Nature* **344**, 31-36.
- Nagasawa, H. (1966). Trace element partition coefficient in ionic crystals. *Science* **152**, 767-769.
- Nandedkar, R. H. (2014). Evolution of hydrous mantle-derived calc-alkaline liquids by fractional crystallization at 0.7 and 0.4 GPa - An experimental study. Department of Earth Sciences. Zurich: ETH Zurich, 232.
- Nichols, G. T., Wyllie, P. J. & Stern, C. R. (1994). Subduction zone-melting of pelagic sediments constrained by melting experiments. *Nature* **371**, 785-788.
- Onuma, N., Higuchi, H., Wakita, H. & Hagasawa, H. (1968). Trace element partition between two pyroxenes and the host lava. *Earth and Planetary Science Letters* **5**, 57-51.
- Oxburgh, E. R. & Turcotte, D. L. (1971). Origin of paired metamorphic belts and crustal dilation in island arc regions. *Journal of Geophysical Research* **76**, 1315-&.
- Pawley, A. R. & Holloway, J. R. (1993). Water sources for subduction zone volcanism - New experimental constraints. *Science* **260**, 664-667.
- Pearce, J. A., Stern, R. J., Bloomer, S. H. & Fryer, P. (2005). Geochemical mapping of the Mariana arc-basin system: Implications for the nature and distribution of subduction components. *Geochemistry Geophysics Geosystems* **6**, 1-27.
- Pertermann, M., Hirschmann, M. M., Hametner, K., Günther, D. & Schmidt, M. W. (2004). Experimental determination of trace element partitioning between garnet and silica-rich liquid during anhydrous partial melting of MORB-like eclogite. *Geochemistry Geophysics Geosystems* **5**, 1-23.
- Pettke, T., Oberli, F., Audétat, A., Guillong, M., Simon, A. C., Hanley, J. J. & Klemm, L. M. (2012). Recent developments in element concentration and isotope ratio analysis of individual fluid inclusions by laser ablation single and multiple collector ICP-MS. *Ore Geology Reviews* **44**, 10-38.
- Plank, T. & Langmuir, C. H. (1993). Tracing trace-elements from sediment input to volcanic output at subduction zones. *Nature* **362**, 739-743.
- Plank, T. & Langmuir, C. H. (1998). The chemical composition of subducting sediment and its consequences for the crust and mantle. *Chemical Geology* **145**, 325-394.
- Plank, T. (2005). Constraints from thorium/lanthanum on sediment recycling at subduction zones and the evolution of the continents. *Journal of Petrology* **46**, 921-944.
- Plank, T., Cooper, L. B. & Manning, C. E. (2009). Emerging geothermometers for estimating slab surface temperatures. *Nature Geoscience* **2**, 611-615.
- Poli, S. & Schmidt, M. W. (1997). The high-pressure stability of hydrous phases in orogenic belts: An experimental approach on eclogite-forming processes. *Tectonophysics* **273**, 169-184.

BIBLIOGRAPHY

- Poli, S. & Schmidt, M. W. (2002). Petrology of subducted slabs. *Annual Review of Earth and Planetary Sciences* **30**, 207-235.
- Prowatke, S. & Klemme, S. (2005). Effect of melt composition on the partitioning of trace elements between titanite and silicate melt. *Geochimica et Cosmochimica Acta* **69**, 695-709.
- Rapp, R. P. & Watson, E. B. (1995). Dehydration melting of metabasalt at 8-32 kbar - Implications for continental growth and crust-mantle recycling. *Journal of Petrology* **36**, 891-931.
- Ringwood, A. E. (1974). The petrological evolution of island arc systems. *Journal of the Geological Society of London* **130**, 183-204.
- Rushmer, T. (1991). Partial melting of 2 amphibolites - Contrasting experimental results under fluid-absent conditions. *Contributions to Mineralogy and Petrology* **107**, 41-59.
- Ryabchikov, I. D. & Boettcher, A. L. (1980). Experimental evidence at high-pressure for potassic metasomatism in the mantle of the Earth. *American Mineralogist* **65**, 915-919.
- Ryerson, F. J. & Watson, E. B. (1987). Rutile saturation in magmas - Implications for Ti-Nb-Ta depletion in island-arc basalts. *Earth and Planetary Science Letters* **86**, 225-239.
- Scambelluri, M. & Philippot, P. (2001). Deep fluids in subduction zones. *Lithos* **55**, 213-227.
- Scambelluri, M., Pettke, T. & van Roermund, H. L. M. (2008). Majoritic garnets monitor deep subduction fluid flow and mantle dynamics. *Geology* **36**, 59-62.
- Schmidt, A., Weyer, S., John, T. & Brey, G. P. (2009). HFSE systematics of rutile-bearing eclogites: New insights into subduction zone processes and implications for the Earth's HFSE budget. *Geochimica et Cosmochimica Acta* **73**, 455-468.
- Schmidt, M. W. (1996). Experimental constraints on recycling of potassium from subducted oceanic crust. *Science* **272**, 1927-1930.
- Schmidt, M. W. & Poli, S. (1998). Experimentally based water budgets for dehydrating slabs and consequences for arc magma generation. *Earth and Planetary Science Letters* **163**, 361-379.
- Schmidt, M. W. & Ulmer, P. (2004). A rocking multianvil: Elimination of chemical segregation in fluid-saturated high-pressure experiments. *Geochimica et Cosmochimica Acta* **68**, 1889-1899.
- Schmidt, M. W., Vielzeuf, D. & Auzanneau, E. (2004a). Melting and dissolution of subducting crust at high pressures: the key role of white mica. *Earth and Planetary Science Letters* **228**, 65-84.
- Schmidt, M. W., Dardon, A., Chazot, G. & Vannucci, R. (2004b). The dependence of Nb and Ta rutile-melt partitioning on melt composition and Nb/Ta fractionation during subduction processes. *Earth and Planetary Science Letters* **226**, 415-432.
- Sekine, T. & Wyllie, P. J. (1982). Phase-Relationships in the System $Kalsio_4-Mg_2sio_4-Sio_2-H_2O$ as a Model for Hybridization between Hydrous Siliceous Melts and Peridotite. *Contributions to Mineralogy and Petrology* **79**, 368-374.
- Sekine, T. & Wyllie, P. J. (1983). Phase-relationships in the join grossularite pyrope 7.5% H_2O at 30 Kb. *American Journal of Science* **283**, 435-453.

- Seo, J. H., Guillong, M., Aerts, M., Zajacz, Z. & Heinrich, C. A. (2011). Microanalysis of S, Cl, and Br in fluid inclusions by LA-ICP-MS. *Chemical Geology* **284**, 35-44.
- Skora, S. & Blundy, J. (2010). High-pressure hydrous phase relations of radiolarian clay and implications for the involvement of subducted sediment in arc magmatism. *Journal of Petrology* **51**, 2211-2243.
- Sorensen, S. S., Grossman, J. N. & Perfit, M. R. (1997). Phengite-hosted LILE enrichment in eclogite and related rocks: Implications for fluid-mediated mass transfer in subduction zones and arc magma genesis. *Journal of Petrology* **38**, 3-34.
- Spandler, C., Hermann, J., Arculus, R. & Mavrogenes, J. (2003). Redistribution of trace elements during prograde metamorphism from lawsonite blueschist to eclogite facies; implications for deep subduction-zone processes. *Contributions to Mineralogy and Petrology* **146**, 205-222.
- Spandler, C., Mavrogenes, J. & Hermann, J. (2007). Experimental constraints on element mobility from subducted sediments using high-P synthetic fluid/melt inclusions. *Chemical Geology* **239**, 228-249.
- Spandler, C., Yaxley, G., Green, D. H. & Rosenthal, A. (2008). Phase relations and melting of anhydrous k-bearing eclogite from 1200 to 1600°C and 3 to 5 GPa. *Journal of Petrology* **49**, 771-795.
- Spandler, C. & Pirard, C. (2013). Element recycling from subducting slabs to arc crust: A review. *Lithos* **170-171**, 208-223.
- Stalder, R., Foley, S. F., Brey, G. P., Forsythe, L. M. & Horn, I. (1997). First results from a new experimental technique to determine fluid/solid trace element partition coefficients using diamond aggregate extraction traps. *Neues Jahrbuch für Mineralogie-Abhandlungen* **172**, 117-132.
- Stalder, R., Foley, S. F., Brey, G. P. & Horn, I. (1998). Mineral aqueous fluid partitioning of trace elements at 900-1200°C and 3.0-5.7 GPa: New experimental data for garnet, clinopyroxene, and rutile, and implications for mantle metasomatism. *Geochimica et Cosmochimica Acta* **62**, 1781-1801.
- Stalder, R., Ulmer, P., Thompson, A. B. & Günther, D. (2000). Experimental approach to constrain second critical end points in fluid/silicate systems: Near-solidus fluids and melts in the system albite-H₂O. *American Mineralogist* **85**, 68-77.
- Stalder, R., Ulmer, P., Thompson, A. B. & Günther, D. (2001). High pressure fluids in the system MgO-SiO₂-H₂O under upper mantle conditions. *Contributions to Mineralogy and Petrology* **140**, 607-618.
- Stalder, R., Ulmer, P. & Günther, D. (2002). Fluids in the system forsterite-phlogopite-H₂O at 60 kbar. *Schweizerische Mineralogische und Petrographische Mitteilungen* **82**, 15-24.
- Staudigel, H. (2003). Hydrothermal alteration processes in the oceanic crust. In: *Treatise on Geochemistry*, 511-535.
- Stern, C. R. & Wyllie, P. J. (1973). Melting relations of basalt-andesite-rhyolite-H₂O and a pelagic red clay at 30 kbars. *Contributions to Mineralogy and Petrology* **42**, 313-323.

BIBLIOGRAPHY

- Stern, C. R., Huang, W. L. & Wyllie, P. J. (1975). Basalt-andesite-rhyolite-H₂O-crystallization intervals with excess H₂O and H₂O-undersaturated liquidus surfaces to 35 kilobars, with implications for magma genesis. *Earth and Planetary Science Letters* **28**, 189-196.
- Stern, C. R. & Wyllie, P. J. (1978). Phase compositions through crystallization intervals in basalt-andesite-H₂O at 30 kbar with implications for subduction zone magmas. *American Mineralogist* **63**, 641-663.
- Stern, R. J. (2002). Subduction zones. *Reviews of Geophysics* **40**, 3-1 - 3-38.
- Sun, S. S. & McDonough, W. F. (1989). Chemical and isotopic systematics of oceanic basalts implications for mantle composition and processes. In: Saunders, A. D. & Norry, M. J. (eds.) *Magmatism in the Ocean Basin: Geological Society Special Publication*, 313-345.
- Syracuse, E. M. & Abers, G. A. (2006). Global compilation of variations in slab depth beneath arc volcanoes and implications. *Geochemistry Geophysics Geosystems* **7**, 1-18.
- Syracuse, E. M., van Keken, P. E. & Abers, G. A. (2010). The global range of subduction zone thermal models. *Physics of the Earth and Planetary Interiors* **183**, 73-90.
- Tatsumi, Y., Sakuyama, M., Fukuyama, H. & Kushiro, I. (1983). Generation of arc basalt magmas and thermal structure of the mantle wedge in subduction zones. *Journal of Geophysical Research* **88**, 5815-5825.
- Tatsumi, Y. & Eggins, F. (1995). Subduction Zone Magmatism. Blackwell Science.
- Tiepolo, M., Oberti, R. & Vannucci, R. (2002). Trace-element incorporation in titanite: constraints from experimentally determined solid/liquid partition coefficients. *Chemical Geology* **191**, 105-119.
- Truckenbrodt, J. & Johannes, W. (1999). H₂O loss during piston-cylinder experiments. *American Mineralogist* **84**, 1333-1335.
- Truckenbrodt, J., Ziegenbein, D. & Johannes, W. (1997). Redox conditions in piston-cylinder apparatus: The different behavior of boron nitride and unfired pyrophyllite assemblies. *American Mineralogist* **82**, 337-344.
- Ulmer, P. & Trommsdorff, V. (1995). Serpentine stability to mantle depths and subduction-related magmatism. *Science* **268**, 858-861.
- Ulmer, P. (2001). Partial melting in the mantle wedge - the role of H₂O in the genesis of mantle-derived 'arc-related' magmas. *Physics of the Earth and Planetary Interiors* **127**, 215-232.
- van Keken, P. E., Kiefer, B. & Peacock, S. M. (2002). High-resolution models of subduction zones: Implications for mineral dehydration reactions and the transport of water into the deep mantle. *Geochemistry Geophysics Geosystems* **3**, 1-20.
- van Keken, P. E., Hacker, B. R., Syracuse, E. M. & Abers, G. A. (2011). Subduction factory: 4. Depth-dependent flux of H₂O from subducting slabs worldwide. *Journal of Geophysical Research-Solid Earth* **116**, 1-15.
- Van Orman, J. A., Grove, T. L., Shimizu, N. & Layne, G. D. (2002). Rare earth element diffusion in a natural pyrope single crystal at 2.8 GPa. *Contributions to Mineralogy and Petrology* **142**, 416-424.

- van Westrenen, W., Wood, B. J. & Blundy, J. D. (2001). A predictive thermodynamic model of garnet-melt trace element partitioning. *Contributions to Mineralogy and Petrology* **142**, 219-234.
- van Westrenen, W. & Draper, D.S. (2007). Quantifying garnet-melt trace element partitioning using lattice-strain theory: New crystal-chemical and thermodynamic constraints. *Contributions to Mineralogy and Petrology* **154**, 717-730.
- Vielzeuf, D. & Schmidt, M. W. (2001). Melting relations in hydrous systems revisited: application to metapelites, metagreywackes and metabasalts. *Contributions to Mineralogy and Petrology* **141**, 251-267.
- Wallace, P. J. (2005). Volatiles in subduction zone magmas: concentrations and fluxes based on melt inclusion and volcanic gas data. *Journal of Volcanology and Geothermal Research* **140**, 217-240.
- Wood, B. J. & Blundy, J. D. (2002). The effect of H₂O on crystal-melt partitioning of trace elements. *Geochimica et Cosmochimica Acta* **66**, 3647-3656.
- Wyllie, P. J. & Ryabchikov, I. D. (2000). Volatile components, magmas, and critical fluids in upwelling mantle. *Journal of Petrology* **41**, 1195-1206.
- Xiong, X. L., Adam, J. & Green, T. H. (2005). Rutile stability and rutile/melt HFSE partitioning during partial melting of hydrous basalt: Implications for TTG genesis. *Chemical Geology* **218**, 339-359.
- Yoder, H. S. & Kushiro, I. (1969). Melting of a hydrous phase - Phlogopite. *American Journal of Science* **267**, 558-582.
- Zack, T., Rivers, T. & Foley, S. F. (2001). Cs-Rb-Ba systematics in phengite and amphibole: an assessment of fluid mobility at 2.0 GPa in eclogites from Trescolmen, Central Alps. *Contributions to Mineralogy and Petrology* **140**, 651-669.
- Zack, T., Foley, S. F. & Rivers, T. (2002). Equilibrium and disequilibrium trace element partitioning in hydrous eclogites (Trescolmen, Central Alps). *Journal of Petrology* **43**, 1947-1974.
- Zack, T., Kronz, A., Foley, S. F. & Rivers, T. (2002). Trace element abundances in rutiles from eclogites and associated garnet mica schists. *Chemical Geology* **184**, 97-122.

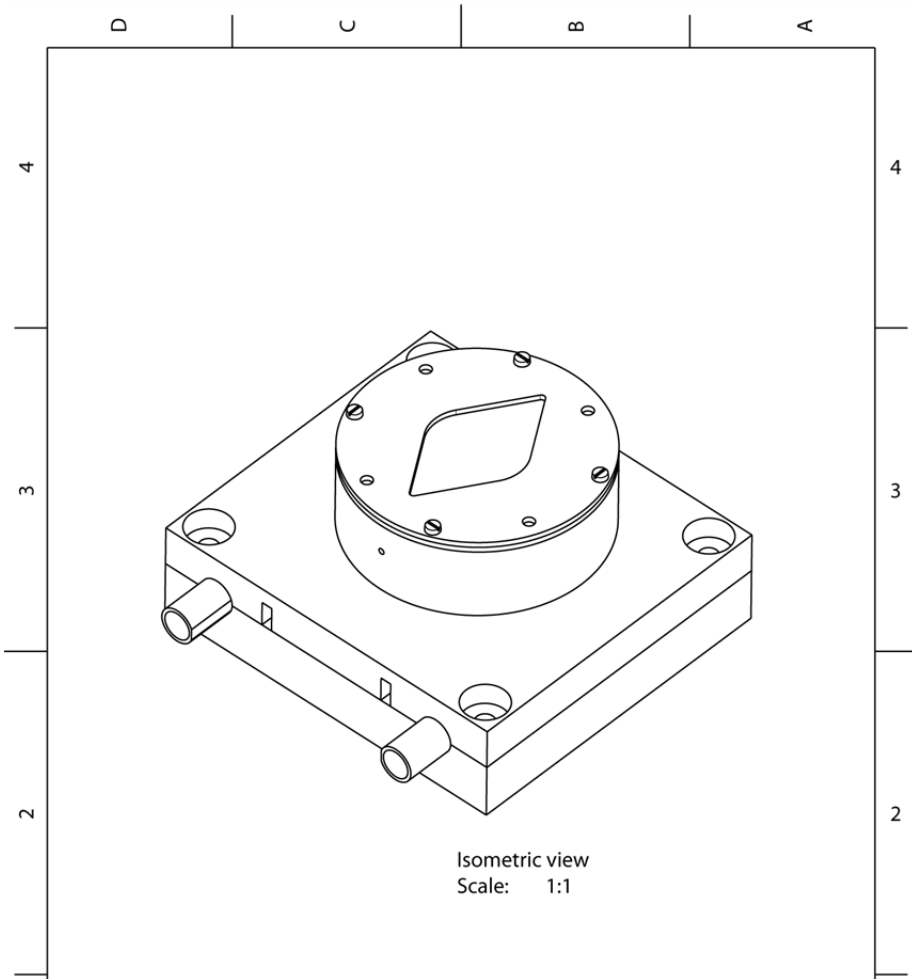
BIBLIOGRAPHY

Appendix A

In this section, the construction plans for the various parts of the newly designed external freezing stage are provided. All construction plans and images were drawn by Dr. Claudio Madonna, ETH Zürich.

- A1 Setup
- A2 Lower plate
- A3 Upper plate
- A4 Copper plate
- A5 Capsule holder (lower part)
- A6 Capsule holder (upper part)
- A7 Ablation chamber
- A8 Glass mount holder (overview)
- A9 Glass mount holder (lower part)
- A10 Glass mount holder (upper part)
- A11 Styrofoam insulation
- A12 Overview images freezing stage

A1 – Setup

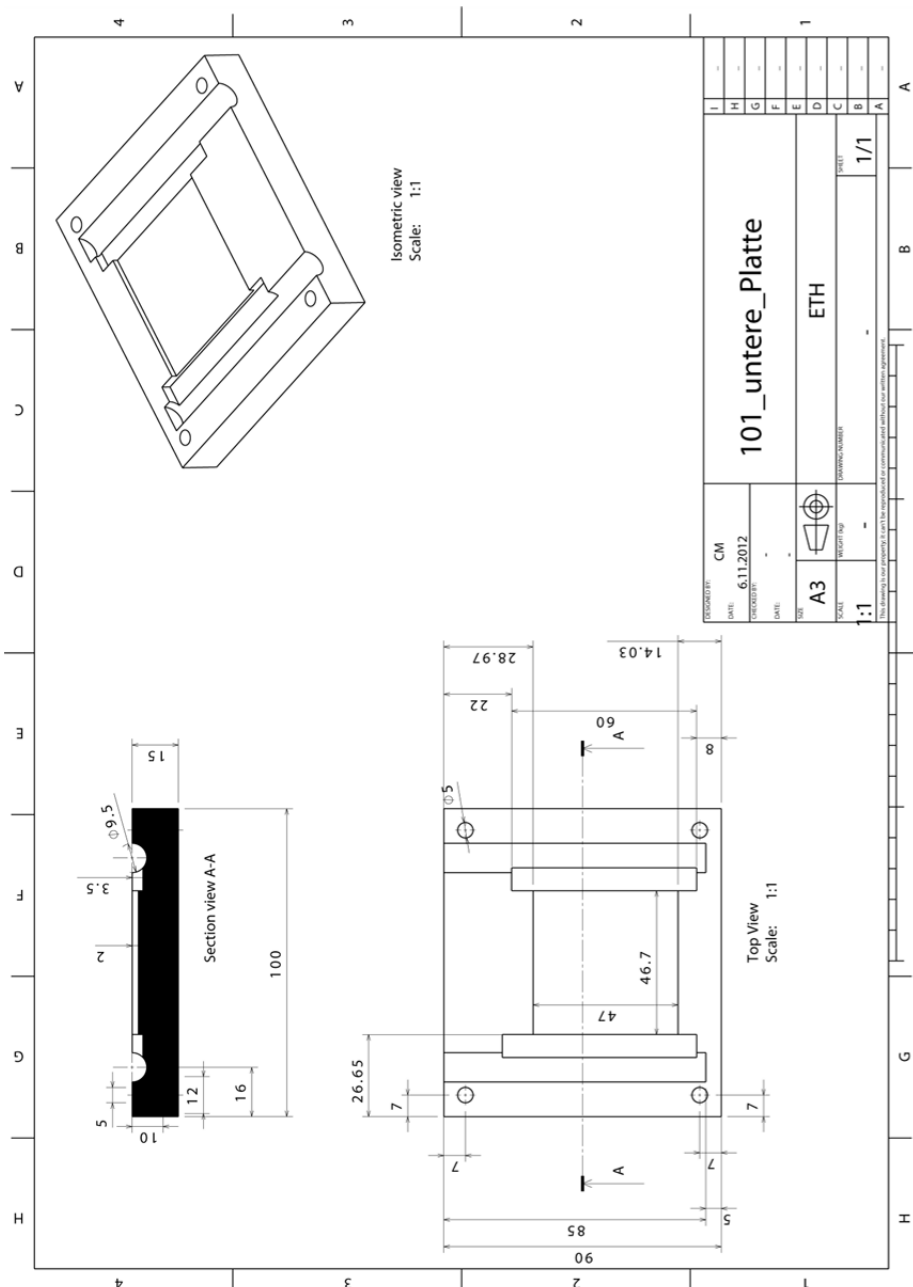


Isometric view
Scale: 1:1

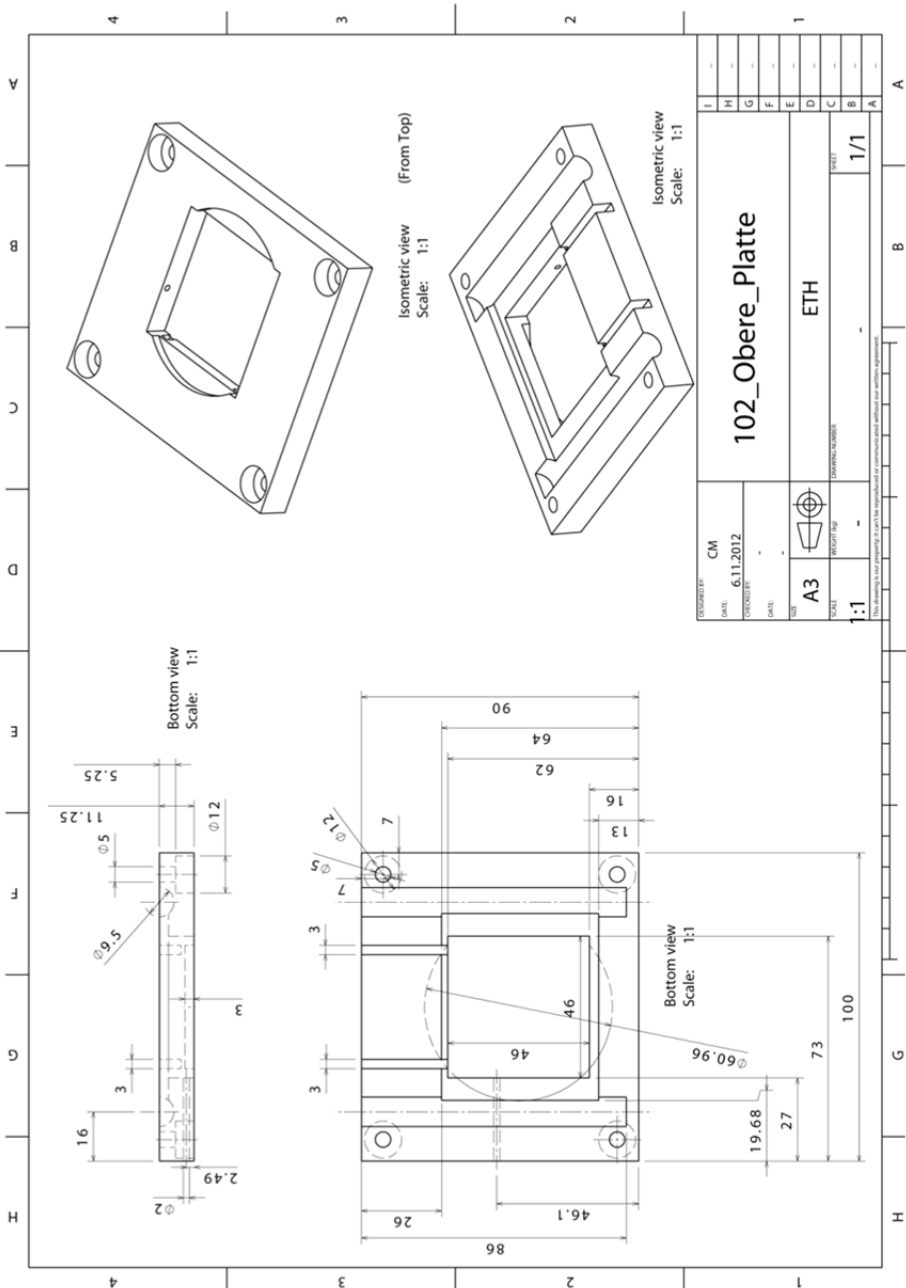
DESIGNED BY: C. Madonna		100-Setup	I	-
DATE: 08.11.2012			H	-
CHECKED BY: -			G	-
DATE: -		F	-	
SIZE: A4		ETH	E	-
SCALE: 1:1	WEIGHT (kg): -	DRAWING NUMBER: -	D	-
		SHEET: 1/1	C	-
			B	-
			A	-

This drawing is our property. It can't be reproduced or communicated without our written agreement.

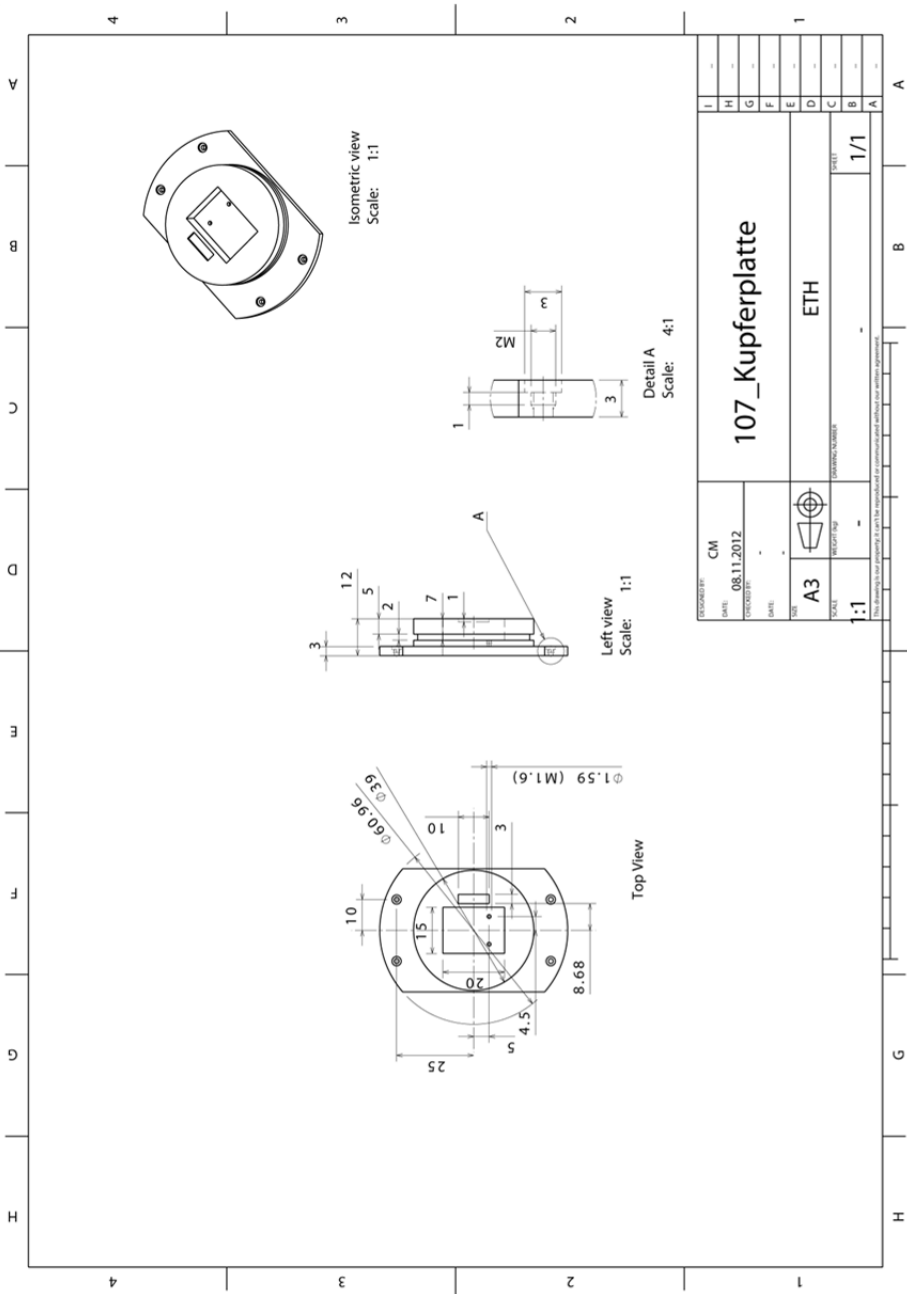
A2 – Lower plate



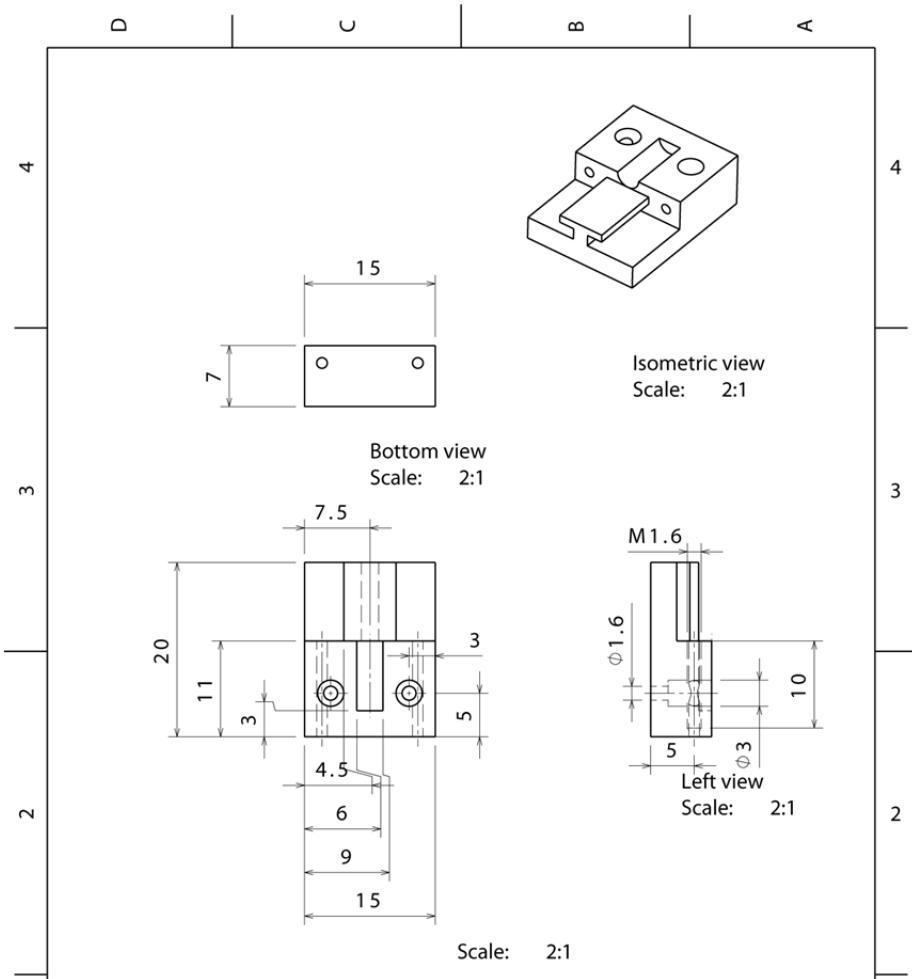
A3 – Upper plate



A4 – Copper plate

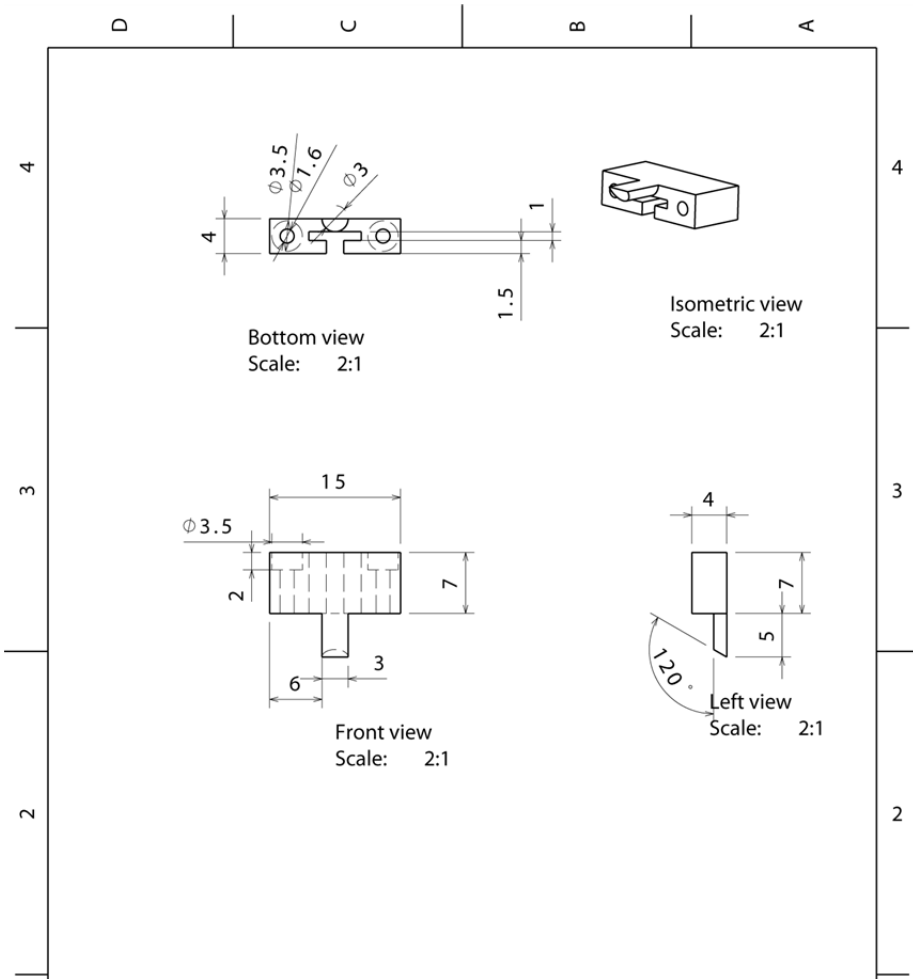


A5 – Capsule holder (lower part)



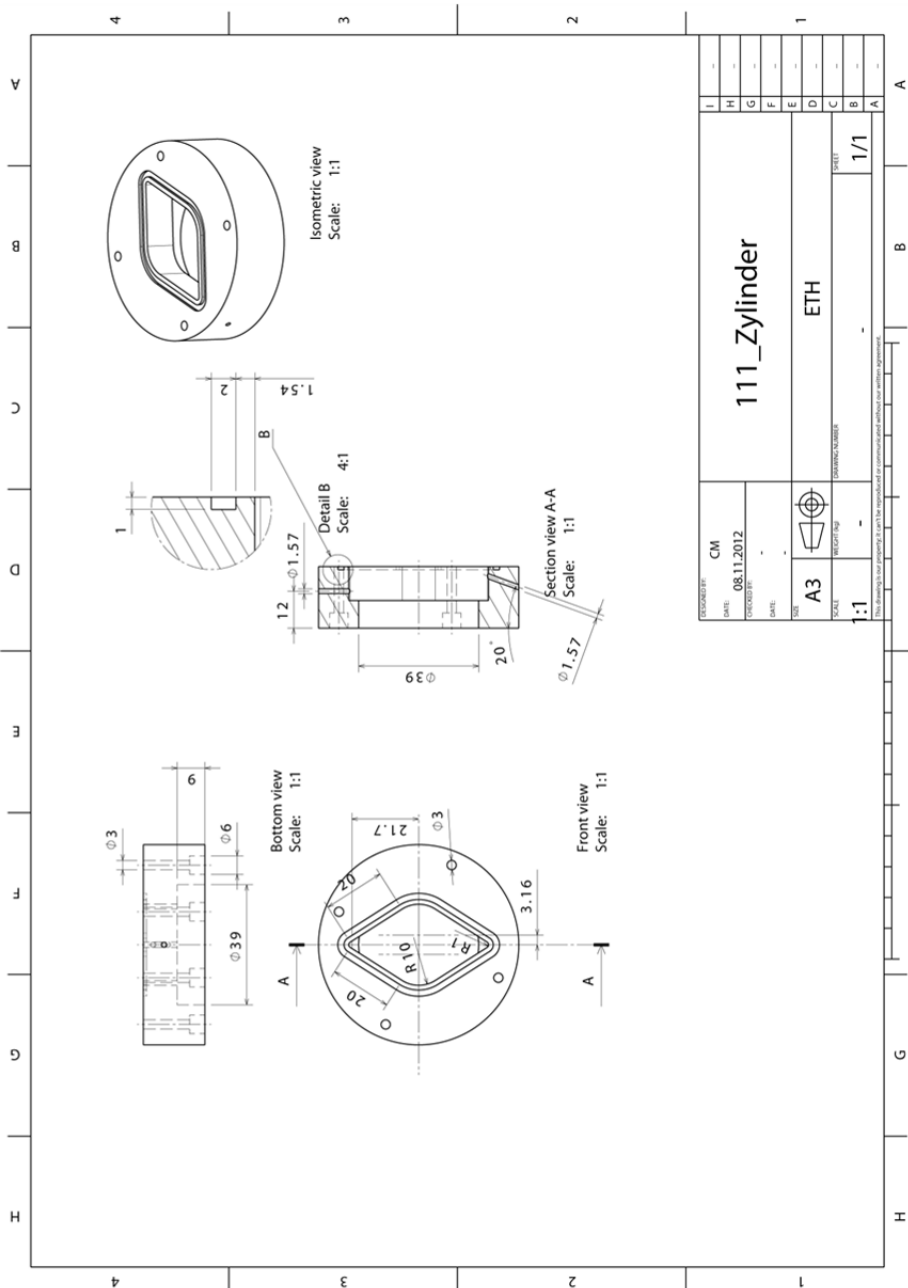
DESIGNED BY: C. Madonna	<h2>109_Probenhalter1</h2>		I	-
DATE: 30.10.2012			H	-
CHECKED BY: -			G	-
DATE: -			F	-
SIZE: A4	<h2>ETH</h2>		E	-
SCALE: 1:1			WEIGHT (kg): -	D
DRAWING NUMBER: -		SHEET: 1/1	C	-
This drawing is our property. It can't be reproduced or communicated without our written agreement.			B	-
			A	-

A6 – Capsule holder (upper part)

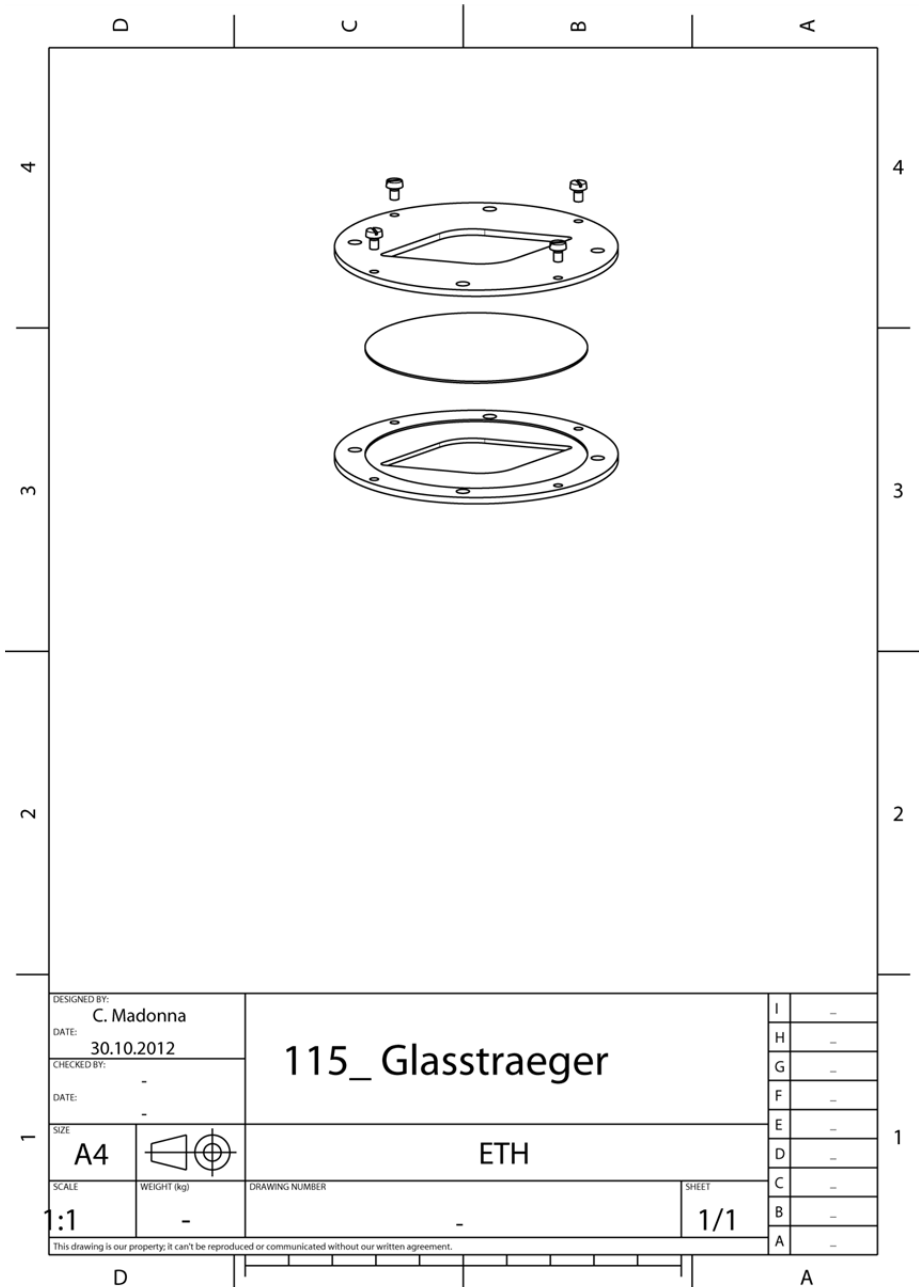


DESIGNED BY: C. Madonna	<h2>110_Probenhalter2</h2>	I	-
DATE: 30.10.2012		H	-
CHECKED BY: -		G	-
DATE: -		F	-
SIZE: A4	<h2>ETH</h2>	E	-
SCALE: 1:1	WEIGHT (kg): -	D	-
DRAWING NUMBER: -	SHEET: 1/1	C	-
This drawing is our property. It can't be reproduced or communicated without our written agreement.		B	-
		A	-

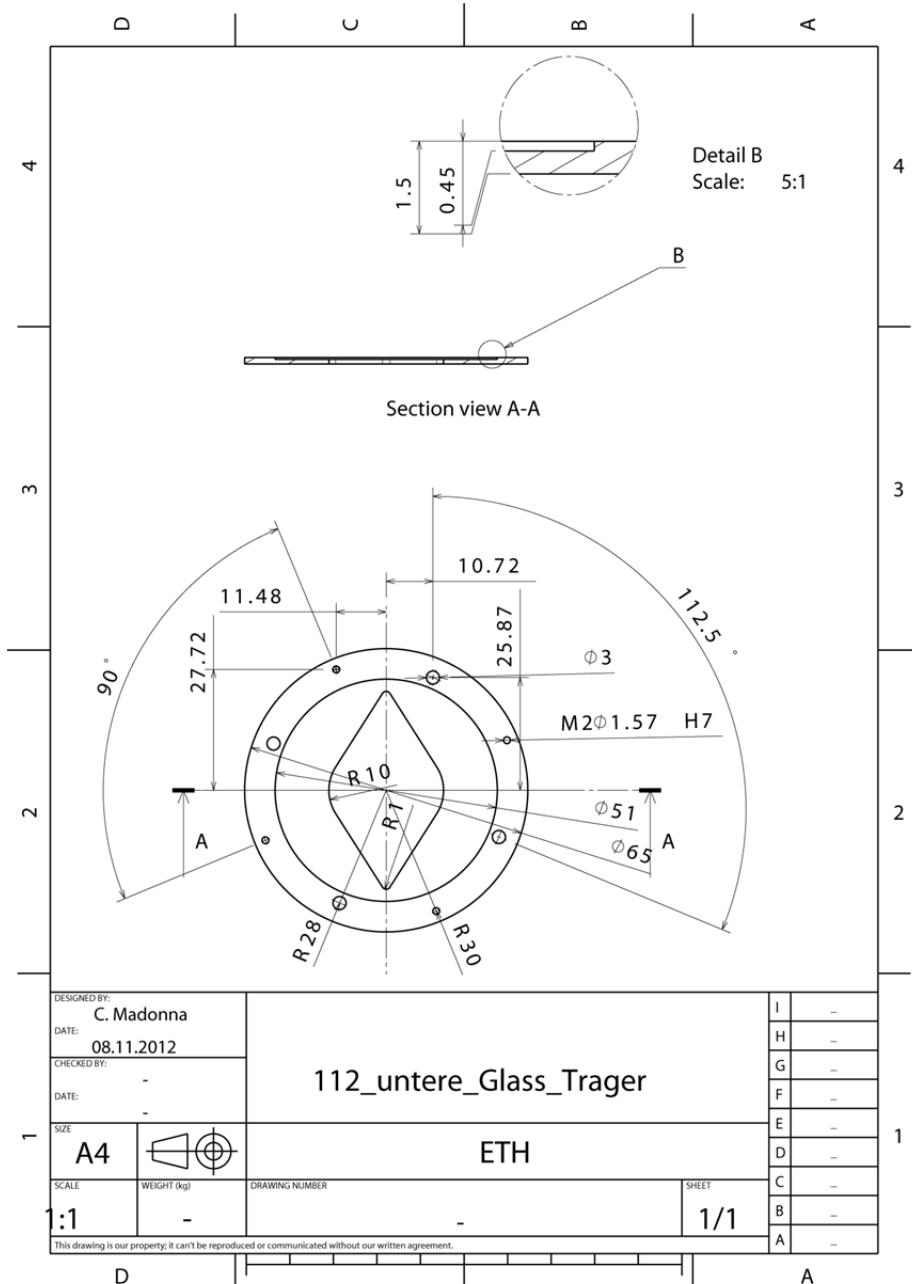
A7 – Ablation chamber



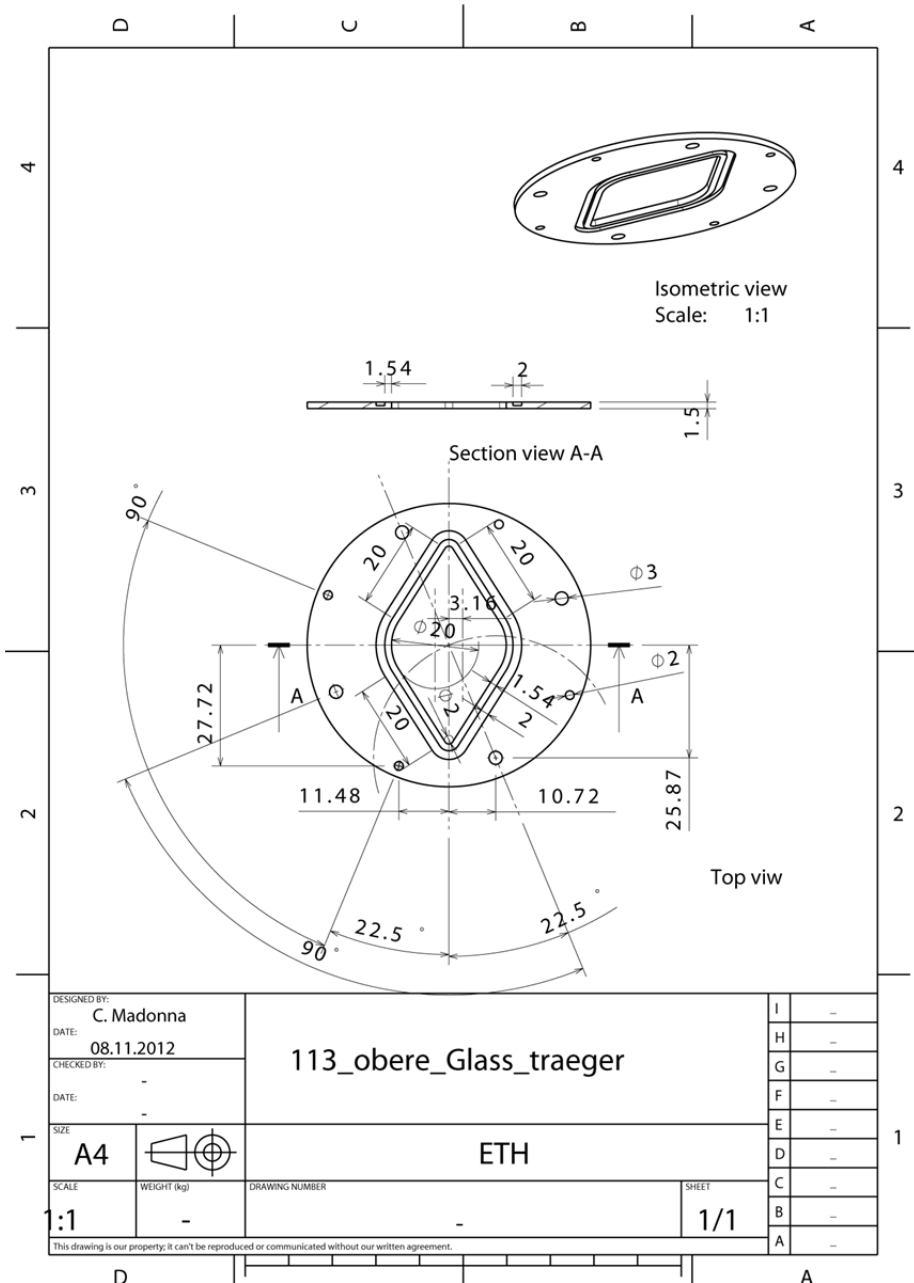
A8 – Glass mount holder (overview)



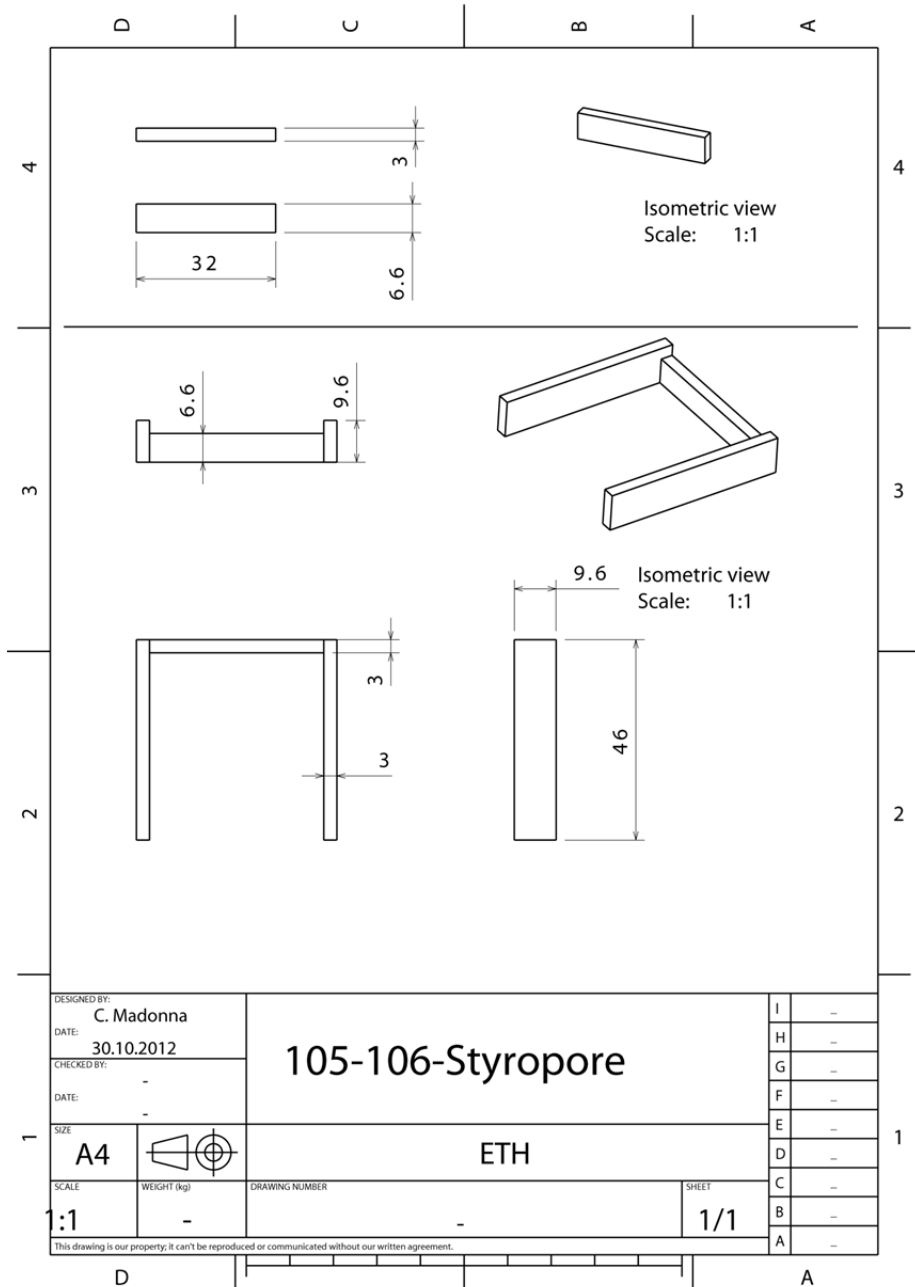
A9 – Glass mount holder (lower part)



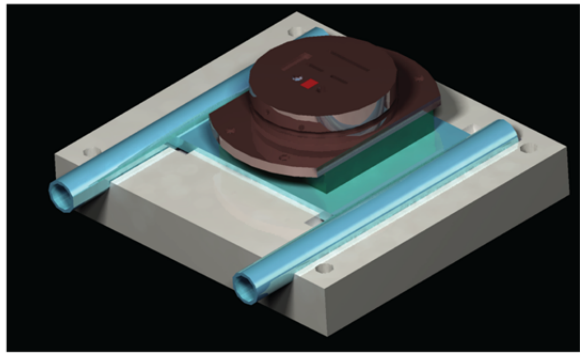
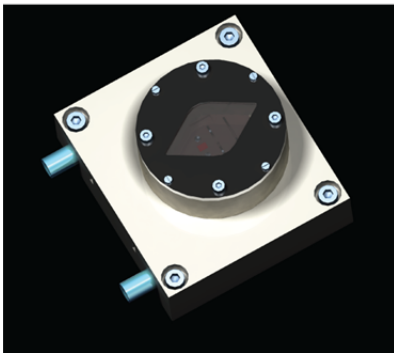
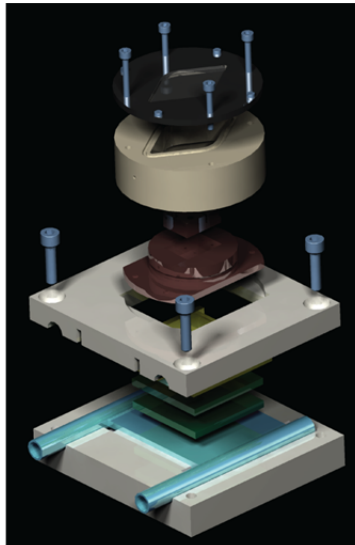
A10 – Glass mount holder (upper part)



A11 – Styrofoam insulation



A12 – Overview images freezing stage



Appendix B

Lattice strain model

To model crystallization and partial melting processes in the Earth's interior, partition coefficients (D-values) between minerals and the coexisting melts are required to obtain realistic models. The D-values are often assumed constant due to the incompleteness of experimentally determined partition coefficients in the literature (for melts, but especially for fluids). However, they are thermodynamic variables and change with pressure, temperature and composition (e.g. Beattie, 1994; Blundy and Wood, 1994, 2003a, 2003b; Wood and Blundy, 2002; Prowatke and Klemme, 2005). An attempt was made in recent years to develop models that allow prediction of partition coefficients. The logarithm of D(mineral/melt) plotted against the ionic radii (r_i) of specific trace elements with the same charge (e.g. REE³⁺) result in a theoretically ideal parabola (Onuma et al., 1968) due to elastic strain energy considerations developed by Nagasawa (1966) and Beattie (1994). The crystal lattice-strain model was formulated (Blundy and Wood, 1994, 2003a, 2003b; Van Westrenen et al., 2001; Van Westrenen and Draper, 2007):

$$D_i(P, T, X) = D_0(P, T, X) \cdot e^{\left(\frac{-4 \cdot \pi \cdot E \cdot N_A \times \left(\frac{r_0}{2} (r_i - r_0)^2 + \frac{1}{3} (r_i - r_0)^3 \right)}{R \cdot T} \right)}$$

where r_0 : ideal radius; E: Young's modulus; R: ideal gas constant; N_A : Avogadro's constant; T: temperature (K) and D_0 : maximum partition coefficient for r_0 .

Figure B1 shows the partition coefficients of garnet at various temperatures for REEs and Sc plotted against their ionic radii. The solid red lines are the weighted fit parabola using the equation given above (Blundy and Wood, 1994). Due to uncertainties in the D-values, especially at the low-temperature experimental runs, the parabola are non-ideal but nevertheless reveal a peak at the HREE consistent with the lattice strain models. Fitting of all three parameters (D_0 , E and r_0) simultaneously is hindered by the interrelated nature of the parameters. We, therefore, fix E for each experiment using the predicted values of Van Westrenen and Draper (2007). Table B1 lists the fixed (E) and fitted (D_0 , r_0) values (based on garnet and volatile major element analyses from Chapter 4 and 5) and compare them to the predicted values of Van Westrenen et al. (2001) and Van Westrenen and Draper (2007). Our results reveal that the obtained D_0 -values are unrealistic large for most runs and r_0 elevated compared to those of Van Westrenen and Draper (2007), but in better

APPENDIX

agreement with those of Van Westrenen et al. (2001). Similar results were observed by Klimm et al. (2008), who performed water-saturated experiments under very similar conditions as those in this study. They argued that discrepancies result from the large temperature dependence of r_0 in the former model (Van Westrenen and Draper, 2007), which was originally developed for anhydrous systems at higher temperatures.

Table B1. Lattice strain fit parameters.

Run Nr.	SL39	1 σ	SL15	1 σ	SL4	1 σ	SL14	1 σ	SL2	1 σ	SL11	1 σ
T (°C)	700		750		800		850		900		1000	
E ¹ (fixed)	660		646		636		631		585		581	
D ₀ (fitted)	1651	180	930	74	1485	207	421	68	125	10	42	2
r ₀ (fitted)	0.935	0.003	0.936	0.003	0.931	0.005	0.939	0.007	0.954	0.005	0.942	0.003
r ₀ (predicted) ¹	0.900		0.904		0.908		0.909		0.913		0.917	
r ₀ (predicted) ²	0.949		0.950		0.951		0.950		0.950		0.948	
Run Nr.	SL21	1 σ	SL23	1 σ	SL24	1 σ	SL17	1 σ	SL25	1 σ		
T (°C)	700		800		900		1000		1100			
E ¹ (fixed)	673		648		608		595		605			
D ₀ (fitted)	76	5	153	4	205	6	19	1	9	0.5		
r ₀ (fitted)	0.961	0.004	0.976	0.003	0.959	0.002	0.965	0.005	0.961	0.004		
r ₀ (predicted) ¹	0.890		0.899		0.907		0.912		0.918			
r ₀ (predicted) ²	0.938		0.942		0.944		0.943		0.943			
Run Nr.	SLK4	1 σ	SLK3	1 σ	SLK2	1 σ						
T (°C)	700		800		900							
E ¹ (fixed)	679		685		634							
D ₀ (fitted)	4350	354	429	67	2786	493						
r ₀ (fitted)	0.951	0.004	0.942	0.007	0.914	0.007						
r ₀ (predicted) ¹	0.891		0.900		0.907							
r ₀ (predicted) ²	0.954		0.943		0.944							

¹ Van Westrenen and Draper (2007).

² Van Westrenen et al., 2001.

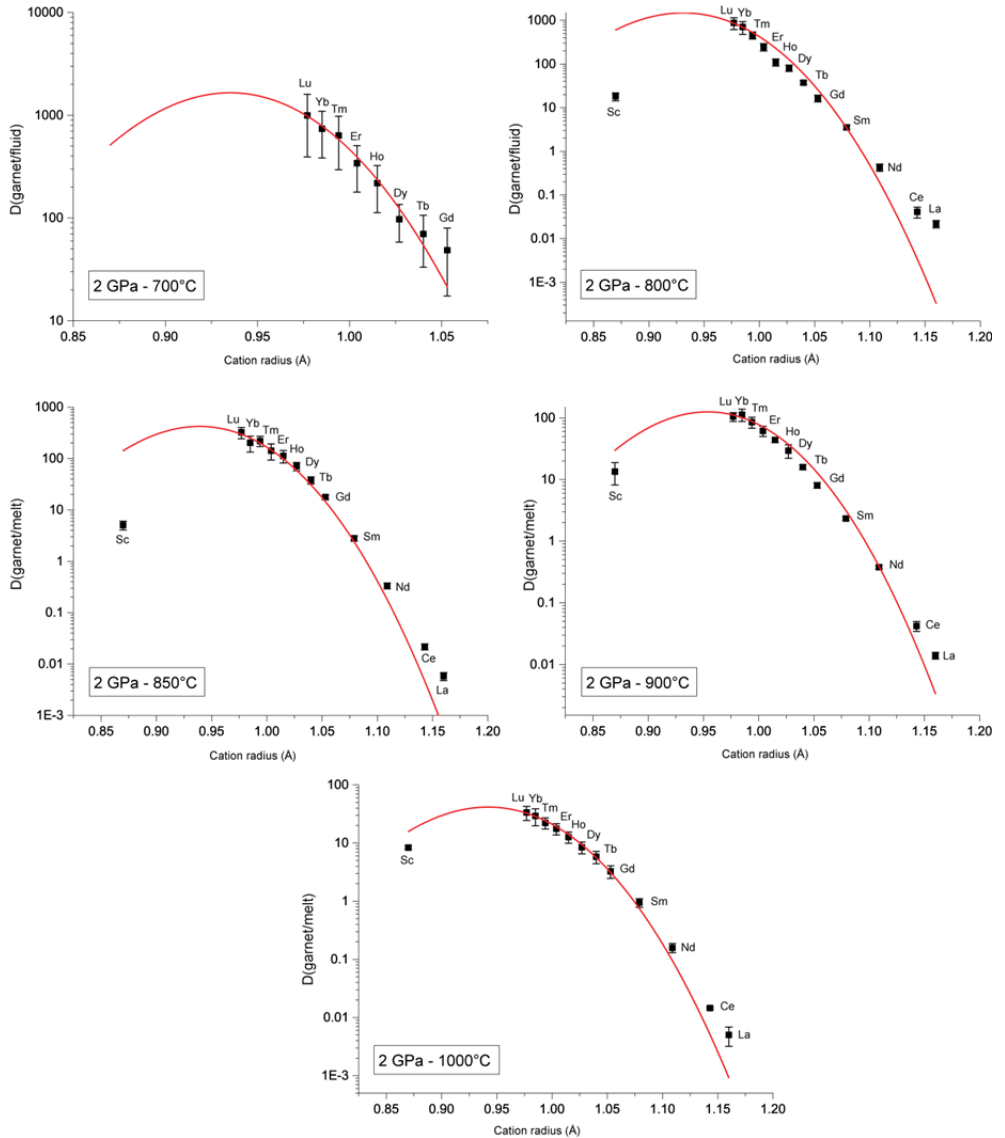


Figure B1. Partition coefficients (REE + Sc) for garnet against cation radius at 2 GPa and 700 to 1000°C (Chapter 4). Red line is a fitted parabola using the equation of Blundy and Wood (1994).

APPENDIX

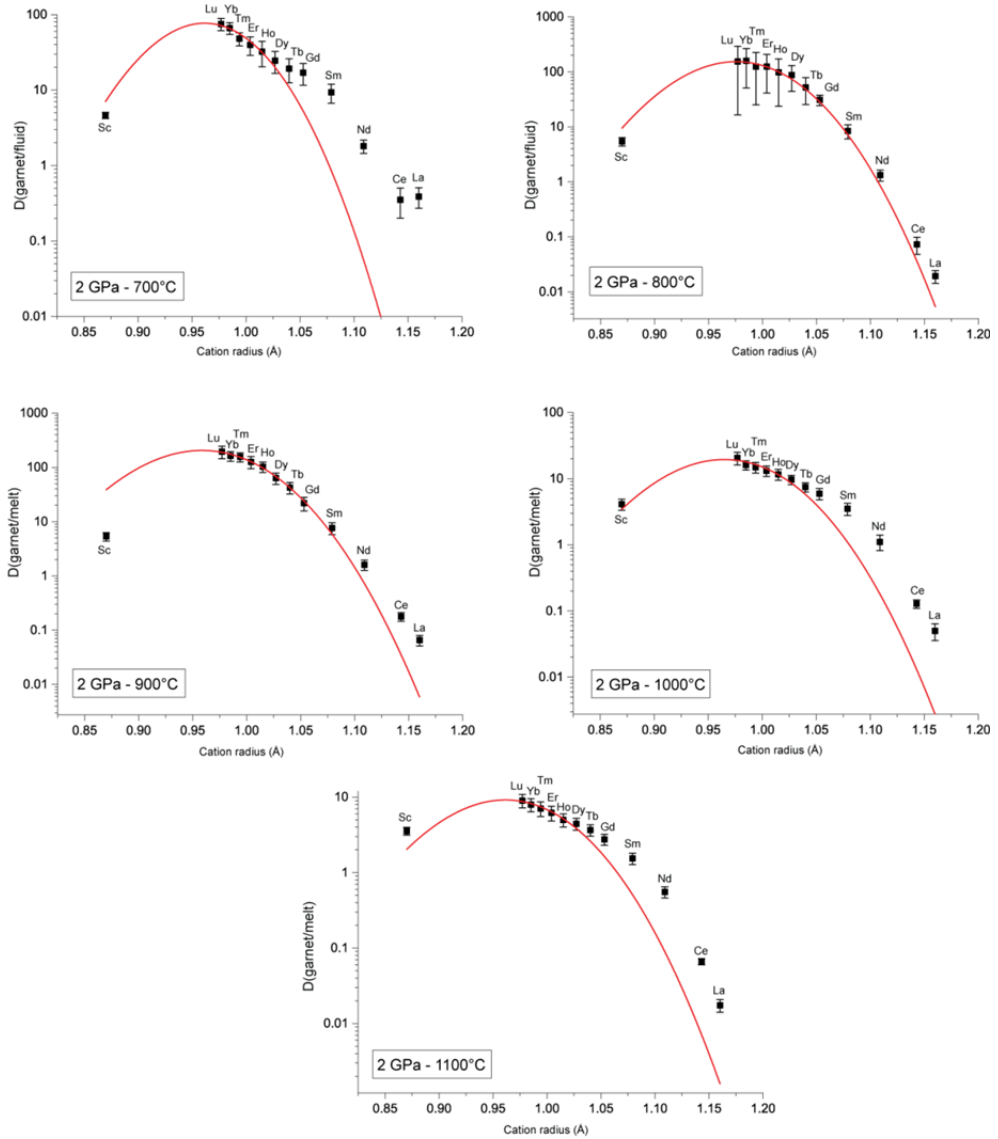


Figure B2. Partition coefficients (REE + Sc) for garnet against cation radius at 3 GPa and 700 to 1100°C (Chapter 4). Red line is a fitted parabola using the equation of Blundy and Wood (1994).

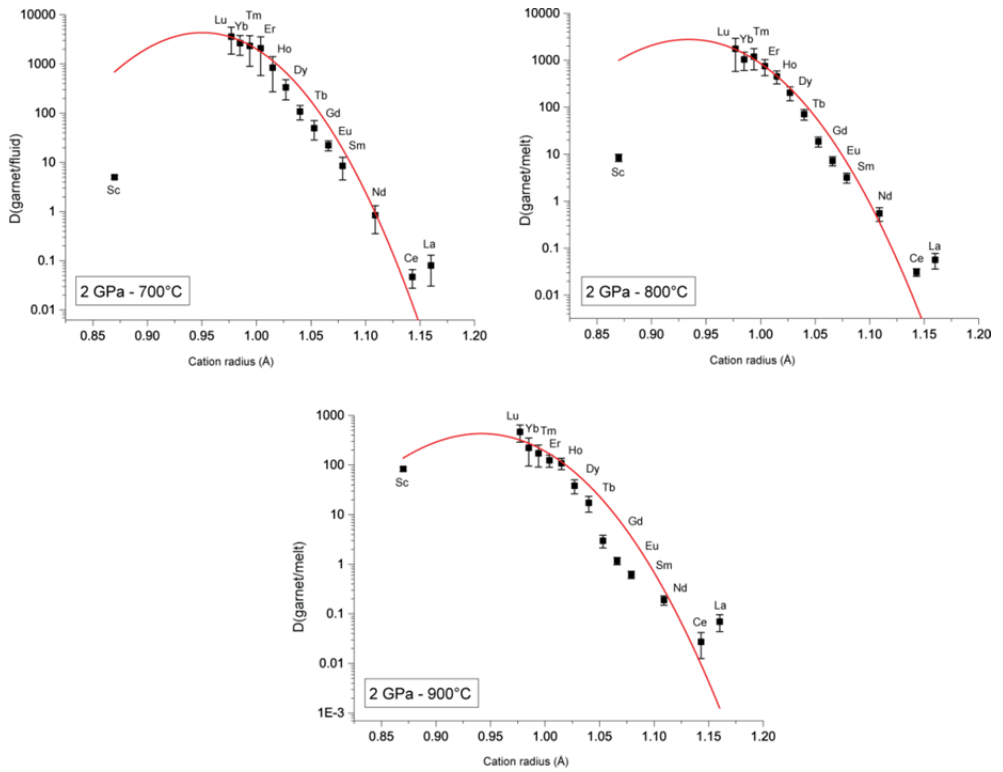


Figure B3. Partition coefficients (REE + Sc) for garnet against cation radius at 3 GPa and 700 to 900°C (Chapter 5). Red line is a fitted parabola using the equation of Blundy and Wood (1994).

Acknowledgements

I am very grateful to my supervisor, Peter Ulmer, in so many respects. When I knocked at his door to ask for a PhD position, he not only took the time and effort to write up a project, but he gave me the opportunity to work as his PhD student despite me lacking basically any background in experimental petrology let alone having ever set a foot into a high-pressure experimental lab. It is because of his continuous support, confidence and patience, his great knowledge, his positive way of handling things and his always open door (not just for me, but for everyone) that this thesis exists in its present form. Thank you so much.

Many thanks to my second supervisor, Thomas Pettke, who is always open and interested in questions and discussions and always has good advice, be it on a professional or personal level. The sessions in his laser-lab were always highly productive and I always left with the feeling that we did whatever possible could have been done. I also very much appreciate his huge effort in correcting the chapters of this thesis, which improved our work a lot.

Thank you, Max, for taking responsibility for this PhD thesis and for the very useful comments and suggestions that improved this work a lot. I am also grateful to Roland Stalder for coming to Zürich and being the external co-examiner and for reading and correcting the thesis very carefully.

Further on, I would like to thank the various people that helped me during the course of this PhD project: Arno and Christian for the help and advice in the piston cylinder labs (especially with the Shaker), Eric for the patient help with the microprobe and the assistance in designing a new, improved freezing stage; your technical knowledge is impressive. Without Urs, Bruno and Lydia the labs would not function as they do, thanks for always taking care and helping out, especially in emergency cases. A special thanks goes to Urs for building the freezing stage. Concerning the freezing stage I also want to thank Claudio a lot for sitting down with me for hours and drawing the construction plans. Claudia and Ursula, your administrative work is very much appreciated, thanks for always take care of everything and everyone. Giuditta, Corey, Markus and Marcel, thank you very much for analyzing solutions and glasses for me and for all the help. Finally, I would like to thank Susanne, who, especially in the final stages of writing up this thesis, helped me a lot in understanding how data can be linked to natural settings. Thanks for all the discussions, ideas and for the time you took to explain and discuss.

I had a whole group of different office mates during the last years, each one participated in the good atmosphere we always had in the office, thank you for your support, the chats, the fun, and the understanding. Thank you, Sasha, for being such a help and a good friend.

ACKNOWLEDGEMENTS

I could now fill a page with names of people that I met here and that improved my life at ETH and Zürich in terms of social life, however, I would like to mention the ones impacting my life the most. To all others, you know how very important and how fun it was/is to spend time with you! Marion and Gabriel, you were the best flat mates one could wish for, thank you so much for your friendship. The person studying and working with me the longest, Daniela, suffered probably the most from my ups and downs during this time. Nevertheless, she still sticks around, for that and for everything else, the good and the bad times, I cannot thank you enough. And to Niko, for being my anchor, especially during the difficult times.

Finally, I want to thank my family for their support, their interest and for making all of this possible.

Curriculum Vitae

Personal information

Name Stefanie Marianne Luginbühl
Date of Birth January 22nd 1980
Place of Birth St.Gallen, Switzerland
Citizenship Swiss

Education

2010 – 2015 PhD at Institute of Geochemistry and Petrology at ETH Zürich, Switzerland
PhD Thesis: Phase relations, compositions and trace element partitioning of solid and mobile phases in the hydrous MORB system at 2-3 GPa.
Committee: Prof. Dr. Peter Ulmer
Prof. Dr. Thomas Pettke
Prof. Dr. Max Schmidt
Prof. Dr. Roland Stalder

2002 – 2009 Diploma in Geology at University Zürich
Diploma Thesis: Relicts of an accretionary wedge: The Casanna nappe
Supervisors: Prof. Dr. Helmut Weissert
Prof. Dr. Stefan Schmalholz

1996 – 2002 Teacher's College, Rorschach, Switzerland

Work experience

2010 – 2014 Teaching assistant at Institute of Geochemistry and Petrology, ETH Zürich, Switzerland (lectures 'Metamorphism' and 'Kristalle und Minerale')
Assistant in field courses and excursions
Assistant for piston cylinder and preparation labs
Organization of the duties and responsibilities within the institute

Language skills

German: native
English: fluent in written and spoken language
French: good, written and spoken

